PREDICTION OF THE EFFECT OF BUILDING FACTORS ON THE MAGNETIC PERFORMANCE OF ELECTRICAL STEELS IN AUTOMOTIVE APPLICATIONS

By

Nicholas James Lewis

A thesis submitted to Cardiff University in candidature for the degree of

Doctor of Philosophy

Wolfson Centre for Magnetics

Cardiff School of Engineering

Cardiff University

July 2017

DECLARATION

This work has not been submitted in substance for any other degree or award at this or any other university or place of learning, nor is being submitted concurrently in candidature for any degree or other award.

Signed ……(candidate) Date ……..……

STATEMENT 1

This thesis is being submitted in partial fulfilment of the requirements for the degree of PhD.

Signed ……(candidate) Date ……..……

STATEMENT 2

This thesis is the result of my own independent work/investigation, except where otherwise stated, and the thesis has not been edited by a third party beyond what is permitted by Cardiff University's Policy on the Use of Third Party Editors by Research Degree Students. Other sources are acknowledged by explicit references. The views expressed are my own.

Signed ……(candidate) Date ……..……

STATEMENT 3

I hereby give consent for my thesis, if accepted, to be available online in the University's Open Access repository and for inter-library loan, and for the title and summary to be made available to outside organisations.

Signed ……(candidate) Date ……..……

ACKNOWLEDGEMENTS

This work was carried out at the Wolfson Centre for Magnetics, Cardiff School of Engineering, Cardiff University and was funded by the EPSRC and Tata Steel UK to which I am grateful for providing the equipment and materials needed to complete this project.

I would like to thank all the people who contributed in some way to the work described in this thesis. Firstly, I thank my academic advisor, Dr Philip Anderson for his advice, comments and ideas. His guidance and professional expertise improved my work and knowledge significantly. Secondly, I would like to thank Dr Jeremy Hall and Professor Antony Moses for their interest in my work, stimulation, encouragement and valuable discussion throughout this investigation.

In addition I also wish to thank Dr Yi Gao, my industrial supervisor for his experience and assistance.

Similarly, I would also like to thank members of the Wolfson Group for a supportive atmosphere and in particular, Dr Christopher Harrison, who provided valuable insights as well as Dr Piotr Klimczyk for this experimental work on bulk properties.

I would like to acknowledge friends, family and my girlfriend Dr Bethan Griffiths who encouraged me during my studies. I wish to express my greatest thanks to my father, Roger and mother, Christine for their constant support and motivation.

Finally, I would like to thank the staff of the electrical workshop, mechanical workshop, IT Support and research office, who provided valuable support.

SUMMARY

Electrical steel is the predominant material used for the magnetic cores of electrical machines, such as the rotors and stators of electric motors. The cutting of electrical steel during the motor manufacturing process is detrimental to the magnetic properties and consequently the properties in operation will be different from those measured, on strips, by the steel manufacturer. The ability to predict the effect of the manufacturing processes on the magnetic performance would be of great benefit to the electrical machine designer.

An enhanced system was developed to measure the local magnetic properties with the addition of being able to accurately map the properties of complex geometries in a time efficient manner. The local magnetic properties of 0.35 mm thick 2.4 % and 3.2 % silicon, punched non-oriented electrical steel rings with constant outer diameter and varying inner diameter were measured to explore and predict the effect of punching.

The distinct contrast in flux density profile between the grades was attributed to spreading of residual stress from punching. The 3.2 % Si samples showed a degradation depth consistent between ring widths and extending 2.5 ± 0.5 mm from the edge, while the 2.4 % Si samples displayed a more gradual decrease.

Original models were proposed to predict the increase in power loss and the flux density profile based on the residual stress distribution. This novel modelling approach, validated using FEM software, could accurately reproduce the flux density profile and showed good agreement with experimental results, within 5% for most data points.

The integration of this four-parameter model into FEM packages could greatly aid the designers of EMs by improving the ability to accurately predict the flux density throughout a motor core, ultimately improving the efficiency of these machines.

LIST OF ABBREVIATIONS

AC	Alternating Current
AWJ	Abrasive Water Jet
CNC	Computer Numeric Control
DAQ	Data Acquisition
DPM	Discreet Permeability Model
DC	Direct Current
EDM	Electric Discharge Machining
ES	Electrical Steel
EV	Electric Vehicle
FEA	Finite Element Analysis
FEM	Finite Element Method
GOES	Grain Oriented Electrical Steel
HAZ	Heat Affected Zone
HEV	Hybrid Electric Vehicle
ID	Internal Diameter
MOKE	Magneto-Optical Kerr Effect
NI	National Instruments
NOES	Non Oriented Electrical Steel
OD	Outer Diameter
RD	Rolling Direction
SST	Single Strip Tester
TD	Transverse Direction
THD	Total Harmonic Distortion
VPM	Variable Permeability Model

CONTENTS

CHAPTER 1.

INTRODUCTION

The development of electric (EV) and hybrid electric (HEV) vehicles has been driven in recent years by the desire to be more environmentally friendly. Almost all automotive manufacturers have active EV/HEV development programmes with the number of models available for purchase increasing year by year. Requirements by governments and consumers for decreases in carbon emissions, improvements in air quality and reduced reliance on fossil fuels has placed an onus on motor manufacturers to improve the fuel efficiency of their vehicles and subsequent reduction of exhaust gas. One method of achieving this is using vehicles powered by the use of electricity such as EV/HEVs where small improvements in machine efficiency can give a significant improvement in range, which is critical to the mass uptake of electric vehicles. Performance improvements on existing designs can be obtained through increasing the efficiency of the traction motor. The functional magnetic material in the core of the motors is crucial for the electro-mechanical conversion and is required to have many and often competing properties.

Few materials satisfactorily balance the different requirements for an electric motor more economically than non-oriented electrical steel (NOES). Mechanical punching, which is low cost and suitable for high volumes, is the most popular cutting method. Therefore the laminations, used in motor cores are largely produced by punching from NOES sheets.

The traction motors that are used in EV/HEVs place significant demands on the materials from which they are made. Designers of these machines require detailed knowledge of the magnetic properties of these materials to allow them to optimise their

designs. This data is made available by the electrical steel producers based on a set of standard tests performed straight off the production line. These tests are performed under conditions and with assumptions that are undermined by the manufacturing process and in particular, the punching of the laminations which introduces plastic and elastic stress/strain resulting in an increase in power loss. The properties of the material in operation, however, are significantly different due to the motor manufacturing processes. The ability to predict the magnetic properties in operating conditions would be of great benefit to the designers of electrical machines.

Considering the growing importance of improved electrical machine efficiency in society, the role that electrical steel plays and the effect the manufacturing processes have on their performance. The main objectives of this research project are as follows;

- Develop experimental methods to investigate and map the variation in the local magnetic properties of electrical steel.
- Develop a detailed understanding of the effect of manufacturing processes, in particular the effect of punching on the magnetic properties of electrical steel.
- Develop a detailed understanding of the effect of operational conditions such as stress on the magnetic properties of electrical steel.
- Create models to predict the effect of punching in electrical steel laminations with the aim of incorporation into existing FEM software.

CHAPTER 2.

BACKGROUND KNOWLEDGE AND LITERATURE REVIEW

2.1. COMMON TERMS IN MAGNETISM

2.1.1. Magnetic Field

A magnetic field is a region of space which experiences a change in energy over the region which sets up an energy gradient. The consequence of this is that a magnetic material placed in this region will experience a force. This force can be manifested as an acceleration of a charged particle, the torque on magnetic dipoles or even changes in the spin states of some atoms.

A magnetic field is produced whenever there is a charge in motion. This could be by the flow of current through a conductor or the orbital motion and spin of the electrons which give each atom its own magnetic dipole moment or just magnetic moment, m. This is a vector specifying the magnitude and direction of the magnetic field produced by that atom. Each atomic moment is very small but the alignment of many atomic moments can produce a measurable magnetic field around a material.

Shown below in Fig. 1. is a bar magnet and its associated field lines which are the direction of the magnetic field at that point. By convention the poles, where the fields lines converge on the surface of the material and where the field is strongest, are designated as north and south with the direction of the field from north to south.

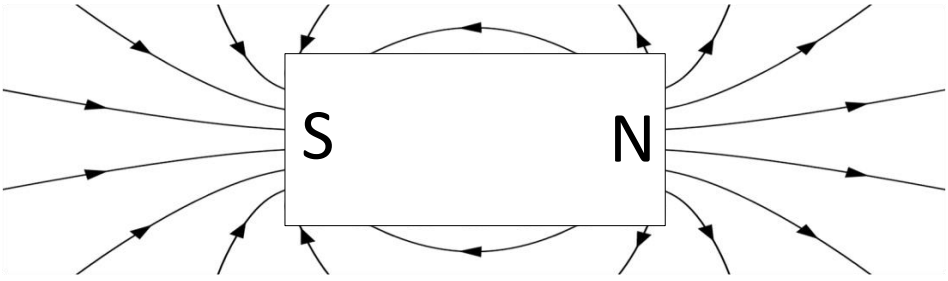

Figure 1: Typical magnetic field distribution for a bar magnet

The strength of the magnetic field generated by an electric current can be calculated using the Biot-Savart law [1] and is in SI units of kg s^{-2} A^{-1} or Tesla, T

$$\delta \boldsymbol{B} = -\frac{\mu_0}{4\pi} I \frac{\boldsymbol{r} \times \delta \boldsymbol{l}}{r^3} \tag{1}$$

The flow of current through a coil of wire, known as a solenoid will create a magnetic field similar to that of a bar magnet shown in Fig. 2. The strength of the magnetic field, *H* inside the solenoid can be defined by (2) where *n* is the number of turns, *I* the current and *l* the length of the solenoid.

$$H = \frac{nI}{l} \tag{2}$$

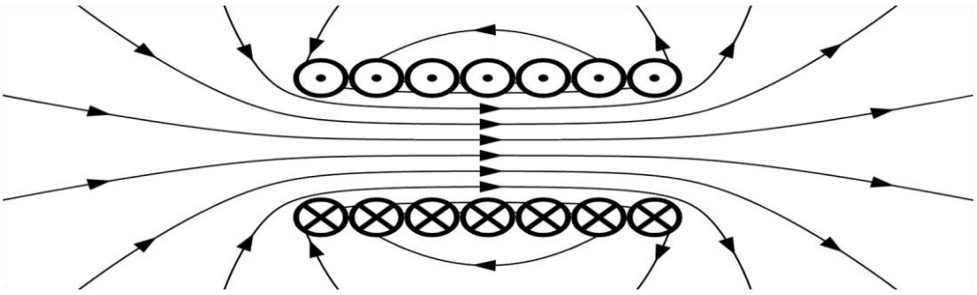

Figure 2: Magnetic field distribution around a solenoid

2.1.2. Magnetic Induction

The magnetic induction, which is also known as the magnetic flux density or just flux density, describes the effect that the magnetic field has on a region of space The relation between B and H can be described by (3)

$$\boldsymbol{B} = \mu \boldsymbol{H} \tag{3}$$

Where in free space $\mu = 1.257 \times 10^{-6}$ Hm^{-1} and is referred to as the permeability of free space or the magnetic constant and given the symbol, μ_0.

A magnetic field acting upon a material will cause alignment of the permanent magnetic dipole as well as induce magnetic dipoles. A material can be categorised as diamagnetic, paramagnetic or ferromagnetic depending on its response to an applied field

and (3) can be rewritten as

$$\boldsymbol{B} = \mu_0 \mu_r \boldsymbol{H} \tag{4}$$

Where μ_r is the relative permeability and for some materials is non-linear.

2.1.3. Origin and Types of Magnetism

Atoms have their own intrinsic magnetic moment, called its spin comprising of contributions from the nucleons spin, the electrons orbital motion and by far the biggest contributor, the electron spin. In most elements, these cancel out but in some, the spin of these outer electrons can sum and as a result the atom can have a net magnetic moment.

The electron, having its own intrinsic magnetic moment known as its spin can be thought of as a tiny magnetic dipole each with its own magnetic moment, m. The electrons inhabit orbital shells of increasing energy each described by their own unique set of quantum numbers *n,l*, and m because of the Pauli exclusion principle. Orbits can contain two electrons provided their spins are antiparallel and this has the effect that the vector sum of the magnetic moments cancel (full shells will also lead to a cancellation of magnetic moments).

Depending on how the shells fill up there are different types of magnetism. Diamagnetism, where atoms or molecules with full atomic shells act in opposition to an applied magnetic field. Paramagnetism consists of atoms with partially filled shells which will align with an applied field. The effect of these two types of magnetism is small compared to that of Ferromagnetism, whose materials such as iron can have permutabilities thousands of times greater.

Ferromagnetic atoms have a half full outer or valence shell and due to another quantum mechanical effect, the exchange interaction which minimises the coulomb force between neighbouring atoms by the arrangement of the valence electrons so that their spins are parallel to one another which results in a net magnetic moment. The electron's

energy levels for iron, showing the partially filled 3d shell with parallel electrons are shown in Fig. 3.

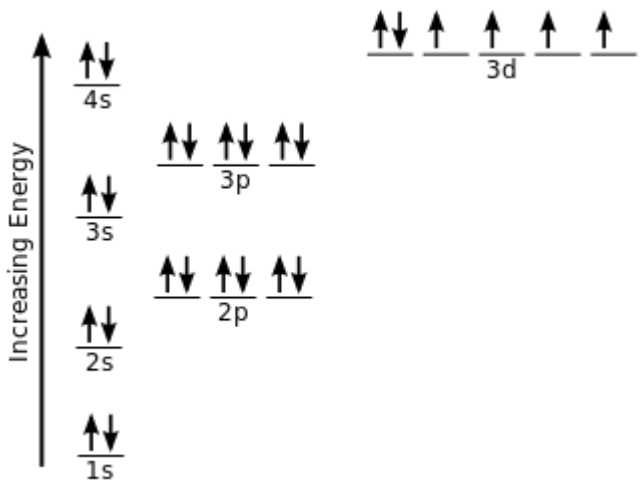

Figure 3: Electron energy levels for iron, a ferromagnetic material with a half filled 3d band.

In a bulk material, this alignment would lead to the material being magnetised to saturation and have a high magnetostatic energy. Since nature always moves towards the lowest energy state, the ferromagnetic material divides itself into small regions called domains [2]. Each domain is magnetised to saturation with its individual atoms aligned parallel and general preferring certain directions called easy axes which are defined by the crystal anisotropy.

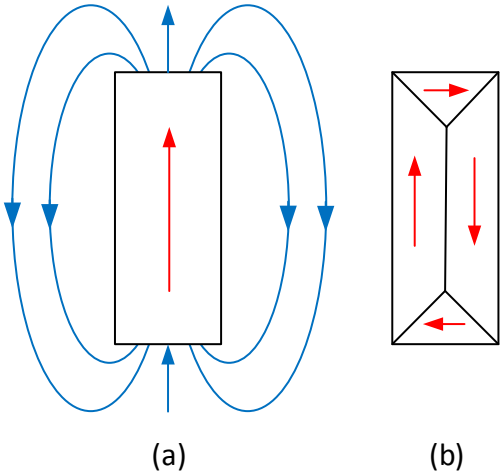

Figure 4: Single domain (a) with a large magnetostatic field and (b) multiple domains including flux closure domains with no stray field.

In order to reduce the magnetostatic field, flux closure domains near the surfaces are created, shown in Fig. 4, these may have an additional energy associated with them.

The domains are separated by narrow regions where the direction of magnetisation changes gradually over the length of this region, these boundaries are called domain walls. There are two types of domain walls Bloch walls, shown in Fig. 5, where the magnetisation vector is perpendicular to the plane of the domain wall and is the type of wall generally found in bulk materials. In thin films, Neel walls exist where the rotation of the magnetisation vector rotates in the plane in a helical manner, shown in Fig. 6.

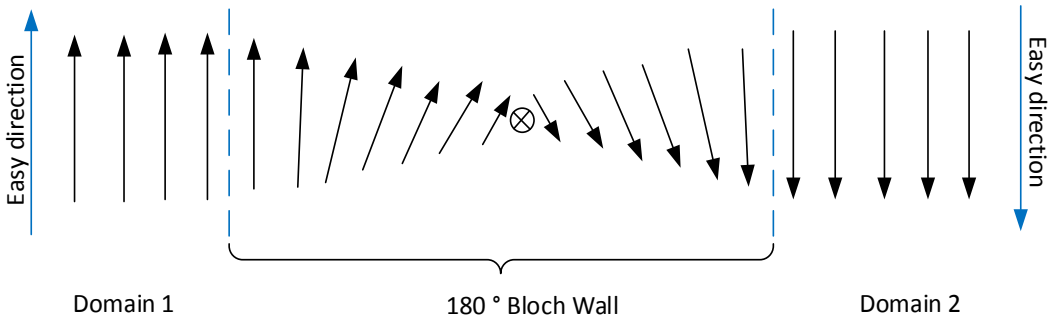

Figure 5a: A Bloch wall where the neighbouring magnetisation vectors gradually rotate 180° over several hundred atomic spacings.

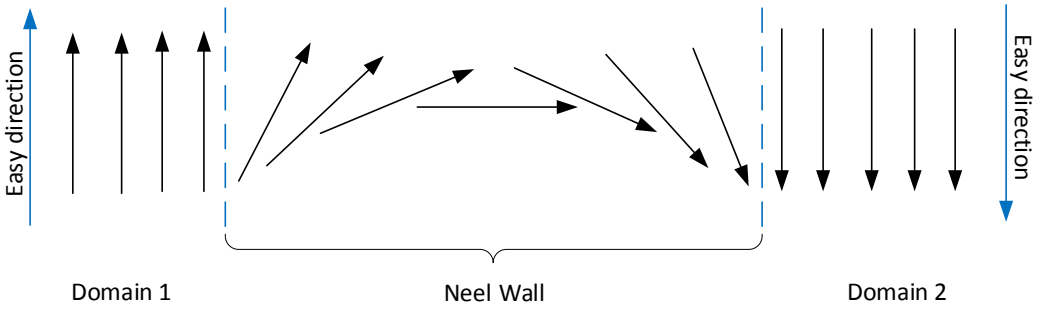

Figure 5b: A Neel wall where the neighbouring magnetisation vectors rotate in the plane.

Domain walls are classified by the angle in which they sweep when going from one domain to another such as 180° or 90° walls. The wall will have an energy associated with it due to non-parallel moments and magnetising vectors directed in a non-easy direction

which is minimised by a reduction in the number and thickness of walls.

In summary, for bulk ferromagnetic materials numerous domains, separated by domain walls, usually Bloch walls, are orientated in such a way throughout the material so to minimise the sum of the magnetostatic, domain wall, anisotropy and magnetoelastic energies, which are discussed further in section 2.2.4 and 2.2.5 respectively.

2.1.3.1. Magnetising Process

When an external magnetic field is applied, it has the effect of aligning the domains in the direction of the applied field. First domains that have a favourable magnetisation direction with respect to the applied field increase in volume at the expense of ones that are not via movements of the domain walls. The motion of the domain walls will be impeded by defects in the crystal lattice caused by grain boundaries, stress centres, dislocations or inclusions. This is because the domain wall energy is reduced near these inhomogeneities and as such the domain walls get pinned at these sites requiring an increase in field strength to overcome these "pinning sites". When domain wall motion can no longer reduce the total energy and if the applied field is increased further the domains will rotate, as shown in Fig. 6.

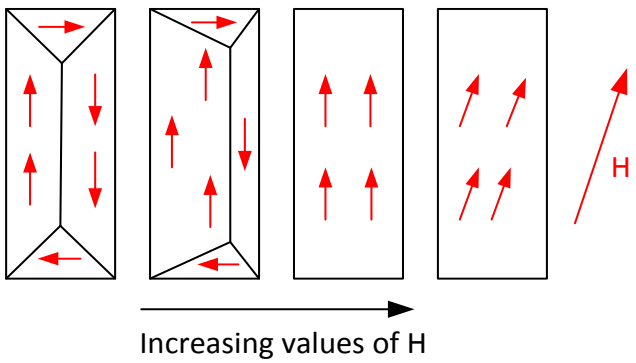

Figure 6: Example of the magnetising process for a simple domain structure.

Continued increase of the applied magnetic field will result in the decrease in the number of domain walls until there is only one domain magnetised in the direction of the

applied field and the material is said to be fully saturated.

With decreasing field strength, the flux density does not trace the same curve but lags behind, this is known as hysteresis. A complete cycle will form a loop known as a hysteresis or BH loop, shown in Fig. 7 from which the materials basic magnetic properties can be deduced.

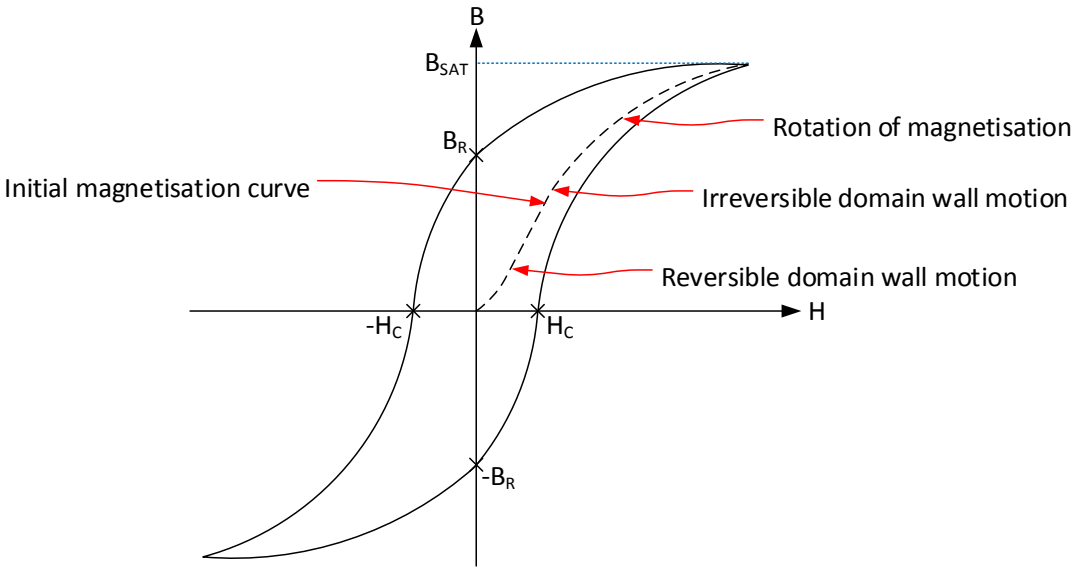

Figure 7: Typical hysteresis or BH loop

When the applied magnetic field is reduced to zero, a certain amount of flux density remains. This is called the remanence flux density, B_R.

2.1.4. Magnetic Materials

The coercive force, H_c , is the magnetic field that is needed to coerce or force a magnetised material to become demagnetised, i.e. have a flux density of $B = 0$. Magnetic materials can be classified into hard or soft materials depending on their coercive force. Soft materials have a narrow hysteresis loop and a low coercive field strength (roughly less than 10^3 A/m) and hard materials have a wider hysteresis loop and a coercive field strength typically greater than 10^4 A/m.

2.2. ELECTRICAL STEEL

Electrical steel, which is also called lamination steel, silicon steel, or transformer steel, is steel that has been manufactured in such a way as to emphasise and take advantage of certain desirable magnetic properties, such as a small hysteresis area (small energy dissipation per cycle, or low core loss) and high permeability. The electrical steel that comprises the cores of electrical machines: transformers, generators and motors can be further classified as low-carbon steel, grain oriented silicon steel and non-grain oriented silicon steel. These materials are collectively referred to as electrical steel with the predominant choice for motor cores being non-grain oriented silicon steel.

Electrical steel is an alloy which consists of iron (Fe) with a small percentage of silicon (Si) between 0 and 6.5% also manganese and aluminium can be added in quantities of approximately 0.5%. A typical commercial grade will contain up to about 3% silicon.

2.2.1. How Does Electrical Steel Differ from Other Steels?

The result of the blast furnace is cast iron which will contain about 4% carbon along with small amounts of other elements including manganese and silicon. Cast iron is brittle and unsuitable for many applications the carbon is reduced to about 0.2% and other elements removed through various manufacturing processes and this is mild steel which is much more suitable for used extensively.

To further enhance the magnetic properties the carbon content is further reduced to as low a level that is economically viable and can be as low as 0.001 % [3]. The magnetic properties of a soft magnetic material depend on its ability to alter its domains as quickly and easily as possible to vary the overall magnetisation of the metal. Any non-metallic inclusions in the metal will hinder the process of domain wall motion and make magnetisation harder. A lot of effort is put into reducing the non-metallic inclusions

incorporating carbon, sulphur, oxygen and nitrogen with levels as low as practically possible [4]. These form carbides, sulphides, oxides and nitrides. For carbon which is highly detrimental a typical level would be less than 0.005%.

Other elements such as silicon, manganese and aluminium which form AlN and MnS are alloyed to the steel to improve the properties [5] the most common being silicon which has the benefits of increasing the electrical resistivity which causes a reduction in the eddy currents and therefore the associated losses. It decreases the crystal anisotropy which causes an increase in permeability. These advantages must be weighed against the fact that silicon additions decrease the saturation induction and can make the alloy brittle so that it will become difficult to work when the silicon content exceeds about 5%

2.2.2. Crystal Structure

As molten iron cools it crystallises the type of crystal and the allotrope of the iron depends on the temperature. Below the Curie temperature, T_C (1043K) the iron has a body centred cubic, bcc crystal structure, shown in Fig. 8. It is the α-iron allotrope known as ferrite.

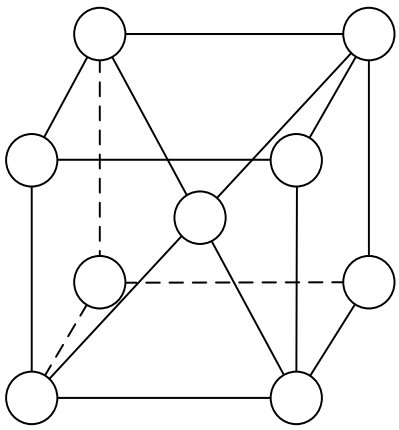

Figure 8 - Crystal structure of body centred cubic (bcc) iron

Iron like many other metals is a polycrystalline material, it consists of many different crystallites or grains which locally form an ordered lattice in 3-dimensions.

These grains then have different orientations throughout the material. The orientation of the grains is called the texture of the material. A material with grains orientated randomly throughout material is said to have no texture. If the orientation of the grains is not random and has a particular preferred orientation the material is said to have texture and the strength of the texture is dependent on the percentage of the grains orientated in the preferred direction. A small percentage is said to have a weak texture while a large percentage is referred to as strong texture.

A popular convention for describing the planes and directions of crystal is *Millar indices* the planes are enclosed in parentheses such as the six faces of a cube: (001), (010), (001), $(\bar{1}00)$, $(0\bar{1}0)$ and $(00\bar{1})$ where the line above the number refers to the antiparallel direction and the indices of any one face enclosed in curly bracket e.g. {100} represent the whole set. Directions are enclosed in square brackets and the directions of the six cube edges would be [100], [010], [001], $[\bar{1}00]$, $[0\bar{1}0]$ and $[00\bar{1}]$. Similarly, the whole set is described using chevrons e.g. ⟨001⟩.

The atoms in metals arrange themselves into crystallographic lattices, repeating 3-dimensional arrays, and a large sample will generally not consist of one lattice but formed of many smaller lattices at different geometric orientations known as grains. On a microscopic level, two types of irregularities can be observed in the lattice structure; point defects affecting individual sites and line defects affecting a plane of atoms. Point defects located at a single lattice site and can include vacancy defects; where an atom is missing, substitutional defects; where a different type of atom replaces a metal one, and interstitial defects; where there exists an atom where there is not normally one. Line defects include edge defects where an additional half plane is inserted into the lattice and screw defects where planes are offset in a helical pattern, shown in Fig. 9.

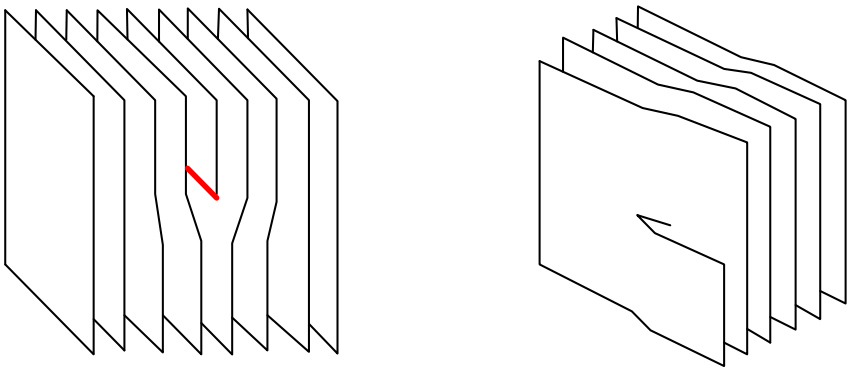

Figure 9 - Edge dislocations (left) and screw dislocations (right)

2.2.2.1. Deformation

Plastic deformation is caused as the dislocations traverse through the material. The less movement of the dislocations the less plastic deformation and the harder a material is said to be. The movement of the dislocations through the lattice structure can be restricted if it comes into contact with anchor or pinning points which are created by the intersection of a second dislocation or contact with interstitial atoms.

2.2.3. Anisotropy

The texture of iron influences the magnetic properties, with it being easier to magnetise the material in some directions compared to others. This is called crystal anisotropy or magnetocrystalline anisotropy. For bcc iron the ⟨100⟩ direction has the lowest density of atoms and is the easy axis, the ⟨111⟩ direction has the highest density of atoms and is the hard direction with ⟨110⟩ being the medium axis. The permeability is highest in the easy direction, lowest in the hard direction and of an intermediate value in the medium direction. [6]

A bulk piece of iron will have many crystal grains each with their own easy axis of magnetisation pointing in random directions, thus the sample as a whole will have similar magnetic properties in all directions. The anisotropy of a single crystal of bcc iron is shown in Fig. 10.

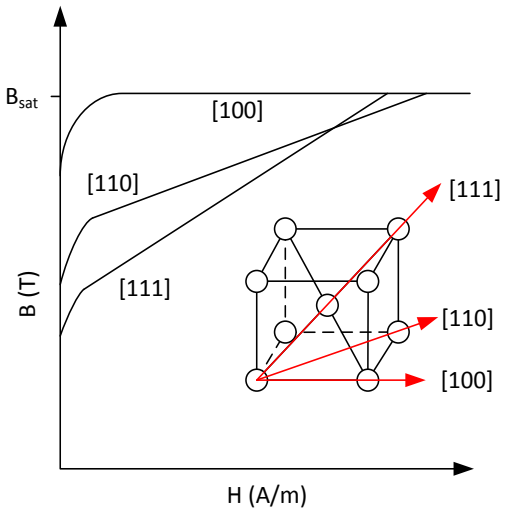

Figure 10 - Magnetic anisotropy of a single crystal of bcc iron. Showing the magnetisation curves for the easy [100], medium [110] and hard [111] directions; (B) magnetisation, (H) magnetising field.

In many materials including rolled metal sheets, the production process will impart some order into the material, increasing the amount of grains whose easy axes are aligned in a common direction, the direction along which the material was rolled, known as the rolling direction (RD). This commonality of the grains easy axis direction results in the material having anisotropic magnetic properties.

The orientation of the grains of electrical steel can be further refined and encouraged through additional manufacturing steps to produce what is known as Grain-Oriented Electrical Steel (GOES). Electrical steel produced without these additional steps is called Non-Oriented Electrical Steel (NOES), which despite its name does have anisotropic magnetic properties but just oriented to a lesser degree.

The physical origin of the crystal anisotropy is the spin-orbit coupling. This is the interaction between the intrinsic magnetic moment of the electron, it's spin S and the magnetic moment provided by its orbital contribution L.

For a demagnetised sample the many domains, although magnetised in random directions, will have a magnetisation direction along one of the six easy directions. In order to orientate the magnetisation vector away from an easy axis, there must be work

done against this anisotropy force and the energy needed to do this is called the Crystal Anisotropy Energy. In a cubic crystal, the value of this energy can be given by (5).

$$E_{anisotropy} = K_0 + K_1(\alpha_1^2\alpha_2^2 + \alpha_2^2\alpha_3^2 + \alpha_3^2\alpha_1^2) + K_2(\alpha_1^2\alpha_2^2\alpha_3^2) + \cdots \quad (5)$$

Where K_0, K_1, K_2,.. are constant that are dependent on the material and Where $\alpha_i = \cos\theta_i$ and θ_i are the angles between the magnetization and the easy axes.

The energy, $E_{anisotropy}$ will be a minimum when M_s is directed along the easy axis.

2.2.4. Magnetostriction

The application of a magnetic field will cause a magnetic material to change shape, this is called magnetostriction conversely applying a tensile or compressive stress will alter the magnetisation. This is called the magnetomechanical or magnetoelastic effect.

A ferromagnetic material below the Curie temperature is divided into domains and when the material is subjected to an applied field the domain walls move and rotate which produces a strain and a resulting change in length. For iron, there is an increase in length and it is said to have positive magnetostriction, shown schematically in Fig. 11.

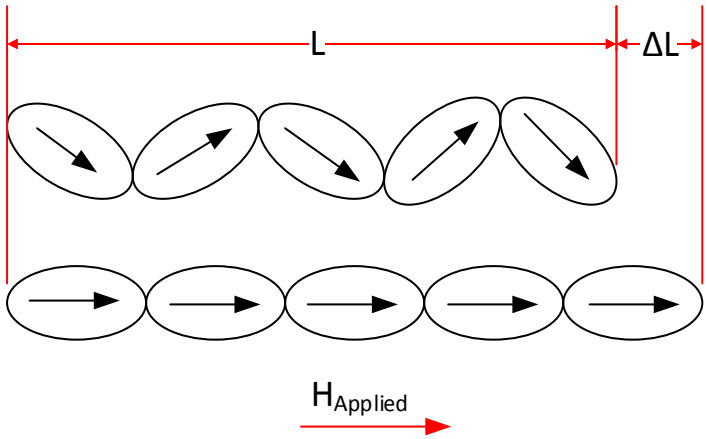

Figure 11:Schematic to illustrate the magnetostriction of a ferromagnetic material

The magnetostriction, λ is defined as the ratio of the change in length to original

length (6).

$$\lambda = \frac{\Delta L}{L} \tag{6}$$

2.2.5. Magnetoelastic Anisotropy

The electrons magnetic moment is generated by its spin and orbital motion. These two factors are connected to each other or coupled, meaning changing one will cause a change in the other, and is called spin-orbit coupling. The orbit of the electron will also be influenced by the atomic nucleus, the arrangement of which makes up the crystal lattice, this is referred to as orbital-lattice coupling. Changing the lattice structure, for example by applying stress can change the shape of the electron cloud, effecting the orbital motion which alters the electron spin and ultimately the magnetisation of a material. This produces a magnet anisotropy called magnetoelastic anisotropy.

For a material with isotropic magnetostriction, the magnetoelastic anisotropy energy per unit volume is given by (7) [6]

$$E_{me} = K_\sigma \sin^2 \theta \tag{7}$$

Where θ is the angle between direction of magnetisation and the stress, σ and K_σ is defined by (8)

$$K_\sigma = -\frac{3}{2}\lambda\sigma \tag{8}$$

Polycrystalline materials, such as electrical steel have magnetostriction constants, λ_{ijk} which are defined for the different crystal axes. Cubic structures like that of electrical steel have two relevant magnetostriction constants λ_{100} and λ_{111} which are measured in the $\langle 100 \rangle$. and $\langle 111 \rangle$. directions respectively. When the material is composed of many grains with varying orientations the magnetostriction constant, λ can be derived using (9) [7]

$$\lambda = \frac{1}{2}(2\lambda_{100} + 3\lambda_{111}) \quad (9)$$

A magnetic material balancing the different energy terms to obtain a minimum energy state must take into account changes in the magnetoelastic energy as a result of stress, whether this is externally applied stress or stress cause by internal inhomogeneities in the microstructure. An increase or decrease in magnetoelastic energy will be determined by the sign of the stress and magnetostriction constant of the material, illustrated in Fig. 12.

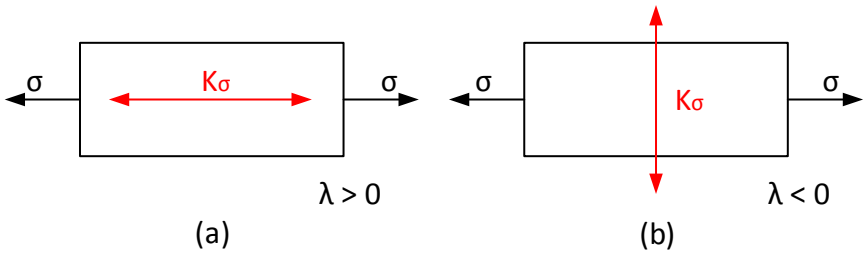

Figure 12 – Orientation of magneoelastic anisotropy for a material with a positive magnetostriction (a) and a negative magnetostriction (b).

The sign of the magnetostriction constant depends on many factors including temperature, strength of magnetising field, the composition of the alloy and direction in which it is measured, and may be positive or negative. Single crystals of Fe-Si alloys with a low Si content measured along the ⟨100⟩ direction have a positive magnetostriction constant, as the Si content increases the magnetostriction constant decreases becoming zero for approximately 6.5 % Si and negative for Si > 6.5 %. The magnetostriction constant in the ⟨111⟩ direction goes from negative to positive with increasing Si, with zero magnetostriction at approximately 5 % Si [3]

For NOES The magnetostriction constant has be observed to vary with orientation to the rolling direction (RD), shown in Fig. 13 taken from [8].

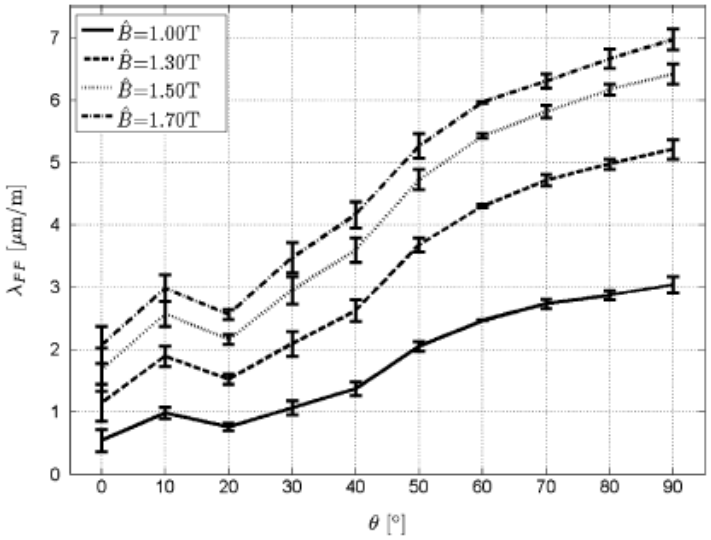

Figure 13 – Peak to Peak magnetostriction of 0.5 mm thick NOES measured at 50 Hz and at various flux densities and angles to the RD.

The application of a tensile stress to a material with a positive magnetostriction constant generates an easy axis of magnetoelastic energy parallel to the stress direction as a result the BH loop to become squarer, while the same tensile stress in a material with a negative magnetostriction constant would result in an easy axis of magnetoelastic energy perpendicular to the stress direction and cause the BH loop to flatten.

2.3. POWER LOSS IN SOFT MAGNETIC MATERIALS

The energy needed for the ferromagnetic material to be magnetised through a hysteresis cycle is not totally conserved. The input provided by the power supply is greater than the output with the difference converted into heat inside the material. This is the power loss sometimes called iron loss or core loss.

The power loss per core mass per magnetising cycle corresponds to the area enclosed by the AC hysteresis loop divided by the density. This is typically multiplied by the frequency to given the specific power loss per mass (10) in units of W/kg.

$$P_{specific} = \frac{f}{\rho} \int H.dB \tag{10}$$

The power loss is usually stated for a given maximum flux density, B_{max} and frequency, f. The total loss is generally split up into two components (11), the hysteresis loss and the eddy current loss.

$$P_{total} = P_{\text{eddy}} + P_{hysteresis} \tag{11}$$

Senda [9] [10] used a needle probe with 10 mm spacing and a Hall effect sensor discussed in section 3.1.1 to measure local power loss in GOES. The measurement point was represented by the midpoint between two needles and it was found that the local flux density and power loss of a sample vary from the measured whole sample average with a standard deviation of 8.5 % and 26.7 %

Xu [11] used a needle probe and Hall sensor to scan GOES samples finding that the local power loss depends heavily on the local flux density and magnetising field, which in turn is influenced by grain boundaries.

2.3.1. Hysteresis Loss

The hysteresis loss is the proportion of the total loss caused by hysteresis and is proportional to the area enclosed by the area of the DC hysteresis loop. In practice, these

are obtained using a quasi-DC loop (AC loop with very low frequency) or extrapolated back to zero frequency.

The principle of minimum total potential energy states that a system will tend towards a state of minimum potential energy. For a ferromagnetic material with no external field, this is achieved by the creation and distribution of domains in which their magnetisation vectors sum to zero. When an applied field is introduced the minimum potential state is when the magnetisation vectors of the domains are aligned with the applied magnetic field until a position of equilibrium is reached; the higher the applied field the more alignment required. This is accomplished by an increase in the size of the domains with magnetisation aligned to the applied field at the expense as those not, followed by the rotation of the domains magnetisation vector to align with the applied field. These two processes have potential energy barriers to overcome in the form of the wall and crystal anisotropy energies respectively causing the movement of the domain walls to happen in a stepwise manner known as Barkhausen jumps. These movements generate micro eddy currents which dissipate energy as heat. The reversal of the direction of the applied field will repeat this process with the domains aligning with the new field direction and tending towards the new minimum.

2.3.2. Eddy Current Loss

The introduction of an alternating current around a ferromagnetic material will generate an alternating magnetic field within the material. Therefore by Faraday's law, an emf will be induced in the material proportional to the rate of change of the magnetic field inducing it. This emf causes a current to circulate within the material (whose direction is stated by Lenz's law), this eddy current experiences a resistance which generates heat. It is these currents and the subsequent energy dissipated as heat that lead to the power loss which is proportional to i^2R where i is the eddy current and R is the resistance of its path.

The size of the current in any particular loop is proportional to the area of that loop. It is because of this that cores are made of stacks of thin laminations electrically insulated from each other in order to reduce the eddy current loss.

These current loops will themselves generate magnetic fields and the summation results in an eddy current magnetic field that is at its maximum in the centre of the material and its minimum on the surface. The superposition of these magnetic fields has the effect of shielding the interior of the material from the applied field so that the applied field is concentrated at the material surface.

The eddy current loss can be calculated from Maxwell's equation with some important assumptions, namely that the magnetisation of the sample is assumed to be uniform in space, always parallel to a single axis and varying sinusoidally with time; this makes it straightforward to calculate the voltage around a closed path. The electrical resistivity is assumed to be isotropic therefore the current is directly proportional to the voltage and the instantaneous power as a product of current and voltage can be calculated.

This gives the classical eddy current loss equation (12) per unit mass. [2]

$$P_{\text{eddy}} = \frac{\pi^2 f^2 B_{max}^2 d^2}{6\rho D} \tag{12}$$

In which the sample has thickness d (m), the density D (kg/m^3) and resistivity ρ (Ωm). The constants can be combined to give the eddy current coefficient (13) as.

$$k_{\text{eddy}} = \frac{\pi^2 d^2}{6\rho D} \tag{13}$$

2.3.3. Excess Loss

There is a difference between the measured loss and what is expected from the addition of the hysteresis and eddy current losses. This is called the excess loss. The excess power loss is also caused by the motion of the domain walls as they are forced to change under the application of an applied field. The loss was characterised by (14) [2].

$$P_{\text{excess}} = \left(\frac{0.1356 w d H_0}{\rho}\right)^{1/2} \left(\frac{dB}{dt}\right)^{3/2} \quad (14)$$

Where w is the width (m) and H_0 is the strength of the demagnetising field generated by the magnetisation within the material (A/m).

2.3.4. Predicting Power Loss

Predicting the power loss at different operating conditions is difficult and in practice often accomplished by using empirical models such as the Steinmetz model (15) developed over 100 years ago which has been modified from the original paper [12] including inserting a component for frequency. The power loss is proportional to the frequency as not only will the walls be moving more often but they will have to move faster, increasing eddy currents and it has been shown by several investigators [6, 13] that the number of walls also increases with frequency.

$$P_{\text{Steinmetz}} = C_m B_{max}^{\propto} f^{\beta} \quad (15)$$

Where C_m is a material coefficient, the power loss was also presented as a two term model with components for hysteresis and eddy current loss (16). Which can approximate the power loss where *p/f* is linear.

$$P_{\text{Steinmetz}} = C_0 B_{max}^{\propto} f + C_e B_{max}^2 f^2 \quad (16)$$

Where C_0 is the hysteresis loss coefficient and C_e is the eddy current loss coefficient calculated using the classical eddy current formula or alternatively by curve fitting to measured data. These formulae were developed for hot rolled steels without additional silicon, (15) and (16) are more suitable for non-oriented than grain oriented electrical steel.

The disagreement between calculated and measured results mandated the development of a three-term model with an “additional” or “excess” loss. The statistical loss model proposed by Bertotti [14] is shown below (17).

$$P_{\text{Bertotti}} = k_{hyst} f B_{max}^{\propto} + k_{eddy} f^2 B_{max}^2 + k_{excess} f^{1.5} B_{max}^{1.5} \quad (17)$$

Where k_{hyst}, k_{eddy} and k_{excess} are the respective loss coefficients. This model is also only valid for linear material and for electrical steel this translates to approximately, $B \leq 1.2\ T$ and $f \leq 400\ T$.

2.4. EFFECT OF STRESS

The core materials in an electric motor are subjected to operational stresses as well as the residual stress and strains from the manufacturing process outlined in section 2.5.3. all of which influence the magnetic properties.

This next section examines how applied stress effects the domain structure of NOES and then discusses how this altered domain structure affects the magnetic properties.

2.4.1. Domain Structure Under Stress

Stress in the Rolling Direction

The application of a tensile stress in the rolling direction (RD) will cause an enhancement of the main domains (RD domains) whose easy axis, [001] is aligned with the RD. The flux closure domains (TD domains) in non-easy directions [010] or [100] will be reduced and removed. Tensile stress in the RD will decrease the magnetoelastic energy of domains aligned with the RD and increase it for domains in the transverse direction (TD).

The growth of the RD domains at the expense of the TD domains will increase the magnetostatic energy and as the tensile stress increases in order to reduce this the domains will narrow and then flux closure domains will be reintroduced.

A compressive stress applied in the RD will have the opposite effect constraining the RD domains whose magnetoelastic energy increases, with a corresponding decrease in the magnetoelastic energy of the TD domains.

Stress in the Transverse Direction

A tensile stress applied in the TD has the same effect as a compressive stress applied in the RD. The value of the corresponding stresses can be determined using Poisson ratio,

ν which is defined as the ratio of transverse to longitudinal strain, ε. Tension has a positive sign and compression a negative sign (18).

$$\nu = -\frac{\varepsilon_{transverse}}{\varepsilon_{longitudinal}} \tag{18}$$

For steel the stress-strain is linear and Hooke's Law (19) applies for values below the yield strength which for NOES is between 315 - 455 MPa [15, 16] where *E* is the Young's modulus.

$$\varepsilon = \frac{\sigma}{E} \tag{19}$$

The compressive stress in the TD for a given tensile stress applied in the RD can be defined using (20).

$$\frac{\sigma_{transverse}}{E_{transverse}} = -\frac{\upsilon\sigma_{longitudinal}}{E_{longitudinal}} \tag{20}$$

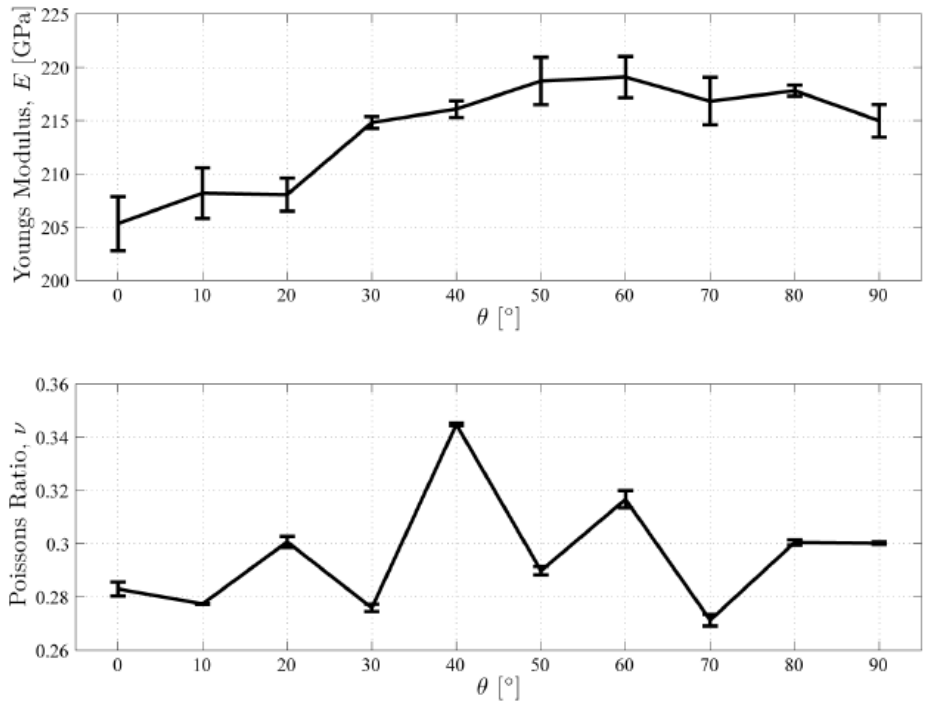

Figure 14: Young's modulus, E *and Poisson's ratio, ν in 0.5 mm thick 2.5 % Si NOES at angle ϑ from the RD from [17]*

NOES is an anisotropic material and as such Young's modulus, *E* and Poisson's

ratio, ν varies with the direction [17]. *E* is greatest in the TD with ν at its maximum value mid-way between the RD and TD, shown in Fig. 14.

2.4.2. Domains Under Stress in an Applied Magnetic Field

The magnetic properties are affected by stress, which to align a sufficient number of domains may require a higher magnetising field and more complex domain wall motion, implying a decreased permeability and increased power loss. Senda et al [18] investigated the effect of stress on the magnetic properties of NOES,

The effect of stress on the power loss at 1.5 T and at 50 Hz is shown in Fig. 15 and the magnetic polarisation, *J* for different applied magnetic fields is shown in Fig. 16

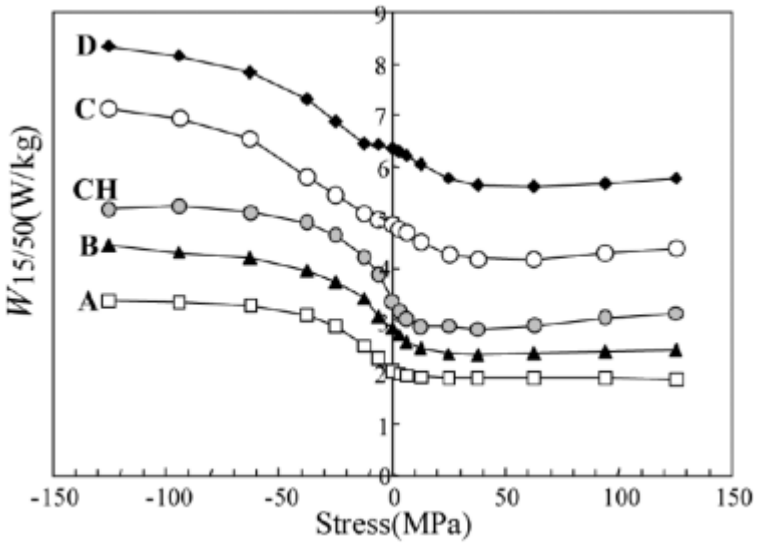

Figure 15: Power loss of NOES under stress at 1.5 T and at 50 Hz. For samples with various Si content. A = 3.4 %, B = 2.8 %, C = 0.8 %, D = 0.1 % and CH = Annealed C. From [18].

Application of tension initially causes an increase in permeability and a corresponding decrease in loss peaking at approximately 10 - 20 MPa. Tensile stress higher than approximately 30 - 50 MPa decreases permeability and increases loss. The beneficial effect on the magnetic properties seen at low fields is attributed to a positive, tensile stress and positive magnetostriction constant, reducing the magnetoelastic anisotropy energy and facilitating the magnetising process. However, several factors

which include applied stress and field strength can change the magnetostriction constant from positive to negative [17], explaining the detrimental effect at bigger values.

The permeability and power loss are more sensitive to compression which shows a much larger decrease in permeability and increase in power loss even for small values of applied stress.

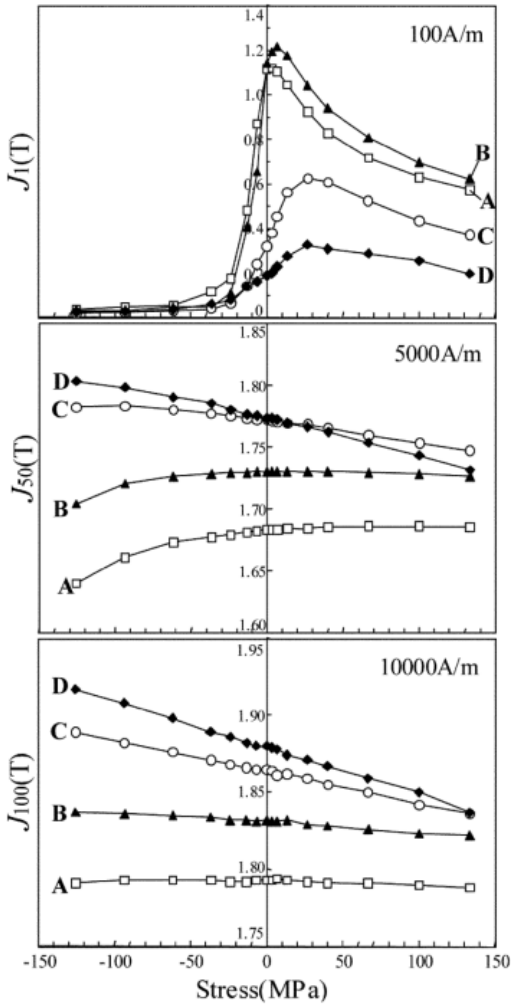

Figure 16: Effect of stress on magnetic polarization, J. For NOES samples with various Si content. A = 3.4 %, B = 2.8 %, C = 0.8 % and D = 0.1 %. From [18].

The domains will organise to achieve the minimum energy, which has many components, the main ones of interest being; Magnetocrystalline anisotropy energy, magnetostatic energy, magnetoelastic energy and the magnetising field energy and the weight of each component to the total energy will vary with the stress.

As tension increases the domains are encouraged to align parallel to the stress vector. For those already aligned the tension will cause refinement. New narrower domains are created, reducing the wall spacing. This reduced spacing means the walls move with a lower velocity and over a shorter distance each cycle, meaning lower eddy currents and therefore lower eddy current losses. Additionally, the amount of domain rotation and 90° domain wall motion which both contribute to losses are reduced. As tension continues to increase then so does refinement and domain wall creation. These walls have an energy cost and after a certain point that cost, in addition to the creation of new closure domains, becomes greater than the saving from the increase in the domains number causing the power loss to increase.

A compressive stress has the effect of aligning the domains perpendicular to the stress vector. As compression increases more domains are oriented perpendicular to the direction of the stress and magnetising field. Therefore, larger magnetising fields are needed resulting in lower permeability and higher power loss.

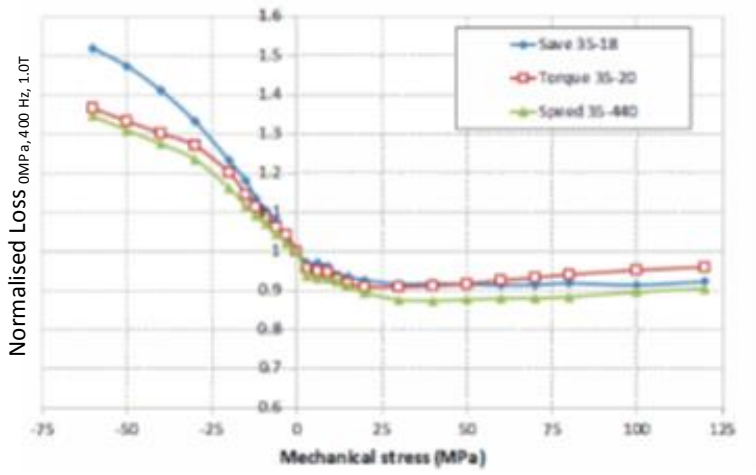

Figure 17: Normalised Loss of different automotive electrical steels. This is measured loss (W/kg) at various applied stress divided by the loss at zero stress at 1.0 T and 400 Hz from [19]

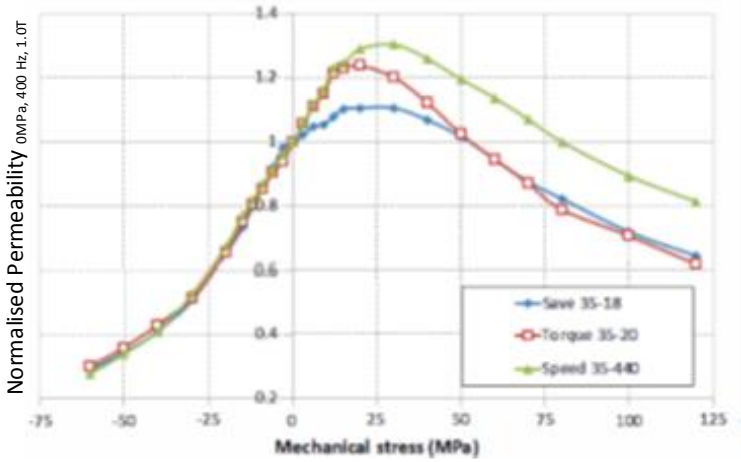

Figure 18: Normalised Permeability of different automotive electrical steels. This is the permeability at various applied stress divided by the permeability at zero stress at 1.0 T and 400 Hz from [19]

These values are in good agreement with those reported by Vandenbossche [19] who applied elastic stress to three automotive electrical steel grades. The power loss relative to their value at 0 MPa is shown in Fig. 17 and permeability in Fig. 18.

Leuning et al [20] investigated tensile loading on 0.5 mm thick NOES with 2.9 % silicon and observed increases in permeability at stresses < 50 MPa when measuring in the TD but not in the RD.

Work by Oda [21] showed that increasing the Si content resulted in a lower increase with increasing compressive stress due to a decreases in the magnetostriction constant. With a 6.7 % Si sample demonstrating a decrease in loss with compressive stress.

2.5. APPLICATION OF ELECTRICAL STEELS IN ELECTRIC MOTORS

One method of achieving the desired developments in EV/HEV's is through improvement in the efficiency of the traction motor. The designers of these motors want high power and torque densities while also increasing efficiency. These demands place significant and competing demands on the material from which they are made.

2.5.1. General Principle – Electromagnetic Induction

Faraday's Law defined mathematically by Maxwell's equations states that

The induced electromotive force, emf, $\mathcal{E}$ in a closed loop, C is proportional to the negative of the rate of change of magnetic the flux passing through an open surface which has C as it's perimeter.

This is the fundamental basis to how electrical machines such as generators, motors and transformers work. In the case of an electric motor, a device that converts electrical energy into mechanical energy the alternating current supplied to the stator generates a magnetic field which interacts with the magnetic field of the rotor, produced with either a permanent magnets or electromagnets and the forces generated can be used to do useful work.

The majority of electric motors will achieve maximum efficiency near 75 % of their rated load with efficiencies in the range of 80 – 97 % [22].

The efficiency of the electric motor is affected by several factors including power loss due to friction, resistive loss in the copper windings and iron loss which occurs because of hysteresis and eddy currents in the electrical steels. Depending on the loading of the motor the iron loss can be between 30 – 90 % [23] of the total losses, therefore, the magnetic properties of the materials used in the motor cores are of great importance.

2.5.2. Materials Used

The functional material in the core of the motors is required to have many and often competing properties as outlined in Table 1. To adequately balance these demands motor core laminations are largely produced by punching from non-oriented steel sheets.

Driving property	Material property
High torque for starting	High permeability
Compact and lightweight	Low loss under high frequency
Small rotor/stator air gap	Good workability
High fuel efficiency	Low loss in typical driving ranges
High revolutions	High strength

Table 1. Driving properties and related core material requirements

Non-Oriented Electrical Steel sheets are measured under conditions of no stress, uniform alternating field, in a given direction with a sinusoidal flux waveform as prescribed by international standard IEC60404-2. However, once operational are considerably different. Currently, there is no suitable model to describe the effect of the manufacturing process. The introduction of such a model would be of great importance to designers of electrical machines in the optimisation of their designs.

2.5.3. Manufacturing Steps

The core materials in an electric motor are subjected to stresses and strains from the manufacturing process which are summarised in Fig. 19.

The first stage of production of a motor involves the cutting of the rotor and stator laminations to the required design from steel sheets. There are several methods available, discussed further in Section 2.6, the most common being punching which introduces plastic stress and strain into the sample when cutting the stator out of steel sheets with compressive stress and strain pronounced near the cut edge.

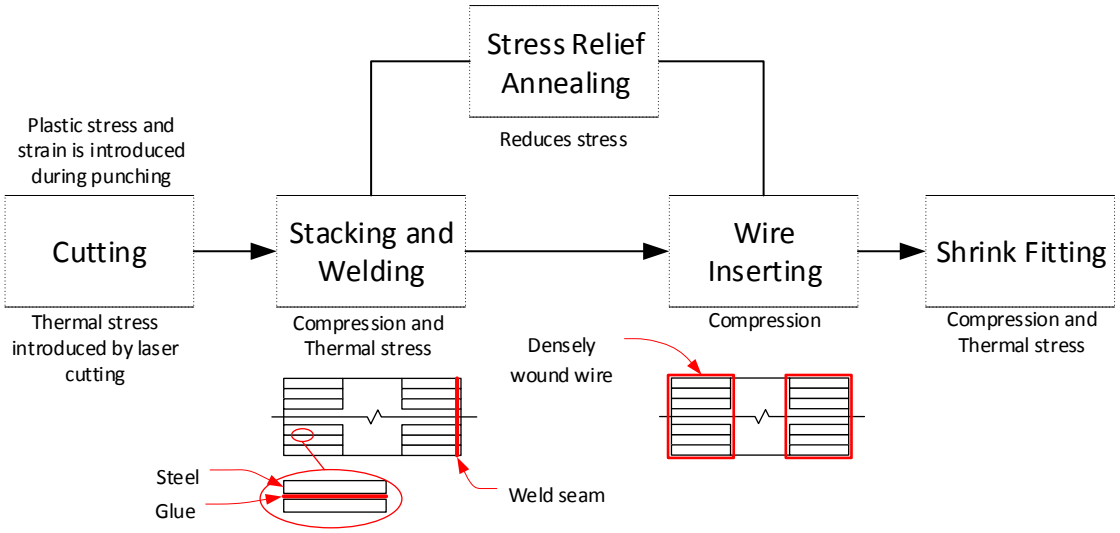

Figure 19: Flowchart of electric motor manufacturing process

The laminations are then assembled into a core potentially several hundred laminations high, which could involve welding or interlocking which can impose additional stress. An insulation coating is applied to the samples potentially introducing stress then joining with either adhesives introducing compression or welding which introduces thermal stress. Some of this initial stress may be removed by stress relief annealing, which involves heating the material up to 700 – 800 °C for several hours and allowing to cool [24]. Although this is rarely done as the organic insulation coatings or joining adhesives can't be exposed to such high temperatures. Compressive stresses are then potentially reintroduced with the insertion of the copper wires wound around the stators to magnetise them and, if fitted into a motor case, this is often done by press fitting or heat shrinking which can introduce more stress although this is likely to be a hoop stress located at the back of the stators and how this would translate to stress in the more critical parts of the stators such as the teeth is uncertain.

2.6. EFFECT OF CUTTING

The cutting process was identified as the most damaging to the magnetic properties when the relative influence of the different manufacturing processes was assessed by Schoppa [25]. The different processes were assessed and ranked in terms of the relative amount of damage caused to the magnetic properties of fully processed non-oriented electrical steel. This was done by comparing the form of J against H before and after different processes, at various flux densities and with samples varying in composition. Processes included cutting, on strips of widths 50mm and length 160mm, pressing and welding conducted on toroidal samples with an outer diameter 100mm and inner diameter 60mm. The manufacturing processes were shown to have the greatest impact within the operating range of 0.5-1.5T and summarised in Table 2 where the number of "+" indicate the importance of the change to the magnetising behaviour by the different processes. Cutting with "+++" can be seen to have the greatest influence on the magnetic properties.

Processing step	Operating range < 0.5 T	Operating range 0.5–1.5 T	Operating range > 1.5 T
Cutting	+	+ + +	+ /0
Pressing during stacking	0	+ / + +	0
Welding	+	+ +	0
Sticking	0	+	0
Automatic stacking, riveting	0/ +	+ / + +	+ /0
Pressing into frame	0/ +	+ / + +	+ /0

Table 2: Effect of different manufacturing process over a range of magnetisation [25]

Processing step	Non-alloyed, low Si-alloyed	Middle Si-alloyed	High Si-alloyed
Cutting	+	+ +	+ + +
Pressing during stacking	0	0	0
Welding	0/ +	+	+ +
Sticking[a]	0	0/ +	+
Automatic stacking, riveting	0/ +	+	+ +
Pressing into frame	+	+	+ +

[a]Coated with organic adhesive coating.

Table 3: Effect of manufacturing process on the specific losses for various Si content electrical steel [25].

Different grades of NOES have different sensitivities to the various manufacturing steps. High silicon alloyed grades (no Si percentages were presented) were reported to

have a larger effect. It was also noted that there was no substantial change in effect by the removal of the cutting burr.

2.6.1. Methods of Cutting

There are several cutting methods available for the production of laminations each with their own advantages.

2.6.1.1. EDM

Electric Discharge Machining (EDM) uses electrical discharge, between two electrodes in a dielectric liquid. When the voltage between the electrodes is increased sufficiently, electrical breakdown of the dielectric takes place causing a current to flow between them, removing material. Wire EDM, uses a brass wire constantly fed from a spool as the tool electrode and water as the dielectric fluid to wash the removed material away. This does not require high cutting forces so reduces residual stresses. It can cut plates up to 300 mm thick with high tolerances as small as ± 0.0025 mm [26] although to reduce costs and time accuracies of 0.3 mm are more typical.

Advantages of EDM include the ability to produce complex shapes out of hard materials to high tolerances. As there is no direct contact between the tool and the workpiece there can be no pressure applied and no risk of distorting small or breakable pieces[27]. High power consumption, slow material removal rate and excessive tool wear are the main disadvantages.[28]

2.6.1.2. Laser

Laser cutting works by using CNC (computer numeric control) to direct a high power laser at the material which will then either vaporise or melt the material which is then blown away by a jet of gas. Kerf widths, the width of material that is removed by the

cutting process as small as 0.5 mm are possible, depending on factors such as cutting speed and power [29]. The three main types of lasers used for cutting are; CO2, Neodymium (Nd) and Neodymium Yttrium Aluminium Garnet (Nd-YAG) [30]. Disadvantages include the high-power consumption and the creation of a heat effected zone (HAZ), an area of material near the edge that has its microstructure and properties altered by the heat generated during cutting. The advantages of laser cutting are that there is reduced contamination and precision may be improved by virtue of not having any tool wear. The processes require optimisation of factors such as laser power, cutting speed and focal length with the latest machines having tolerances dependent on geometry in the range of ± 0.1 mm to ± 0.7 mm [31].

2.6.1.3. Waterjet

Waterjet cutting uses a high-velocity stream of high-pressure water (typical pressures about 400 MPa) forced through a small diameter nozzles to cut materials. For harder materials such as steel, abrasive particles such as garnet aluminium oxide are suspended in the stream [32], a typical set up is shown in Fig. 20.

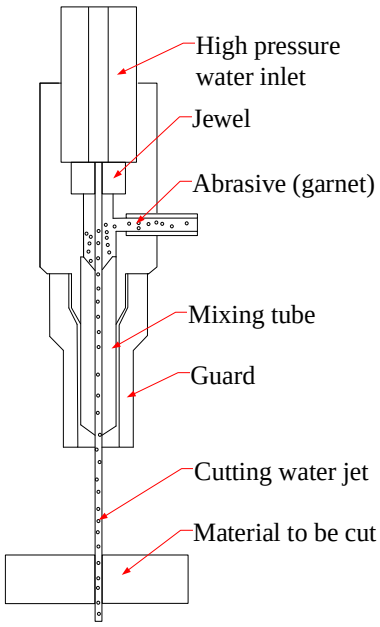

Figure 20 – Typical AWJ cutting setup

This is referred to as abrasive waterjet cutting (AWJ). The main benefit of AWJ is there is no heat affected zone (HAZ) so can be used for heat sensitive materials. It can cut complex geometries and AWJ has a kerf or cut width of 0.5 – 1.5 mm. with some user optimisation of factors such as nozzle height.[33]

2.6.1.4. Punching

Punching is a process that forces a tool called a punch through the workpiece into a die which has been custom made to the geometry of the item that is to be produced. These tool pieces are usually made of hardened steel or tungsten carbide. Factors that influence the quality include tool wear, punch-die clearance as well as thickness and other material properties.

This is often the most cost-effective process for medium to high volumes and can create multiple shapes relatively fast and in high volumes. It is not as accurate as other methods and creates a burnished region all over the edge. The shearing process, shown in Fig. 21, starts with cracks forming on the top and bottom surfaces which join resulting in separation of the material. This creates a rough fracture surface and a burnished surface. [34] Burnishing is plastic deformation caused by friction and heat as one surface slides over another causing surface hardening and generate compressive residual stresses.

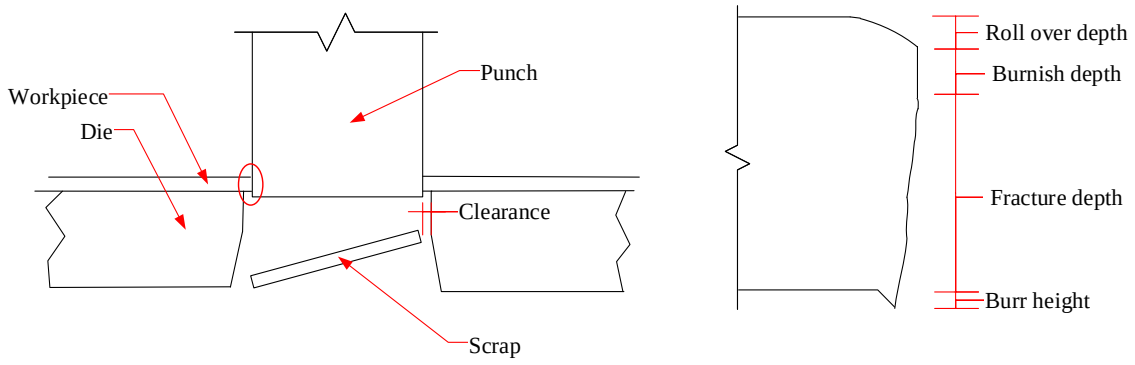

Figure 21 Left: Shearing process consisting of punch and die. Right: Sheared edge showing the formation of burnishing and burr.

Along with other factors, such as punch force and speed, the clearance has a big impact on the quality of the cut. The edges becoming rougher and the deformation zone increasing as the clearance increases. Typical values are in the range of 2 – 8 % of the sheet thickness but may be as small as 1 % [34]. The ratio of burnished to fractured areas increases with material ductility and decreases with increasing sheet thickness and clearance. Blunt tools are a major source of burrs, the height of which increases with increasing clearance and ductility.

2.6.1.5. Summary of Cutting Methods

An overview of the main cutting methods is provided in Table 4.

	Waterjet	**Wire EDM**	**Laser**	**Punching**
Tolerances	Average of ± 0.025 mm [33]	Average of ± 0.3 mm but ± 0.005 attainable [26]	± 0.2 mm [35]	Fair but ± 0.005 attainable [36]
Thickness	25 mm or higher [34]	30 cm [26]	Material dependent, Steel ≈ 20 mm [31]	Works well with thin sheets
Cutting speed	5-10 times faster than EDM when thickness is under 25 mm	5-10 times slower than waterjet	Very fast cutting in thin, non-reflective materials	Fast batch production when initial and setup programming are done
Edge quality	Good	Excellent	Excellent	Fair
Material distortion	No distortion but possible hazing near cut edge	No	Possible	Some
Heat affected zone	None	Some	Yes	None
Material limitation	Works in virtually all materials except hard ceramics	Only works in conductive materials	Only non-reflective metals	Not good for brittle or hardened materials
Process	Cold supersonic abrasive used to cut material	Spark erosion used to remove material from electrically conductive materials	Thermal process	Shearing process

Table 4: Summary of waterjet, wire EDM, laser and punching methods for metal cutting.

2.6.1.6. Economic Considerations

Lasers, water jet and EDM may be more cost effective for low volume, from prototype to hundreds of laminations. savings can be made because inventory can be reduced through quick set-ups. The programming is minimal and the cost of ownership can also be less because no tools needs to be stored. However the ongoing energy cost is higher and the initial investment of a laser cutting machine is greater than that of a punching machine.

Punching which has a higher set up time due to tool production and set up lends itself to larger batch sizes; hundreds to thousands. Ongoing energy costs are low with the cost of producing a part in a punching machine is far less than to make in a laser. On thin thicknesses and simple geometries no laser can compete with the cost of the punching.

2.6.2. Effect of Cutting on Magnetic Properties

It has been known for some time that the cutting of electrical laminations degrades the magnetic properties. The effect of cutting is greater at the cut edge and diminishes as you move further away from the edge and into the interior of the sample. The terminology in the literature is that of a “damaged zone” or “degraded region” extending a certain depth into the sample. The degradation of the magnetic properties referred to, typically implies, a lower permeability with an increase in power loss pronounced in the damaged zone. This also reduces the average over the whole sample. The effect was quantified by Nakata [37] in 0.35 mm thick NOES using conductive paste on the top and bottom surfaces to create an electrical contact. The author found pronounced degradation within 5 mm of the cut but limited to the first 10 mm with a reduction in flux density up to 50 % at the cut edge for measurements at 0.91 T. Senda et al [38] also reported that the degradation depth increased with a decrease in the magnetic field in experiments using

0.5 mm thick NOES but, contrary to Nakata, estimated the extent at 1.5 – 2.5 mm. Vandenbossche [39] describes a 6.5 mm deep degraded region for M235-35A electrical steel with a drop at the cut edge of 83 % at 1.0 T with increases in the number of cut edges increasing power loss. The same 80 mm wide sample cut 14 and 42 times when compared to an uncut reference case showed an increase in power loss of 17.3% and 50.7% respectively (measured at 1.0 T , 400 Hz).

It is clear that the magnetic properties are altered by cutting in a way that negatively affects the performance of the electrical machines. The degree to which this happens depends on many factors but can be broadly divided into three main groups; The material, the cutting process used and the geometries involved.

2.6.2.1. Material Properties

Several investigators have attempted to determine the extent of changes in the microstructure near the cut due to mechanical cutting. Optical microscopy has been used to examine the grain morphology [40-42] showing clear grain deformation in the first 0.5 mm from the edge of punched samples. An example of optical microscopy at the cut edge is shown in Fig. 22. Domain pattern observations using a Kerr effect microscope were carried out by Senda [38]. Who reported a degraded zone, indicated by altered domain patterns which decreased in size with increasing magnetic field ranging from 1 – 5 mm. The hardness distribution at 40 μm intervals from the cut edge of mechanically sheared NOES was investigated by Omura [43] for different thicknesses. The grain size between samples was consistent however other material properties such as Si content were omitted.

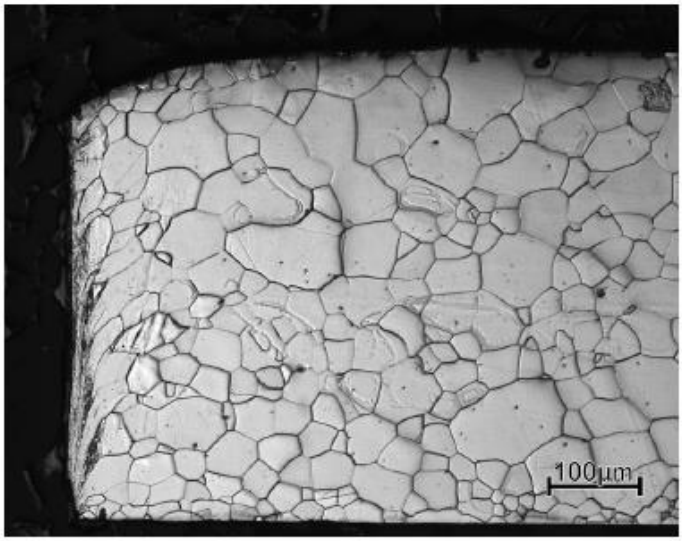

Figure 22: Optical micrograph of 0.5 mm thick medium Si NOES by mechanical cutting form [41]

FEM modelling of the cutting process showed a predominately compressive stress distribution at the cut edge and correlated an increase in plastic deformation to an increase in hardness, shown in Fig. 23.

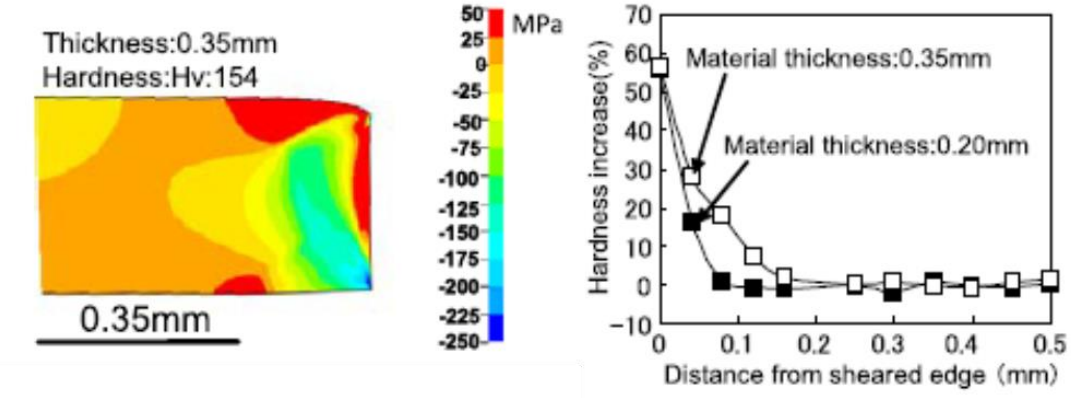

Figure 23: FEM modelling of stress distribution (left) and hardness increase (right)in sheared face of 0.35 mm thick NOES from [43]

This process was taken further by Cao [44], who used nanoindentation in the vicinity of the punched edge of 2 % NOES to estimate the distribution of residual stress which is shown in Fig. 24.

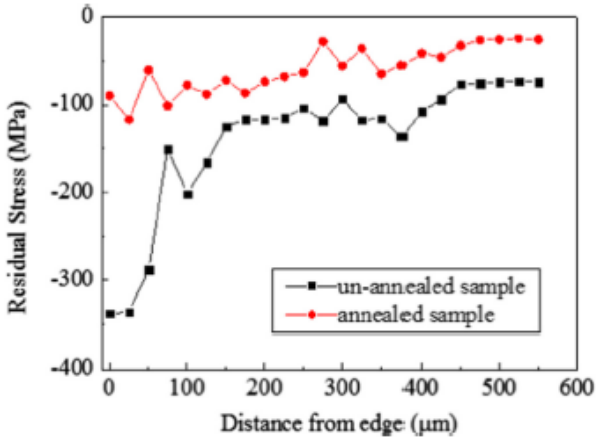

Figure 24: Residual stress distribution near the punched edge of 2 % NOES from [44]

The area up to 0.55 mm from the edge is in compression and even after annealing which does relieve much of the stress but still compressive stress in excess of 100 MPa at the edge. It is unfortunate that measurements were not taken further into the sample as the stress has yet to level off so the full extent of the compressive area was not appreciated. Hardness measurements were taken over a wider area by Pulnikov [45] showing a sharp increase in approximately the first 0.3 mm but also a more gradual increase up to 10 mm from the cut edge. The application of compressive stress in the direction of the sample thickness reduced the distance from the cut edge in which the hardness was elevated.

Estimates for the size of the damaged zone have been performed by Loisos [46] with the use of localised search coils to measure flux density in NOES. The samples with Si content ranging from < 0.2 % to 3.2 % and correlating with an increasing grain size (lowest Si samples having the smallest grain size and highest Si samples having the largest grains) were cut with a guillotine and indicating a degraded zone over 5-6 mm with small effects up to 10 mm density which is in broad agreement with Nakata [37] and Rygal [47] who also used search coils on similar grades to identify that high grain size and silicon content had more of an effect, with grain size being the more important of the two.

A higher density of grains would cause more dislocation pile-up closer to the edge

and prevent the spread of plastic deformation through the sample.

2.6.2.2. Cutting Process

The effects on the magnetic properties of different cutting methods have been studied by several researchers. Loisos [46] compared the effect on flux density measured with local search coils wrapped through 0.5 mm drilled holes of cutting NOES with a Nd:YAG laser and a power guillotine against a control uncut sample. Mechanical cutting was found to has a greater effect pronounced over 5-6 mm with small effects up to 10 mm. This is in agreement with Peksoz [48] who also used search coils at varying distances from the punched edge for four 0.5 mm thick NOES samples of varying silicon content and grain size, "fluctuations" in flux density were described within 5 mm from the cut edge however only the results of one sample, magnetised at 1.0 T and 50 Hz, were reported. This is in contrast to work by Emura [40] whose work investigating different cutting techniques using 2 % NOES Epstein strips. Punching, second only to photo-corrosion displayed plastic deformation extending approximately 0.3 mm from the cut edge and had a lower power loss and higher permeability than laser cutting, which had no signs of grain deformation.

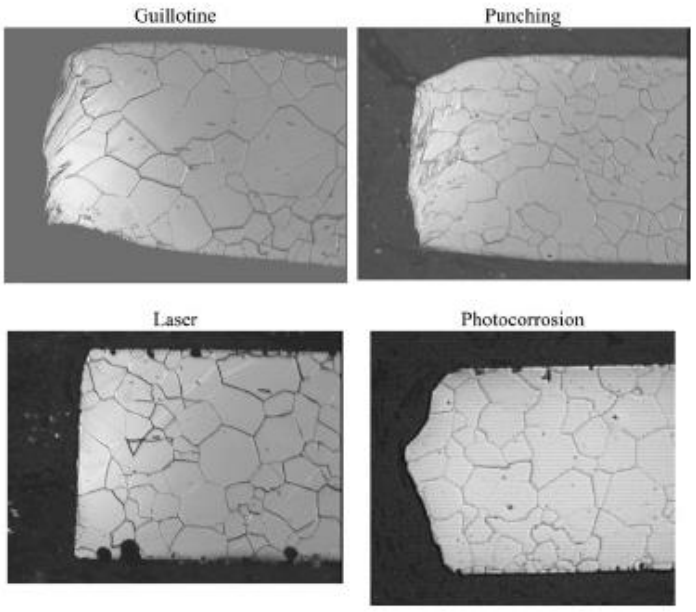

Figure 25 - Edges profiles after different cutting methods and before annealing from [40]

The additional stresses induced by the drilling of the holes for the search coils could potentially contribute to the larger degraded zone. The edge profiles for different cutting methods are shown in Fig. 25. The reason for this contradiction is that mechanical cutting has a greater local effect constrained close to the cut edge whereas the effects of laser cutting extended over the whole sample as shown by Siebert [49] using dark field imaging to look at the flux density across the width of 2.4 % NOES (material grade M330-35A) samples punched or cut with a solid-state laser shown in Fig. 26. It is interesting to note the asymmetry of the laser cut samples which is suggested to be due to the sequential nature of laser cutting with the second cut displaying a greater deterioration due to the different temperature distribution.

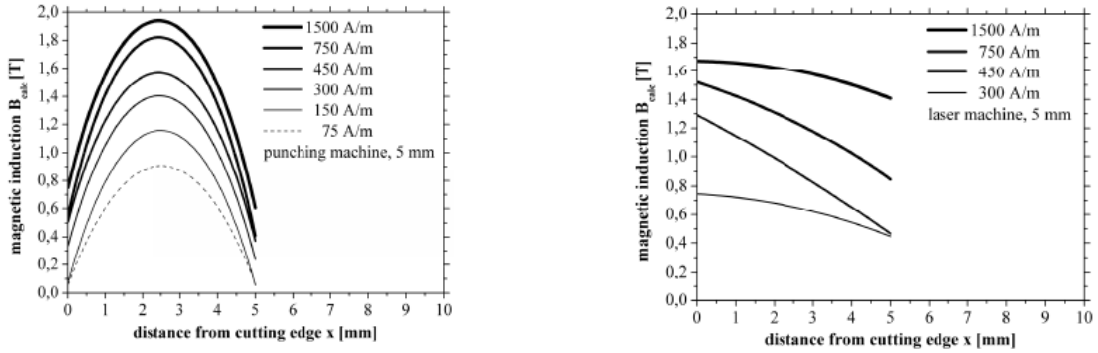

Figure 26: Flux density across the width of 5 mm M330-35A NOES samples with both sides (cut edges at 0 mm and 5 mm) either punched or laser cut from [49]

Naumoski [50] investigated punching and laser cutting of 0.35 mm thick 2.8 % silicon NOES with wire EDM samples annealed after cutting as reference samples. The magnetic properties near the cut edge were investigated using the magneto-optical Kerr effect (MOKE) and hardness measurements. Hofmann [51] takes a similar approach with strips of M330-35A and both find laser cutting is the most harmful method with deterioration of the domain pattern, indicated by poor contrast in the MOKE images over a larger zone than that observed by mechanical cutting which itself is larger than wire EDM sample, which has a narrow zone. The cutting method was shown to have no effect

on the conductivity.

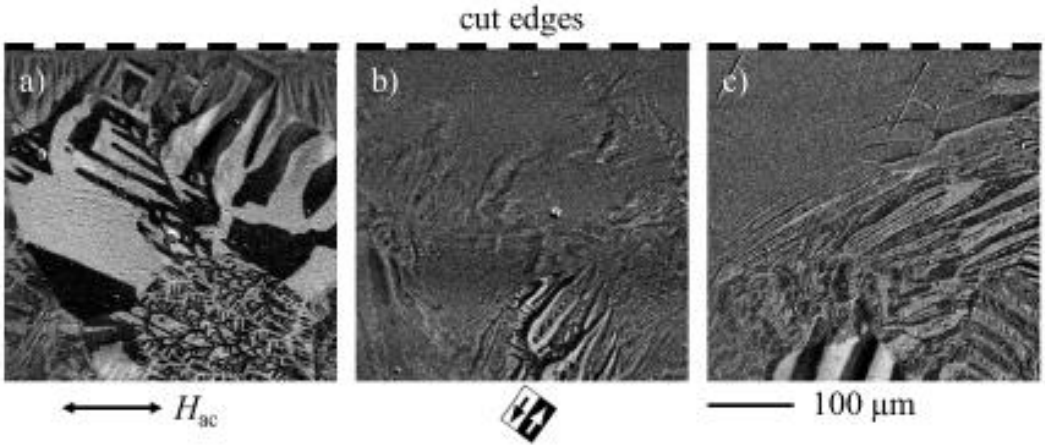

Figure 27: MOKE micrographs of the cut specimens at (a) wire EDM (b) guillotine-cut, and (c) laser-cut edges at a field amplitude of 1460 A/m. The cut edges are at the top side of the contrast enhanced micrographs taken from [51].

Much of the work regarding cutting methods uses Epstein strips or sheets with measurement using SSTs or Epstein frames and conclusions extrapolated to the more complex geometries of motor cores. To address this Bayraktar [23] constructed four 5.5 kW induction motors with the only difference being the cutting technique used for the laminations. The cutting methods used were wire EDM, punching, laser and AWJ with the efficiency of the motors measured using a power analyser. Summarised in Table. 5.

Cutting Technique	Efficiency %	Iron Loss (W)
WEDM	85.61	553
Punching	85.16	562
Laser	83.47	664
AWJ	83.1	712

Table 5: Efficiency and iron loss of 5.5 kW induction motors using different cutting methods.

Laser cutting does require optimisation and many laser cutting specialists would claim to be able to match the efficiency of other methods.

All cutting methods cause deterioration of the magnetic properties although by

different mechanisms, mechanical and AWJ cause plastic deformation and laser and EDM create thermal stress. WEDM is the consistently less deteriorating to the magnetic properties [23, 42] than other methods with the possible exception of AWJ which has been reported by some authors [52] to be the least degrading method. However, the punching process, once the die is made, is straightforward and widely used in industry as it can produce large volumes of laminations in a quicker and more cost-effective manner than other methods. Its position as the most common method for the production of motor core laminations is unlikely to change.

2.6.2.3. Geometry

The geometry of the cut and of the sample has significant influence. As sample sizes decrease, the ratio of the cut length and degraded volume to total sample volume generally increases with more complex patters more likely to have more pronounced degradation.[39, 53, 54]

2.6.2.4. Cut Edge Characterisation

There has been considerable interest in the last few years in characterising the changes to the magnetic properties in the zone near the cut edge as well as determining the volume over which these changes take place. There are two approaches to determining the magnetic properties indirectly using hardness measurements or neutron grating interferometry or directly measuring the flux density with needle probes or search coils.

2.6.2.5. Summary of Previous Work on Cut Edges

Punching and shearing of NOES causes an increase in hardness and residual compressive stress potentially extending up to 1 mm from the cut edge. This stress field results in the deterioration of the magnetic properties namely a reduction in flux density

and permeability and an increase in power loss extending from the cut edge to the whole sample but concentrated in up to the first 3 - 5 mm. The distribution of flux is pushed from the cut towards the middle of the sample. Annealing of the sample after cutting can help recover the magnetic properties.

Influence	Summary
Material	An increase in grain size which is influenced by silicon results increases degradation.
Cutting Process	Punching creates plastic deformation and grain misorientation at the cut edge and has a more pronounced effect at the edge but less of an overall effect when compared to laser cutting which introduces thermal stress. The cutting settings (clearance, tool state, laser power etc.) have a large influence WEDM is the least degrading.
Geometry/ Width	The number of cut faces (more faces per unit volume increases degradation) and the order they are cut in are influencing factors. Narrow widths are more heavily influenced due to overlapping stress fields.

Table 6: Summary of damaged zone widths with different measurement techniques.

2.6.3. Modelling the Effect of Cutting

There is considerable interest in being able to predict how the material properties and manufacturing steps such as those outlined in Fig. 19 affect the magnetic properties. Currently, the magnetic properties are measured using Epstein frames or sheet testers at the steel plant. However, further manufacturing processing steps used in producing motors render the magnetic properties post production much more uncertain. The use of Finite element software used by the motor designers currently takes no account of the impact of the manufacturing steps. As a result, there have been several attempts to model magnetic properties and in particular, the losses after cutting.

2.6.3.1. Distribution Models

There have been several models proposed to describe the magnetisation distribution within a sample considering the degradation at the cut edge.

Vandenbossche et al [39] suggest.

$$J(H,x) = \mu_0\big(\mu_r(H,N=0) - \Delta\mu_{cut}(H)\eta(x)\big)H \tag{21}$$

Where $\mu_r(H,N=0)$ is the relative permeability without cutting. $\Delta\mu_{cut}(H)$ is the maximum permeability drop at the cut edge defined by the difference between the permeabilises of the undamaged and damaged samples and scaled using the function *F(N)*.

$$\Delta\mu_{cut}(H) = \frac{\mu_r(H,N=0) - \mu_r(H,N)}{F(N)} \tag{22}$$

$\eta(x)$ a parabolic function both of which are determined from experiments. *x* is the distance from the edge. *N* is the number of cut edges and *H*, the magnetic field strength which is assumed to be constant. This is an acceptable assumption for strips but would not be applicable to stators. Schoppa proposed the hyperbolic model (23) for *J*, with the flux density calculated as $B = \mu_0 H + J$

$$\widehat{J_1}(x) = \widehat{J_0} - \widehat{J_1}\cosh(A\,{}^{x}/_{x_0}) \tag{23}$$

Where x_0, is half the sample width and J_0, J_1 and *A* are all experimentally determined for each material, it should be noted that this is obtained from a secondary source [55], the original being his thesis, in German. The best fitting function obtained using Matlab is used by Peksoz [48] with parameters *a-d* obtained from eight experimental data sets (four different NOES grades, 1.0 and 1.5 T at 50 Hz) which used search coils to measure the flux density at various distances, *x* from a punched edge.

$$B_{\max}(T) = \frac{a}{(1+e^{b-cx})^{1/d}} \tag{24}$$

These models are only applicable to mechanically cut samples as the profile for a laser cut sample, described in section 2.6.2.2 is rather different. There is also no frequency term in any of the models.

2.6.3.2. Finite-Element Models

Gmyrek [56, 57] used an approach of dividing a sample into an undamaged zone in the centre with damaged zones adjacent to the cut edges (defined as partially damaged)

The inputs needed for the calculations were obtained from measurements of an annealed ring sample 200 mm OD and 160 mm ID (undamaged sample) and one where the ring is cut into five concentric rings (damaged sample). The permeability of the damaged zone μ_D was initially assigned a relative permeability of 1 and later refined using (25). The damaged edge width was calculated at 1.87 mm.

$$\mu_{\mathrm{D}} = \mu_1 - \frac{(\mu_1 - \mu_{\mathrm{PD}})a}{\Sigma x} \tag{25}$$

Specific power loss curves for the damaged and undamaged samples were used to calculate the partially damaged (*PD* subscript) sample (28). The damaged zone power loss was determined to be proportional to the square of the flux density.

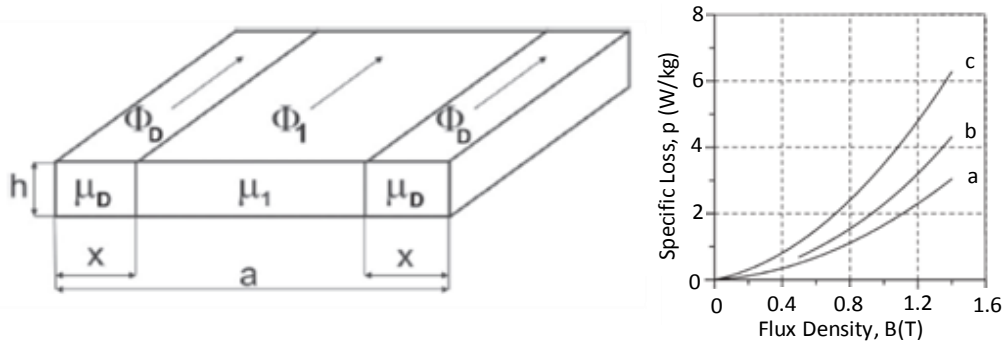

Figure 28: Model of material strip and specific power loss curves for a) damaged b)partially damaged and c)undamaged samples from [57]

$$P_{AVPD}ahl\rho = c\mathrm{B}_{\mathrm{D}}^2\Sigma xhl\rho + P_1(a - \Sigma x)hl\rho \tag{26}$$

ρ is the mass density, *l* is the magnetic circuit length, *c* is the specific loss constant. The power loss prediction (26), although accurate to within 5 %, relies on measured data to take account of factors such as silicon content and cutting parameters also there is no frequency component.

Bali [58] also uses the approach of dividing the sample with an undamaged zone in the centre and damaged zones adjacent to the cut edges. Measurements for two sets of samples (1 and 2) of different widths were made in an Epstein frame and didn't require knowledge of the degradation depth which is an advantage as *d* varies due to its sensitivity to material and cutting parameters. The flux density and power loss are determined using (27) and (28) where γ_i is the ratio of the degraded volume to the total volume and $p_{loss} = c_1 B + c_2 B^2$ where c_1 and c_2 are parameters identified by regression.

$$\begin{bmatrix} 1-\gamma_1 & \gamma_1 \\ 1-\gamma_2 & \gamma_2 \end{bmatrix} \begin{bmatrix} B_{nd} \\ B_{dg} \end{bmatrix} = \begin{bmatrix} B_1 \\ B_2 \end{bmatrix} \tag{27}$$

$$\begin{bmatrix} 1-\gamma_1 & \gamma_1 \\ 1-\gamma_2 & \gamma_2 \end{bmatrix} \begin{bmatrix} p_{nd} \\ p_{dg} \end{bmatrix} = \begin{bmatrix} p_1^* \\ p_2^* \end{bmatrix} \tag{28}$$

Where B_1 and B_2 are the average magnetic flux densities for each sample and p_1^* and p_2^* are the corresponding average loss densities. The subscripts *nd* and *dg* refer to the non-degraded and degraded zones respectively.

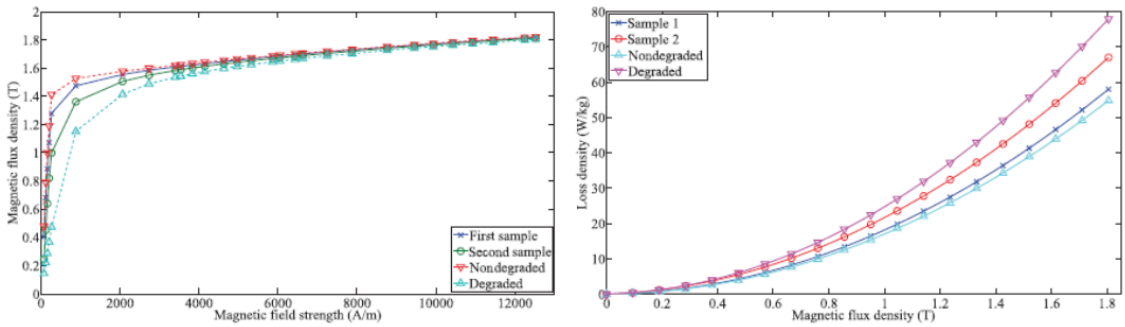

Figure 29: BH curves (left) and loss curves (right) for sample 1 , sample 2 ,degraded and nondegraded material parts for M400-50A at 250 Hz from [58]

Alternatively, in [59], an exponential degradation profile is proposed based on [37, 60] which negates the need for measurements and is incorporated into FEM models, modifying the BH curve and power loss coefficients in discreet bands throughout the material using the so-called degradation factor $\gamma(s)$ shown in (29) where s is the distance from the cut edge and δ_s is the "degradation skin depth".

$$\gamma(s) = \begin{cases} 1 - (1 - \hat{\gamma})e^{-s/\delta_s} & where \quad s < \delta \\ 1 & \quad s \geq \delta \end{cases} \tag{29}$$

Elfgen [61] uses the mathematical description of the permeability described in [39] to produce a continuous model to describe the local magnetic properties with model parameters identified from SST measurements on M330-35A samples. These are however laser cut which as shown in Fig. 26 will have a different distribution profile than the parabolic profiles used which are more suitable for mechanically cut samples.

Vandenbossche [62] proposed a power loss formula (30) that takes into account the cut edge effect by incorporating a numerical model proposed in [39] and shown in (21)

$$\begin{aligned} P(x, J(x), f_0) = S_{hyst}(x)\left(1 + (1 - r).\frac{J_{min}(x)}{J_P(x)}\right) J_P(x)^{(\alpha(x)+\beta(x)J_{P(x)})} f_0 \\ + S_{eddy}\sum_{n=1}^{\infty}\left(J_{P,n}(x)\right)^2 (nf_0)^2 + S_{exc}(x)\sum_{n=1}^{\infty}\left(J_{P,n}(x)\right)^{1.5} (nf_0)^{1.5} \end{aligned} \tag{30}$$

The *J(H,x)* curves are calculated from experimental data obtained using a specific process involving the cutting samples into increasingly narrow strips also described in [39]. This needs to be done for each material under consideration. S_{hyst} , S_{exc} , α and β are fitted from Epstein data with their *x* dependence assumed to be one of exponential decay and S_{eddy} calculated using (13). FEM models are split into zones where the parameters for each zone are determined by taking the value of the continuous functions of *x* at the midpoint of each zone. Modelled power loss is calculated for each zone and when compared to measured values performs better than a homogenous model but still underestimates, despite the considerable effort involved, in obtaining the parameters.

Hofmann et al [51] used a 2-D-FEA model with homogenous material properties but modified the hysteresis and excess power loss coefficients to account for the effect of cutting. The required parameters have to be measured from a sample of the same width and cutting type as that modelled so general implementation would require an extensive database.

2.6.3.3. Stress Models

An alternative approach is to measure or model the stresses and strains produced by cutting from which the magnetic properties can be derived. Ossart [60] determined the stress distribution in punched NOES using hardness measurements and relates this to the flux density using (31) which was developed using uniaxial stress tests in the RD, how accurate this would be with more complex geometries is unknown.

$$B(H, \varepsilon_p) = \frac{H}{v_0(\varepsilon_p) + v_1(\varepsilon_p)H + v_2(\varepsilon_p)H^2} \tag{31}$$

Where $v_0(\varepsilon_p)$ is also modelled by analytic functions, which are not described and no reference is provided. Additionally [63] includes the effect of long range residual stress and their impact on the magnetic properties which, according to the author, are smaller but act over a larger volume of the material and therefore have a considerable influence.

Crevecoeur et al [64] also determined the magnetic properties using the plastic strain. This model required the strain measurements obtained from deformed samples measured in an SST and signals obtained using the needle probe method.

2.6.3.4. Power Loss Models and Correction Factors

Formulas such as those described in section 2.3.4. have been used to predict the power loss in electrical steels, without taking into account the effect of cutting or nonlinear behaviour. Attempts have been made to obtain correction factors with varying success. Liu [53] proposed the following correction factor.

$$K_{\text{cutting}} = C_1 + (C_2/width) \tag{32}$$

where the width is in mm and C_1 and C_2 are cutting factor coefficients, their origin is not specified and the coefficients presented for a given material don't agree with the calculated values provided. Hofmann et al [51] modify the power loss coefficients to incorporate the effect of cutting into loss calculations.

The five Parameter "IEM-formula" (33) was developed in attempt to address some of the inaccuracies for nonlinear material behaviour

$$P_{\mathrm{IEM},5}=a_1 B_{max}^2 f + a_2 B_{max}^2 f^2 (1 + a_3 B_{max}^{a_4}) + a_5 B_{max}^{1.5} f^{1.5} \quad (33)$$

Where the parameters a_1 to a_5 are obtained by mathematically fitting to measured data sets. Eggers [65] compared the IEM and Bertotti models at higher frequencies after including a skin effect factor [66] in the eddy current loss component and found the IEM formula to be the more accurate for NOES grades tested. Steentjes et al [67] further develop the IEM model to include a parameter for rotational loss, produced as a result of the magnetic field and flux rotating in the plane of the lamination, which happens behind the teeth of stators [68]. The author then proceeded to incorporate the effect of cutting [69] by adjusting the hysteresis component a_1 (34) where *S* is the cut edge proportion defined as the cut edge length per unit mass and *d* the best fit line gradient.

$$a_1(\mathrm{S}) = a_{1;ref} + \mathrm{d}(\mathrm{S}\text{-}S_{ref}) \quad (34)$$

2.6.4. Summary

The effects of cutting on the magnetic properties are complex. Factors such as material properties, measurement parameters (flux density and frequency), type of cutting method used as well as the amount of cut faces and individual sample geometry all play a part. Due to this wide range of influencing factors the results presented in the literature vary considerably and as such it important to state which factors apply when providing results or giving predictions.

Several approaches to modelling the effect of cutting have been proposed with the main limiting factor being model parameters which are obtained from experimental data sets. With so many factors influencing these experimental data sets the wider applicability of models derived using them can be brought into doubt.

CHAPTER 3.

LOCAL MAGNETIC PROPERTIES MEASUREMENT SYSTEM

This chapter describes the methods and methodology used in the design and construction of a novel magnetising, measurement and positioning system used to address the objectives of this thesis. The requirements of the system are as follows

- To perform measurements of the local magnetic properties including; magnetic field, H, flux density, B, power loss and permeability.
- Ability to accurately specify the position of the local measurements.
- Capability to map local properties of motor core laminations of various geometries in an efficient manner.

A system previously developed at Cardiff University to measure the global magnetic properties of electrical steel was further developed to provide simultaneous measurement of both global and local properties of electrical steel samples [11].

The system requirements were divided into three parts, the magnetising, measurement and positioning systems. The magnetising system created the field which magnetised the test sample at user defined conditions. The measurement system determined the global and local properties of interest which were; flux density, magnetising field strength, power loss and permeability. Flux density waveform information would feedback to the magnetising system to keep the magnetising conditions within set tolerances so that each measurement was taken under the same conditions. The positioning system was used to position and move the probe from one location to the next.

3.1. TESTING OF SOFT MAGNETIC MATERIALS

The magnetic properties of interest, generally power loss, permeability etc depend on the flux density, *B* and magnetic field strength, *H* and are strongly influenced by the shape of the material so it is considered good practice to denote what kind of sample was used; Epstein frame, sheet, ring core etc. To measure *B* and *H* several methods have been developed.

The magnetic field, *H* can be measured indirectly or directly. For indirect measurements *H* can be determined from Ampere's law (35) using the current, *I* in the primary coil, with number of turns, N_1 and magnetic path length, *l*.

$$\mathrm{H}=\frac{IN_1}{l} \tag{35}$$

Direct methods, include Rogowski-Chattock coils [70], H coils and Hall effect sensors discussed in section 3.1.1. which measure the tangential component of the magnetic field just above the sample surface and assume the magnetic field measured to be the same as inside the sample.

Indirect methods have the advantage of a larger signal but the path length is not known precisely and they take an average for the entire sample and as such direct measurements are the preferred choice for localised measurements.

The flux density is typically calculated using Faraday's Law (36) from the voltage, V induced in a secondary coil, with area, *A* wrapped around the sample, N_2 times.

$$\frac{dB}{dt}=-\frac{V}{N_2A} \tag{36}$$

Local *B* measurements are more complex needing either the placement of small localised search coils, which apart from the small signals, are destructive as it is necessary to drill small holes in the sample. Another option is the needle probe method suggested by Werner [71] which is non-destructive.

The measurement of localised properties would require small probes, which still produce a useable signal positioned as close as possible to the sample. The probe should produce a linear signal, responding to both positive and negative fields and operate over a wide range of temperatures and magnetic fields.

3.1.1. Hall Effect Sensors

A magnetic field will exert a Lorenz force on charged particles. This is most evident for a thin conducting plate through which current flows. When a magnetic field is applied perpendicular to the plate the electrons are forced towards the sides. The voltage measured as a result of this build-up of charge is called the Hall effect. The Hall voltage is given by (37) where *n* is the density of mobile charges and *e* is the electron charge, shown in Fig. 30.

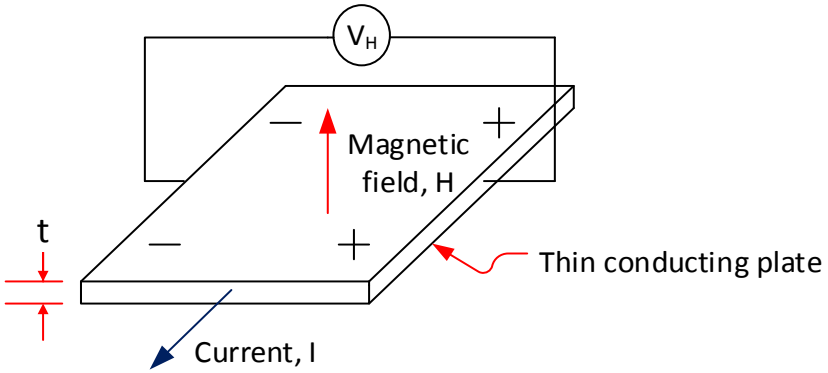

Figure 30: Diagram illustrating the Hall effect

$$V_H = \frac{IH}{net} \tag{37}$$

The Hall voltage is linearly proportional to the magnetic field and is sensitive and stable over a wide range of field strengths and temperatures. Hall effect sensors are widely commercially available, of small size and relatively cheap.

Hall effect sensors have been used by Stupakov [72] to measure the field at different heights above a NOES sample. There was considerable noise at the low field strengths

which the author attributes to thermal effects. Increasing the number of magnetising cycles over which the field was averaged resulted in a smoother BH loop. A Hall sensor was used by Xu [11] to measure the local magnetic field and deemed it to have a measurement uncertainty of 1.09 %.

Commercially available Hall probes can be as small as 4 mm x 3mm with an accuracy of ± 3 % and a magnetic range of -53 kA/m to +53 kA/m [73]. The ease of constructing devices using Hall sensors coupled with their simplicity of use and small sensitive area make them suitable for the measurement of local magnetic properties. Due to these advantages a Hall effect sensor was selected to measure the local magnetic field.

3.1.2. The Needle Probe Method

The needle probe method was proposed initially by Werner [71] as a non-destructive way of measuring the local induction without the difficult task of drilling small holes in the specimen, shown in Fig. 31. His method involved using a one turn coil constructed out of a pair of needles which at the time proved difficult due to the small output voltages generated. The induced voltage in a search coil with N turns, height, h and width, l_{ab} is given by (38).

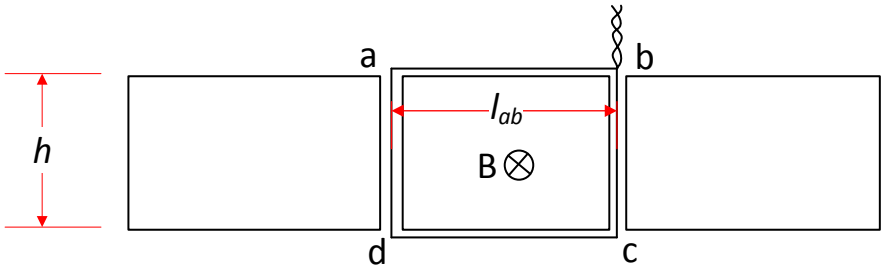

Figure 31: Search coil method for the local measurement of flux density

$$V_{coil}=Nhl_{ab}\frac{dB}{dt} \tag{38}$$

The needle probe method measures the potential difference that is produced because of the eddy currents generated by an alternating flux density between a-b in Fig. 32.

Starting with Faraday's law we write (39).

$$\int_C E.dl = -\int_{S_1} \frac{\partial B}{\partial t} dS \tag{39}$$

Where *C* represents the path *abcda*, S_1 is the area enclosed by *abcd* and *E* is the electric field intensity we can rewrite (39) as (40).

$$V_{ab}+V_{bc}+V_{cd}+V_{da} = \int_{S_1} \frac{\partial B}{\partial t} dS \tag{40}$$

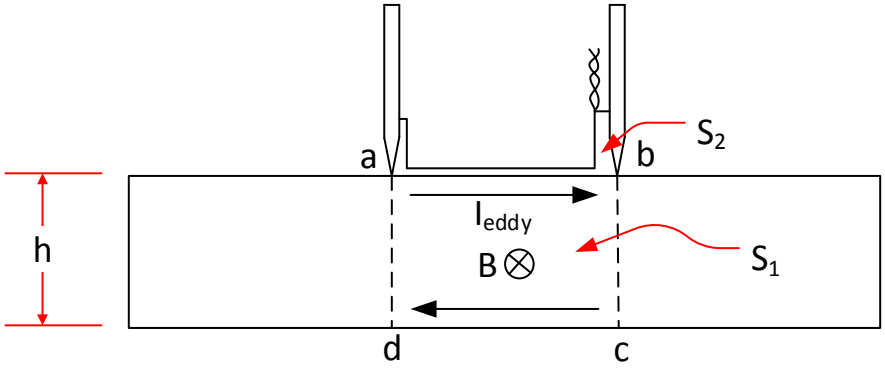

Figure 32: Needle probe method for the local measurement of flux density

Assuming the flux distribution within the sample is symmetrical with regards to the centre axis parallel to the surface on which the needles are places we can write;

$$V_{needle} = V_{ab} = V_{cd} \tag{41}$$

And assuming that,

$$V_{bc} = V_{da} \tag{42}$$

We can rewrite (40) as.

$$V_{needle} = \frac{1}{2}\int_{S_1} \frac{\partial B}{\partial t} dS - V_{bc} \tag{43}$$

Where V_{bc} is the voltage error due to the vertical component of the electric field. If we assume that the measurement is sufficiently far enough from the edge so that $V_{bc} = 0$ then (43) can be simplified to (44).

$$V_{needle} = \frac{1}{2} h l_{ab} \frac{dB}{dt} \tag{44}$$

It was shown by Yamaguchi who conducted a theoretical analysis of the needle

probe method [74] that the voltage between the needles must also include the flux generated by loop formed by the connecting wires and sample surface. It is described by (45) where B_{air} is the flux density in the area, S_2.

$$V_{needle} = \frac{1}{2} h l_{ab} \frac{dB}{dt} - \int_{S_2} \frac{dB_{air}}{dt} dS \tag{45}$$

Comparing (38) to (45) the voltage measured by the needles is shown to be approximately half the voltage generated by a one turn search coil if the following assumptions are assumed to be true;

- The spacing between the needles is large compared to the sample thickness so that the sample thickness can be neglected and
- The component arising from the air flux is small and can be neglected by having the wires close to the sample and tightly twisting them as suggested by Zurek et al [75].

The flux distribution in a poly crystalline structure will always display some asymmetry due to being composed of grains with various sizes and orientation. As such the domain structure will cause inaccuracies [74] with the larger domains of GOES having more of an effect than the smaller domains found in NOES.

With regards to the needle separation, Loisos et al [76] compared needles spacings of 25, 11.5 and 4 mm to search coils of the same spacing on 0.5 mm NOES with errors increasing from 2 % up to 12.5 % for the 4 mm spacing, a spacing to thickness ratio of 8:1.

Error considerations in addition to the air flux include the influence of vertical electric field components which are particularly troublesome at the sample edge. To avoid this Pfutzner [77] suggested a minimum distance between needle and edge of $t/2$ with the needle positions also relevant. Needles placed on the same side of the sample will

underestimate at the edge whereas needles placed on opposite sides will over estimate [78]. An underlying assumption is uniform flux density through the sample thickness and as such, a symmetrical yoke set up should be used in the magnetising system, to maintain accuracy [9]. Causes of measuring error often cited include local stresses and non-homogeneities in the material structure [78] [74]. While it is true that these factors would induce errors in extrapolating the bulk average from the local measurement, if the flux density at that particular location is the primary concern then they do not present an issue in this regard. They may however create a difference in flux density between the top and bottom half and potentially introduce non-zero vertical electric field components.

Modifying the needle probe to try to have two sets of needles opposite each other on the top and bottom faces was performed by Loisos [76, 79]. The author compared search coils to modified needle probe and the traditional needle probe consisting on two needles on the same side. The modified needle probe showed greater agreement with the search coils at smaller needle spacings which was attributed to the vertical electric field components cancelling each other out. However, as noted by the authors it does require access to both sides of the sample, a practical consideration that is not always possible.

Zurek suggested an alternative set up where the electrical connection points made by the needles are replaced with capacitive plates [80]. The author notes that there are major difficulties to be overcome with an additional shortcoming that the necessary application of conductive paste is difficult with its location not easily changed so would be unsuitable for mapping properties. This method does have the advantage of being completely non-destructive. The needle probe method although described as non-destructive does require an electrical contact meaning the coating may need removing which if done carefully can result in a damage free surface, however, the needles are pushed into the sample (usually spring loaded) to get a good connection. Variation in the local flux density does not

exceed 1.5 % for needle loads under 300 g [9].

Although it has limitations the needle probe method because of it’s non-destructive nature and ease of repositioning was selected to measure the local flux density.

3.2. MAGNETISING SYSTEM

The computer controlled, AC magnetising system consisted of a desktop PC with National Instruments Labview 2014 (32 bit) installed, a National Instruments DAQ PCI 6120, EP4000 Europower 4000W power amplifier, an air-cooled isolation transformer, a 1 Ω resistor and a magnetising coil.

The magnetising waveform and voltage were generated by the PC using the "main with H coil – single frequency.vi" in LabView and the NI PCI 6120 card. The waveform was then amplified and fed through the air-cored isolation transformer to eliminate DC offset produced by the amplifier. The strength of the magnetising field produced by the coil was calculated using the current, obtained by measuring the voltage across the non-inductive resistor. The magnetising system set up is shown in Fig. 33.

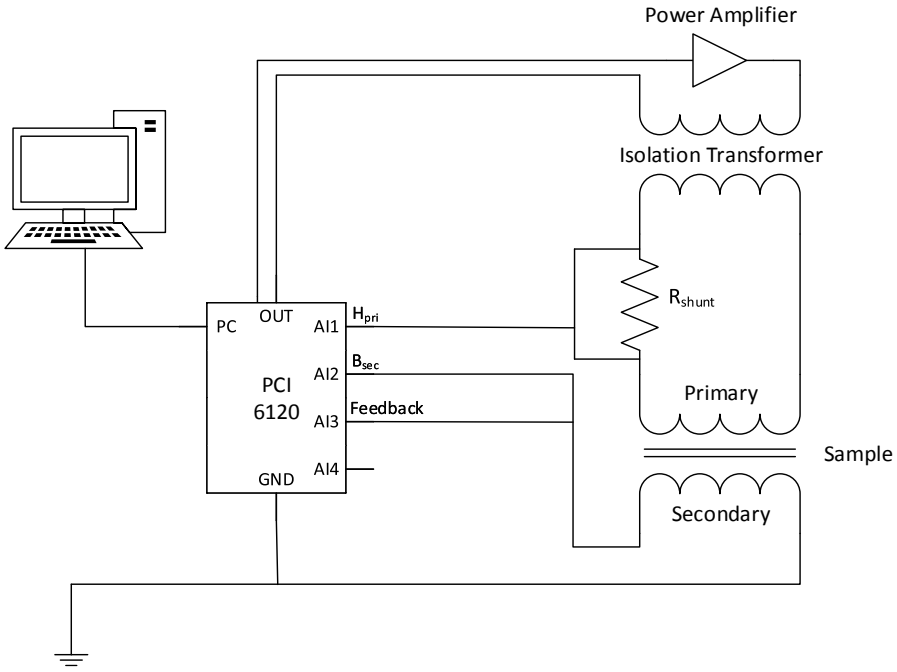

Figure 33: Magnetising system consisted of a desktop PC with National Instruments LabView 2014 (32 bit) installed, National Instruments DAQ PCI 6120, EP4000 Europower 4000W power amplifier, an air-cooled isolation transformer, a 1 Ω resistor and a magnetising coil.

The use of a commercial data acquisition card enabled an analogue output to be generated with a sampling rate of 4 MS/s. The card can simultaneously sample up to 4 input channels with a maximum voltage of 42V and a maximum sampling rate of 800

kS/s [81]. The system controlled the flux density waveform maintaining the wave shape even at high frequencies. In addition to the magnetising current (voltage across the non-inductive resistor) and the secondary voltage an additional input was added to monitor the voltage output from the previous generation of the control algorithm, this fast feedback improved processing time. A schematic of the algorithm is shown in Fig. 34.

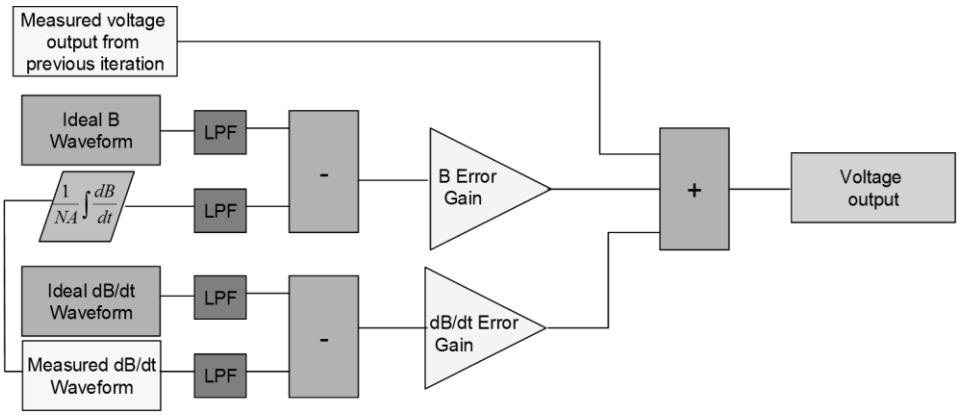

Figure 34: Waveform control algorithm.

The user friendly graphical user interface which allowed the input of the test and material parameters and presentation of results is shown in Fig. 35

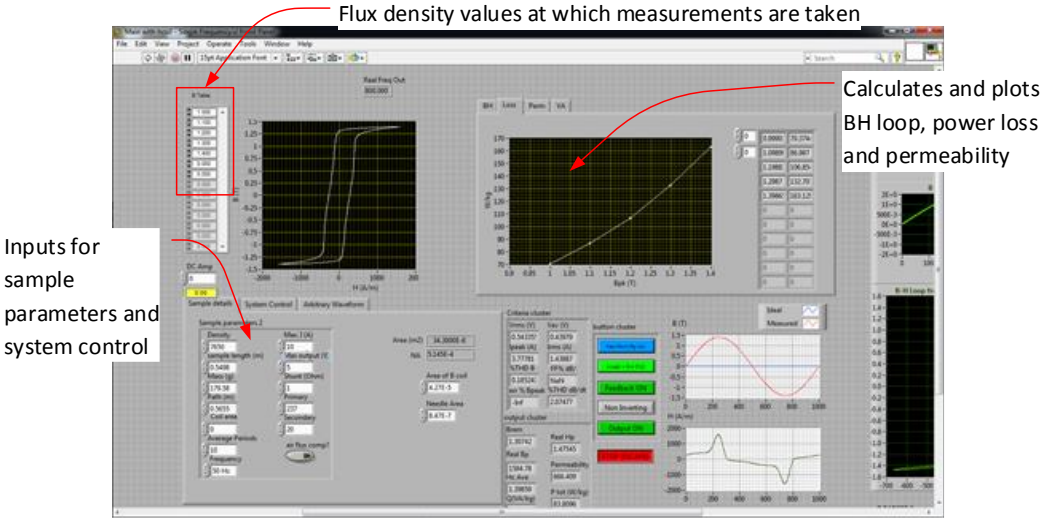

Figure 35: LabView interface for the magnetising system. The sample properties as well as the magnetising conditions are defined including percentage error of peak flux density (B_{peak} value), the total harmonic distortion (THD) and the form factor (FF) of the induced voltage in the search coil.

Existing LabView programs had to be re written to be suitable to simultaneously measure local properties. The magnetising system was designed and simulated using

Solidworks before being built. The positioning system was designed, built and coded. These systems were then incorporated together to produce a device capable of measuring complex geometries a property which is not available on other measurement systems.

3.2.1. Magnetising Coil Design

A coil system was designed and built, the geometry of which was influenced by the shape of the samples, which for these experiments were ring samples. The design consisted of three winding formers shown in Fig 36 with design specifications in Fig 37. The Cardiff University selective laser sintering facilities were used for the rapid prototyping of the parts using the EOS, model P7000 which has a 700 mm x 380 mm x 580 mm build chamber and can produce the parts in polyamide.

The original design and modelling consisted of three coils separated by 120° however it proved necessary to introduce a supporting base to prevent the bending of the sample with the application of the probe and to prevent movement of the sample between measurements. To facilitate this the three winding formers were placed as close to an equal angular distance from each other, 90° separation. Allowing room for the base, unfortunately this did increase the spacing between the measurement location and the coils. The setup use is shown in Fig. 36.

Figure 36: Coil system design consisting of three winding formers with a 150 mm ID ring sample

3-Coil Design

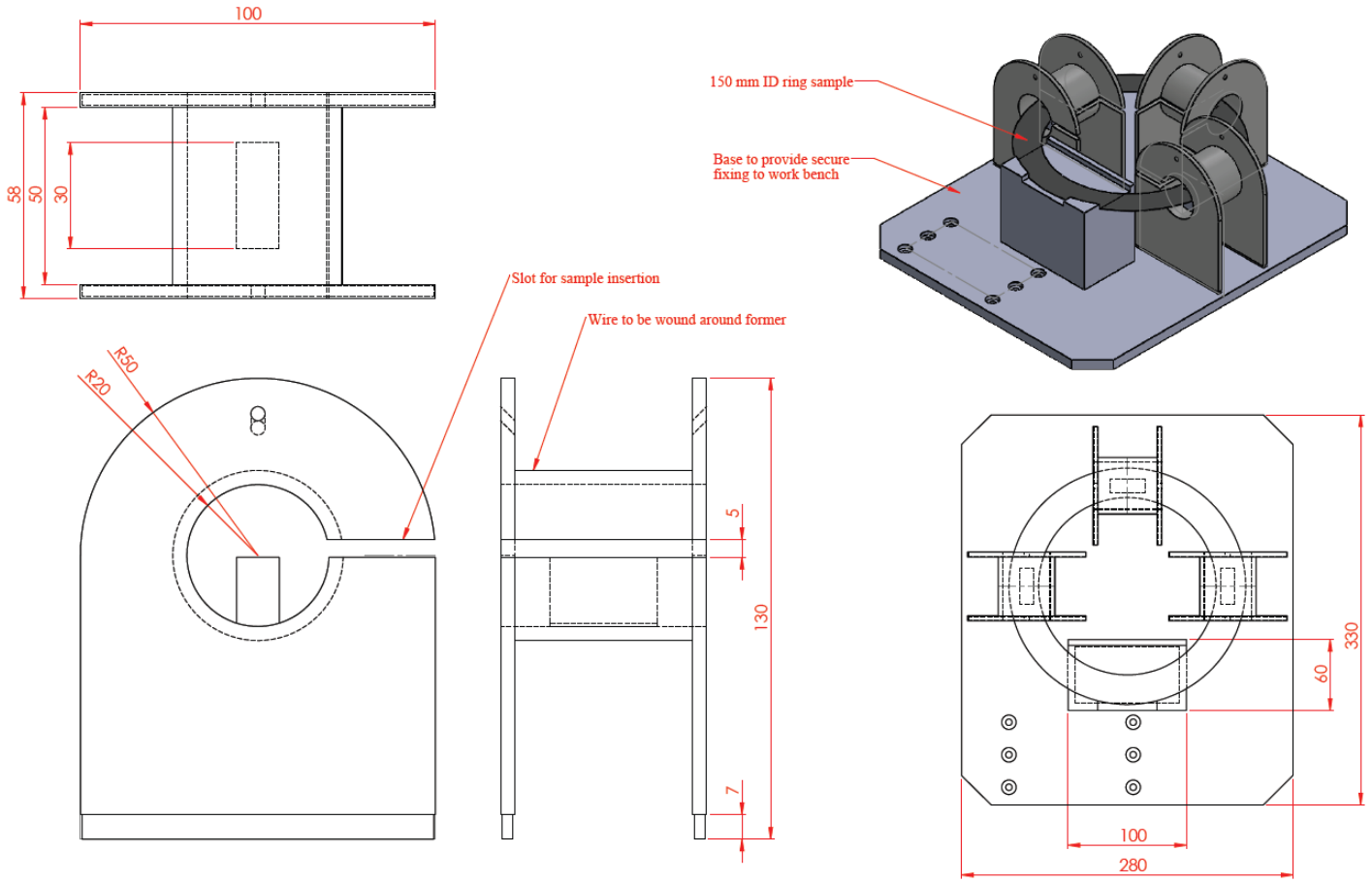

Figure 37: 3-Coil magnetising system specification.

The advantage was that the three winding formers were not in direct contact with the ring sample which sat freely on the supporting blocks so that no additional stress was applied. The sample was easily rotated to measure local properties at different locations around the ring. However rewinding of the secondary coil was necessary.

Fig. 38 shows the bulk magnetic field measurements at 1.0 and 1.3 T and 400 Hz obtained using the 3-Coil system. Measurements were performed on M250-35A ring samples with a 150 mm ID and 200 mm OD. The magnetic field H is calculated using (46) from the current, I in the primary winding, obtained by measuring the voltage across a 1 Ω non-inductive resistor and where N is the number of turns and l is the path length.

$$H = \frac{\mathrm{NI}}{l} \tag{46}$$

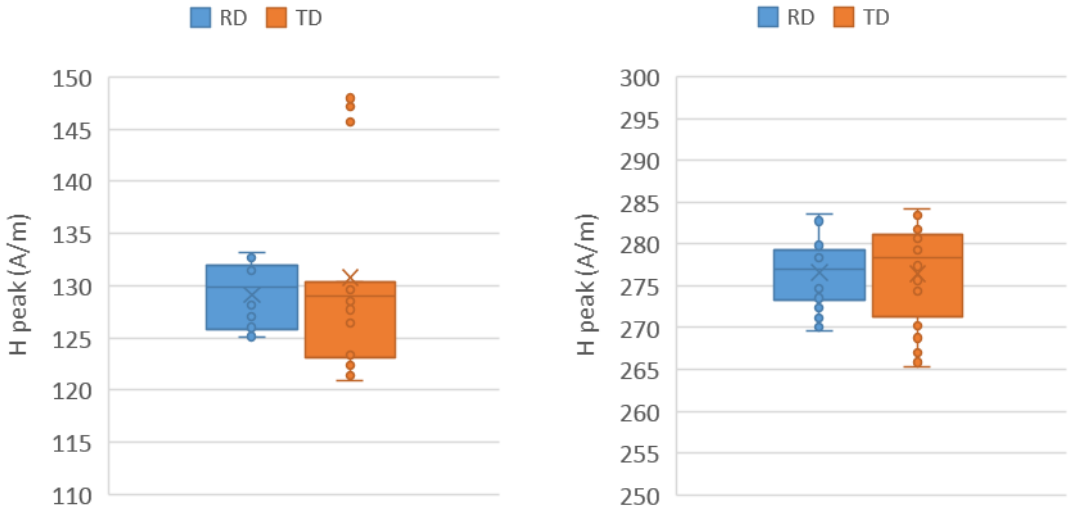

Figure 38: Bulk magnetic field measurements using the 3-Coil system calculated from the primary current measured at 1.0 T (left) and 1.3 T (right) at 400 Hz.

The magnetic field measurements obtained with the 3-Coil design had a standard deviation < 5 % for all orientations and flux densities with the one exception being 7.2% at 1.0 T in the TD. Generating stable measurement conditions became increasingly difficult as the field increased. The measurement of the bulk properties was taken by the

secondary coil which was wound around approximately 270° of the sample which included all three magnetising coils and was on the opposite side of the sample to where the local properties would be measured. The largest angular distance between windings was due to the base size. This, coupled with the non-uniform field generated by the winding formers, raised the question of whether the bulk properties measured at one side of the ring were an accurate approximation of the bulk properties of the ring in the region where the local measurements were taken. To investigate this further, FEM modelling of the magnetising system was performed using Comsol Multiphysics 4.3b. There was a decrease of only 1 % in the average flux density at the local measurement location compared to the secondary measurements at 1.0 T shown in Fig. 39. However, this increased rapidly with increasing field.

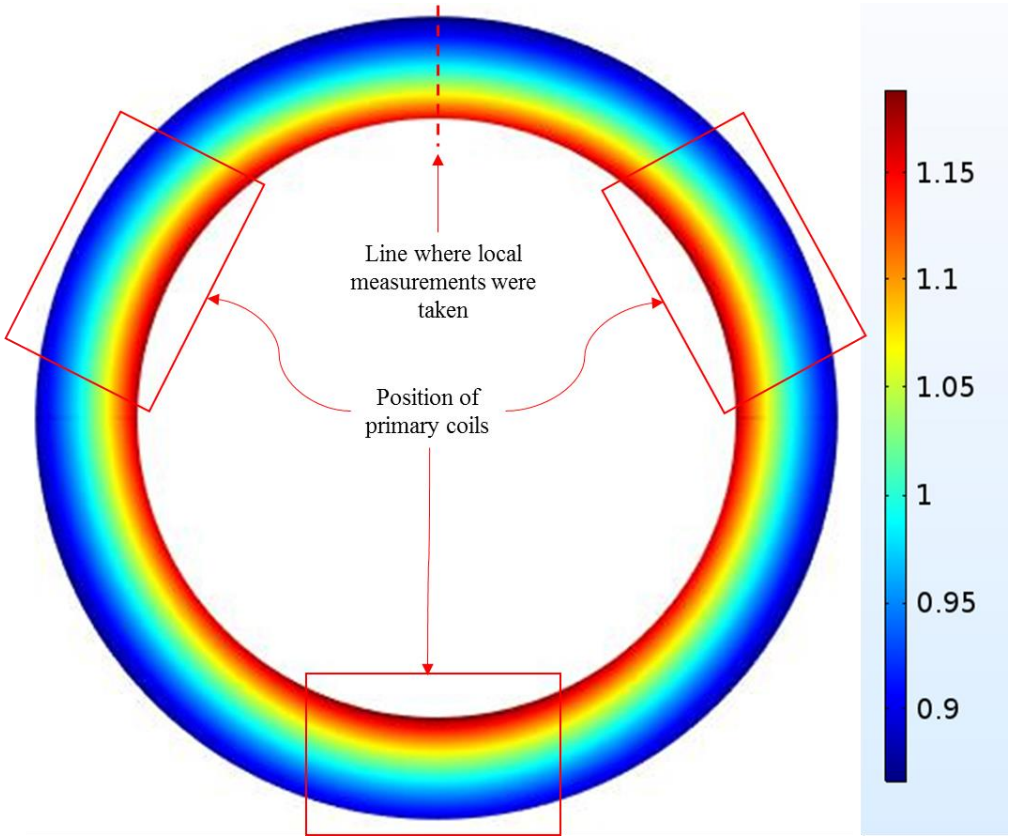

Figure 39 – Simulation of flux density in 150 mm ID ring of M250-35A electrical steel for a value of 1.0 T measured in the secondary coil using the 3-Coil magnetising system.

Fig.40 shows that the highest flux density was found in the parts of the sample

within the coils. When 1.5 T was reached in the secondary coil the sample within the coil would be approaching saturation while sections between the coils, where the local measurements would be taken could be more than 10 % lower.

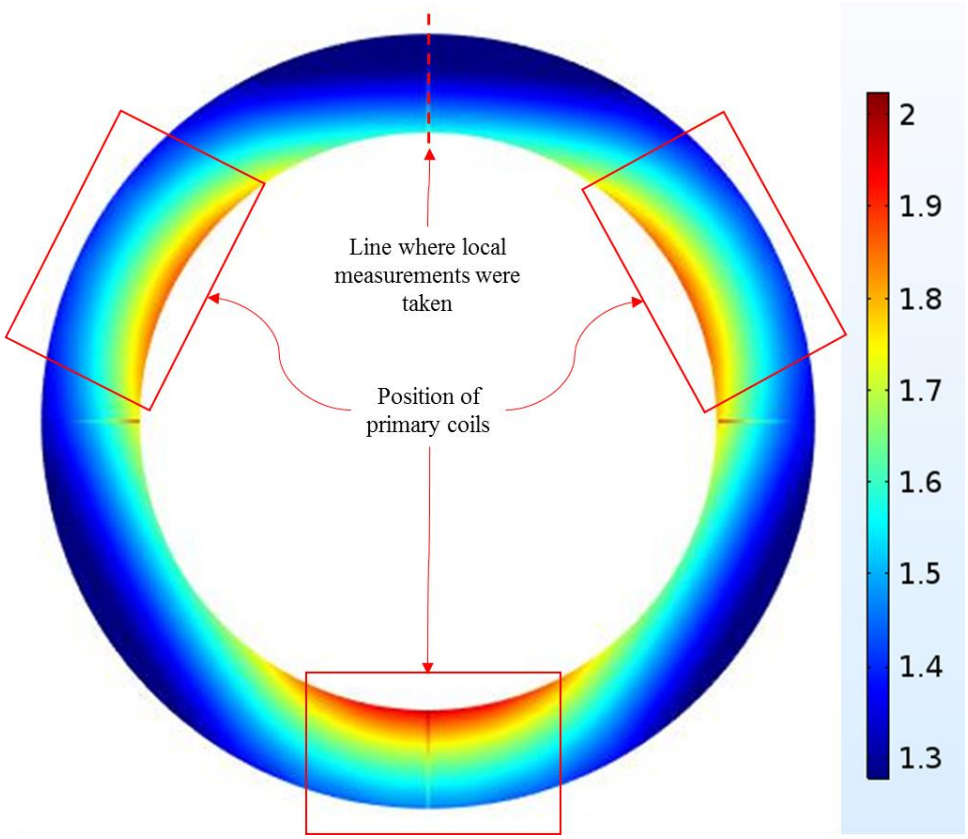

Figure 40 – Simulation of flux density in 150 mm ID ring of M250-35A electrical steel for a value of 1.5 T measured in the secondary coil using the 3-Coil magnetising system.

The coil system was redesigned to address this problem. The second design, shown in Fig. 42 with design specifications in Fig. 41, was an enclosed case. The improved design allowed uniform winding around approximately 90% of the sample via the placement of guiding grooves in the case. The secondary coil was placed on a moveable collar which was positioned as close as possible to the location where the local measurements were taken. The top case which contained the ring was detachable from the base to allow the use of different size cases to accommodate different size samples and facilitate the easy changing of samples.

Enclosed Case

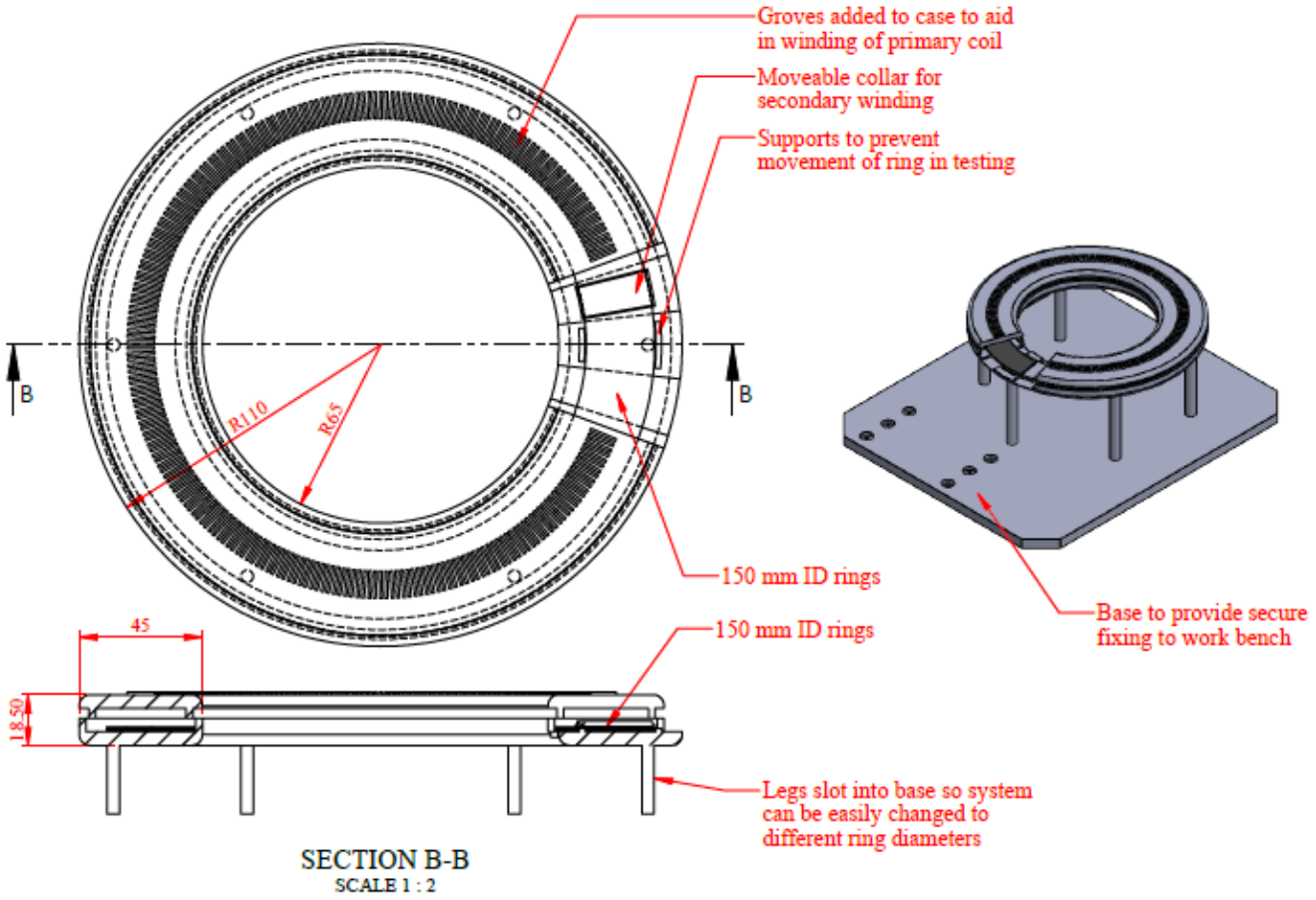

Figure 41: Enclosed case magnetising system specifications

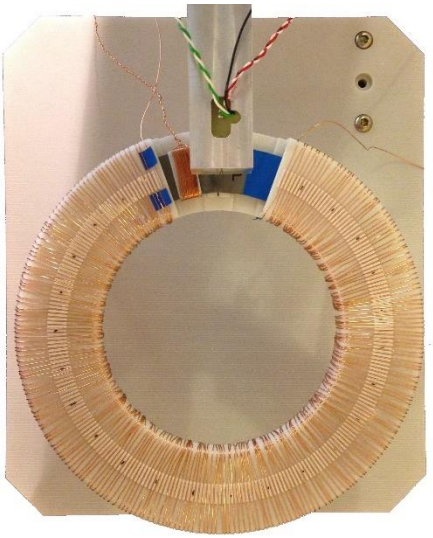

Figure 42: Coil system design consisting of Enclosed case with a 150 mm ID ring sample

The maximum number of guiding grooves and as such the number of windings on this design was limited by the resolution of the SLS production to 237 turns.

Fig. 43 compares the bulk magnetic field using the 3-Coil and Enclosed case setups on M250-35A ring samples with a 150 mm ID and 200 mm OD at 1.0 T and 400 Hz.

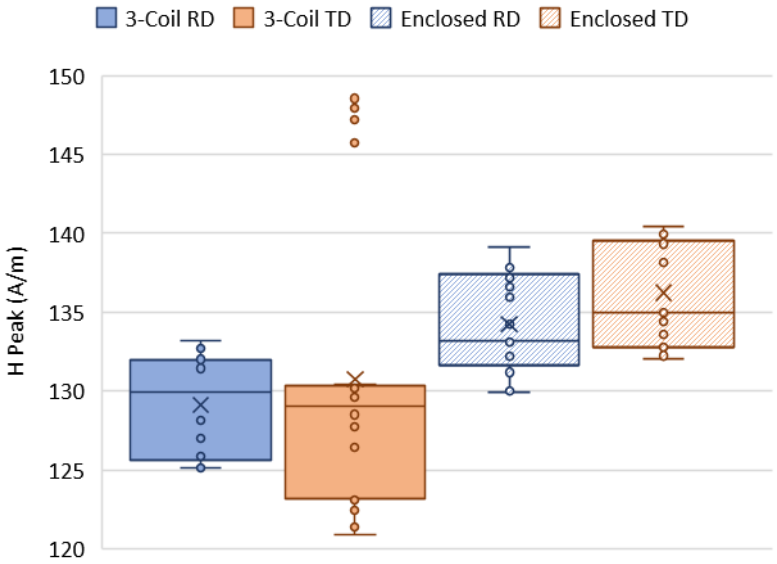

Figure 43: Comparision of 3-Coil and Enclosed case magnetising system design with a 150 mm ID ring sample measured at 1.0 T and 400 Hz

The Enclosed case design has a tighter spread and reduced standard deviation with higher mean values as a result of the secondary coil being located outside the primary

coil. To reach the flux density measurement point a higher field is necessary, confirmed by FEM modelling shown in Fig. 44 and Fig. 45.

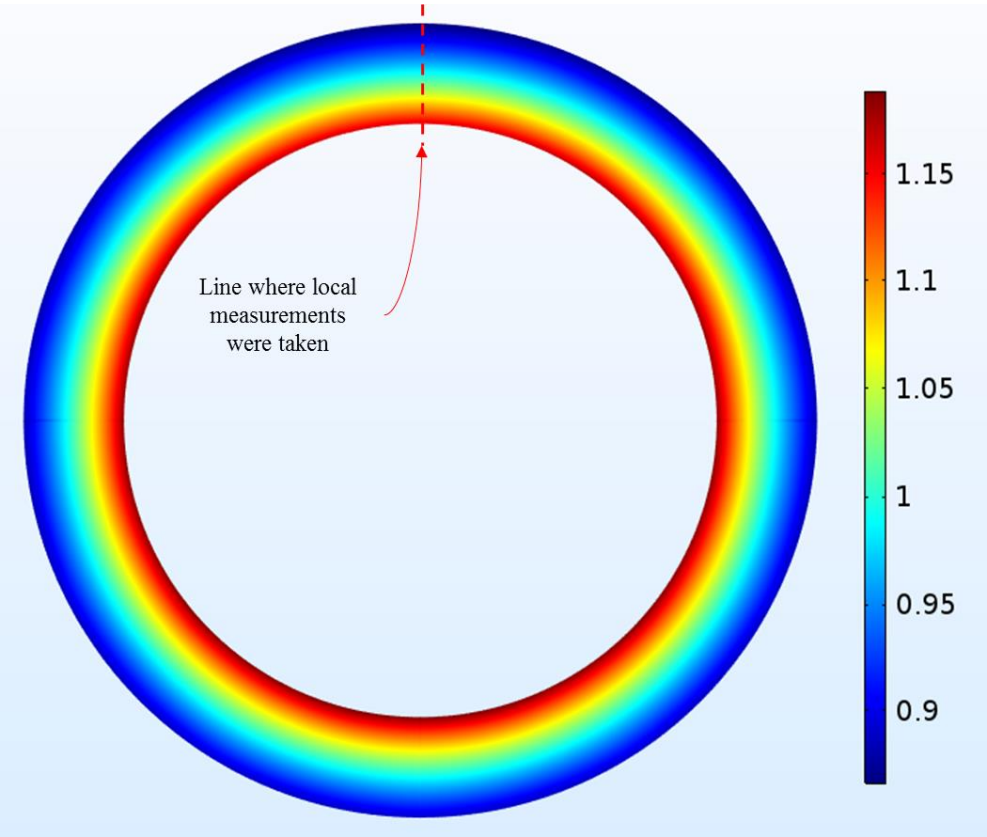

Figure 44 – Simulation of flux density in 150 mm ID ring of M250-35A electrical steel for a value of 1.0 T measured in the secondary coil using the Enclosed case magnetising system.

The lower H peak values in the 3-coil system were due to approximately 60 % of the secondary coil being inside the winding formers where the flux density was highest meaning the measurement conditions were reached at a lower magnetic field compared to a secondary coil located outside of the primary windings. With a secondary coil covering only a small section of the ring as it was in enclosed case the texture at that position has a much greater influence when compared to a coil covering a much larger percentage of the ring. The observation in the variation between the RD and TD noted for higher flux density when measured using the enclosed case but not the 3-coil system which displays similar values irrespective of orientation.

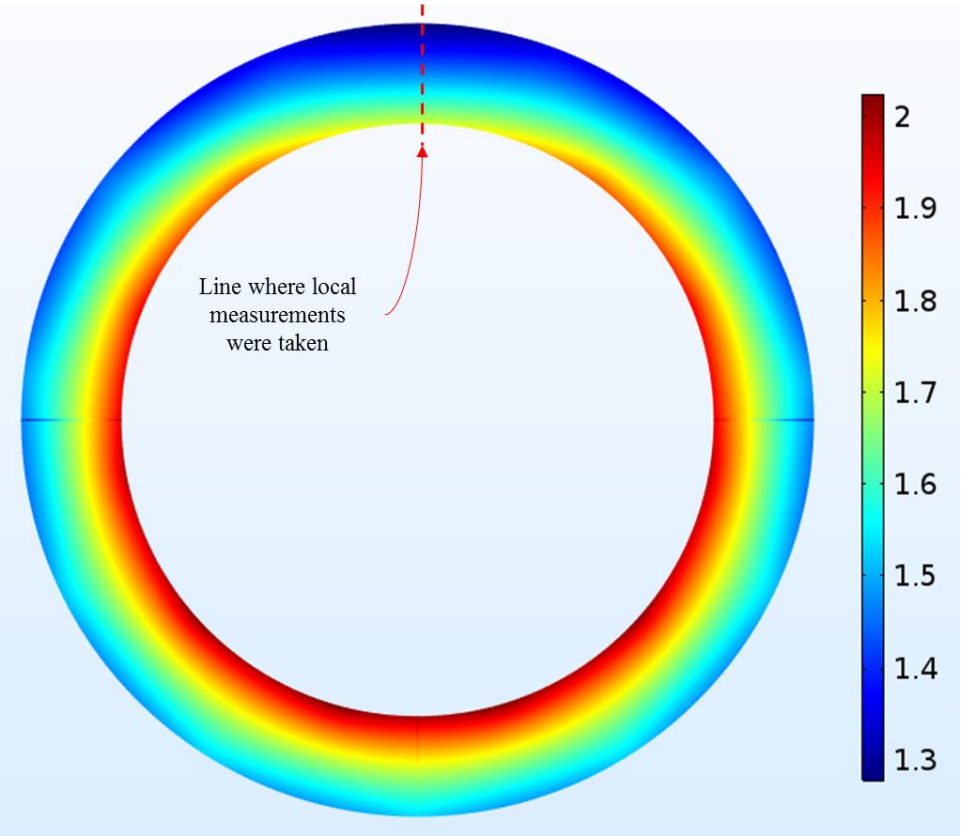

Figure 45 – Simulation of flux density in 150 mm ID ring of M250-35A electrical steel for a value of 1.5 T measured in the secondary coil using the enclosed case magnetising system.

Having the ring supported by a much greater proportion meant a large supporting base was unnecessary so the secondary coil could be placed closer to where the local measurements were taken. This allowed the bulk measurements to reflect more accurately the material properties in the region where the local measurements were taken. The winding grooves provided an easily repeatable winding set up for different samples.

Generating stable measurement conditions, as with the 3-Coil system did prove difficult at fields above 1.5 T as to reach flux densities which were measured by the secondary coil placed in the gap, areas within the coil would be driven into saturation. The difference between the secondary coil and local measurement position was reduced for the enclosed case system as shown in Table 7.

	3-Coils Design		Full Coil Design	
Secondary coil flux density	Flux density probe line	% decrease	Flux density probe line	% decrease
1.000	0.991	0.93%	0.998	0.19%
1.300	1.276	1.82%	1.296	0.32%
1.500	1.345	10.36%	1.477	1.51%

Table 7: Comparison of the decrease in average flux density at the location of the probe line compared to flux density measured by the secondary coil for both magnetising system designs.

3.2.2. Summary

Both coil designs have the advantage of being stress free, the 3-Coil design allows easier rotation of the sample in order to measure at different locations.

The results of the bulk magnetic field measurements shown in section 3.2.1. indicates that out of the two options the enclosed case has better repeatability likely due to more uniform winding. The bulk properties at which the local measurements were taken were more representative of that area of the sample when the secondary coil was placed as close as possible. Because of this and the more stable measurement conditions attainable and as a results the wider range over which measurements could be taken, the enclosed case design was chosen.

3.3. MEASUREMENT SYSTEM

The system was modified to include local measurement methods, shown in Fig. 46. Due to the limited number of inputs it was necessary to remove the fast feedback. Feedback was still employed using digital waveform control [82]. However, it increased processing time, which did make it more difficult to obtain stable measurement conditions.

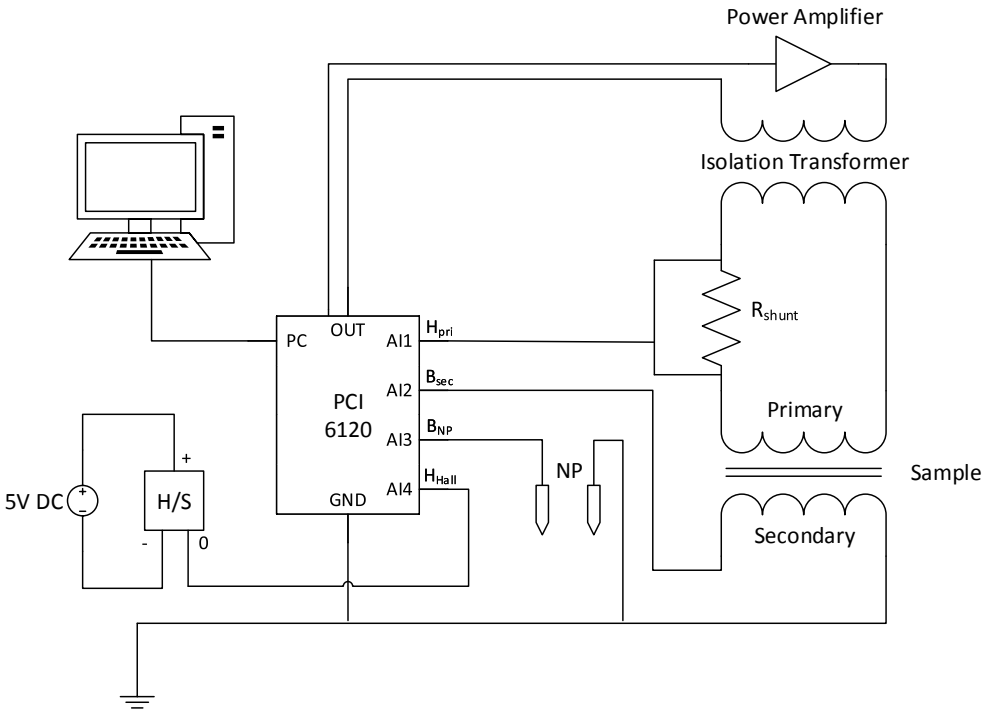

Figure 46: Magnetising system with inclusion of Hall sensor and Needle probe inputs for local measurements

3.3.1. Local Magnetic Field, H

The local magnetic field was measured by a Hall effect sensor, as this non-destructive method could easily be moved across the sample. Two different Hall effect sensors were trialled; a single axis, Honeywell SS495A1 and a 2-axis Melexis MLX91204. Both were analogue, ratiometric and linear Hall effect sensors. Their output voltage was linearly proportional to the strength of the magnetic field.

3.3.1.1. Hall Scale Factor

The Hall scaling factor was obtained by experiment. A magnetic field measured by a Lakeshore 480 Fluxmeter was produced by a 470/500 mm long 110 mm diameter solenoid with 1840 turns of a 2.12 mm diameter wire and a resistance of 4 Ω powered by a Kepco bipolar operational power supply/amplifier. A Farnell stabilised DC power supply unit, set at 5 V provided the input for the Hall effect sensor and output voltage measured by an Agilent 3458A digital multimeter. The Hall effect sensor had an output voltage that was dictated by the supply voltage and linearly proportional to the strength of the magnetic field. The Fluxmeter and Hall effect sensor were placed in the middle of the solenoid, shown in Fig. 47. The field strength as measured by the Fluxmeter was increased and the corresponding output voltage measured at field strengths up to 10 mT at intervals of 1 mT to determine the rate of change of voltage, from which the Hall effect scale factor was calculated using (47).

Figure 47: Top: Lakeshore Fluxmeter and Kepco power unit. Bottom: 1840 turn solenoid used for generation of the magnetic field for Hall probe calibration.

$$F_{Hall} = \frac{1}{\mu_0 \times gradient} \quad (47)$$

Fig 48 shows the results for Hall voltage output for the single-axis Hall effect sensor at different field strengths with an accuracy calculated in section 2.1.1.1 of 2.9 %.

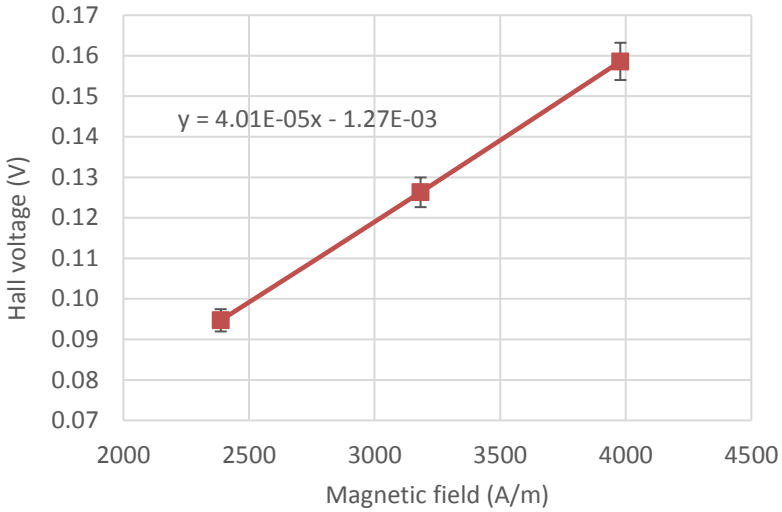

Figure 48: Hall voltage output of the single-axis sensor for different magnetic field strengths.

Fig. 49 shows the results for Hall voltage output for the 2-axis Hall effect sensor at different field strengths orientated in the x-axis (left) and y-axis (right) with an accuracy determined in section 2.1.1.1 of 4.1 %. Table 8 shows the calculated Hall scale factors for the two sensors.

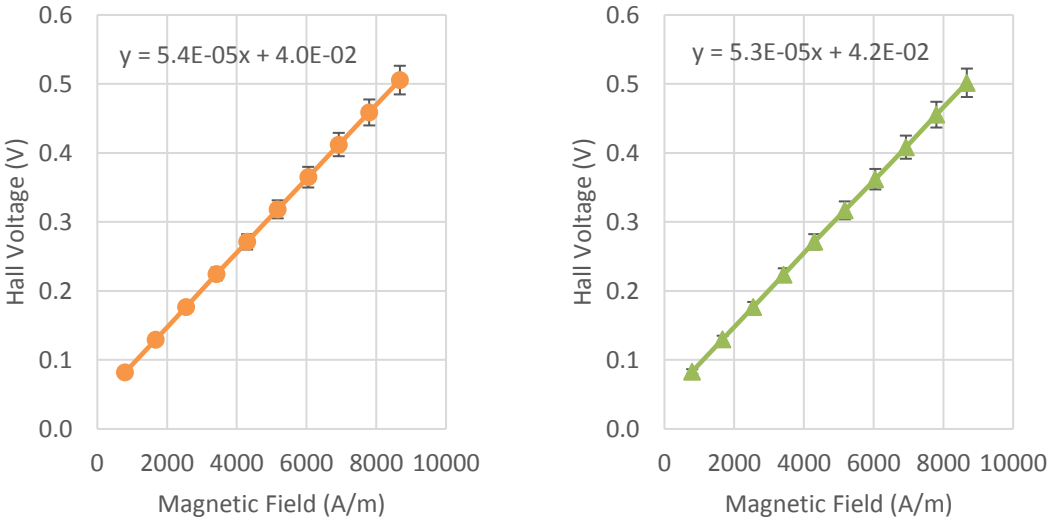

Figure 49: Hall voltage output for different field strengths with the sensor orientated in the x-axis(left) and y-axis (right).

Hall effect sensor model	Hall Scale Factor
Honeywell SS495A1	24907
Melexis MLX91204	17022

Table 8: Hall scale factors for single axis (Honeywell) and 2-axis (Melexis) Hall effect sensors.

Both Hall effect sensors display good linearity. The single axis probe with the smaller chip size allowed for better resolution with the single axis chip able to fit in between the needle point test probes. The values for the Hall scale factors show good agreement with the those calculated by Xu [11] who also used Honeywell SS495A1 Hall effect sensors.

3.3.1.2. Uncertainty Analysis

Tables 9 and 10 detail the uncertainty in the value obtained in the calibration of the Single axis and 2-axis Hall effect sensors respectively used to obtain the Hall scaling factor. The declared uncertainty is 2.9 % for the Single axis and 4.1 % for the 2-axis Hall effect sensor. The uncertainties were determined using the method described in UKAS M3003 [83].

- The accuracy of the NI PCI 6120 DAQ as quoted by the manufacturer at an output of ± 10 V is ± 6.7 mV giving an accuracy range of ± 0.067 %.
- The frequency setting is controlled by the base clock accuracy of the DAQ and has an accuracy of ± 0.01 %.
- The current was manually adjusted until the Lakeshore Fluxmeter reading was within 0.01 of the required value and has a manufacturer-specified accuracy of 0.05 %. The estimated relative uncertainty is ±1.05 %
- The Honeywell SS495A1 series Hall-effect sensor has manufacturer specified linearity error of ±1.0 %

Source of uncertainty	± %	Probability distribution	Divisor	Ci	Ui ± %	Vi or Veff
Accuracy of NI PCI-6120 DAQ	0.067	Normal	2.000	1	0.0335	∞
Frequency setting	0.010	Normal	2.000	1	0.0050	∞
Fluxmeter	1.050	Normal	2.000	1	0.5250	∞
Hall Sensor accuracy	1.000	Normal	2.000	1	0.5000	∞
Output Voltage	0.300	Normal	2.000	1	0.1500	∞
Input Voltage	0.100	Normal	2.000	1	0.0500	∞
Repeatability	2.500	Normal	2.000	1	1.2500	∞
Sum of squares					2.1143	
Combined uncertainty					1.4541	
Expanded uncertainty					2.9081	
Declared uncertainty in Bpeak at a confidence level of 95 %					2.9	

Table 9: Uncertainty analysis for the calibration of the single axis Honeywell Hall effect sensor.

Source of uncertainty	± %	Probability distribution	Divisor	Ci	Ui ± %	Vi or Veff
Accuracy of NI PCI-6120 DAQ	0.067	Normal	2.000	1	0.0335	∞
Frequency setting	0.010	Normal	2.000	1	0.0050	∞
Fluxmeter	1.050	Normal	2.000	1	0.5250	∞
Hall Sensor accuracy	3.100	Normal	2.000	1	1.5500	∞
Output Voltage	0.300	Normal	2.000	1	0.1500	∞
Input Voltage	0.100	Normal	2.000	1	0.0500	∞
Repeatability	2.500	Normal	2.000	1	1.2500	∞
Sum of squares					4.2668	
Combined uncertainty					2.0656	
Expanded uncertainty					4.1312	
Declared uncertainty in Bpeak at a confidence level of 95 %					4.1	

Table 10: Uncertainty analysis for calibration of the 2-axis Melexis Hall effect sensor.

- The Melexis MLX91204 Series Hall-effect sensor has manufacturer specified linearity error of ±3.1 %
- The output voltage measured by the Agilent 3458A multimeter has a manufacturer-specified uncertainty of ± 145 μV when operating in the 10 V giving a relative uncertainty of ± 0.3 %
- The power was supplied to the Hall effect sensor with a Farnell stabilised power supply. The 5 V operating voltage was check using an Agilent 3458A multimeter having an uncertainty of ± 145 μV and measured to an accuracy of 2 d.p. giving a relative uncertainty of ± 0.1 %
- The repeatability was determined. Measurements were repeated four times. Two times the largest standard deviation as a percentage gives uncertainty of ± 4.2 %.

3.3.2. Local Flux Density, B

The needle test point probes were used to measure the local flux density as described in Section 3.1.2.

3.3.2.1. Needle Probe Separation

The needle probe consisted of two, phosphor bronze spring loaded 2-part needle tip probes with diameter 1.03 mm. Three different needle separations were trialled with tip separations 2.436 ± 0.024 mm, 4.84 ± 0.06 mm and 10.16 ± 0.06 mm. Measurements were repeated twice at seven different locations across the central section of a 150 mm ID, 200 mm OD grade M250-35A ring sample in both the RD and TD directions. The probe was moved radially with positions given about the centre of the sample, the negative direction towards the OD and the positive direction towards the ID as outlined in Fig 50. The range of bulk flux densities and frequencies at which measurements were taken was shown in Table 11.

Flux density (T)	Frequency (Hz)
1.0	200 / 400 / 800
1.1	200 / 400 / 800
1.2	200 / 400 / 800
1.3	200 / 400 / 800*
1.4	200 / 400 / 800*
1.5	200 / 400 / 800*

*Table 11: Range of bulk flux density and frequencies at which measurements were taken. * or maximum flux density and frequency possible dependent on material properties and secondary voltage signal.*

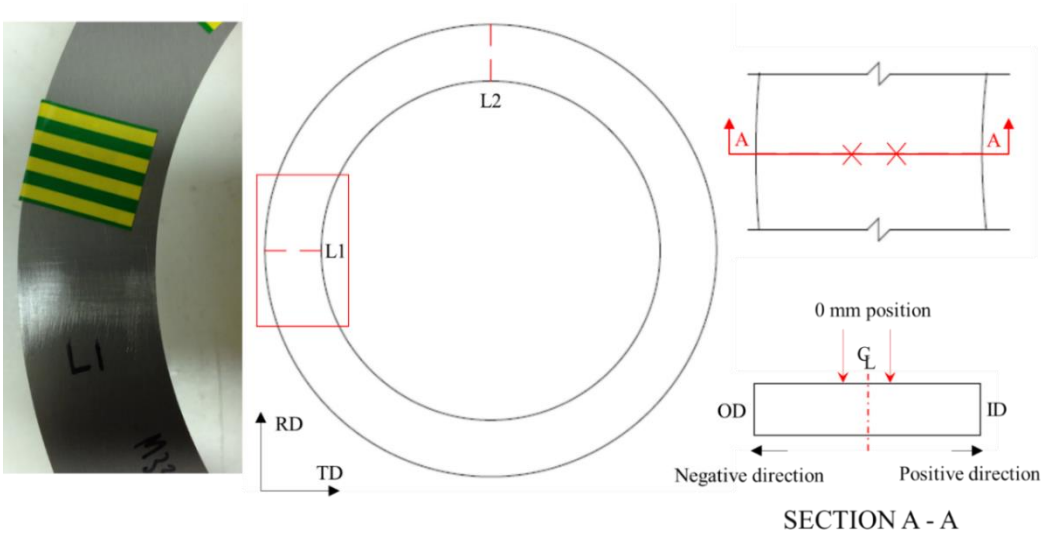

Figure 50: Position of needle probe measurements.

3.3.2.2. 1.0 T 400 Hz

Fig. 51 and 52 show measurements that were performed on M250-35A ring samples with a 150 mm ID and 200 mm OD at 1.0 T and 400 Hz.

The simulation results for the enclosed case design described in section 3.2.1. and shown in Fig 44 are included for comparison (green line) and displays a reasonable agreement with the different needle separations with the best fit in the TD with that of the 2.5 mm probe measurements although it should be noted that anisotropy is not accounted for in the modelled results.

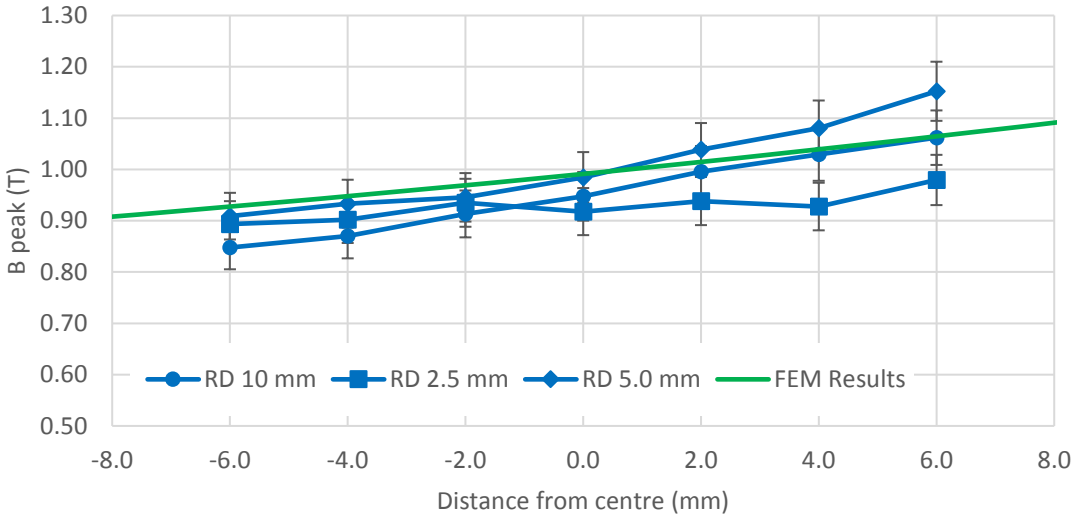

Figure 51: Flux density measurements with different needle separations in the RD at 1.0 T and 400 Hz.

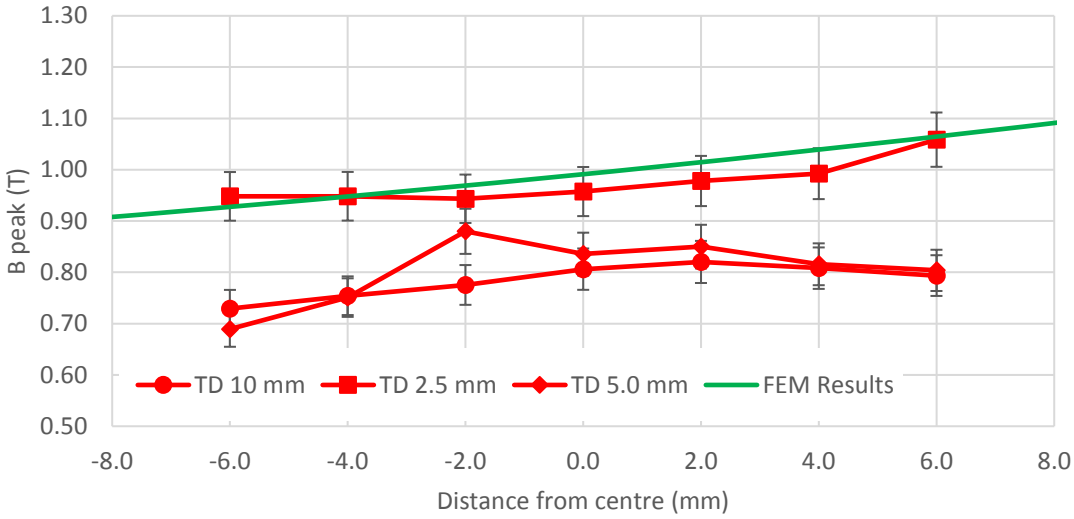

Figure 52: Flux density measurements with different needle separations in the TD at 1.0 T and 400 Hz.

3.3.2.3. 1.3 T 400 Hz

Fig. 53 and 54 show measurements performed on M250-35A ring samples with a 150 mm ID and 200 mm OD at 1.3 T and 400 Hz.

The simulation results for the enclosed case design described in section 3.2.1. are included for comparison (green line) and agrees equally well with the measurements of the different needle separations with no one separation proving more accurate that the others.

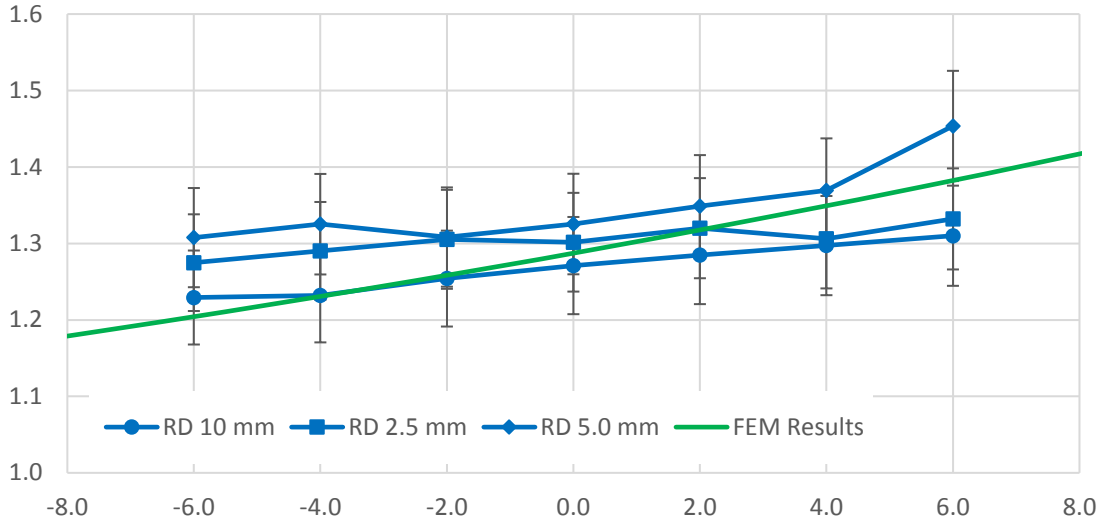

Figure 53: Flux density measurements with different needle separations in the RD at 1.3 T and 400 Hz.

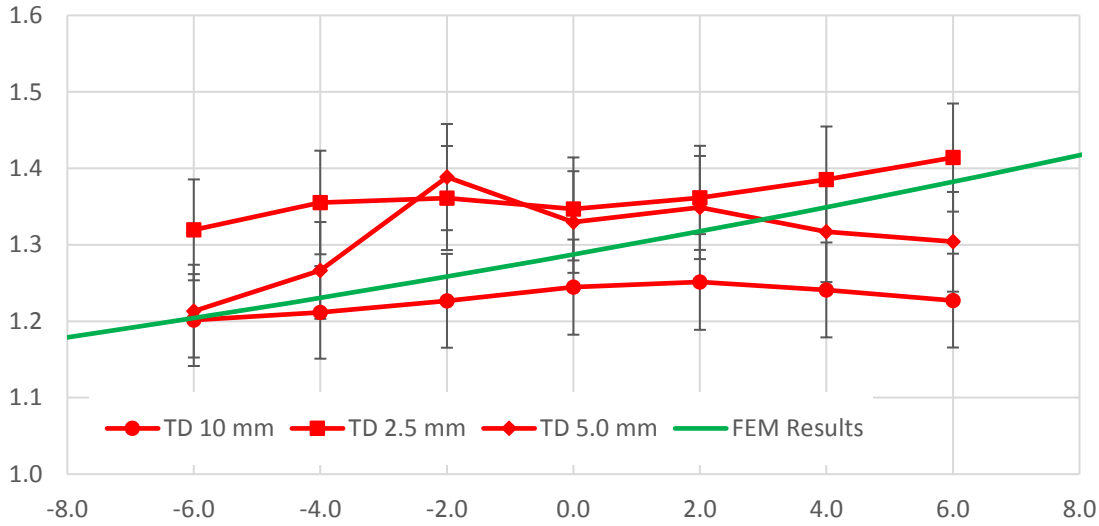

Figure 54: Flux density measurements with different needle separations in the TD at 1.3 T and 400 Hz.

Due to the small number of samples a statistical analysis was performed to determine whether there was any significant difference between the values obtained with different needle tip separations. A dependent t-test was performed to check if the difference in the measured means was significant. The samples were checked for normality using the Shapiro-Wilk test [84]. The results show that there is no significant difference between the means measured in the RD but when measured in the TD the 2.5 mm separation is significantly greater than the 10 mm separations. The distance from the centre of the sample is measured to the point mid-way between the needles which is the

average flux density over the span between the needles. The dips in flux density towards the extremes obtained with the 10 mm needle spacing are likely to be because the area over which the flux density is averaged includes low flux density regions close to the edge. These would not be included in smaller span measurements. Larger or steeper low-density regions in the TD may also explain the increased mean from flux density measurements with the smaller span.

There is a general increase in flux density from the outer edge inwards which is explained by the increase in the magnetic field, H with decreasing radius.

There is anomalous result noted at -2.0 mm from the centre for the 5.0 mm needles in the TD, a possible explanation could be a poor needle connection due to the springs sticking or the incomplete removal of insulation coating.

3.3.2.4. Frequency Variations

Fig. 55 and 56 show measurements performed at the 0 mm position for different frequencies on M250-35A ring samples with a 150 mm ID and 200 mm OD at 1.0 T.

In conclusion, the flux density measurements are comparable when measured in the RD. There is variation in the TD with needle separation however when considered with the bulk flux density and with the increased resolution and access to smaller width samples it is reasonable to conclude that needle separations in the region of 2.5 mm would be suitable for investigating the local properties.

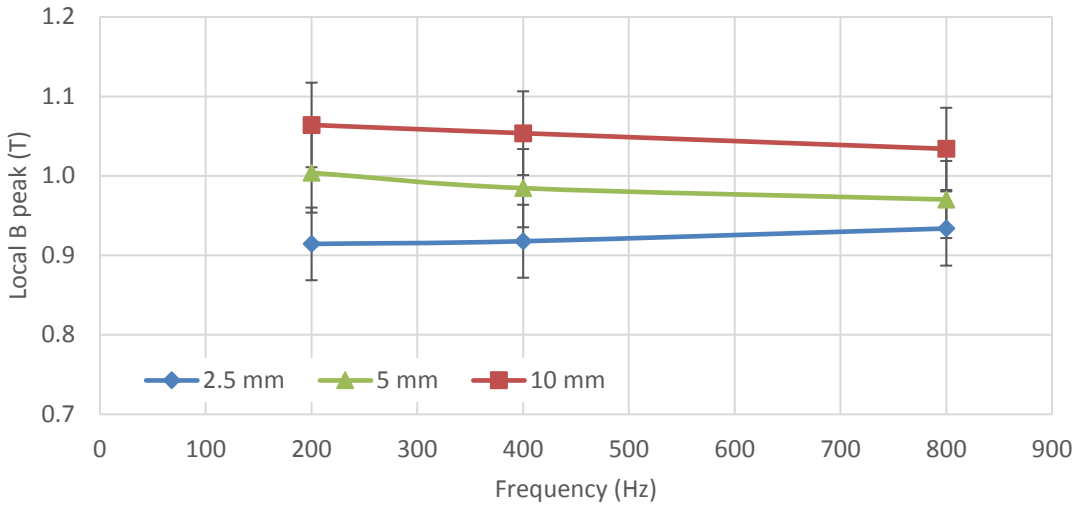

Figure 55: Variations in local flux density with frequency taken at a bulk flux density of 1.0 T and measured in the RD.

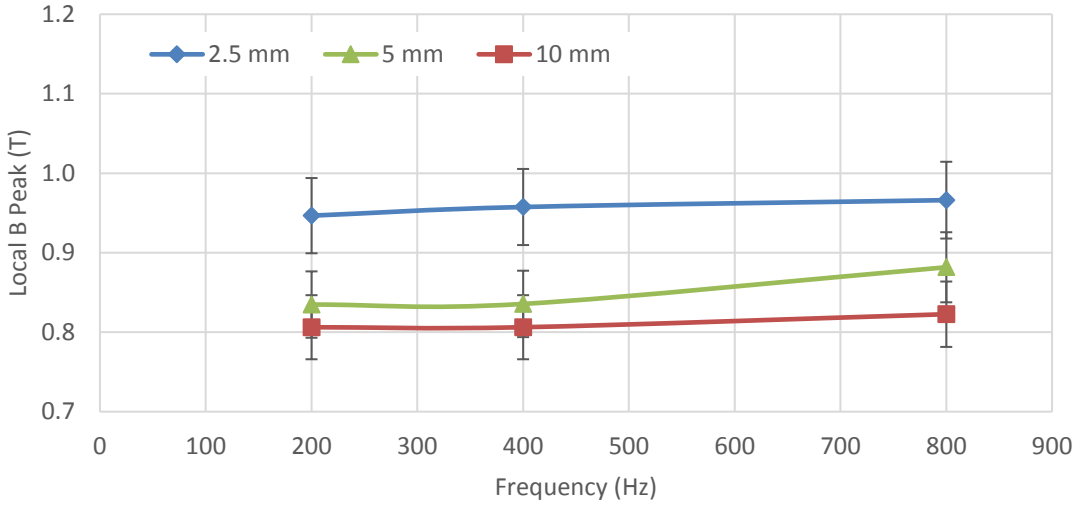

Figure 56: Variations in local flux density with frequency taken at a bulk flux density of 1.0 T and measured in the TD.

3.3.2.5. Uncertainty Analysis

Table 12 details the uncertainty determined in the measurement of flux density by different needle separations. The uncertainties were determined using the methods described in UKAS M3003 [83].

- The accuracy of the NI PCI 6120 DAQ as quoted by the manufacturer at an output of ± 10 V is ± 6.7 mV giving an accuracy range of ± 0.067 %.
- All samples were measured three times using an Avery Berkel balance. The

smallest division was 0.01 g, and the largest uncertainty is ± 0.025 %.

- The frequency setting is controlled by the base clock accuracy of the DAQ and has an accuracy of ± 0.01 %.

Source of uncertainty	± %	Probability distribution	Divisor	Ci	Ui ± %	Vi or Veff
Accuracy of NI PCI-6120 DAQ	0.067	Normal	2.0000	1	0.03350	∞
Mass (Balance calibration)	0.025	Normal	2.0000	1	0.01250	∞
Needle separation	0.985	Normal	2.0000	1	0.49250	∞
Frequency setting	0.010	Rectangular	1.7321	1	0.00577	∞
Sample length	0.459	Normal	2.0000	1	0.22950	∞
Sample density	0.007	Rectangular	1.7321	1	0.00404	∞
B wave form	1.000	Rectangular	1.7321	1	0.57735	∞
Accuracy of positioning system	2.180	Normal	2.0000	1	1.09000	∞
Repeatability	2.740	Rectangular	1.7321	1	1.58194	∞
Sum of squares					4.32052	
Combined uncertainty					2.07859	
Expanded uncertainty					4.15717	
Declared uncertainty in Bpeak at a confidence level of 95 %					4.2	

Table 12: Uncertainty analysis for local flux density measurements obtained using a needle separation of 2.44 mm. Larger separations resulted in the same declared uncertainty.

- The sample length was calculated as $2\pi r_{mean}$ with the sample measured with a rule with divisions of 0.5 mm. The precision of the ruler is ± 0.25 mm. The maximum calculated uncertainty is ± 0.459 %.
- The manufacturer provided sample density was 7600 kg/m3 and 7650 kg/m3 for M250-35A and M330-35A respectively. Assuming an accuracy of ±0.5 kg/m3 the uncertainty is ± 0.007 %.

- The needle separation was measured with a Mitutoyo measuring microscope accurate to 0.001 mm. The measurement was repeated five times producing a result of 2.436 ± 0.024 mm. The uncertainty is ± 0.985 %.
- The B waveform was controlled using Labview. The Bpeak and form factor were set to ± 0.1 % and ± 1 % respectively.
- The positioning system used, a Parker cross roller series has a manufacturer provided accuracy of ± 3.0 µm. Measurements were made every 1 mm with the initial measurement position obtained by placing the probe on the surface of the sample close to the edge and moving it in 0.1 mm increments until the outermost needle is not in contact with the sample. It was then moved back 0.25 mm giving an uncertainty in the initial position of 0.1 mm. The total relative uncertainty increases with decreasing width to a maximum of - 2.18%.
- From repeated measurements, the repeatability had an estimated uncertainty of ± 2.8 %

3.3.3. Measurement Probe Design

Needle tip separation (mm)	Hall effect sensor model	Hall effect sensor dimensions (mm)
2.436 ± 0.024	Honeywell SS495A1	4.06 x 3.0 x 1.6
4.84 ± 0.06	Honeywell SS495A1	4.06 x 3.0 x 1.6
10.16 ± 0.06	Melexis MLX91204	6.20 x 4.98 x 1.73

Table 13: Dimensions and components for the different measurement probes used.

3.3.3.1. Single Axis Probe

Fig 57 shows a schematic of the single axis measurement probe, with a photograph of the constructed probe in Fig. 58.

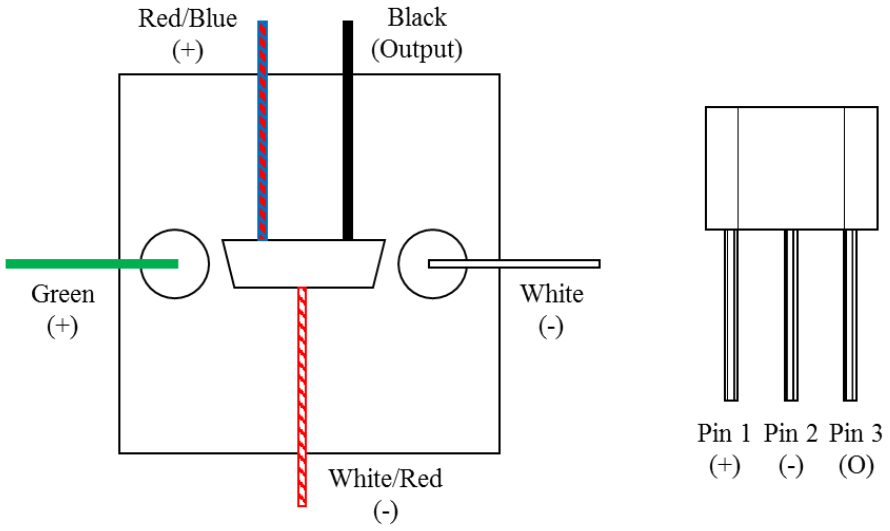

Figure 57: Left, plan of measurement probe circuit board for single axis Hall effect sensor showing connection configuration and wire colours. Right, front view of single axis Hall effect sensor with pin connections.

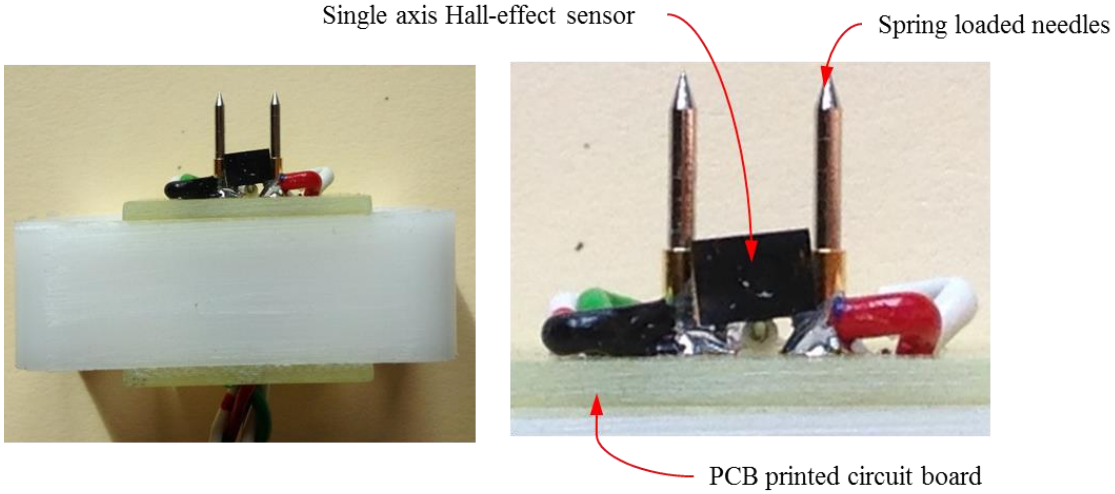

Figure 58: Measurement probe with 5 mm needle tip spacing for local magnetic measurements.

The positive (green) and negative (white) needles were connected to an input of the DAQ as was the Hall sensor output (Black wire). The Hall sensor positive and negative pins were connected to an external power supply. A disadvantage of their small size is

the intricate nature of their construction and even though they were assembled by an experienced technician some misalignment is still evident.

3.3.3.2. 2-Axis Probe

Fig 59 shows a schematic of the 2-axis measurement probe, with a photograph of the constructed probe in Fig. 60.

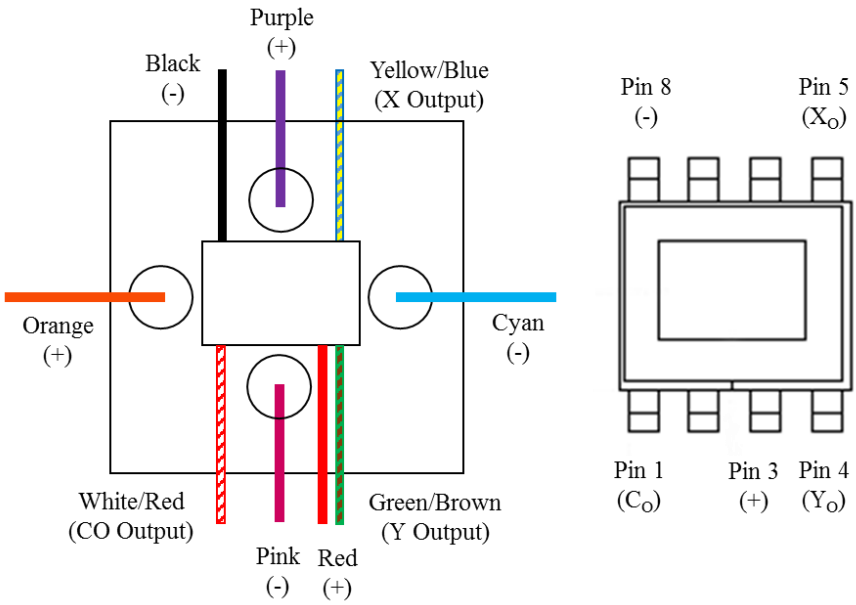

Figure 59: Left, plan of 2-axis measurement probe circuit board showing connection configuration and wire colours. Right, plan view of 2-axis Hall effect sensor with pin connections.

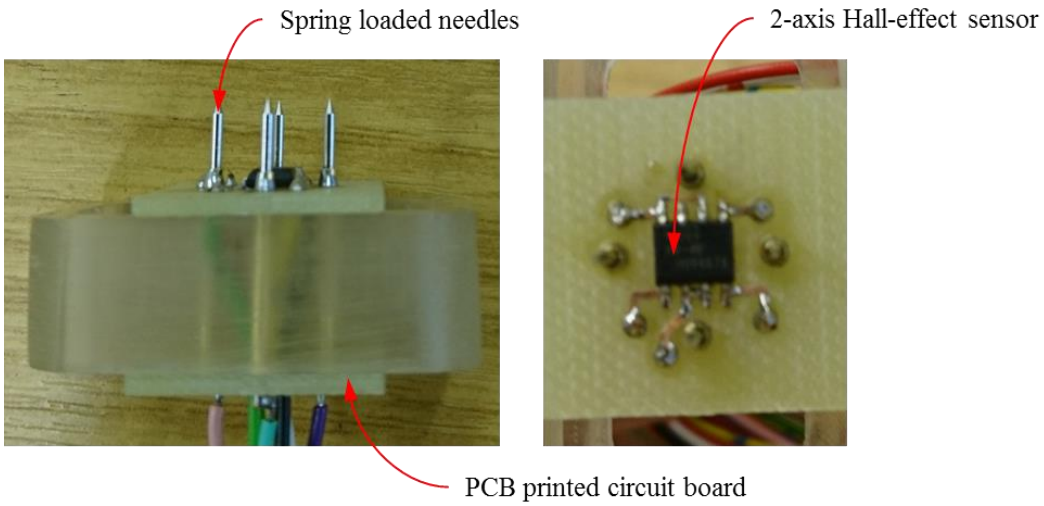

Figure 60: 2-Axis measurement probe with 10 mm needle tip spacing for local magnetic measurements.

3.3.4. Summary

There was scope for different size probes to be constructed for different applications with the size of the probes determined by the physical size of the components involved. The single axis probe allowed for a smaller needle tip spacing without a decrease in accuracy, which provides higher resolution and was deemed essential for investigations of the cut edge and measurements of samples with a width less than 10 mm. When using ring samples the use of a single axis probe was acceptable as both the magnetic field and flux density in the radial direction can be neglected. However for more complicated geometries where the field is not so uni-directional a 2-axis probe would be preferable provided it could either be miniaturised or that the needle tip spacing closer than 10 mm was not needed.

For this work it was decided to use 2.5 mm needle spacing as this provided a high resolution without any significant effects on accuracy this was coupled with a single axis Hall effect sensor, necessitated by the input channels available on the DAQ card. Table 14 lists the probe specifications to be used in the investigation into the effect of stamping.

Probe specification	
Hall effect sensor	Honeywell SS495A1
Needle tip separation	2.436 mm

Table 14: Probe specifications that were taken forward.

3.4. POSITIONING SYSTEM

The positioning system consisted of a three-axis computer controlled positioning system connected to an aluminium arm in which the probe was mounted. The Parker positioning system consisted of a desktop PC running ACR-View software with which the motion was configured and programmed using the Acrobasic programming language, shown in Fig. 61. It was then downloaded to an ACR9000, a motion controller for controlling servo and stepper drives. Each axis used a Parker/Compumotor S57–51 stepper motor powered by a Parker S Drive, with an accuracy of ± 0.083° and a repeatability of ± 0.083°. Each motor is connected to a Parker Daedal 4900 series ball bearing linear positioner with a fine screw and accuracy of 2 µm per 25 mm travel. The X, Y and Z axes have a maximum of 100 mm of travel

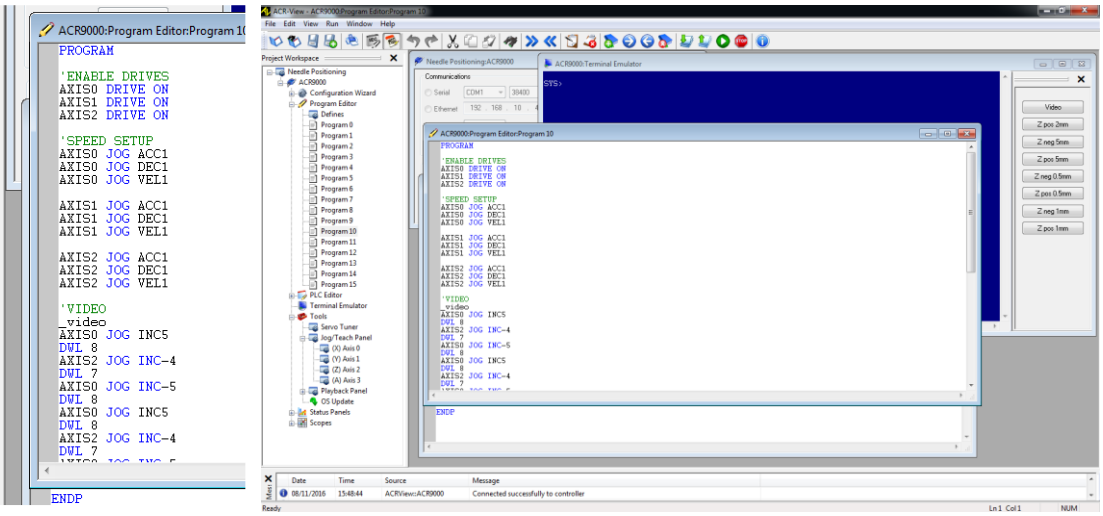

Figure 61: Screen shot of the control interface for the positioning system within using ACR view

The aluminium arm was fixed to one of the linear positioning stages. After a measurement had been taken the probe was lifted from the sample and moved to the next point. When measuring different locations on the ring, the probe was raised, and the sample rotated in the case underneath. The setup is illustrated in Fig. 62.

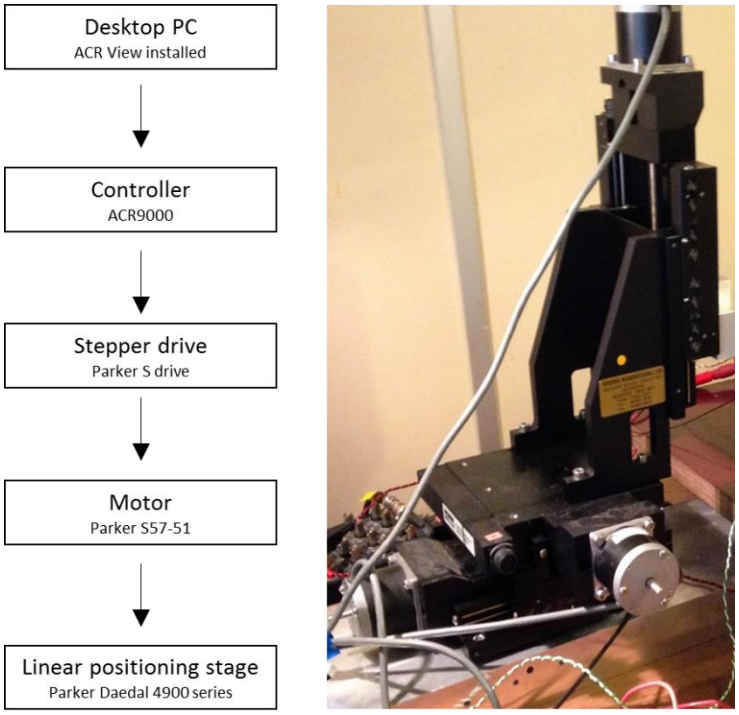

Figure 62: Left, Flowchart showing positioning system setup. Right, Parker cross roller linear positioning stages

For the controller to function correctly and motion to occur a current must flow through the *Enable input*, shown in Fig. 63. To override this fail-safe the enable connector at the bottom left of the controller was connected to an 5 – 24 V external power unit (Anode (+) pin 1 and cathode (-) pin2).

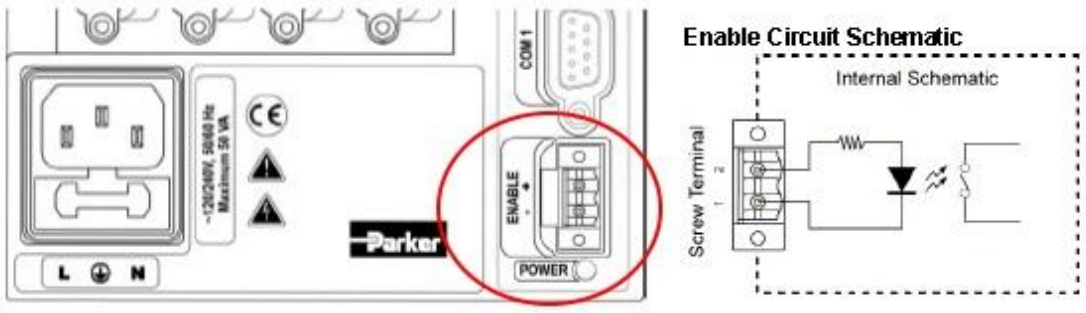

Figure 63: Location of Enable input on ACR 9000 controller that must be connected to a power supply to allow operation.

To assess the accuracy of the positioning system several simple programs were written to control the movement of the linear positioning stages. One of the programs is shown in Fig 65.

```
    PROGRAM

 'ENABLE DRIVES
AXIS0 DRIVE ON
AXIS1 DRIVE ON
AXIS2 DRIVE ON

  'SPEED SETUP
AXIS0 JOG ACC1
AXIS0 JOG DEC1
AXIS0 JOG VEL1

AXIS1 JOG ACC1
AXIS1 JOG DEC1
AXIS1 JOG VEL1

AXIS2 JOG ACC1
AXIS2 JOG DEC1
AXIS2 JOG VEL1

  'NEXT POINT
   _lastpoint
AXIS0 JOG INC7
     DWL 8
AXIS2 JOG INC2
     DWL 3
AXIS0 JOG INC-7

     ENDP
```

Figure 65: Positioning program used in ACRview to control the movement of linear positioning stages.

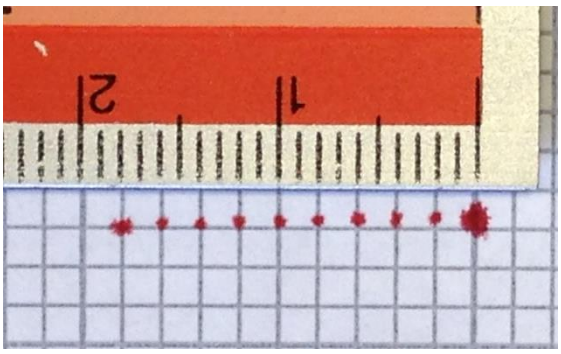

Figure 64: Test of 1.0 mm linear motion

The program would move the positioning arm around a grid, part of which is shown in Fig. 64 where marks would be made at predefined coordinates. The distances between the points were confirmed utilising a metal ruler with 0.5 mm divisions. The positioning arm specifications are shown in Fig. 66.

The manufacturer specifications of repeatability for the Parker cross roller series is ±3.0 µm. This level of precision could not be confirmed because of the testing equipment available however it was confirmed that it would be able to position the measurement probe over a complex array of positions to within an accuracy of at least 0.5 mm which was suitable for the needs of this project.

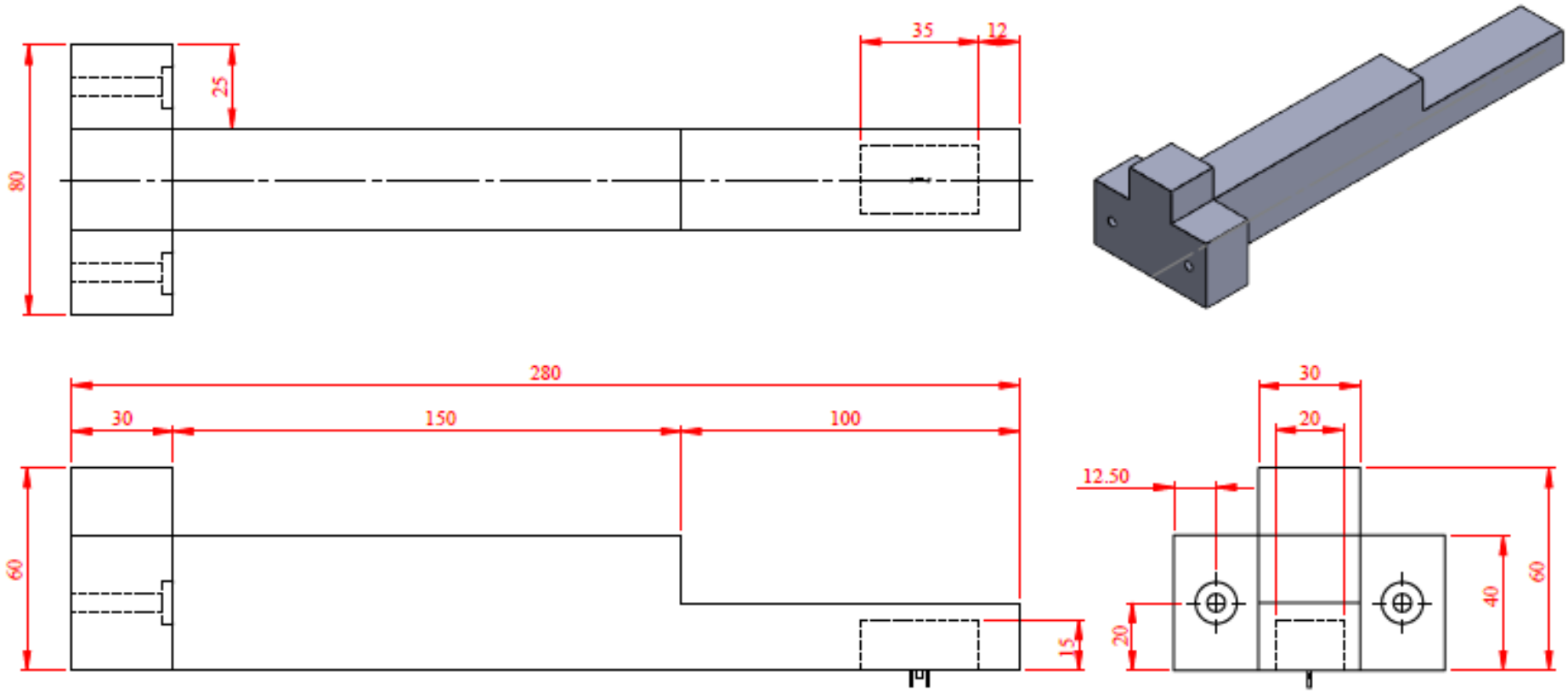

Figure 66: Aluminium arm fixed to computer controlled positioning system used to house measurement probe.

3.5. CONCLUSIONS

In conclusion, the requirements have been addressed and can be summarised as; The enclosed case, design B was the most suitable option, which minimised the unwanted variations resulting due to the gap in the primary windings. This design will be used for assessment of stamping discussed in future chapters.

A measurement probe consisting of a single axis Hall effect sensor would be suitable for strips and ring samples, providing the plane of the Hall sensor is in the radial direction where the component of the magnetic field is negligible. The smaller chip size allows for a smaller separation in needle spacing which would provide better resolution and would be a necessary when investigating narrow parts of motor laminations such as the teeth.

The positioning system can be programmed for any arrangement of points in three dimensions and can move accurately over many points.

CHAPTER 4.

MEASUREMENT AND ANALYSIS OF LOCAL MAGNETIC PROPERTIES AND MATERIAL CHARACTERISATION

This chapter details the experimental work carried out on two different grades of electrical steel. Section 1 describes the method used to obtain the data while Sections 2 and 3 present the results and discussion respectively.

4.1. METHOD

4.1.1. Local Measurement of the Magnetic Properties

The system described in Chapter 3 consisting of the enclosed case magnetising system and single-axis probe, was used for simultaneous measurement of both global and local properties of ring samples.

The enclosed case had a 237 turn primary winding, using 0.5 mm thick enamelled copper wire and a 15 turn secondary winding, which was wound on a moveable collar to obtain the global flux density. The tolerances, defined in the LabView interface, were the percentage error of peak flux density (B_{peak} value), the total harmonic distortion (THD) and the form factor (FF) of the induced voltage in the search coil. They were initially set as 0.1 %, 10 % and 1.0 % respectively.

The secondary coil was made by wrapping a 0.5 mm thick enamelled copper wire around a Polyamide collar with dimension 15 mm x 4 mm x width of sample and was positioned 10° (approximately 17 mm) from where the local measurements would be taken. This was to make as direct a comparison as possible between the bulk and local measurements as the flux density, particularly for higher fields and thinner samples, would decrease significantly in the gap between the rings. The use of the collar also allowed the sample to be rotated within the case so different positions on the ring could

be accessed.

4.1.1.1. Sample Preparation

Ring samples with a constant outer diameter (OD) of 200 mm and the various inner diameters (ID) shown in Table 15 were punched from coils of M250-35A (coil no. 1772596) and M330-35A (coil no. 1782832) non-oriented electrical steel (NOES). The steel was provided by Tata Steel/Cogent Power and punched using new tooling by Wingard & Co,Baltimore, U.S.A.

OD (mm)	ID (mm)	Width (mm)
200	150	25
200	160	20
200	170	15
200	180	10
200	190	5

Table 15: Dimensions of M250-35A and M330-35A samples showing outer diameters (OD), inner diameters (ID) and width

The variation in chemical composition of the two grades, which also include small amounts of other elements that are consistent between the grades is detailed in Table 16 with information from the manufacturer datasheets summarised in Table 17. [15, 16]

Grade	C %	Si %	Mn %	Al %
M250	0.0045	3.2000	0.1000	0.8500
M330	0.0035	2.4000	0.1500	0.3000

Table 16: Chemical composition of M250-35A and M330-35A samples

Grade	Thickness (mm)	Resistivity (μΩcm)	E, RD (N/mm^2)	E, TD (N/mm^2)	Yield strength (N/mm^2)
M250	0.35	55	185 000	200 000	455
M330	0.35	42	200 000	210 000	315

Table 17: Manufacturer provided material data for M250-35A and M330-35A samples

4.1.1.2. Measurement Locations

Local measurements were taken at 1 mm intervals and at three locations, perpendicular, parallel and at 45° to the rolling direction (RD). The probe was moved in a radial direction across the sample measuring the local properties in the tangential direction. Measurements at different locations, shown in Fig. 67 and were taken at a constant bulk flux density as measured by the secondary coil and were taken at the frequencies and globally measured flux density, as measured by the secondary coil, shown in Table 18.

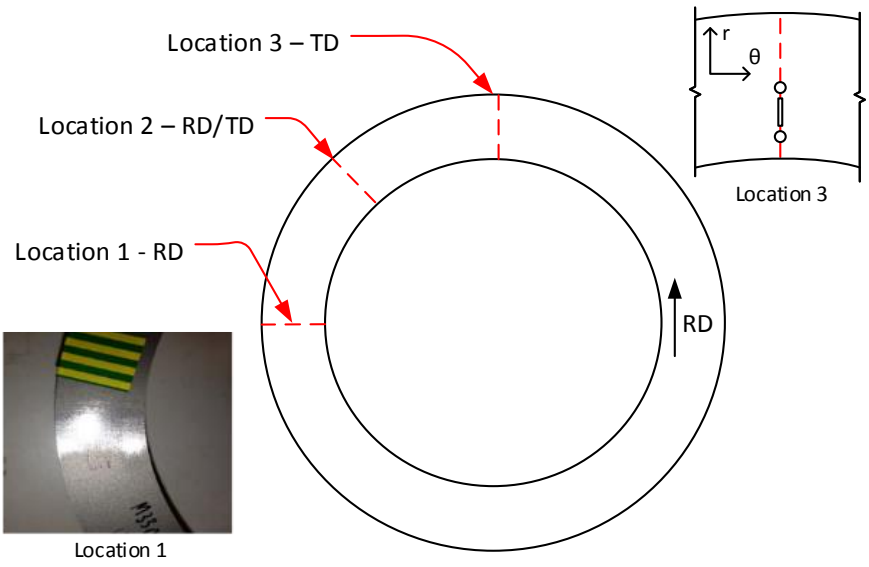

Figure 67: Illustration of ring sample showing the three locations at which measurements were taken. in relation to the rolling direction. The probe was moved in a radial direction across the sample measuring the local properties in the tangential direction. To access the next location the ring was manually rotated inside the Enclosed case.

Flux density (T)	Frequency (Hz)
1.0	200 / 400 / 800
1.1	200 / 400 / 800
1.2	200 / 400 / 800
1.3	200 / 400 / 800*
1.4	200 / 400 / 800*

Table 18: Frequencies and global flux densities at which local measurements were taken

4.1.2. Microscopy

The microstructure along the cross section of the rings was viewed to determine variation in grain deformation with distance from the cut edge.

4.1.2.1. Sample Preparation

10 mm sections of the rings were cut the using the AGIE Excellent, wire EDM machine at Cardiff University, shown in Fig. 68 and Fig. 69. The ring sections from location 2 TD/RD (at 45° to the RD) were chosen as they were more representative of the overall ring properties and mounted using Bakelite thermosetting (Resin-6) powder, which was pressed using a Struers Primopress Mounting Press at 160 ºC for 4 min heating and 2 min cooling with a force of 28 N, shown in Fig. 70.

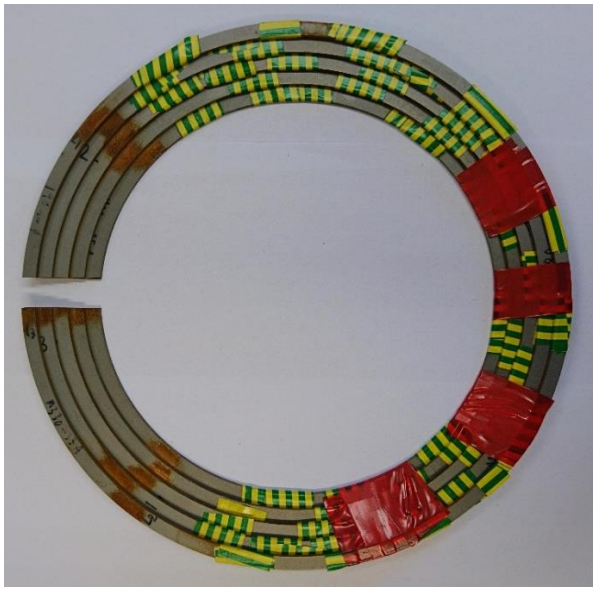

Figure 68: 10 mm section cut from ring samples of both grades by wire EDM

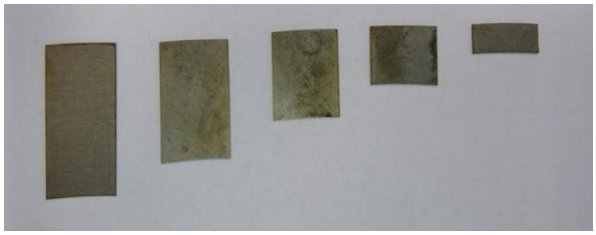

Figure 69: Sections from 150 mm (left)) and 180 mm (second right) mounted

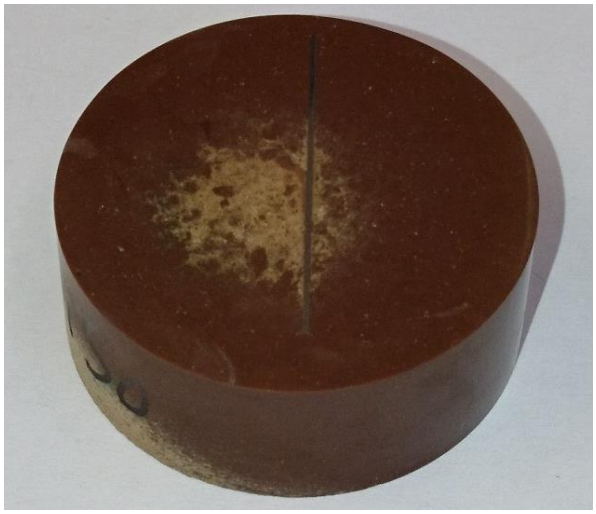

Figure 70: Mounted cut section of 150 mm ID M330-35A sample

The cross section of the ring sample was then ground with different grade of silicon carbide (SiC) abrasive paper with grit sizes of 600, 1000, and 4000. Polishing was then performed using different discs which contained lubricant and diamond compounds of sizes 14 and 6 μm (Kemet) then 3 and 1 μm (DiaPro). The samples were cleaned between

each stage using acetone. Then, the samples were etched using 10 % Nital (10 % HNO_3 + 90 % ethanol) for 30 sec. The optical microscopy study was performed using a Nikon ECLIPSE LV 100.

4.1.3. Uncertainty Analysis

There is always a certain amount of doubt regarding how close any measurement is to the true value. To express this, two parameters are stated, the size of a range around a certain value that we think the true value lies and how confident we are that the true value is in that range. For example, for a measurement such as;

50 mm ± 1 mm at a confidence level of 95%

States that we are 95 % confident that the true value is between 49 mm and 51 mm. The uncertainties calculated below are determined using the method described in UKAS M3003 [83]

4.1.3.1. Uncertainties in Local Bpeak and Hpeak

Table 19 summarised below is the uncertainty in the determination of the local B peak and Hpeak measurement in the same manner to those in 3.3.2.5.

Source of uncertainty	Declared uncertainty in Bpeak at a confidence level of 95 %
Local Bpeak – Needle Probe	4.2
Local Hpeak – Hall Effect Sensor	6.5

Table 19: Uncertainty analysis for local B peak.

4.1.3.2. Uncertainties in Power Loss and Permeability

Table 20 details the uncertainty in the determination of local power loss measurements.

Source of uncertainty	± %	Probability distribution	Divisor	Ci	Ui ± %	Vi or Veff
H measurement	6.470	Normal	2.0000	1	3.23500	∞
B measurement	4.160	Normal	2.0000	1	2.08000	∞
Loss dependence on Bpk, δLoss/δBpk = 1.91 where Bpk uncert = 4.16%	4.160	Rectangular	1.7321	1.91	4.58726	∞
Repeatability	4.340	Normal	2.0000	1	2.17000	∞
Sum of squares					40.5435	
Combined uncertainty					6.36738	
Expanded uncertainty					12.73476	
Declared uncertainty in Loss at a confidence level of 95 %					12.7	

Table 20: Uncertainty analysis for local power loss and permeability.

- The uncertainty for B and H is inherited from Table 5 and 6 respectively and the sensitivity coefficient is calculated from the catalogue data (δLoss/δJpeak)
- The calculated uncertainty for permeability performed in a similar manner has a repeatability of 5.70 and a sensitivity coefficient of 1.60 resulting in a declared uncertainty of 12.3 %.

4.1.3.3. Accuracy and Limitations

The Hall probe records a lower reading when compared to the value calculated from the magnetising coil. a possible explanation for this is that the Hall probe is not located directly on the sample. This was investigated with measurements made at different heights from the sample using a modified probe, with the needles removed as to take measurements closer to the surface, shown in Fig. 71 and Fig. 72.

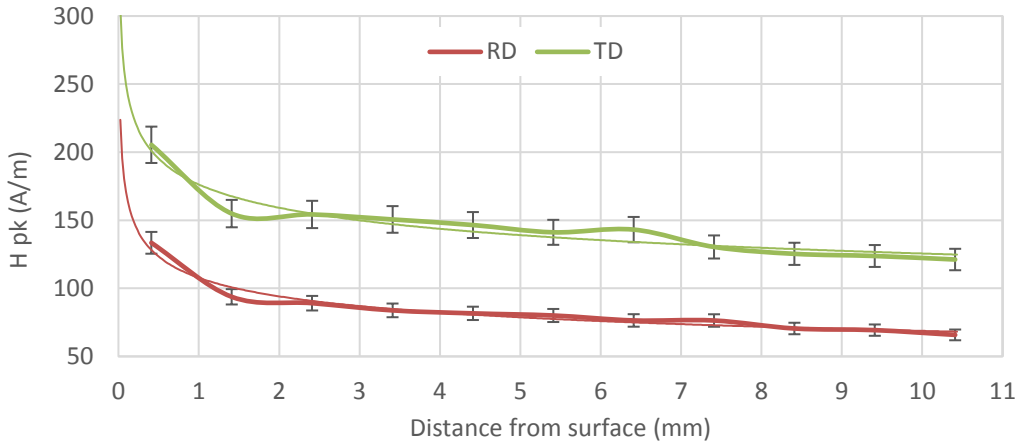

Figure 71: Local magnetic field measured in the RD and TD with Hall effect sensor at different heights from the surface of a M250-35A, 150 mm ID sample at 1.0 T and 400 Hz

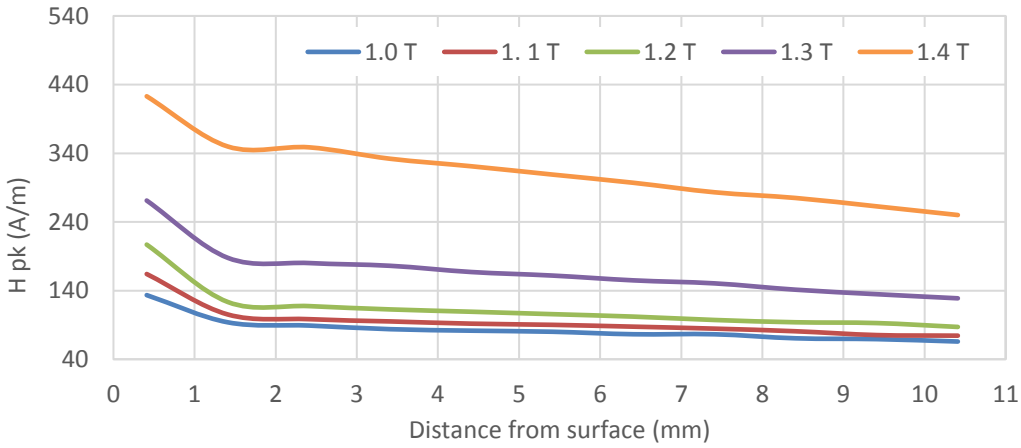

Figure 72: Local magnetic field measured in the RD with Hall effect sensor at different heights from the surface of a M250-35A, 150 mm ID sample for various flux densities and at frequency 400 Hz.

There is a rapid decrease in the first 1 – 2 mm with a more gradual linear decline thereafter. The field values 1 mm from the surface can be predicted with a reasonable accuracy from measurements taken at a distance of 3 or 4 mm. This is done using a power law with the parameters obtained from curve fitting to experimental data. For the M250-35A sample shown in Fig 71 which was measured at 1.0 T and 400 Hz the powers for which the distances are raised to are 0.2 and 0.15 for the RD and TD respectively. This rate of decay with distance is slower than would expected, the magnetic field on the central axis of a dipole follows an inverse cube law however this is only valid far away with increasing inaccuracies at closer distances, with off axis predictions not trivial. An

alternative model would be that of a current carrying wire which varies as the reciprocal of the distance. The use of a power term has the disadvantage that these approaches tend to infinity as the distance tends to zero so the assumption that the field strength at a small distance is equivalent to the surface values would be necessary.

This system used rings as an approximation to motor stators which has the advantage of creating a uniform magnetic field provided the coils are evenly wound around the whole sample. However, to make the measurements the magnetising coil only covered 90% of the sample. Local measurements were taken at the position where the flux density is lowest, mid-way between the ends of the coils and at the same global flux density controlled by the secondary coil which was located closer to the end of the coil where the value is greater than the average value of the local measurements. The global flux density measurement point will be less than the average for the sample. This difference grows with an increase in flux density and decrease in sample width and prevents measurements being taken at greater flux densities as modest increases in flux density at the position of the secondary coil require more substantial increases in the sample.

4.2. RESULTS

4.2.1. Local Measurements of the Magnetic Properties.

The following section displays a selection of the results of measurements taken across the width of the two different grade samples described in Section 4.1.1. The measurements were taken at the three locations defined in Section 4.1.1.2, Fig. 67 and at the magnetising conditions listed in Table 18 of the same section.

4.2.1.1. Comparison of Local and Bulk Measurements.

There is a clear difference in the magnetic properties with respect to the rolling direction (RD) for both grades. The measurements were taken along a line perpendicular to the rolling direction display the lowest values of H and the highest permeability.

The difference between the average values for the bulk and local measurement for the flux density (B pk) are within experimental error, however, the variation in measurements of the magnetising field (H Pk) are significant and increase with field strength. As the magnetising field is used to determine the power loss and permeability this disagreement is carried over.

For all the graphs shown in Section 4.2.1, the legends indicate the direction of flux. Triangular markers indicate measurements taken when the probe moved across the sample in the transverse direction, with the direction of magnetisation in the rolling direction (RD). Square markers indicate that the probe was moved across parallel to the rolling direction (TD). Diamond markers were taken at 45° to the RD. Bulk measurement is the mean global measurement for the sample and Local is the mean average of the probe measurements. The zero position on the x-axis used Fig. 74 onwards specifies the centre of the sample with the positive direction moving towards the ID edge and negative direction towards the OD edge. This is illustrated in Fig. 73.

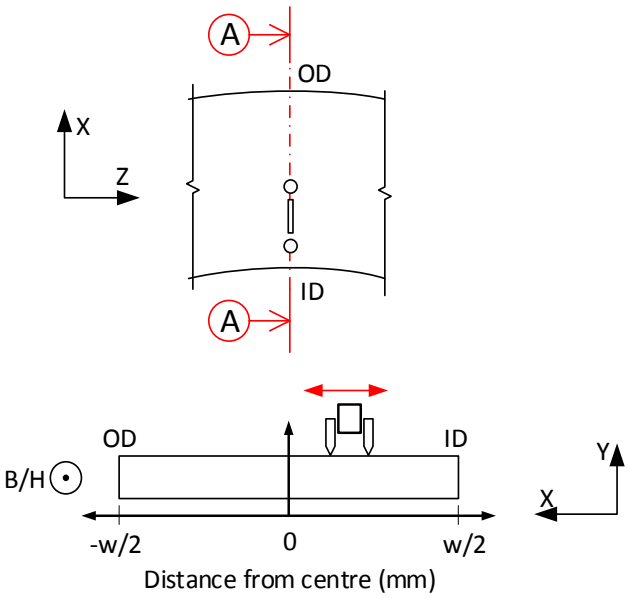

Section A – A

Figure 73: Plan view of a section of the ring sample with typical measurement location (top) and Section A – A (bottom) showing probe position in relation to sample centre line with flux travelling perpendicular to the direction of the line along which the probe is moved.

M250-35A, 150 mm ID, 1.0 T, 400 Hz

Fig. 74 (a) to (d) shows the measurements of H peak, B peak, Power loss and permeability respectively for M250-35A, 150 mm ID sample at 1.0 T and 400 Hz conducted using the method outlined in section 1.1.

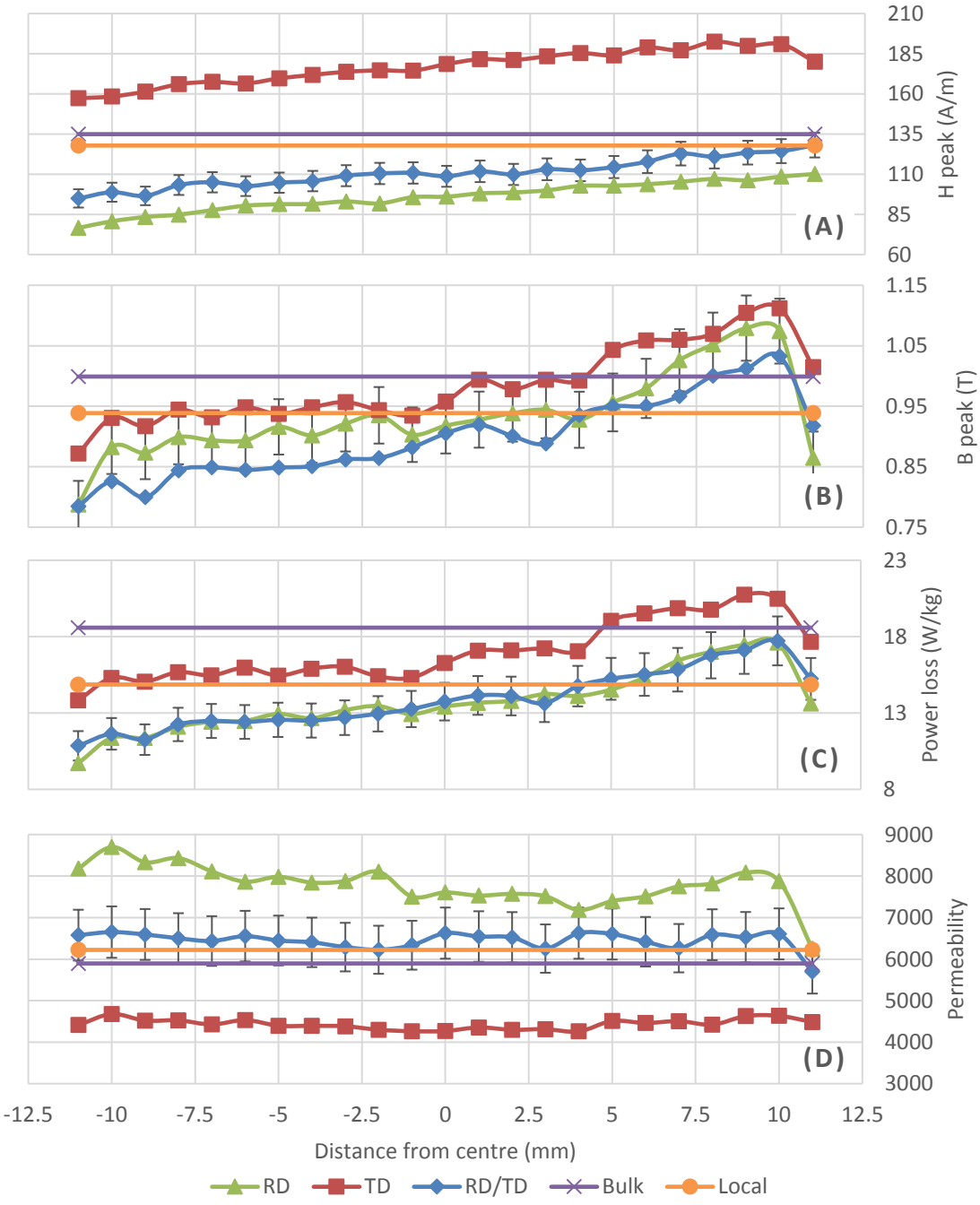

Figure 74 - Local measurements of (a) H peak, (b) B peak, (c) Power loss and (d) permeability for M250-35A, 150 mm ID sample at 1.0 T and 400 Hz.

M250-35A, 150 mm ID, 1.3 T, 400 Hz

Fig. 75 (a) to (d) shows the measurements of H peak, B peak, Power loss and permeability respectively for M250-35A, 150 mm ID sample at 1.0 T and 400 Hz conducted using the method outlined in section 4.1.

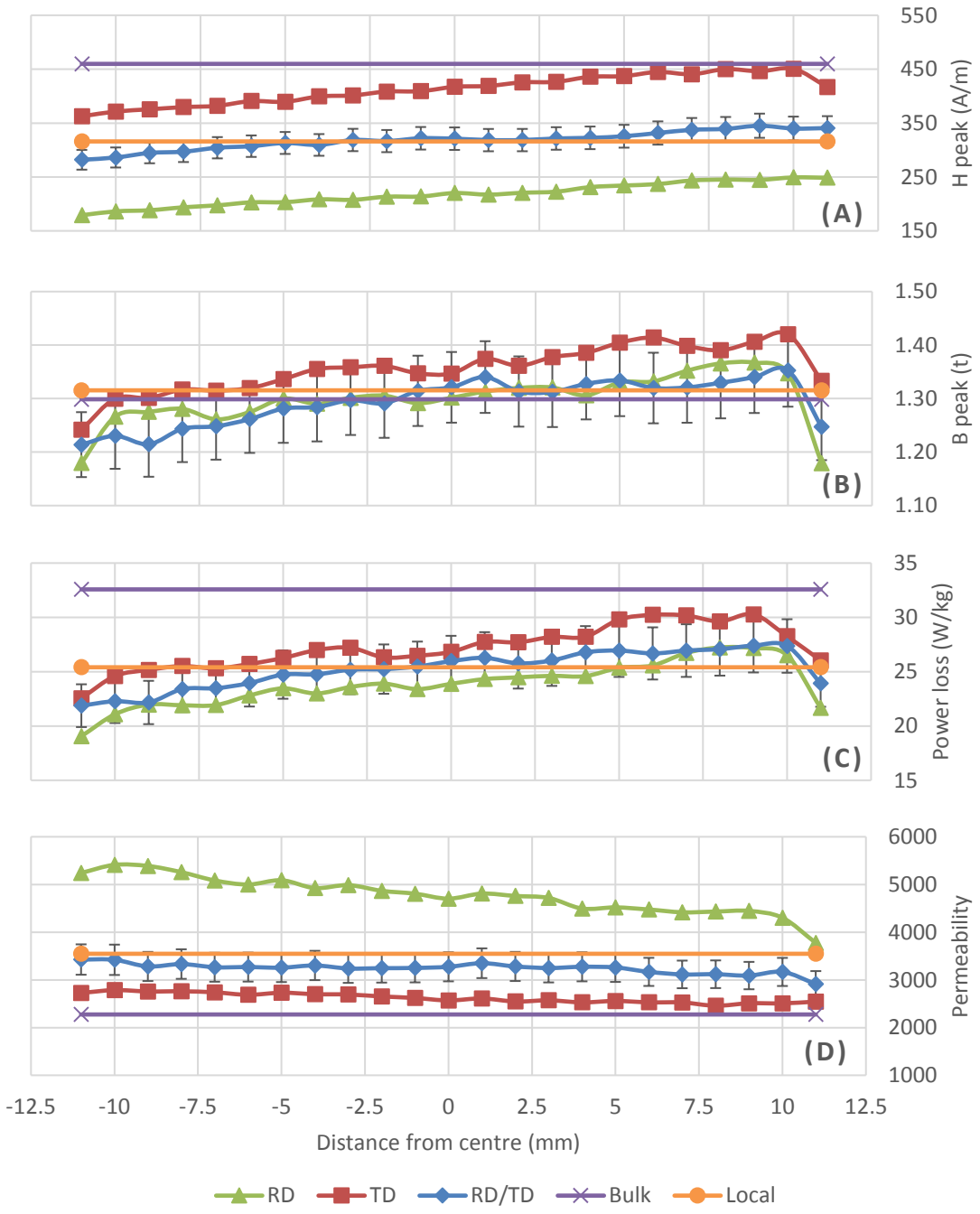

Figure 75 - Local measurements of (a) H peak, (b) B peak, (c) Power loss and (d) permeability for M250-35A, 150 mm ID sample at 1.3 T and 400 Hz.

M250-35A, 180 mm ID, 1.0 T, 400 Hz

Fig. 76 (a) to (d) shows the measurements of H peak, B peak, Power loss and permeability respectively for M250-35A, 180 mm ID sample at 1.0 T and 400 Hz conducted using the method outlined in section 4.1.

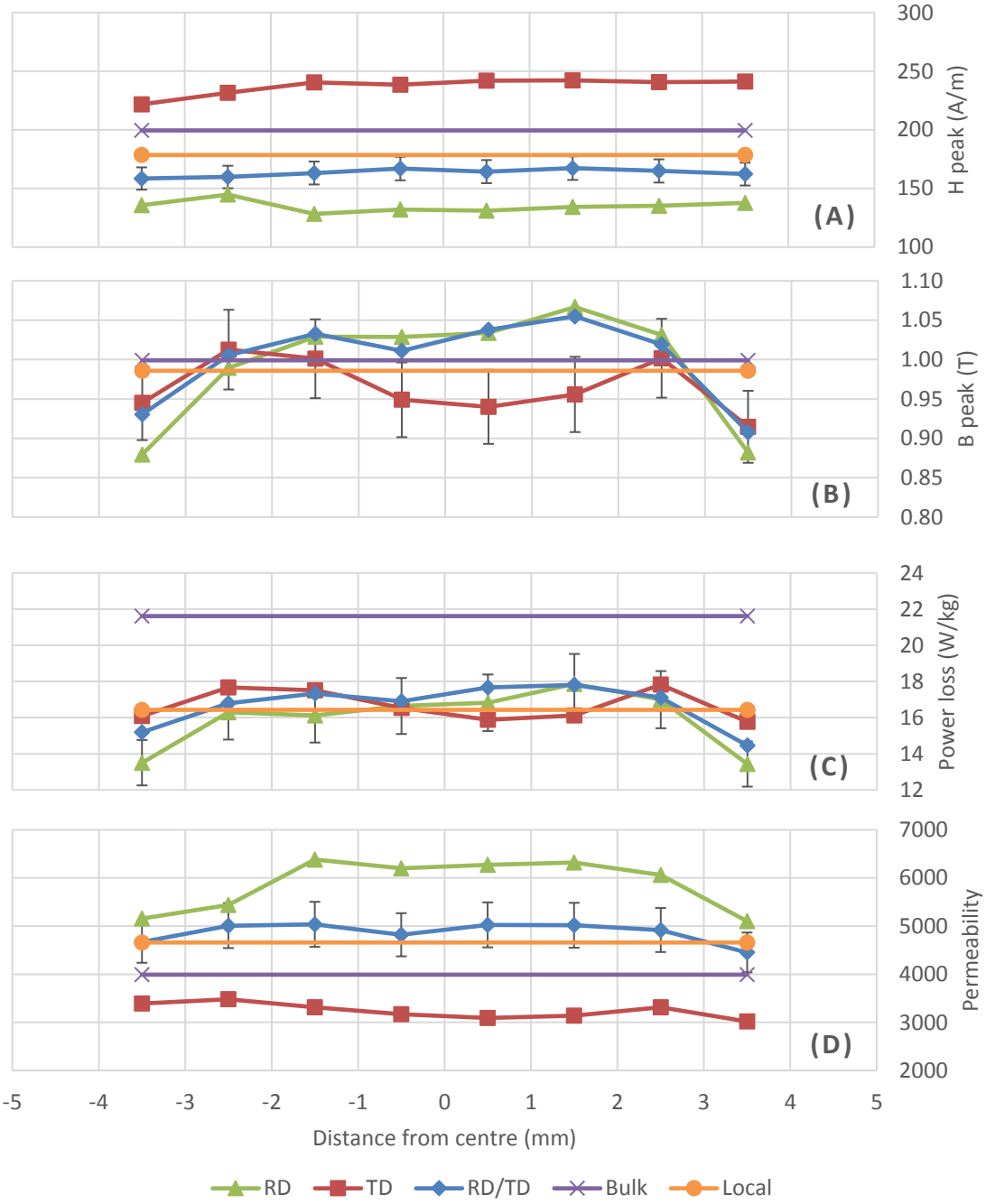

Figure 76 - Local measurements of (a) H peak, (b) B peak, (c) Power loss and (d) permeability for M250-35A, 180 mm ID sample at 1.0 T and 400 Hz.

M250-35A, 180 mm ID, 1.3 T, 400 Hz

Fig 77 (a) to (d) shows the measurements of H peak, B peak, Power loss and permeability respectively for M250-35A, 180 mm ID sample at 1.3 T and 400 Hz conducted using the method outlined in section 4.1.

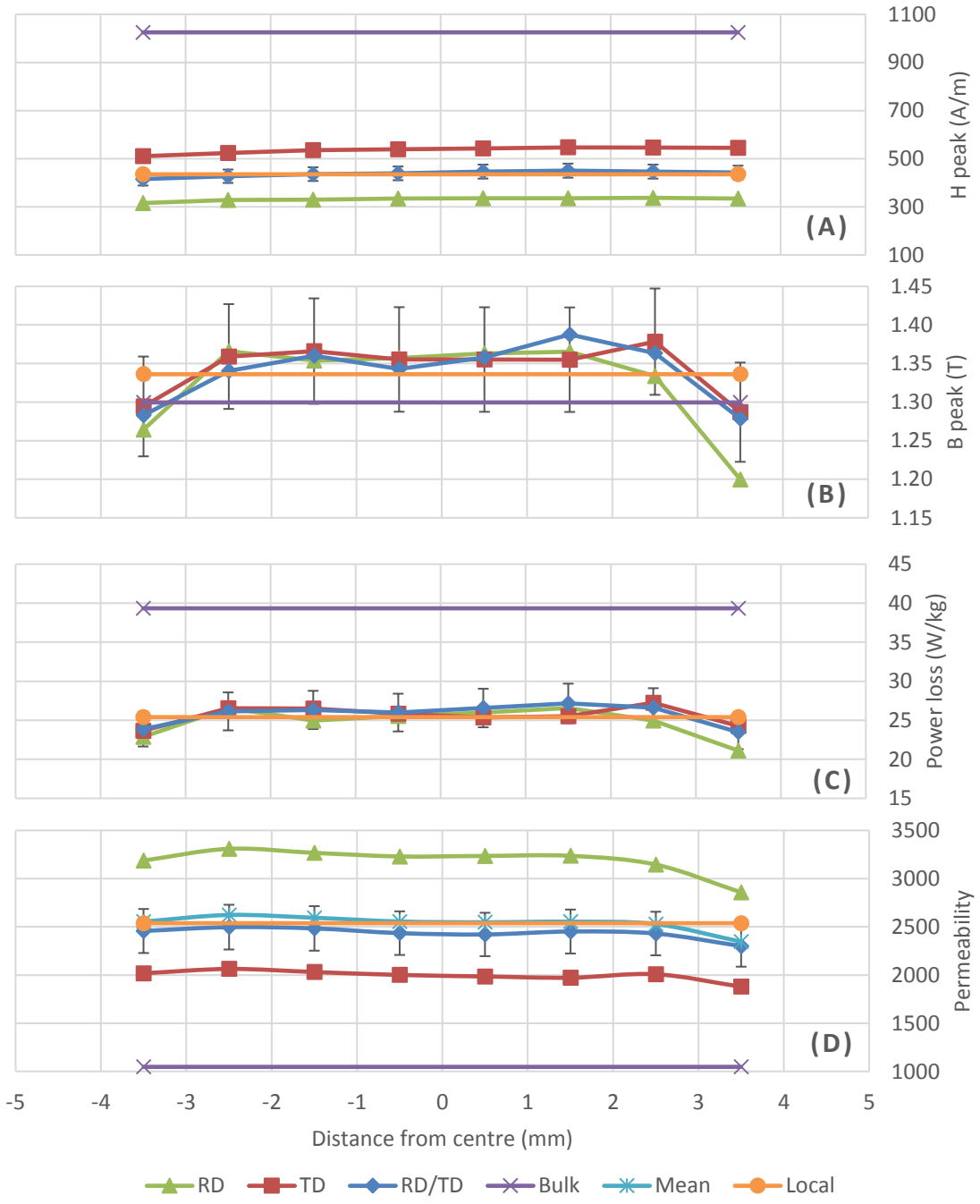

Figure 77 - Local measurements of (a) H peak, (b) B peak, (c) Power loss and (d) permeability for M250-35A, 180 mm ID sample at 1.3 T and 400 Hz.

M330-35A, 150 mm ID, 1.0 T, 400 Hz

Fig 78 (a) to (d) shows the measurements of H peak, B peak, Power loss and permeability respectively for M330-35A, 150 mm ID sample at 1.0 T and 400 Hz conducted using the method outlined in section 4.1.

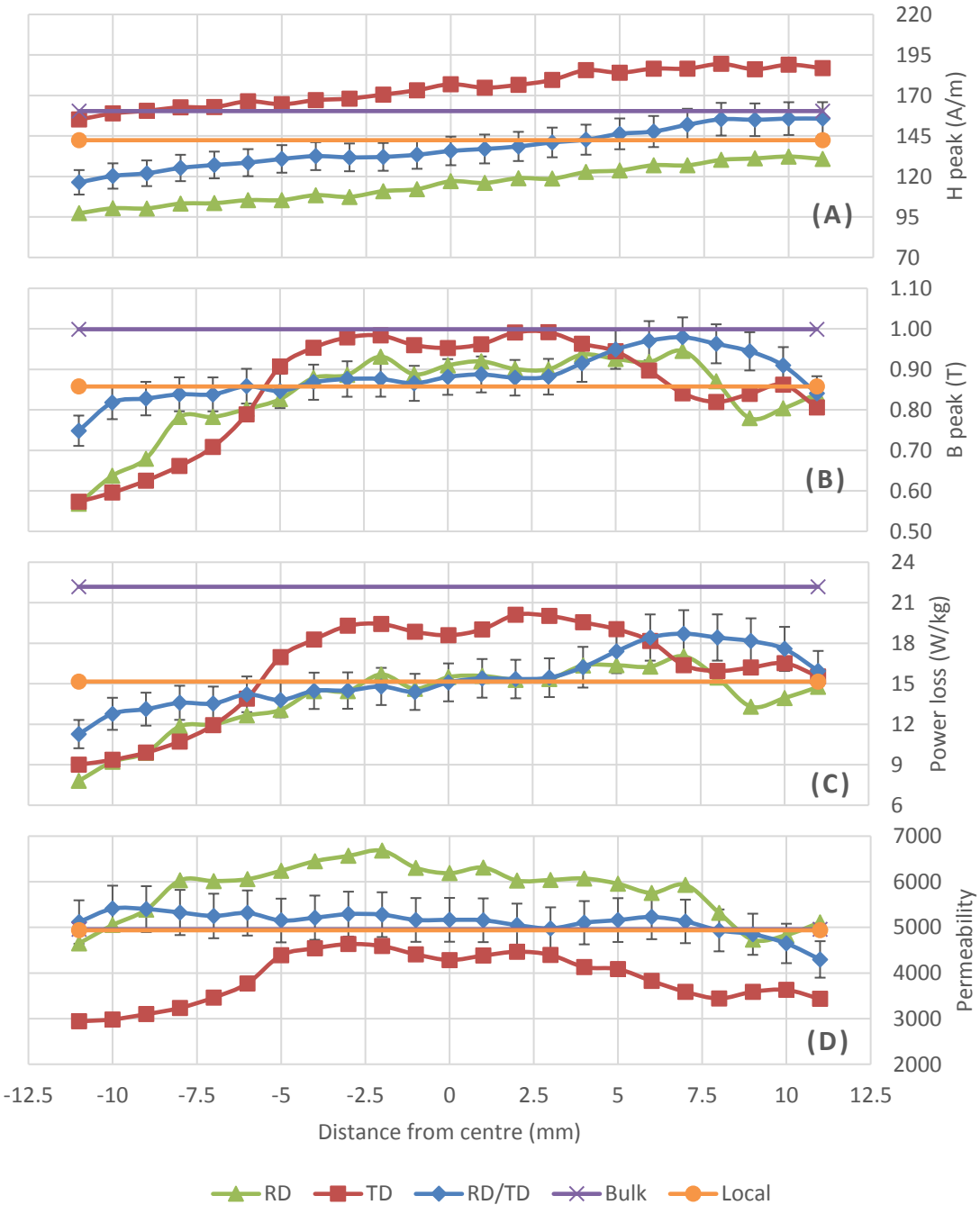

Figure 78 - Local measurements of (a) H peak, (b) B peak, (c) Power loss and (d) permeability for M330-35A, 150 mm ID sample at 1.0 T and 400 Hz.

M330-35A, 150 mm ID, 1.3 T, 400 Hz

Fig 79 (a) to (d) shows the measurements of H peak, B peak, Power loss and permeability respectively for M330-35A, 150 mm ID sample at 1.3 T and 400 Hz conducted using the method outlined in section 4.1.

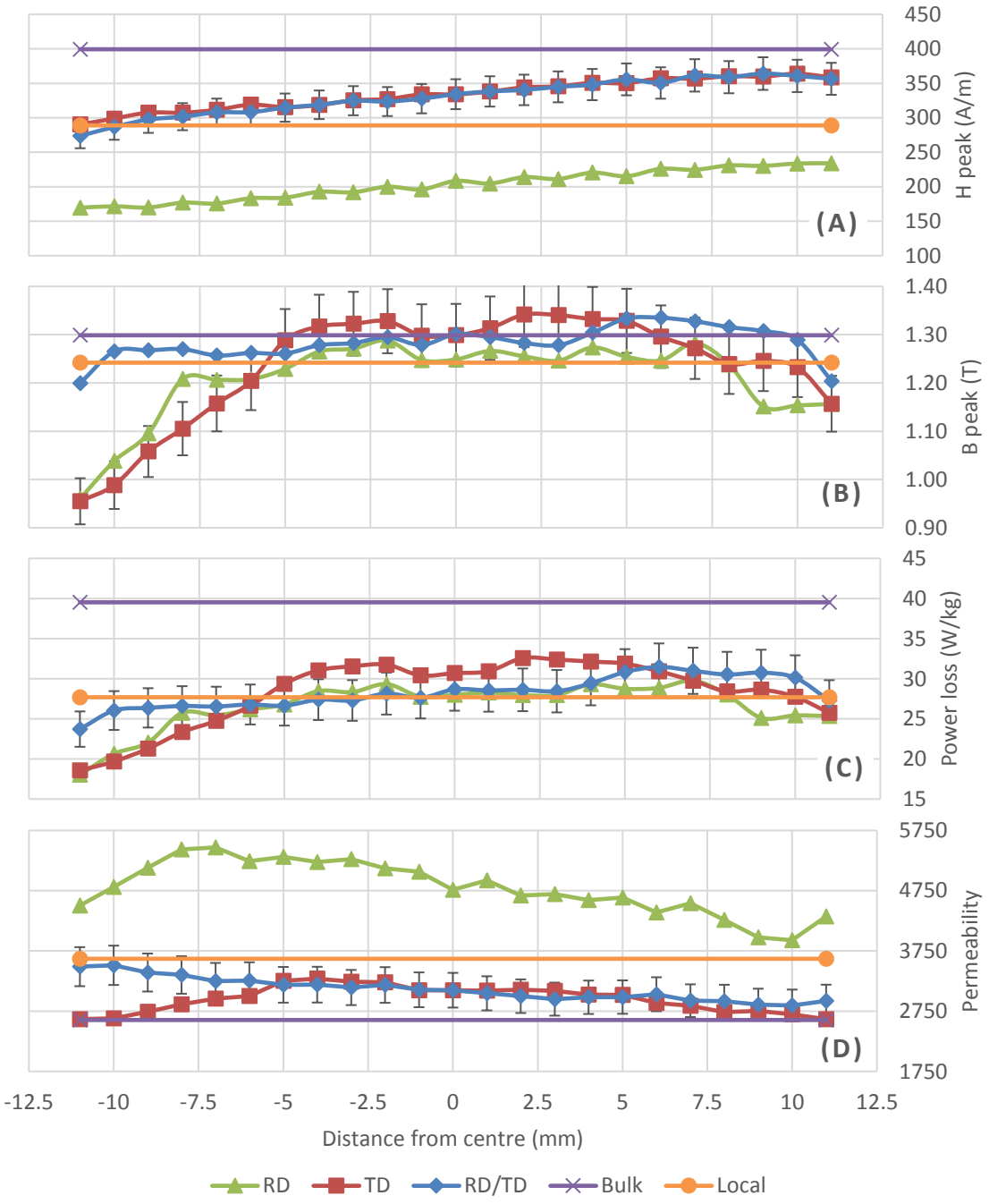

Figure 79 - Local measurements of (a) H peak, (b) B peak, (c) Power loss and (d) permeability for M330-35A, 150 mm ID sample at 1.3 T and 400 Hz.

M330-35A, 180 mm ID, 1.0 T, 400 Hz

Fig 80 (a) to (d) shows the measurements of H peak, B peak, Power loss and permeability respectively for M330-35A, 180 mm ID sample at 1.0 T and 400 Hz conducted using the method outlined in section 4.1.

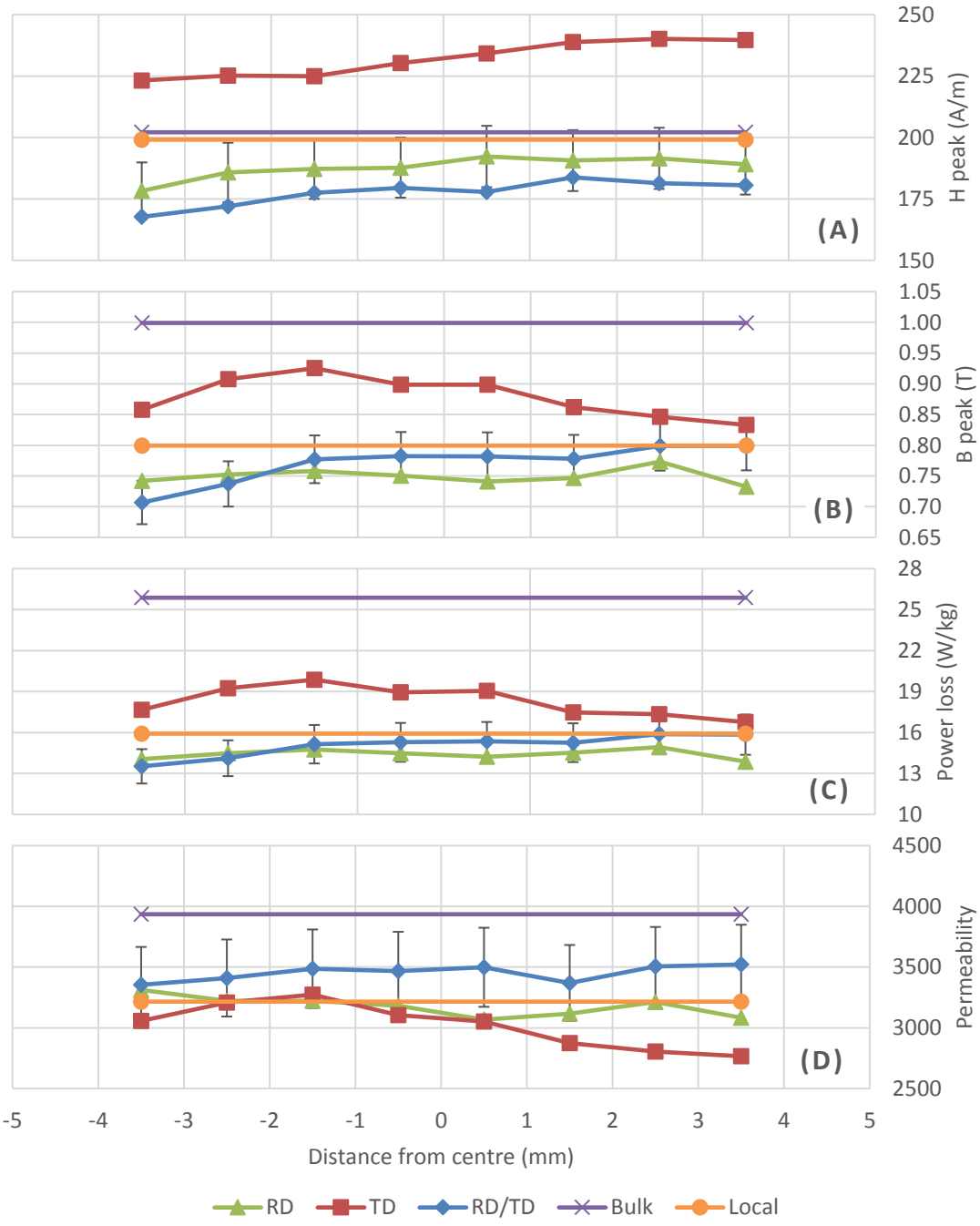

Figure 80 - Local measurements of (a) H peak, (b) B peak, (c) Power loss and (d) permeability for M330-35A, 180 mm ID sample at 1.0 T and 400 Hz.

M330-35A, 180 mm ID, 1.3 T, 400 Hz

Fig 81 (a) to (d) shows the measurements of H peak, B peak, Power loss and permeability respectively for M330-35A, 180 mm ID sample at 1.3 T and 400 Hz conducted using the method outlined in section 4.1.

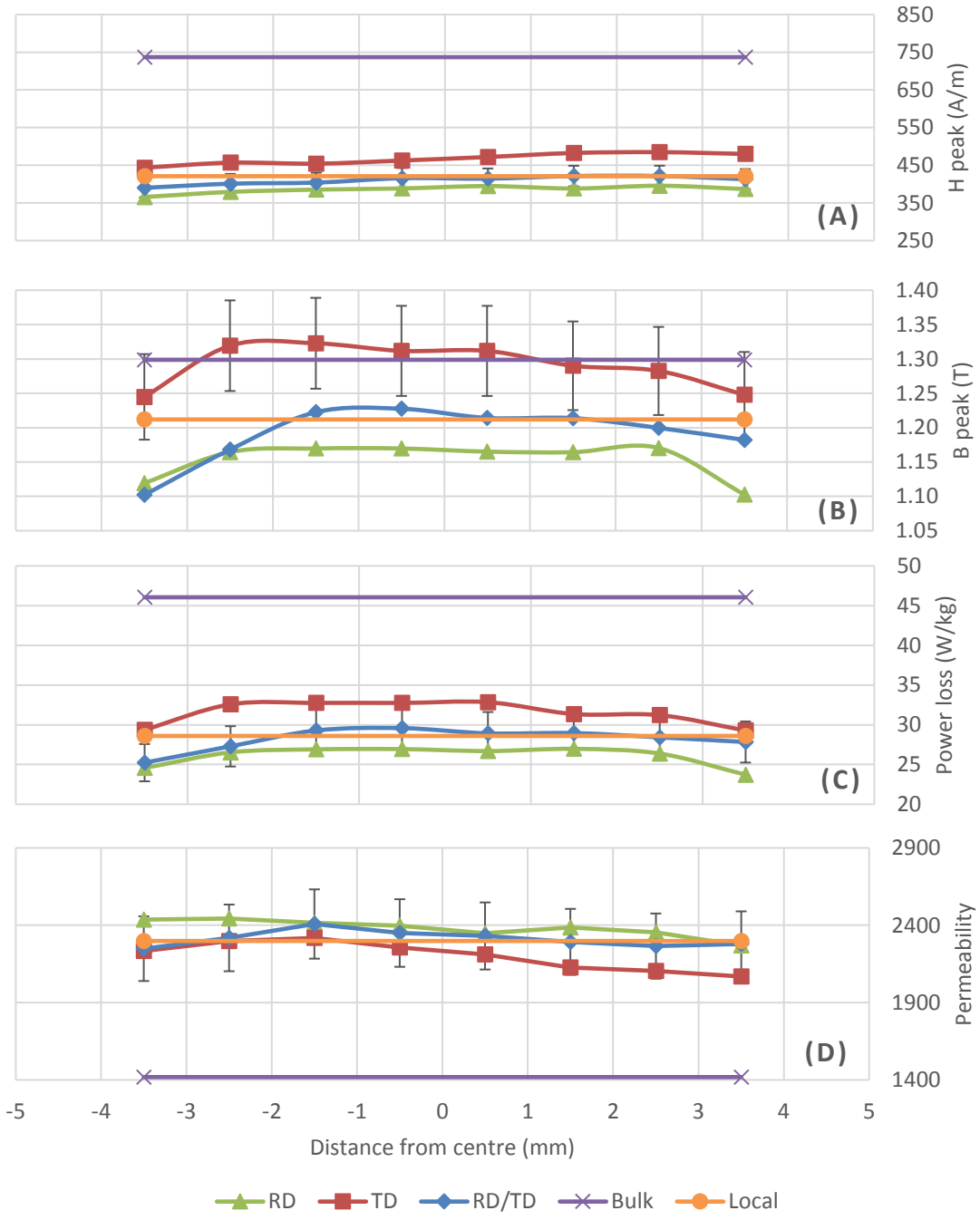

Figure 81 - Local measurements of (a) H peak, (b) B peak, (c) Power loss and (d) permeability for M330-35A, 180 mm ID sample at 1.3 T and 400 Hz.

4.2.1.2. Normalised Values of Different Width

The following section displays the mean average of the three locations normalised over the width of the sample, shown in Fig. 82 and Fig. 83. This is calculated by dividing the measurement position by the sample width (48) so that the x-axis for all samples extends from -0.5 at the OD to 0.5 at the ID

$$normalised\ value\ (x) = \frac{x}{w} \tag{48}$$

The 190 mm ID sample measuring only 5 mm in width only has three local measurements taken and as such these local measurements become less distinguishable from the bulk measurements. As the effect of punching is most pronounced over the first 2 -3 mm the entire sample is severely degraded. This is especially true for the M250-35A samples which has a effect concentrated near the cut edge unlike the M330-35A sample where the degradation is more gradual.

M250-35A, 1.0 T, 400 Hz

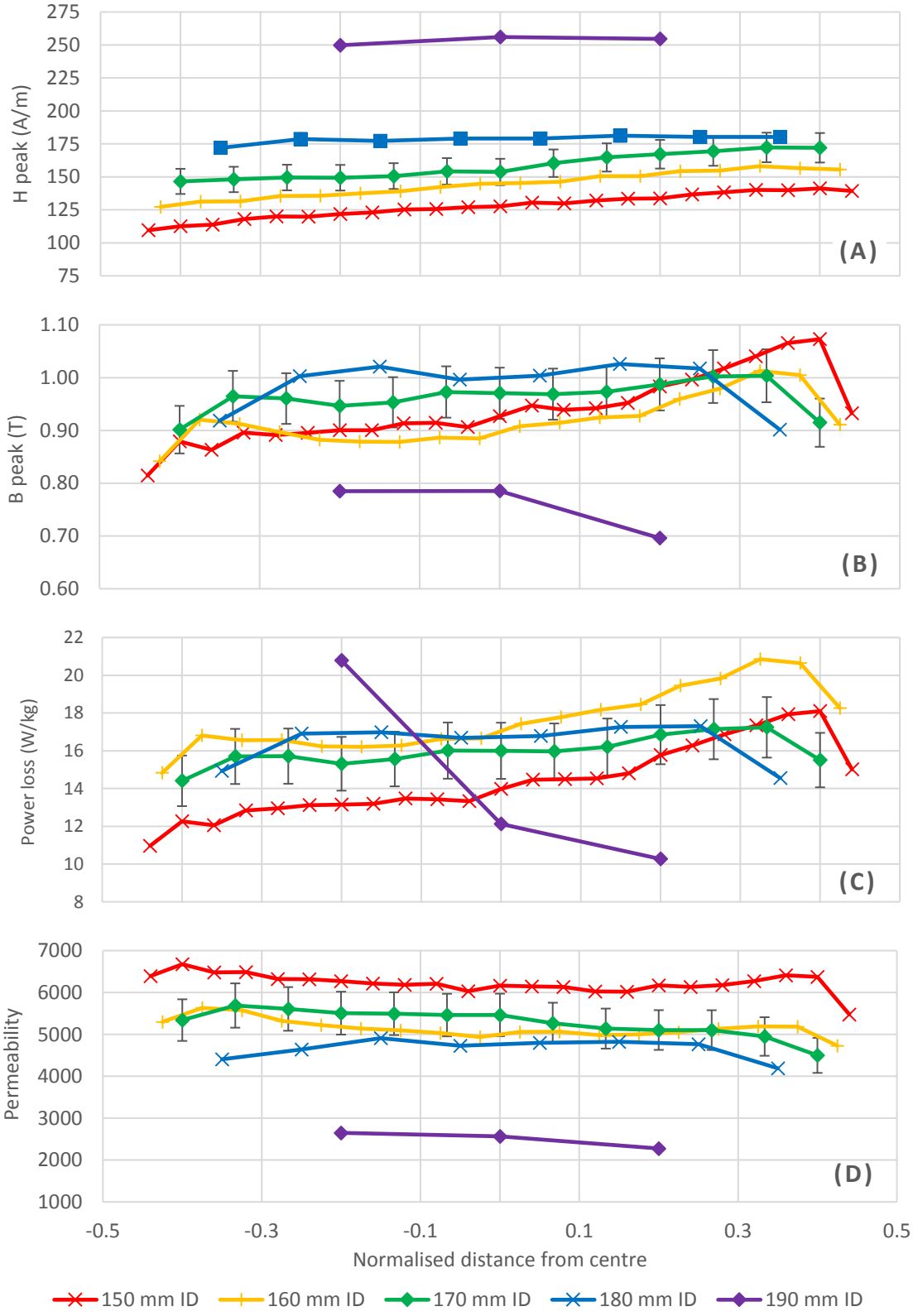

Figure 82 –Measurements of (a) H peak, (b) B peak, (c) Power loss and (d) permeability for M250-35A, at 1.0T and 400 Hz. Normalised for different sample widths.

M330-35A, 1.0 T, 400 Hz

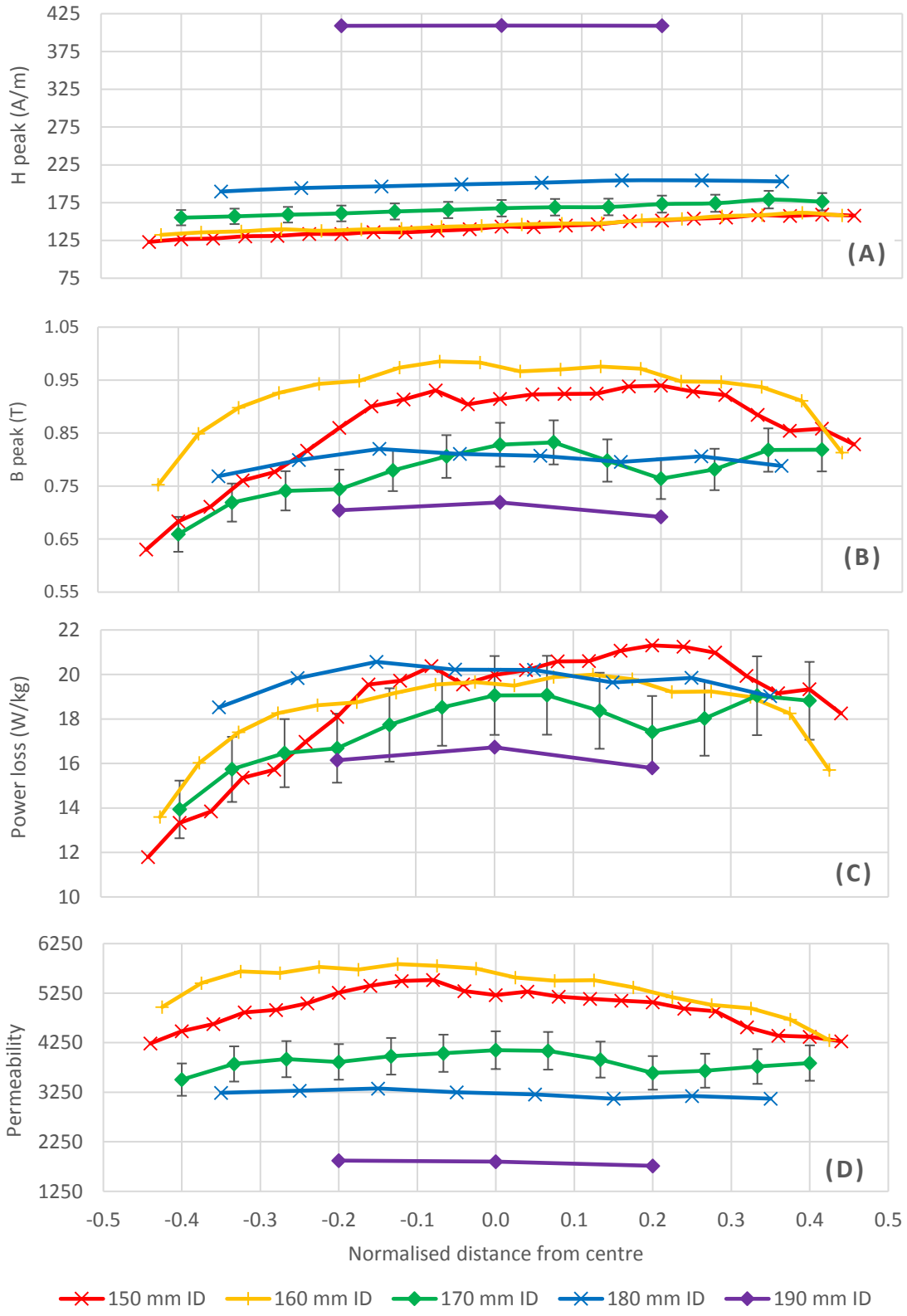

Figure 83 –Measurements of (a) H peak, (b) B peak, (c) Power loss and (d) permeability for M330-35A, at 1.0T and 400 Hz. Normalised for different sample widths.

4.2.1.3. Variations with Frequency.

The following section displays in Fig. 84 and Fig. 85 the mean average for the three locations at different frequencies; 200 Hz, 400 Hz and 800 Hz for the 150 mm ID ring and at a globally measured flux density of 1.0 T

The flux density is the same at the different frequencies however the magnetising field and the power loss both increase with frequency whereas the permeability decreases as frequency increases.

M250-35A, 150 mm ID, 1.0 T,

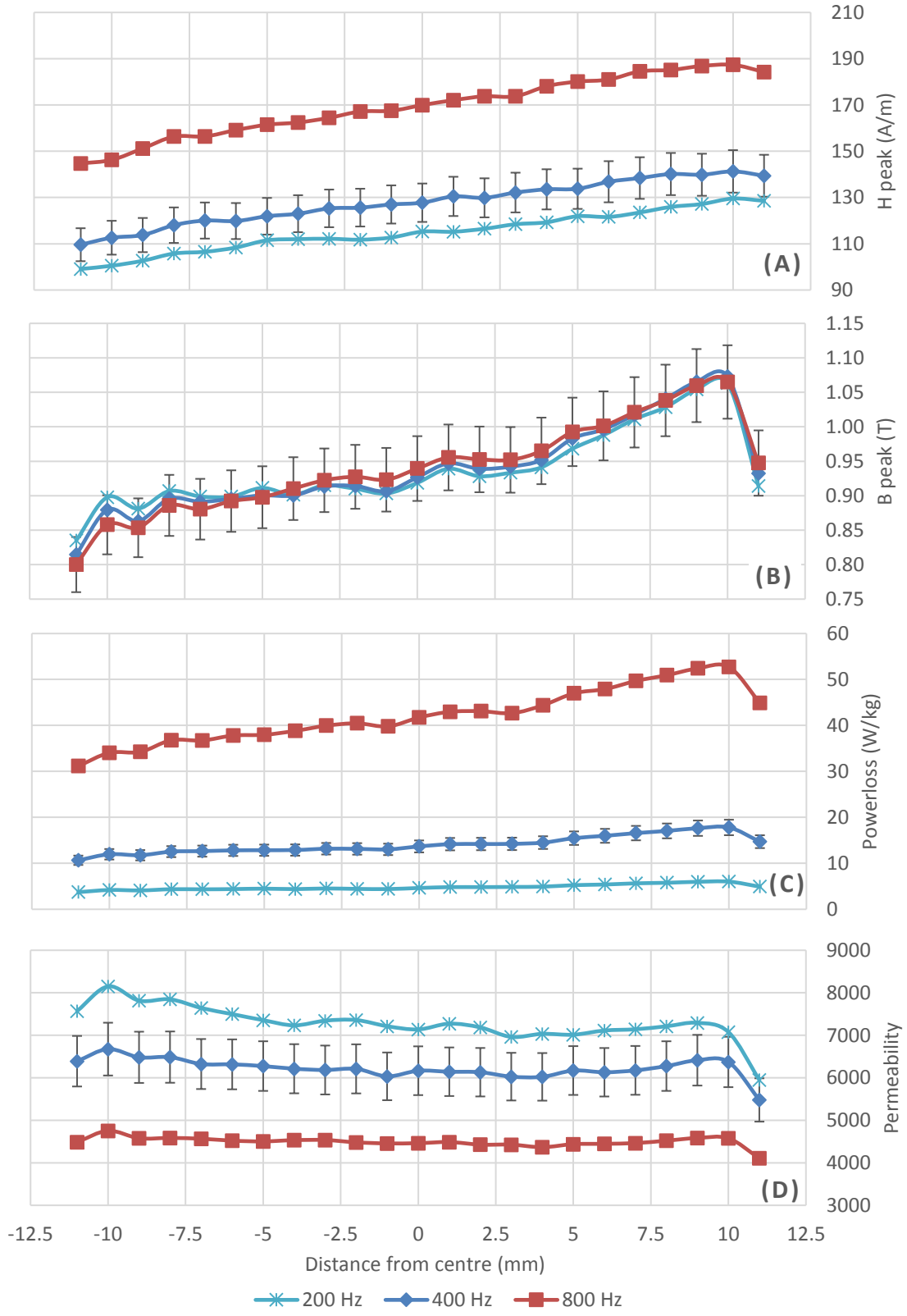

Figure 84 –Measurements of (a) H peak, (b) B peak, (c) Power loss and (d) permeability for M250-35A, 150 mm ID at 1.0T and 200 Hz, 400 Hz and 800 Hz.

M330-35A, 150 mm ID, 1.0 T,

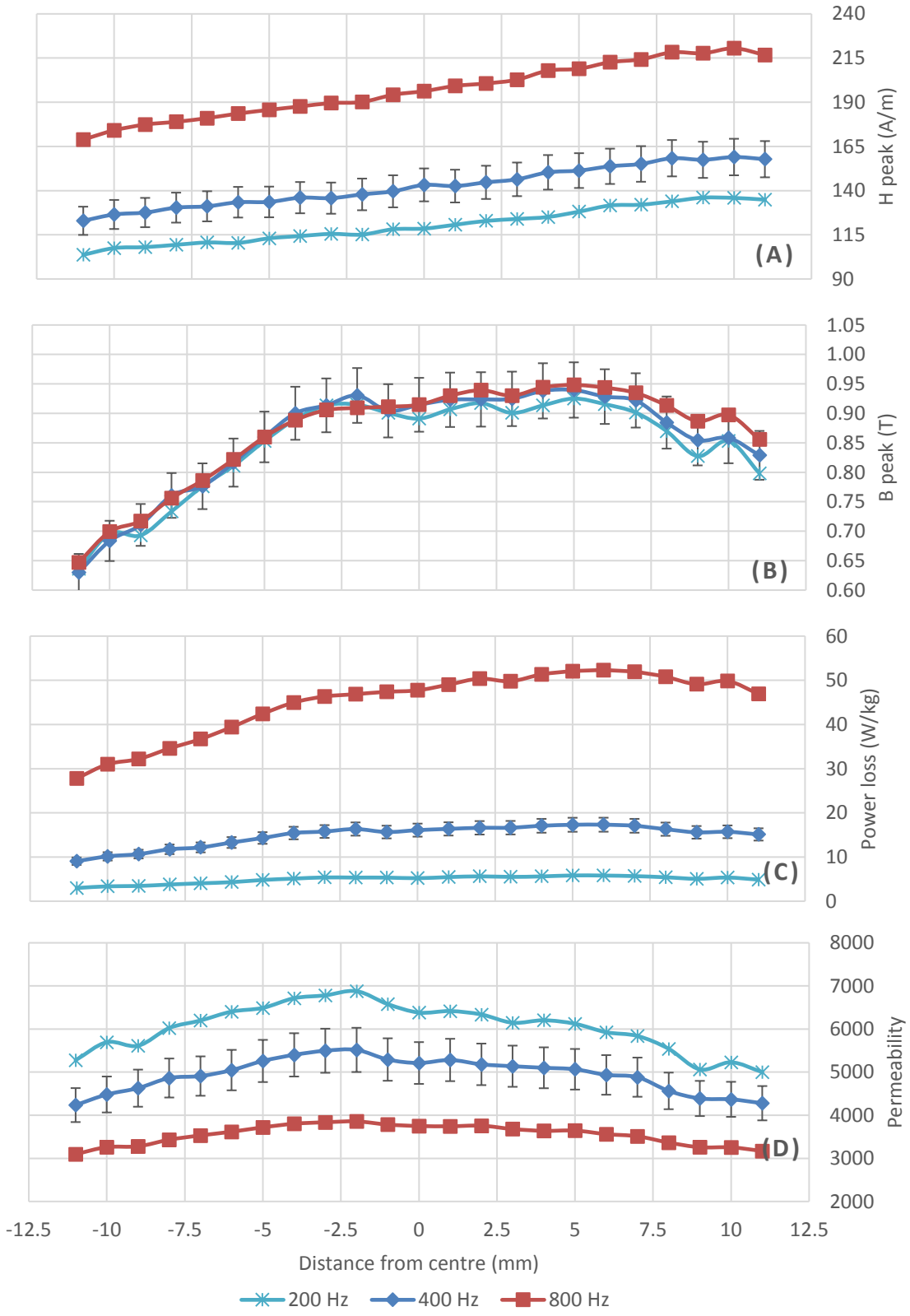

Figure 85 –Measurements of (a) H peak, (b) B peak, (c) Power lo loss and (d) permeability for M250-35A, 150 mm ID at 1.0T and 200 Hz, 400 Hz and 800 Hz.

4.2.2. Microscopy

4.2.2.1. Optical Microscopy of the Cut Edge Face

The following images show the optical microscopy results obtained using the method described in Section 4.1.2. Images were taken across the width of the sample and were stitched together using Adobe Photoshop CS3.

The is an observed curvature of the larger, 25 mm wide samples which is not seen in the smaller, 10 mm samples. The M250-35A grades with a larger silicon content have a larger average grain size.

M250-35A, 150 mm ID

Fig 86 and 87 show the optical microscopy images of the M250-35A, 150 mm ID sample. OD edge on the right and ID edge on the left.

Figure 86 – Optical microscopy of M250-35A, 150 mm ID

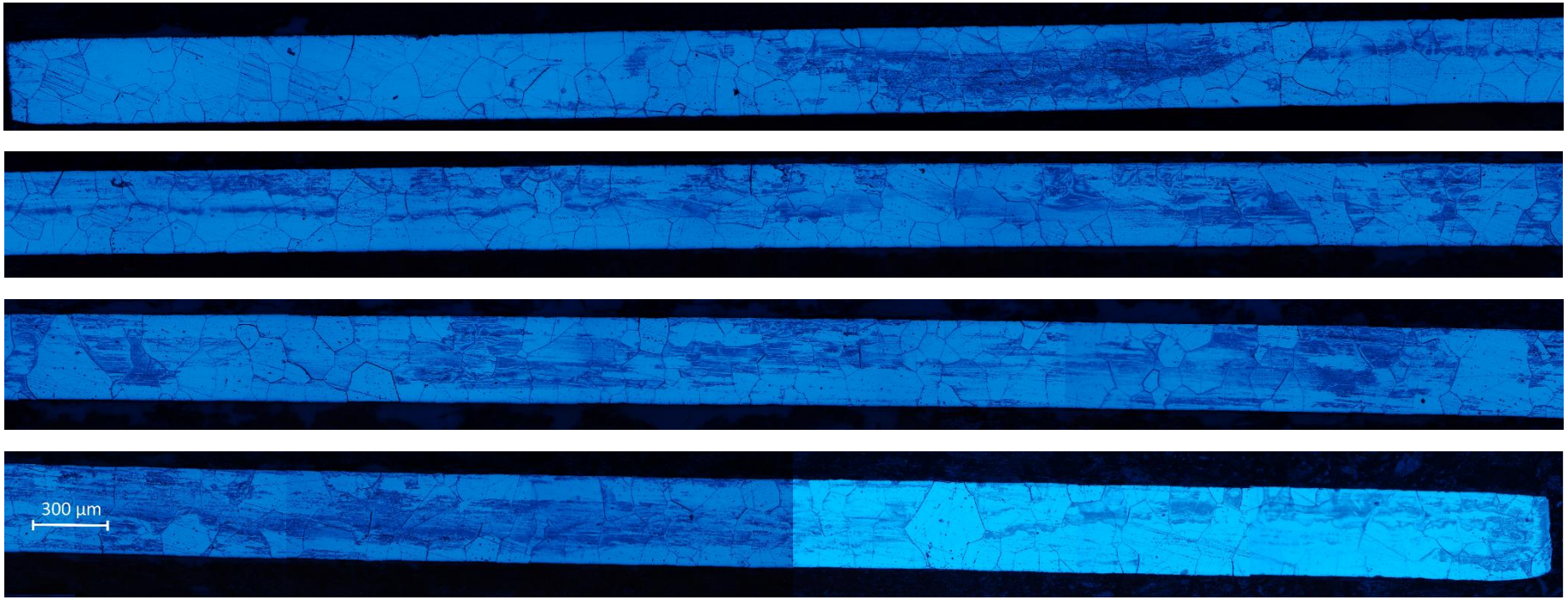

Figure 87 – Increased scale optical microscopy of M250-35A, 150 mm ID.

M250-35A, 180 mm ID

Fig 88 and 89 show the optical microscopy images of the M250-35A, 180 mm ID sample. OD edge on the right and ID edge on the left.

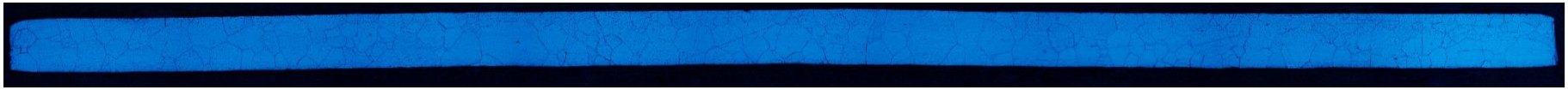

Figure 88 – Optical microscopy of M250-35A, 180 mm ID

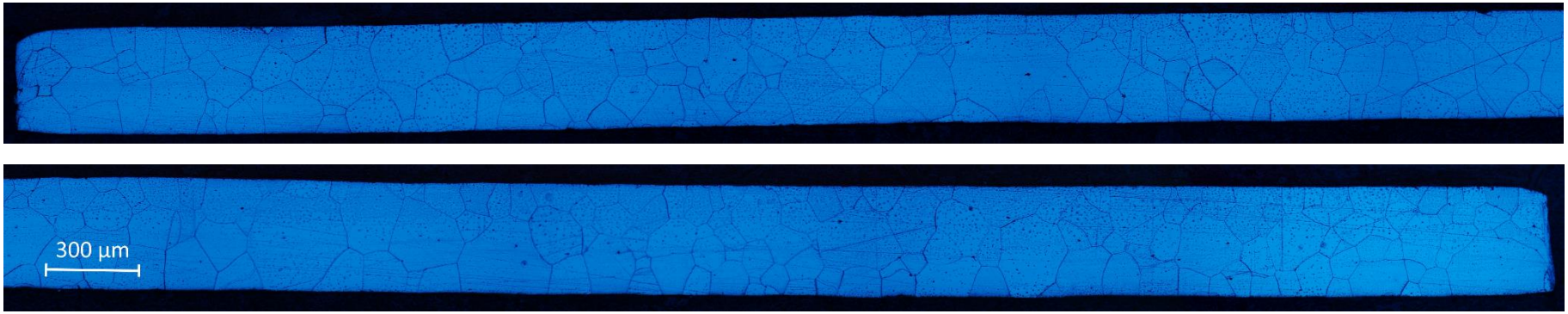

Figure 89 – Increased scale optical microscopy of M250-35A, 180 mm ID.

M330-35A, 150 mm ID

Fig 90 and 91 show the optical microscopy images of the M330-35A, 150 mm ID sample. OD edge on the right and ID edge on the left.

Figure 90 – Optical microscopy of M330-35A, 150 mm ID

Figure 91 – Increased scale optical microscopy of M330-35A, 150 mm ID.

M330-35A, 180 mm ID

Fig 92 and 93 show the optical microscopy images of the M330-35A, 180 mm ID sample. OD edge on the right and ID edge on the left.

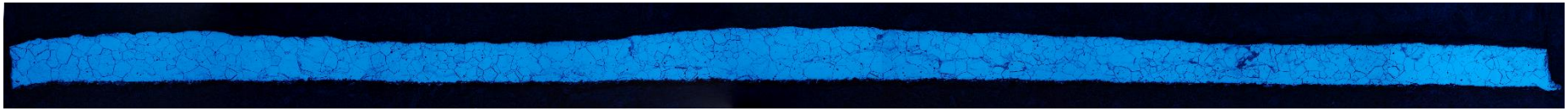

Figure 92 – Optical microscopy of M330-35A, 180 mm ID

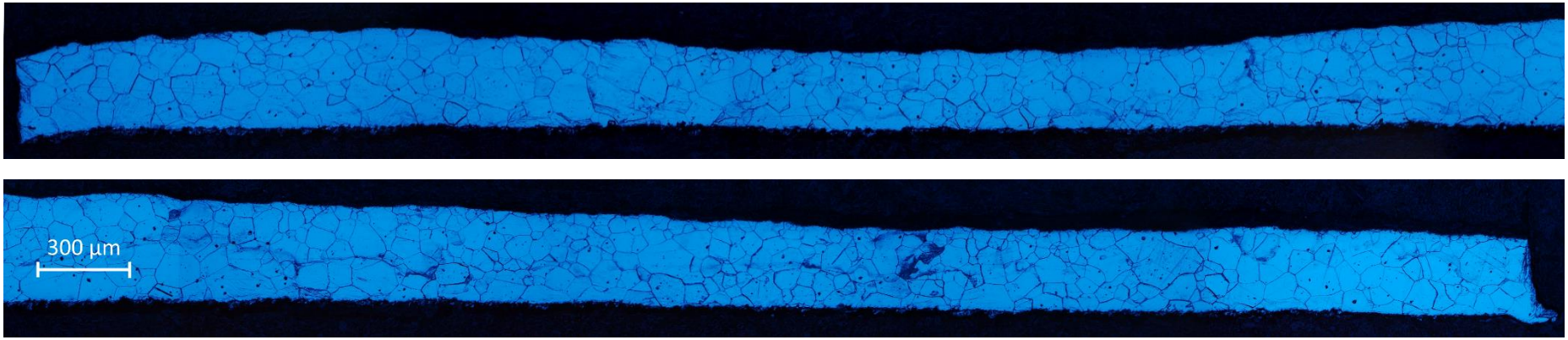

Figure 93 – Increased scale optical microscopy of M330-35A, 180 mm ID.

4.3. DISCUSSION AND ANALYSIS

4.3.1. Local Measurement of Magnetic Properties

4.3.1.1. Comparison of Local and Bulk Measurements.

The following section compares the results for both the bulk and local measurements shown in of Section 4.2.1.1 as well as examining the profiles of the local measurements.

Magnetising Field, H peak

The peak value for the local magnetising field, H as measured by the Hall effect sensor increases in a linear manner with distance from the outer edge of the ring sample toward the inner edge. This is the profile that would be expected from Ampere's Law (49) when calculating the magnetic field inside a toroidal solenoid, as the radius, *R* increases the field strength, *H* which is proportional to the current, *I* and number of turns, *N* decreases.

$$\mathrm{H} = \frac{\mathrm{NI}}{2\pi R} \tag{49}$$

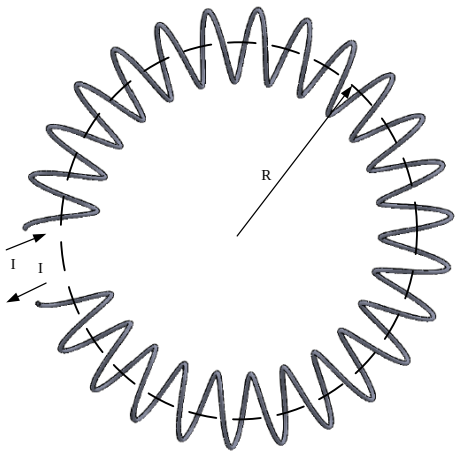

Figure 94 - Magnetic field inside of a toroidal solenoid at radius, R with current I, number of turns N

For air, or another isotropically magnetisable material, filled solenoid the field strength would be the same for constant values of radius (assuming it is uniformly

wound), however, the results presented in Section 4.2.1.1 show a dependence on the orientation of the sample. The anisotropy of the material is clearly seen. Local measurements are taken at a fixed bulk flux density, measured using the secondary coil with the applied field needed to induce the required flux density between 24 % and 90 % higher for measurements at in the TD compared to the RD .

	150 mm	**180 mm**
M250 – 35A	90 %	68 %
M330 – 35A	58 %	24 %

Table 21: Increase in magnetising field needed in TD compared to RD

The increase in the magnetising field necessary is outlined in Table 21 and defined by (50). It is consistent for the different flux densities up to 1.3 T but does decrease as the samples get narrower.

$$H_{TD} = (100\ \% + \mathrm{X}\ \%)H_{RD} \tag{50}$$

Where X is the percentage increase shown in Table 8. It has been known for many years that the permeability is greatest when the field is applied in the direction in which the sheets where cold rolled [3].This enhances the growth of [001] grains in the RD [85] and with the M250-35A sample having a higher degree of anisotropy, possibly due to having larger grains.

The other noticeable characteristic of the magnetic field measurements is the marked discrepancy between local and the bulk reading, shown in Fig. 95. Bulk values can be over 50% higher than the local measurements the difference increases for higher fields and narrower samples.

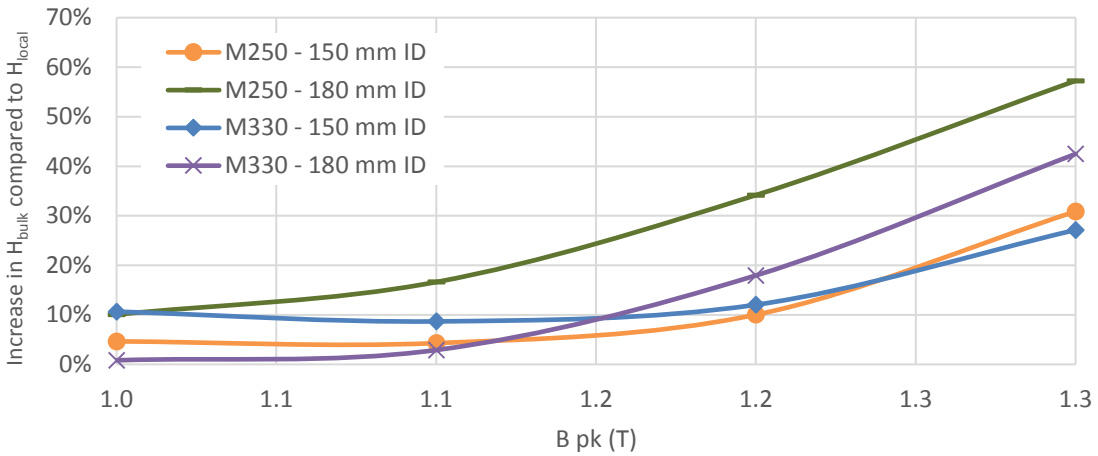

Figure 95: Percentage difference between Hbulk and Hlocal for different grades, ID's and flux densities measured at 400 Hz

A possible explanation for the inconsistency could be the height at which the Hall effect sensor was positioned, above the level of the coil. When calculating the magnetic field at the centre of a solenoid as is done for the H_{bulk} it is assumed to be constant and consists of the superposition of the magnetic fields produced by each wire loop. This is demonstrated using the simple set up in Fig. 96 consisting of four wires carrying current *I*. The magnetic field at point, P_1 is the sum of the fields generated by each wire. The vertical components cancel leaving the horizontal components which all point in the same direction, in this example to the left.

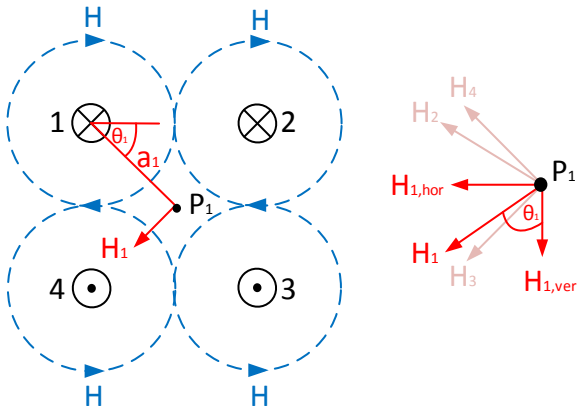

Figure 96: Example representation showing the magnetic field contribution from four current carrying wires acting at a point, P located between top and bottom rows of wires.

The magnetic field experienced at point P_2 ,above the top of the wires, where the

Hall sensor is placed is also the sum of the fields generated by each wire shown in Fig. 97. However, in this case the horizontal components do not point in the same direction with the smaller contributions, due to the shallower angle from wires 1 and 2 acting in opposition to wires 3 and 4.

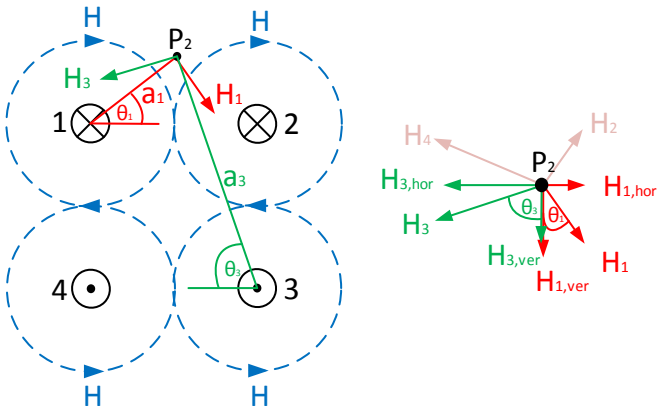

Figure 97: Example representation showing the magnetic field contribution from four current carrying wires acting at a point, P located above top row of wires.

Using the geometry of the test apparatus and using the Biot-Savart Law the magnetic field at a distance, *a* for a wire carrying current *I* can be described by (51) and the horizontal component described by (52)

$$H_i = \frac{I}{2\pi a_i} \tag{51}$$

$$H_{i,horizontal} = H_i \sin\theta_i \tag{52}$$

This suggests that the magnetic field at P_2 i.e. the local measurement would be approximately 43 % of that measured at P_1 i.e. the bulk measurement an underestimation as most of the local measured measurements are at least 80 % of the bulk.

The mechanism described using this simple set up explains why the local values are consistently lower that the bulk measurements. Further developing this model to loops instead of wires we find it is proportional to the area of the loop so could account for the change with decreasing width. However, it doesn't take into consideration increases in field strength of differences in grades. To test this hypothesis future setups should

endeavour to place the Hall effect sensor at a level below that of the top of the wire loop to mitigate this effect.

When the normal of the surface enclosed by the secondary coil is parallel to the RD a higher proportion of the domains have their easy axis also pointing in this direction. With increasing field strength, the domains oriented with the magnetising field grow, and due to the high proportion of domains aligned on this axis, can do so using the lowest energy magnetisation mechanism; 180° wall motion. As the secondary coil is moved around the sample to the RD/TD more energy, i.e. a higher field compared to the RD is necessary to reach the same flux density due to not as many domains oriented parallel to the magnetisation axis which is 45° to the RD. Those oriented can grow using 180° wall motion. However, as there are not as many as at the RD location some domains will have to grow using 90° wall motion which is more energetically demanding. Moved around further still to the TD location even fewer domains have their easy axis parallel to the magnetisation vector. At this location, even less domain growth can be accomplished due to 180° wall motion with more of the higher energy 90° wall motion needed. This requires a further increase in field strength to grow the number of grains needed to reach the required flux density. The indicative domain structure at the different measurement locations is shown in Fig. 98.

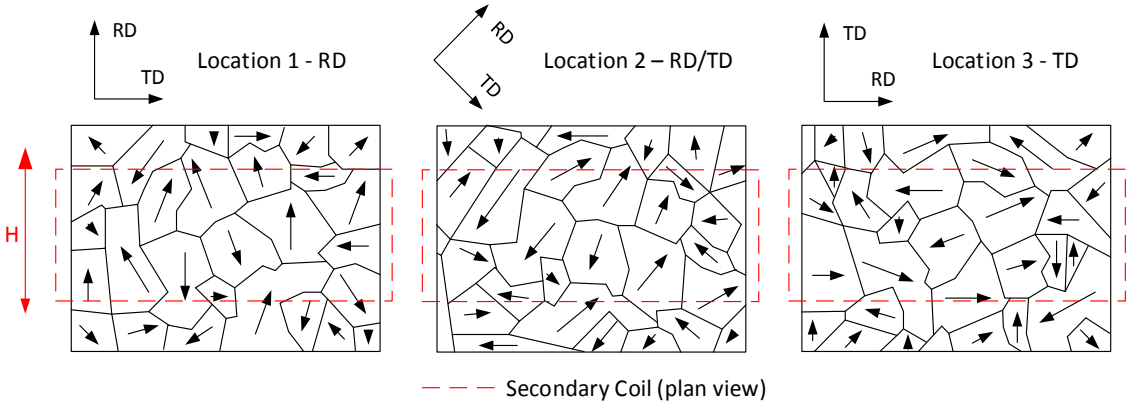

Figure 98: Plan View showing indicative domain structure at the different measurement locations

For measurements taken in the RD (location 1) the domains can sufficiently align themselves with the magnetising field through mostly 180° wall motion. As the angle between the magnetising field and RD increases the domains can't align using predominately 180° wall motion requiring an increase in the amount of 90° wall motion and domain rotation. This more complex wall motion requires an increase in the magnetising field to reach the same flux density implying a decrease in permeability and an increase in power loss.

Measurements of the magnetising field taken at a mixed direction are found to be approximately the mean of RD and TD measurements, there is a bias toward the RD measurements (lower than the average) at the lower flux densities measured, 1.0 T, however, it regresses towards the mean as the flux density increases. This could be explained if at the RD/TD locations we assume that the percentage of grains whose easy axis are aligned in the magnetisation direction is mid-way between than that of the RD (highest alignment) and the TD (lowest alignment). At the lower flux densities, there would be enough aligned domains to achieve sufficient alignment through predominantly 180° wall motion i.e. using wall motion resembling the RD locations. As the flux densities increase it becomes increasingly necessary to recruit more domains which need 90° wall motion to achieve the required domain alignment. As a result, the resemblance to the RD becomes less as the flux density increases. The RD/TD magnetising field for the 150 mm ID grade M330-35A sample tends towards the TD as the field increases, this could be due to the grain structure at the RD/TD location being similar to the TD, unlike the mixed direction of other samples. The 180 mm ID grade M330-35A shown in 2.1.1. shows the lowest field in the RD/TD direction, unlike the other samples however is still with in experimental error.

For the 3.2% Si, M250-35A and the 2.4% Si, M330-35A sample the indirect bulk

values calculated from the primary coil and those measured by the Hall effect sensor are comparable at low field strengths but quickly diverge as the field increases with the bulk measurements becoming significantly larger than the average of the locally measured, Hall probe values.

Flux Density, B peak

Proximity to the edge is associated with a decrease in flux density. For the M250-35A, 3.2% Si sample this change is abrupt and occurs at 2.0 ± 0.5 mm and is consistent with all measurements in the range 1.0 to 1.4 T and at 200 to 800 Hz. The M330-35A samples displayed a more gradual change. Dislocations that are created in grains can pile up at the grain boundaries which produces large concentrations of stress [86]. This pile up, which acts like a crack, is caused by the slip planes of neighbouring grains not lining up and is proportional to the size of the grain [87]. The larger the grain, the larger the pile up and the larger the stress. The larger grains of the M250-35A samples could restrict the propagation of dislocations into the interior of the sample resulting in a more pronounced effect near the edge unlike the M330-35A samples, which allow the dislocations to diffuse further into the sample display a more gradual effect. The punching of the electrical steel generates plastic stress/strain and increases the number of dislocations localised near the edge. These act as pinning sites impeding the motion of domain walls causing a decrease in the permeability, this is reflected in the flux travelling in the more easily magnetised central region with a reduced flux density at the edges. A material with uniform permeability would be expected to have a linear flux density profile which tracks the applied field which is not seen here.

The flux density was observed to dip in the centre of some samples. This can be explained by the large residual stress, at the edge transitioning to smaller compressive and tensile stresses in the centre.

The residual stress distribution in the plane of a typical cross section is illustrated in Fig. 99. There will be large values of residual compressive stress immediately adjacent to the cut edge, which will decrease with distance from the edge sharply at first then more gradually with smaller amounts of residual stress penetrating into the sample interior. The punching which may result in bowing of samples will result in the top face being in tension while the bottom face is in compression.

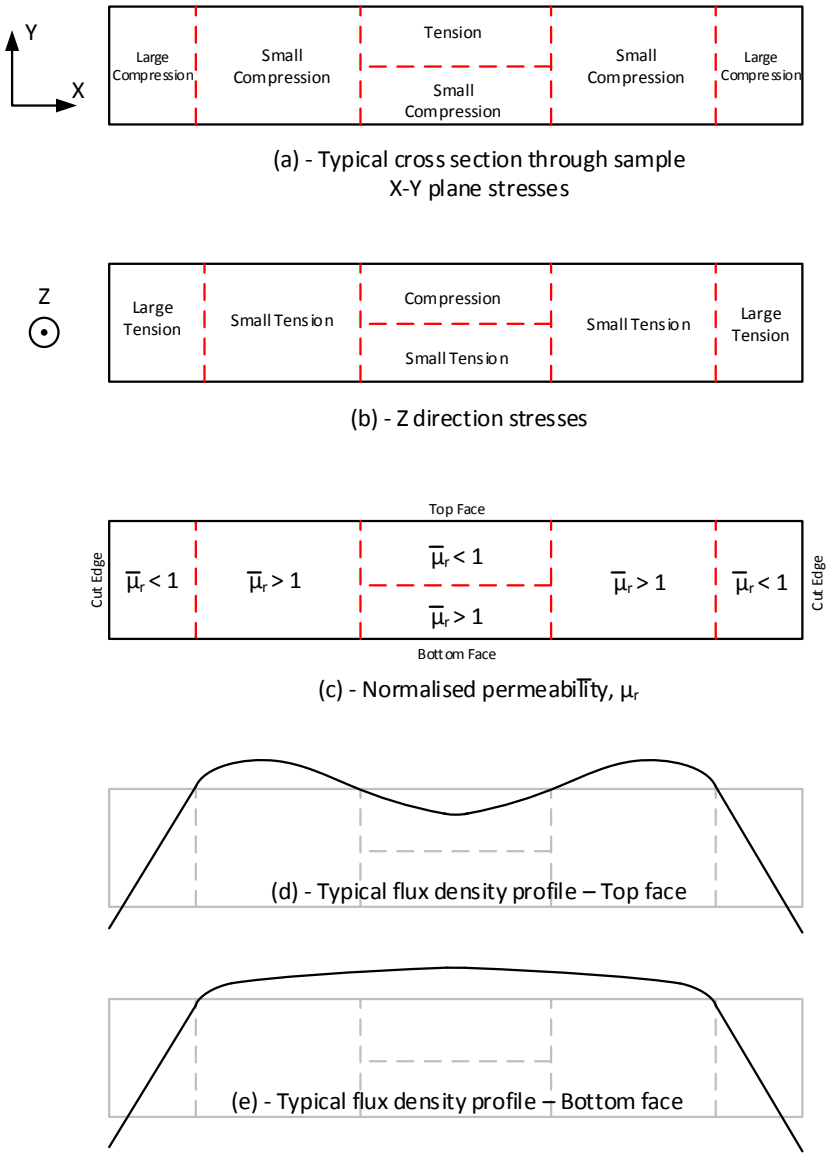

Figure 99: Simplified stress distribution and associated relative permeability in a punched strip

Normalised permeability is greater than one when a small tensile stress is applied in the magnetisation direction. For B < 1.5 T and f < 400 Hz this is approximately between

0 MPa and 40 ± 10 MPa of tension. Poisson's ratio which is the ratio of strain in the lateral and axial directions, for NOES is described in Section 2.4.1 and is approximately 0.34 indicates that a compressive stress of 13 ± 3 MPa in the x or y-direction would produce a tensile stress of 40 MPa in the direction of magnetisation, the z-direction.

The magnitude of the change in flux density observed at the edge compared to the centre is related to the location at which it is taken. The greatest change is observed where the flux is travelling in the RD and the least when the flux is travelling in the TD. When in the RD, increases in magnetisation can be achieved mainly using 180° domain wall motion in the central part of the sample. As the angle to the RD increases and the availability of 180° domain wall motion decreases the flux is forced to use more complex mechanisms located towards the edges.

Power Loss and Adjusted Power Loss

Other reported results indicate that the highest loss is observed at 55° to the RD [88] [89] [90] which is contrary to what is observed here. The RD/TD location was expected to show the largest loss however the losses were consistently higher in the TD although it should be noted that there is a reasonable uncertainty in these measurements.

The calculated power loss displays a dependence on the value of the flux density, B at the position at which it is measured. As a result, the power loss profile tracks that of the flux density. This displays a lower value in the region near the edge compared to the centre. This is because of the lower values of B near the edge, as the flux prefers to travel towards the centre. As power loss increases with increasing B the power loss was corrected across the sample by determining the rate of change of the power loss with B and normalising it across the width.

The mean of the local measurements across the sample was analysed for the different width samples over the range of 1.0 to 1.4 T. The rate of change, *m* calculated

from the linear relationship was used to correct the power loss using the following formula (53).

$$P_{corrected} = m(B_{normalised} - B_{local}) + P_{local} \quad (53)$$

This approach could be used predict the power loss distribution in saturated samples where the flux won't be able to modulate its density towards the centre of the sample and it would be reasonable to expect it to be more uniform over the width.

M250-35A, 150 mm

Fig 100 (a) to (c) shows the corrected power loss and local B peak for the M250-35A, 150 mm ID sample at 1.0 T and 1.3 T at a frequency of 400 Hz.

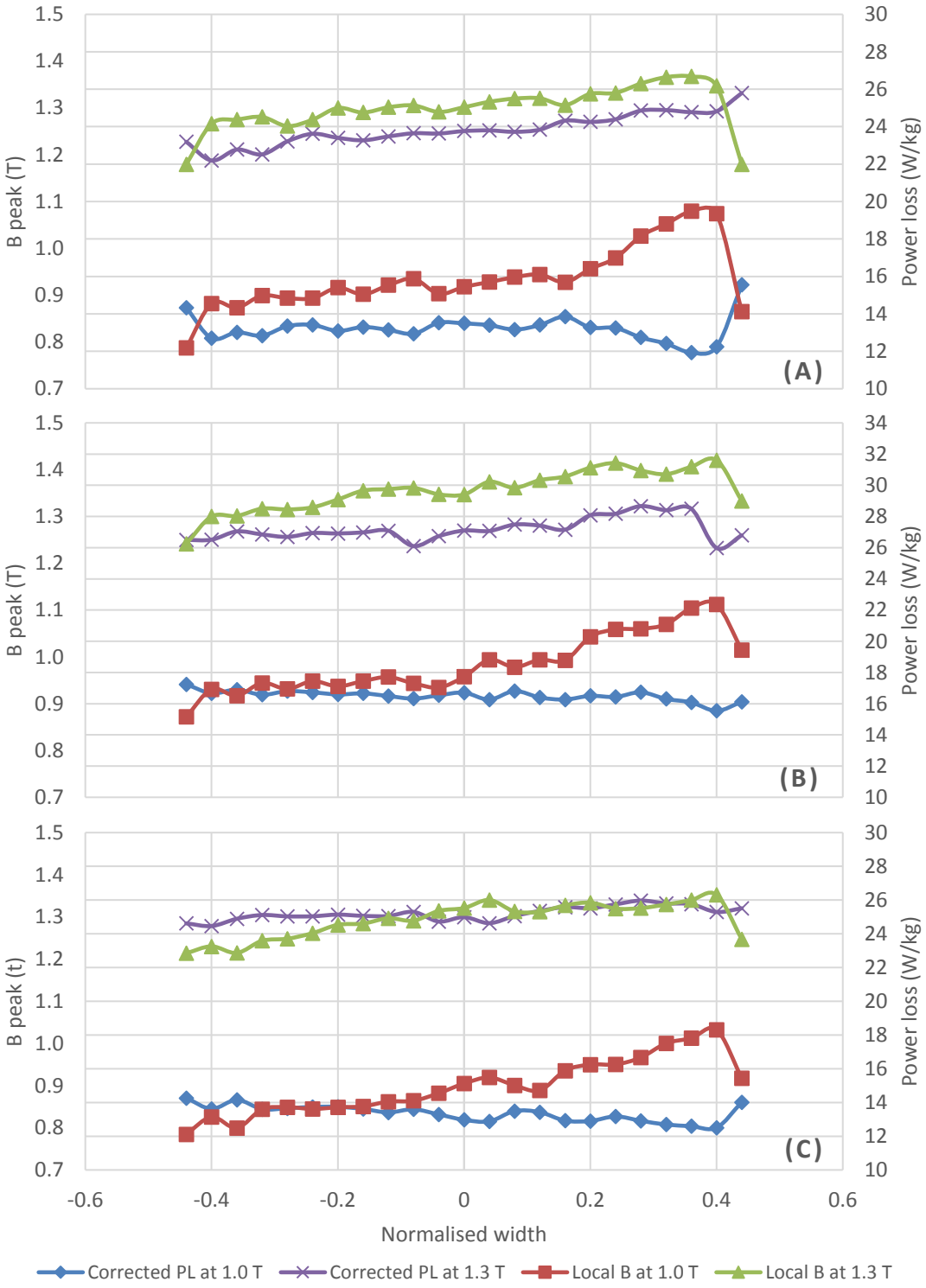

Figure 100 – Corrected power loss and local B peak in the (a) RD, (b) TD and (c) TD/RD

M250-35A, 180 mm

Fig 101 (a) to (c) shows the corrected power loss and local B peak for the M250-35A, 180 mm ID sample at 1.0 T and 1.3 T at a frequency of 400 Hz.

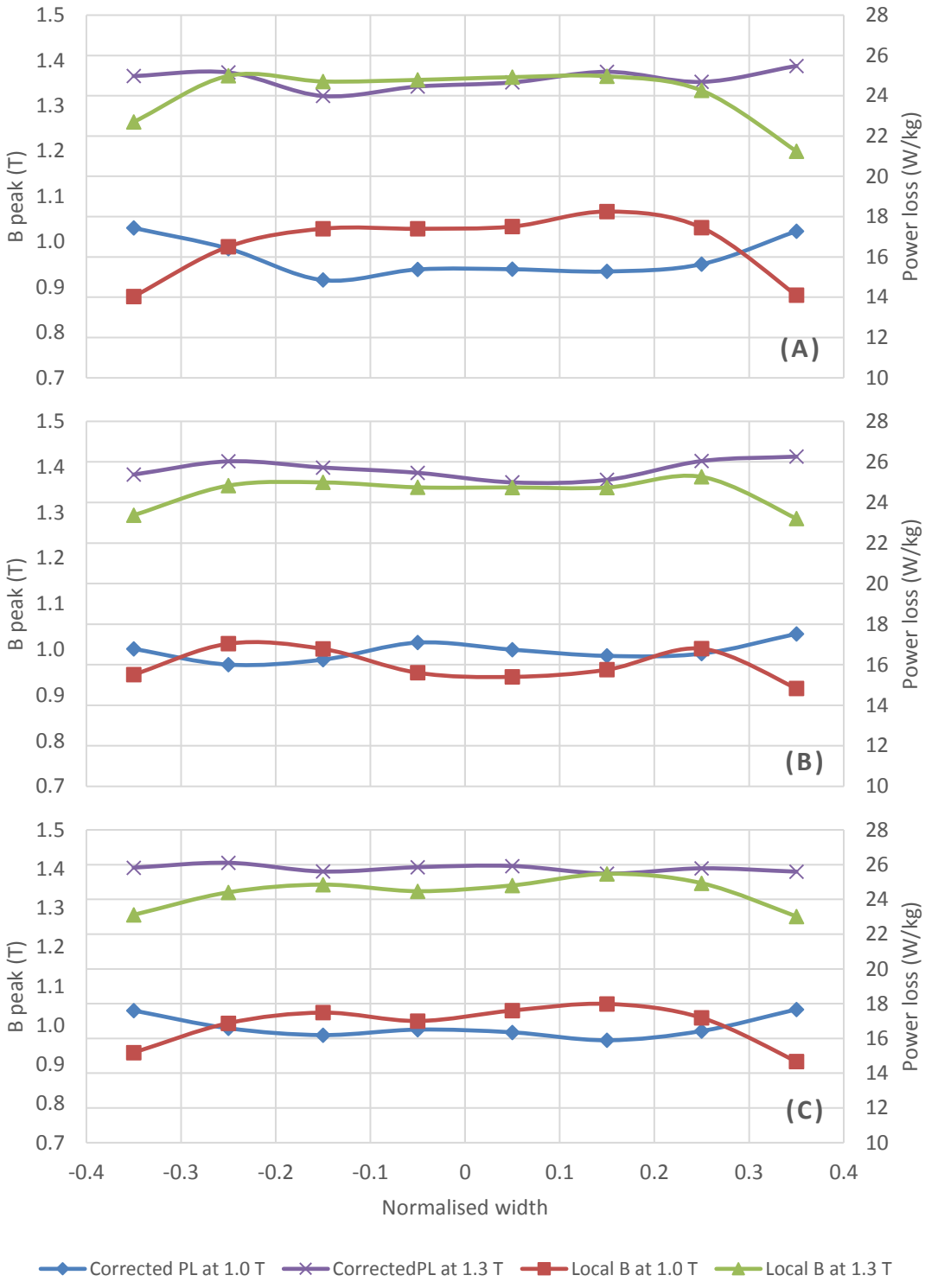

Figure 101 – Corrected power loss and local B peak in the (a) RD, (b) TD and (c) TD/RD

M330-35A, 150 mm

Fig 102 (a) to (c) shows the corrected power loss and local B peak for the M330-35A, 150 mm ID sample at 1.0 T and 1.3 T at a frequency of 400 Hz.

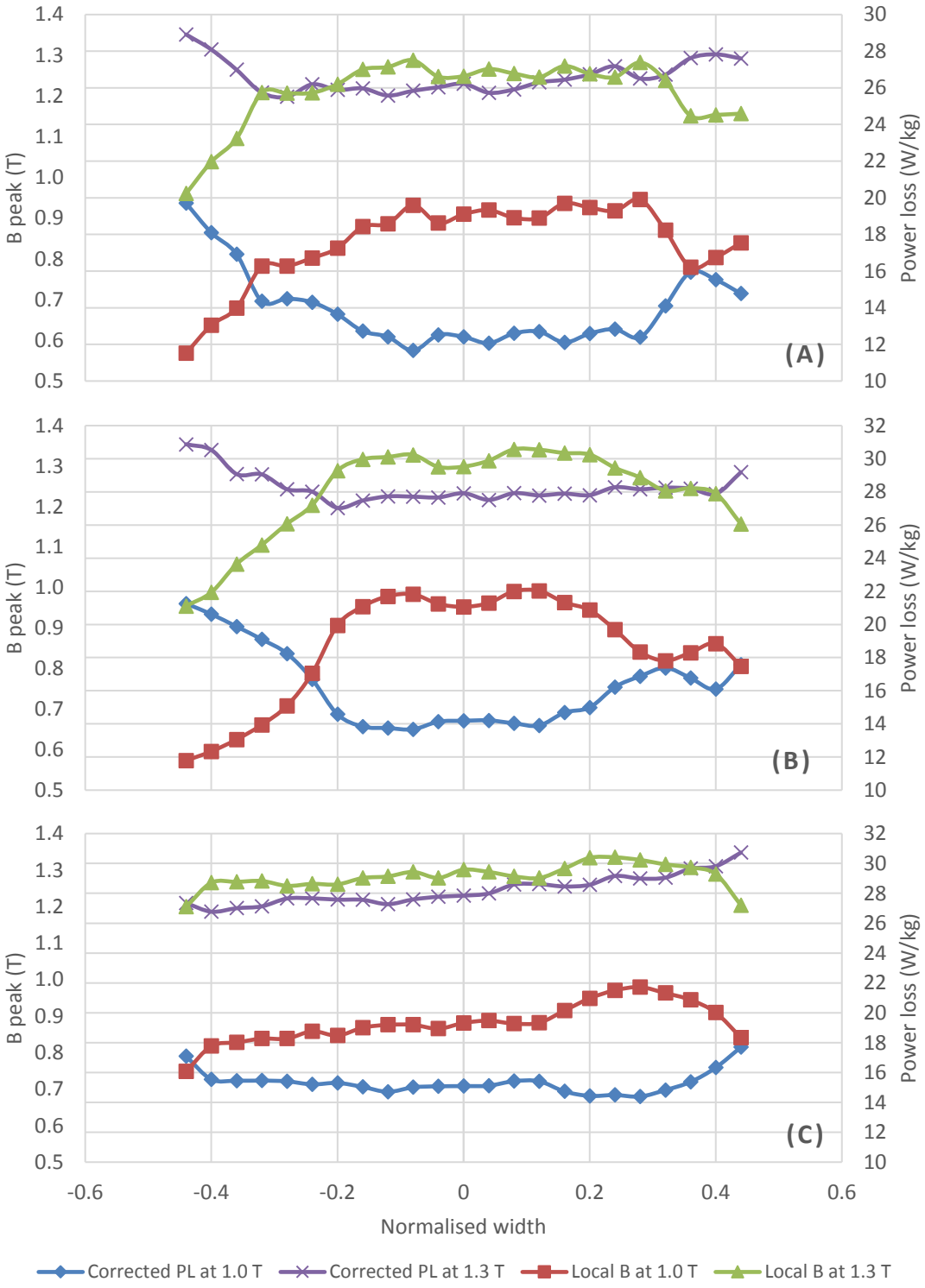

Figure 102 – Corrected power loss and local B peak in the (a) RD, (b) TD and (c) TD/RD

M330-35A, 180 mm

Fig 103 (a) to (c) shows the corrected power loss and local B peak for the M330-35A, 180 mm ID sample at 1.0 T and 1.3 T at a frequency of 400 Hz.

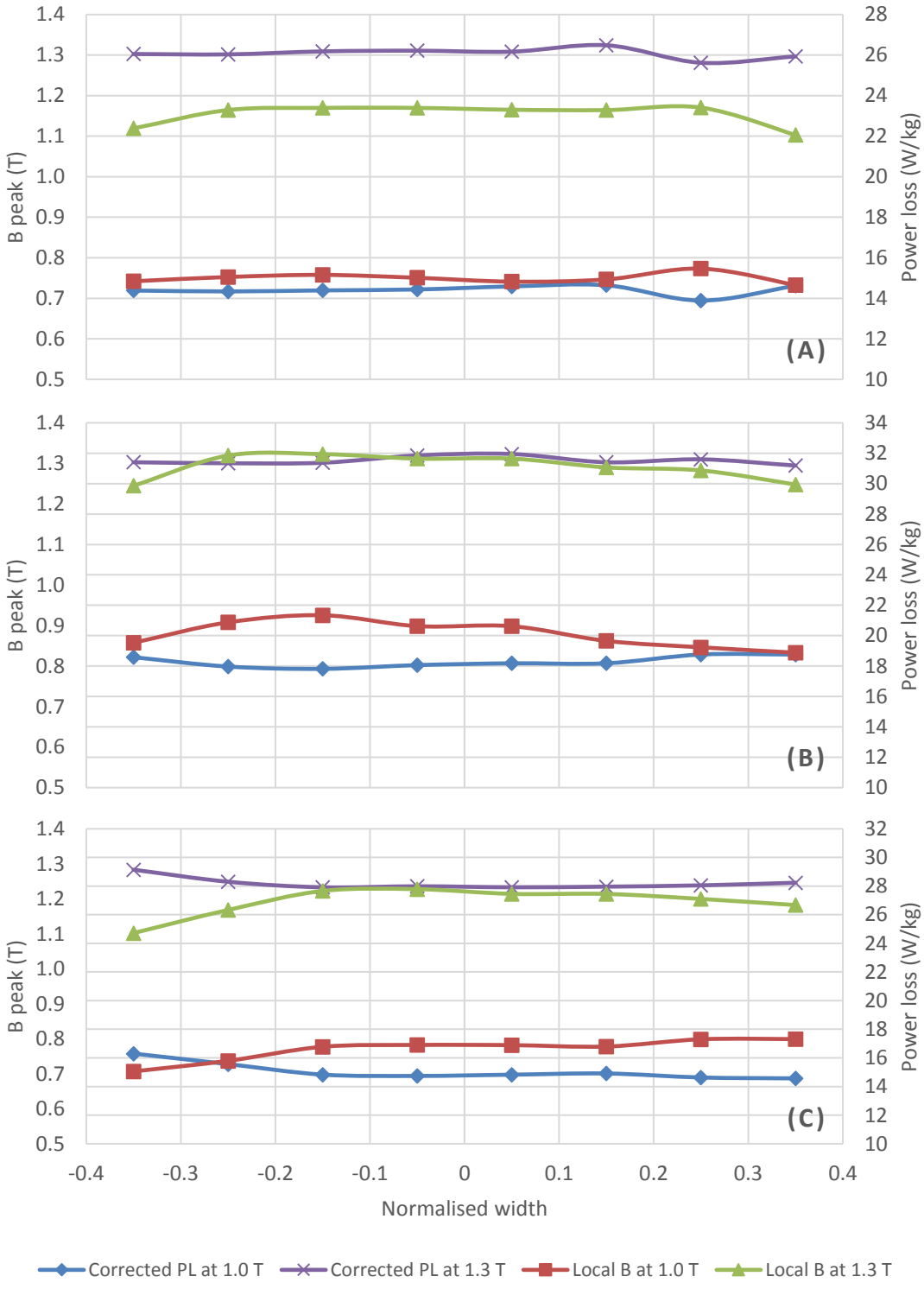

Figure 103 – Corrected power loss and local B peak in the (a) RD, (b) TD and (c) TD/RD

4.3.1.2. Normalised Values of Different Width

Section 4.2.1.2. displayed the mean average of the three locations normalised over the width of the sample. These were calculated by dividing the measurement position by the sample width so that the x-axis for all samples extends from -0.5 at the OD to 0.5 at the ID

There is a clear trend of increasing H peak and decreasing permeability as width decreases with a pronounced effect for the 5 mm wide sample. As the zone of peak degradation extends over the first 2.0 to 2.5 mm it is conceivable that this entire sample is within the degraded zone. This zone has a consistent depth for the different samples and as such takes up a larger proportion of the total width as samples narrow, evidenced by the peaks in the flux density moving towards the centre of the samples

The peaks and central dip become less visible as the sample get narrower. This is partly due to the profile being "stretched" as it is normalised and partly due to the meeting of the stress field in the centre and the reducing proportion of undegraded zone acting to reduce the depth of the central dip. The M330-35A sample having a more gradual change in flux density doesn't display this characteristic.

4.3.1.3. Variations with Frequency.

Measurements have typically been measured at 1.5 T and 50 Hz. However, for high frequency applications, such as the traction motors of HEV's, results at 1.0 T and 400 Hz are more often used nowadays. A typical drive cycle will range from lower revolution, high torque requirements for pulling off and hill climbing to top end speed above 15000 rpm. The relationship between rotational speed, ω (rpm), frequency, f (Hz) and number of poles, p for the synchronous speed for an electric induction motor (full load speed, obtained by multiplying by a slip rating will be slightly less) can be describe by (54)

$$\omega = \frac{120f}{p} \tag{54}$$

For a typical EV or HEV motor having 4 to 6 poles and accepting that there are many influencing factors, for example; wheel size, we can estimate a range of 200 Hz to 800 Hz with a typical cruising speed in the middle at approximately 400 Hz.

The flux density is the same at the different frequencies as this is held constant. However, the magnetising field and the power loss both increase with frequency. The magnetising field increases with frequency for constant flux density as the permeability is a frequency dependent function that decreases as frequency increases. The skin depth, the area of the material near the surface, through which the majority of the flux travels, also decreases with frequency. The flux density is an average calculated by dividing the flux through the whole sample by the area. As frequency increases and the area through which the flux travels decreases, more and more flux has to be pushed through this smaller and smaller area in order to maintain the same "average" flux density, this requires more complex wall motion in this small area, which requires a larger magnetising field and implies a lower permeability.

The power loss component that is least sensitive to frequency is the hysteresis loss, which is the loss component that is primarily effected by cutting, as a result there is no observable difference in the flux density and power loss profiles at increased frequencies, at least up to 800 Hz.

Due to the small needle area, a relatively weak signal is generated. An increase in the frequency results in an increase in the signal strength and provides more stable measurement conditions. The downside of this however, is a decrease in skin depth and an increase in the non-homogeneity of the flux through the sample.

4.3.1.4. Development of Alternative Methods

Towards the end of the project, an alternative to using needles was trialled. This involved the printing of a conductive ink consisting of a silver nanoparticle dispersion in triethylene glycol monomethyl ether, shown in Fig. 104a and 104b. The ink was printed onto a platen heated to 60 °C and was cured at 175 °C for 30 minutes. The printing was undertaken by The Centre for Process Innovation (CPI) in Sedgefield, County Durham using a Dimatix DMP2800.

This process relies on the same principle as the needle probe method but uses the conductive ink as an alternative to the needle. This has the advantage of being able to measure the flux density in lamination throughout the height of the stack as the depth of the ink is ≈ 100 nm where the needles are limited to the top lamination.

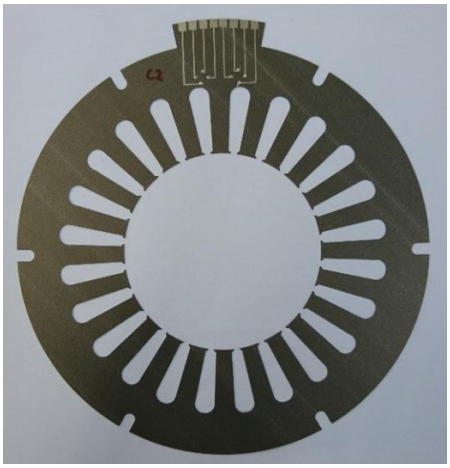

Figure 104a: Stator with four passes of 0.5 mm wide printed conductive tracks.

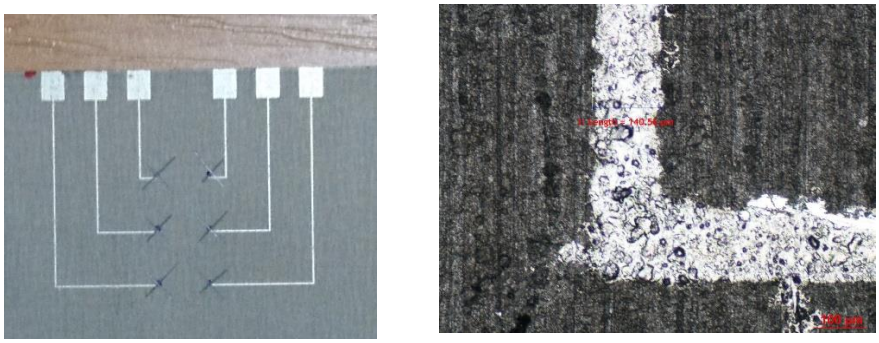

Figure 104b: Left – Epstein samples with one pass of 0.1 mm wide printed silver tracks. Right - Image of one pass of printed silver track with specified width 0.1 mm (measurement reads 140.56 µm)

Initial printing trials showed a good bond between the deposited silver ink and the surface of the samples. The spreading of the ink was approximately 1.4 times the specified track width which is considered acceptable. However, one printing pass failed to produce a conductive path along the tracks. The thickness of one printed track is ≈100 nm and this could result in two possible reasons why a conductive path was not obtained; a higher resistance due to the small cross-sectional area of the track and discontinuities in the track created by variations in height of the coating which can be of the order of 1000 nm.

These possibilities were addressed with further work increasing the number of printer passes and it was determined that a minimum of four printer passes is necessary to achieve a conductive path. However, this resulted in more spreading of the ink with tracks running into each other. The insulation coating was removed at the desired measurement site with a scalpel and lining up the ink with the measurement site proved difficult increasing the number of nonconductive tracks.

At present, it is not a viable method but if suitably developed it would allow the considerable reduction of the probe size and a smaller gap in the primary windings resulting in more uniform magnetising conditions. It also has the potential to be used in working motors and to measure the flux density throughout the stack height and not just the top lamination.

4.3.2. Microscopy

4.3.2.1. Optical Microscopy of the Cut Edge Face

The images were analysed using an open source Java image processing program called ImageJ [91, 92]. The average of five measurements was used to determine the sample thickness at the centre and both edges for each sample, shown in Fig. 106. The grain size was determined using a linear intercept procedure in accordance with ASTM

standard for determining average grain size [93]. This can be summarised as follows;

A line of known length is drawn on the sample, the number of times a grain boundary intercepts the line is counted with each given a score of 1 with points where three grains intersect (point 3 in Fig 105) given a score of 1.5. The line length is divided by the total score to give the mean grain size. An example is given in Fig. 39.

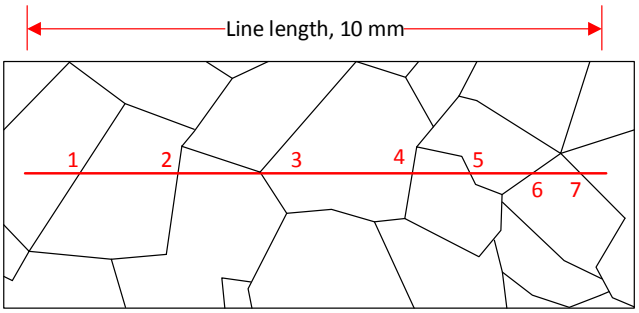

Figure 105 – Example demonstrating linear intercept procedure for a single line. The line length 10 mm is divided by a score of 7.5 to give the mean intercept length of 1.33 mm.

As relatively short lines are used to get local measurements and as these are thin anisotropic samples the average of six lines at different orientations; two horizontal, two vertical and two diagonal are used to generate the average grain sizes. An example of this is shown in Fig. 107.

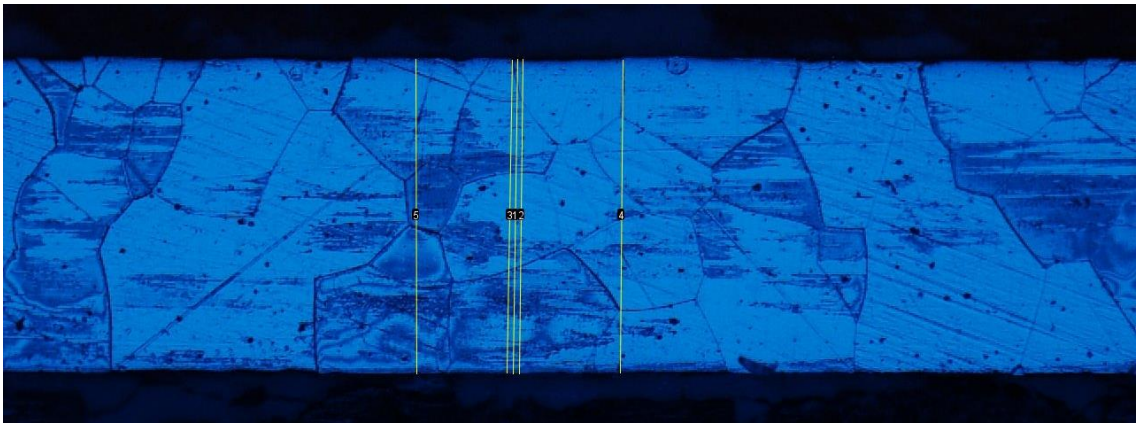

Figure 106 –Average thickness of sample from five measurements. The example is shown at the centre of the 150 mm wide M250-35A sample.

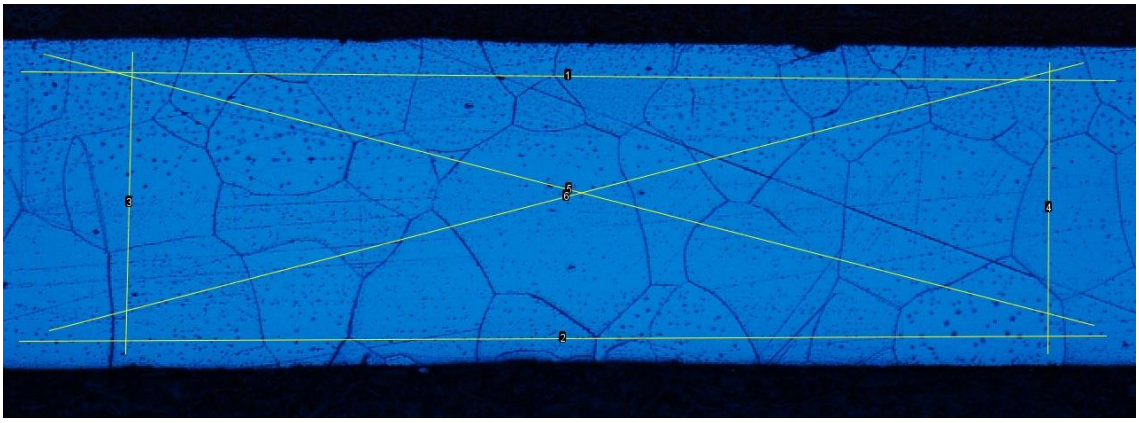

Figure 107 – Intercepts counted along the line and divided by the line length to obtain mean intercept length and averaged over different orientations. The example is shown at the centre of the 180 mm wide M250-35A sample.

The variation in thickness and grain size is summarised below in Tables 22 – 25.

	M250 - 35A 150 mm ID		
	OD Edge	**Centre**	**ID Edge**
Grain Size (µm)	95 ± 5	143 ± 69	93 ± 23
Thickness (µm)	332 ± 4	354 ± 1	307 ± 5

Table 22: Average grain size and sample thickness at different locations for M250-35A, 150 mm ID sample.

	M250 - 35A 180 mm ID		
	OD Edge	**Centre**	**ID Edge**
Grain Size (µm)	101 ± 11	113 ± 36	90 ± 20
Thickness (µm)	300 ± 7	361 ± 4	321 ± 4

Table 23: Average grain size and sample thickness at different locations for M250-35A, 180 mm ID sample.

	M330 - 35A 150 mm ID		
	OD Edge	**Centre**	**ID Edge**
Grain Size (µm)	77 ± 14	72 ± 17	58 ± 11
Thickness (µm)	303 ± 6	360 ± 4	304 ± 9

Table 24: Average grain size and sample thickness at different locations for M330-35A, 150 mm ID sample.

	M330 - 35A 180 mm ID		
	OD Edge	**Centre**	**ID Edge**
Grain Size (µm)	65 ± 10	63 ± 19	58 ± 8
Thickness (µm)	291 ± 1	355 ± 8	264 ± 12

Table 25: Average grain size and sample thickness at different locations for M330-35A, 180 mm ID sample.

There appears to be a decrease in grain size at the edges, with a larger reduction observed in the 25 mm wide, 150 mm ID samples compared to the 10 mm wide, 180 mm ID samples. However, the difference in grain size at the edges compared to the centre is not statistically significant. The samples are significantly thinner at the edges with this region of reduced thickness extending approximately 0.5 – 1.0 mm into the samples and are particularly pronounced over the first 0.1 – 0.2 mm.

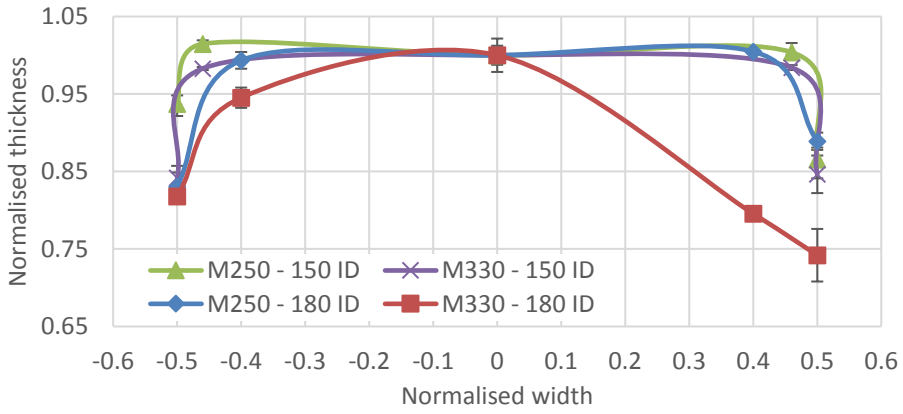

Figure 108 –Normalised sample thickness normalised for different width samples

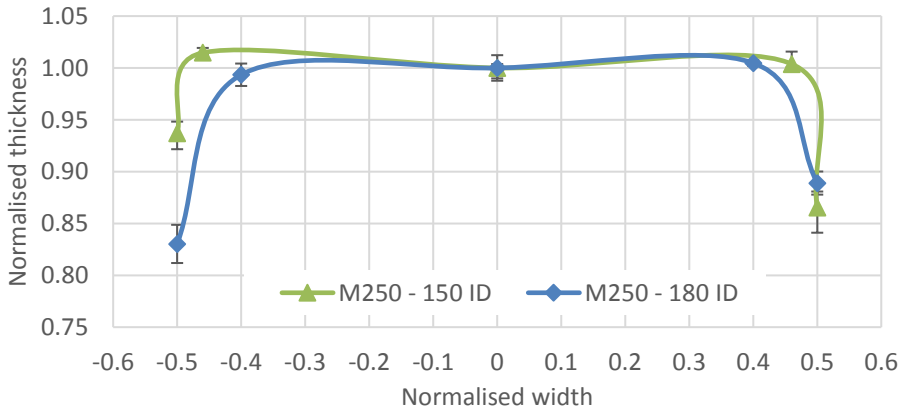

Figure 109 –Normalised sample thickness normalised for different width samples

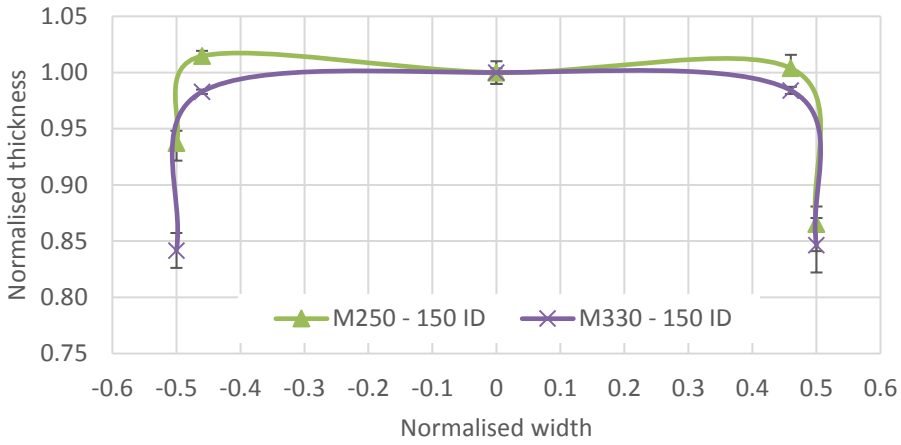

Figure 110 –Normalised sample thickness normalised for different width samples

The compression observed at the edges is a result of the large punching forces needed to shear the samples. As the ID increases and width decreases the area of the cut face will increase requiring a larger force. This hypothesis would explain the increased compression observed in the narrower samples. It would follow that the M330 samples with a lower yield strength compared to the M250 samples would require a lower punching force and show less compression at the edge. This is not what is observed here. The difference possibly due to other factors such as grain size and silicon content. The small sample size and lack of knowledge regarding the optimisation of the punching make it difficult to draw firm conclusions.

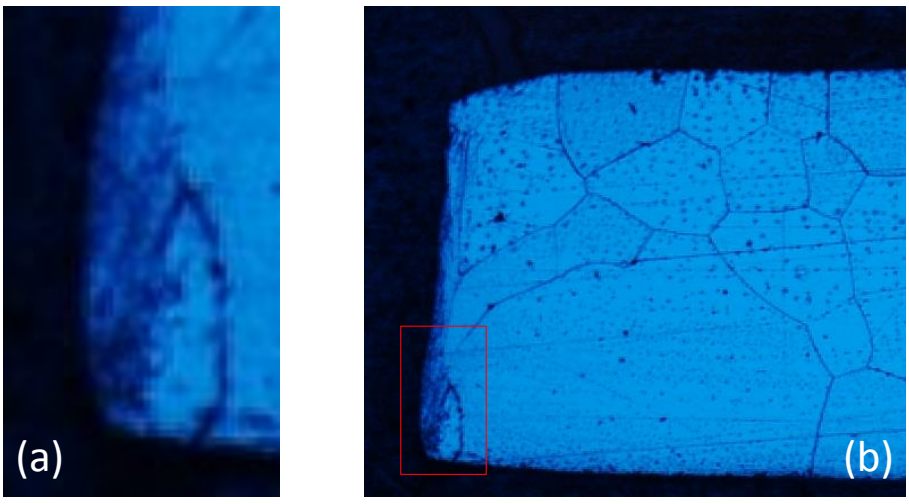

Figure 111 –ID edge of M250-35A 180 mm ID sample indicating thin band at cut edge (a) and zoom in section (b)

All samples show thin bands extending approximately 10 – 30 μm from the cut edges where individual grains are not observable.

To observe the grains a weak acid is used to etch the surface with the grain-boundary atoms more easily and rapidly corroded than the atoms within the grains this brings them out as darker lines. These dark bands at the edge are likely to be the outcome of the plastic deformation induced by the punching causing residual stress and defects in the crystal lattice and reducing the quality of the image.

4.3.3. Summary

Two commonly used lamination materials produced using an industrial punching process were investigated. The local magnetic properties were mapped at different locations relative to the RD. It was discovered that the profile is not always parabolic as assumed to be the case in the literature and depends on material properties.

Optical microscopy indicated the presence of residual compression at the cut edge and bowing in the centre of the samples as a result of the large punching forces necessary to shear the samples.

A new physical theory was developed to explain the different profiles observed by mapping how the change in residual stress effects the permeability.

CHAPTER 5.

MODELLING OF FLUX DENSITY AND POWER LOSS

5.1. METHODS

As described in Chapter 2 the effect of stamping which is widely used in the manufacture of motor laminations affects the magnetic properties of the laminations with an amplified effect near the edge. The modelling approach taken was to divide the lamination material into segments each responding differently to the stamping, then the separate segments were recombined to predict the effect of stamping on the entire lamination. The model was refined to optimise the procedure for material segmentation producing a model which can be easily incorporated into electromagnetic finite element software. These models can be used in the design of the rotor and stator laminations used in electrical machines to assess the distribution of flux through the material and minimise the power loss for different designs, with the aim of improving the efficiency. To facilitate the straightforward application of these models it was necessary to minimise the number of inputs and for the inputs used to be obtained via relatively simple measurements or available material data. The simplicity of implementation must be balanced against the accuracy of the prediction which must still be beneficial and advantageous to the motor designer.

Model A was used to estimate the size of the magnetically degraded region due to cutting and provide estimates for power loss for samples of different widths. This could be used to construct power loss estimates for laminations by deconstructing the complex shapes into a series of simpler geometries and summing the power loss from the different parts. Model B proposed a varying permeability profile that can predict the variation in flux density throughout a lamination. Both can be incorporated into FEM models. The

models were applied to same ring geometries so that a direct comparison could be made. However, they should be applicable to more complex designs. The following section outlines the modelling approach used.

5.1.1. Model A – Discreet Permeability Model (DPM)

This model incorporated the effect of punching in the power loss prediction by dividing the sample into discrete bands, that is the ring was considered as being made up of several concentric rings each assigned different properties. This first attempt adopted the simplest approach of three bands with an "undamaged" zone in the centre and two "damaged" zones at either edge.

Consider a thin slice of the ring cut along the radial direction with width, $w = \frac{OD-ID}{2}$, height, h and depth δθ where θ is small enough so that the curvature can be neglected and it can be considered a cuboid. With a cross sectional area, $A = hw$ which will consist of an area damaged by the punching process, A_d and an undamaged area, A_u as shown in Fig. 112. The damaged area is defined to be an area of the sample with a reduced permeability. The value *d* refers to the length of cumulative damaged width from both edges. The flux is assumed to travel perpendicular to the slice plane.

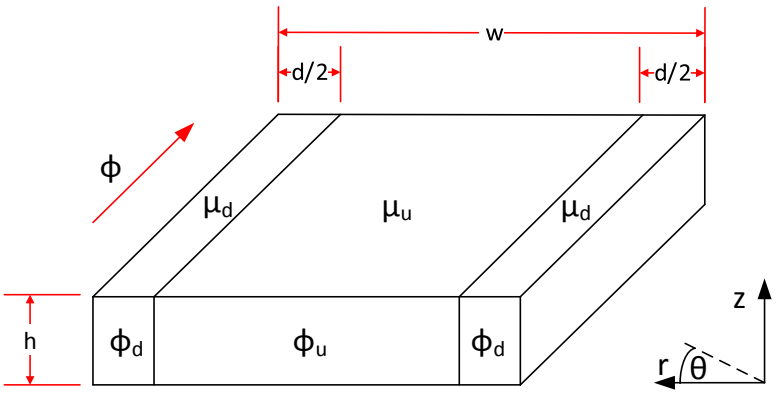

Figure 112: Cross section of lamination displaying edge regions with no flux and central region through which the flux travels.

The flux passing through the sample, ϕ_w defined in (55) consists of the flux through the damaged area, ϕ_d and the flux through the undamaged area, ϕ_u and the flux density, B_w similarly defined in (56).

$$\phi_w = \phi_d + \phi_u \tag{55}$$

$$B_w = \frac{dB_d + (w-d)B_u}{w} \tag{56}$$

The total power loss, P_w is considered to be the sum of the power loss through the damaged region, P_d and the power loss through the undamaged region, P_u.

$$P_w = P_d + P_u \tag{57}$$

The magnetically damaged area is defined as having a lower permeability than the rest of the sample. In this simple model A_d is assumed to be damaged to such an extent as to have a permeability no greater than that of free space and all of the flux travels through A_u, (56) reduces to;

$$B_u = \frac{w}{w-d} B_w \tag{58}$$

Although a three-term power loss model could be argued to be more accurate, with punching thought to affect mainly the hysteresis component, it was decided to use a Steinmetz based model (59) where the power loss is proportional to the square of the flux density to simplify calculations and minimising calculation time for this initial model.

$$P_{\text{Steinmetz}} = C_{hyst} B_{max}^2 f + C_{eddy} B_{max}^2 f^2 \tag{59}$$

The power loss in a particular region is assumed to be a result of domain wall motion only in that same region. It was assumed that power loss in each region is proportional to the square of the flux density passing through that region i.e. $P_u \propto B_u^2$. It was also assumed that with a negligible amount of flux travelling through the damaged regions and therefore little or no domain wall movement, the total power loss is that of the undamaged region alone i.e. $P_w = P_u$ which leads to the following equations.

$$P_u = k_u B_u^2 \tag{60}$$

$$P_w = k_u \left[\frac{w}{(w-d)}\right]^2 B_w^2 \tag{61}$$

The calculated values for the power loss were compared to the measured values. The extent of the damaged region from the cut edge and the proportionally constant were selected to minimise the difference between the measured and calculated result. This is calculated as a simple percentage difference and was within 5% for most cases. The values of d and k_u were calculated to minimise the cumulative error using the built-in solver in Microsoft Excel.

5.1.2. Model B – Variable Permeability Model (VPM)

If we consider the punching of a small section of the sample shown in Fig. 113.

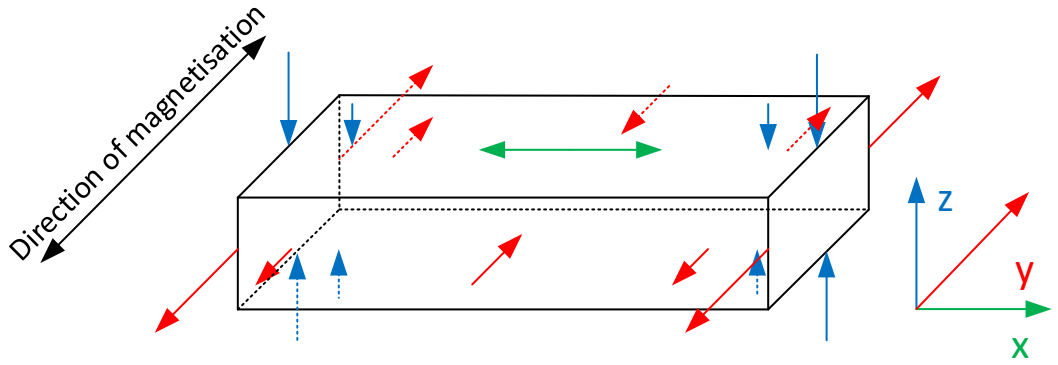

Figure 113: Stress distribution in a small section of the lamination and magnetised parallel to the Y axis. Pairs of arrows directed towards each other indicate compression while arrows in opposite directions indicate tension. The size of the arrows indicates the relative magnitude of the stress.

The shearing at the edges will result in the edge face becoming compressed in the z-direction, as seen in Section 4.2.2 with residual compression values as described in Chapter 2 ranging from 10s to 100s MPa. This is shown by the blue arrows and translates to tensile residual stress in the y-direction which quickly decreases with distance from the cut edge. In the centre of the sample residual tension in the x-direction, peaks in the centre of the sample and translates into residual compression in the y-direction. A simple

approximation of the stresses across the sample width and acting parallel to the magnetisation vector is illustrated in Fig. 114.

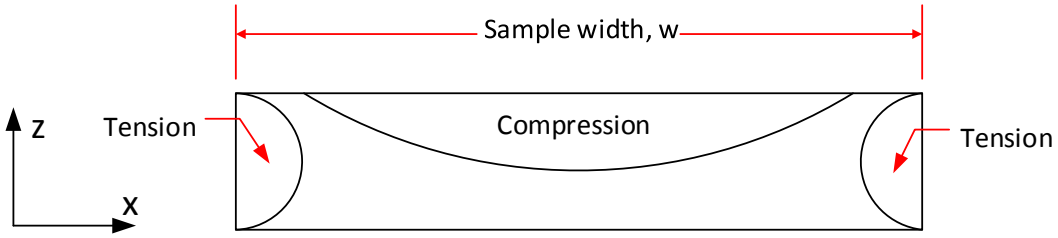

Figure 114: Simplified stress distribution within the cross section (XZ plane) of a punched steel lamination. Showing the stress acting in the direction of magnetisation, the Y direction. i.e into the page.

Consider the effect of the tensile component of the stress. Assuming levels of stress are more than 30 to 50 MPa as lower values would increase permeability as shown in Fig. 18, an increase in stress will result in a decrease in permeability. As the magnitude of the tensile component decreases with distance from the edge we can conclude that the permeability will increase with distance, illustrated in Fig. 115. Functions that decrease quickly and then level off such as hyperbolic curves and exponential decay curves are found to fit the changes in hardness [94] and associated residual stress [44] well. For simplicity, and ease of calculations, an exponential decay function (increasing form) was chosen, which can be described by (62)

$$\mu_{tensile}(x) = \beta\mu_{bulk}(1 - e^{-\alpha_1 x}) \tag{62}$$

Where x is the distance from the edge and α, β are constants which describe the rate at which the permeability increases and the limiting value respectively.

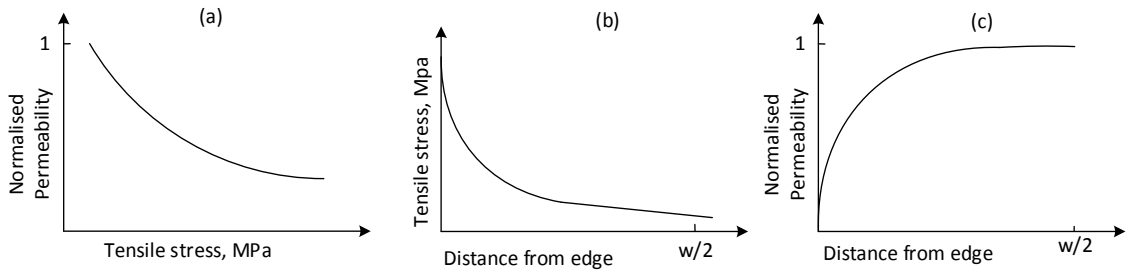

Figure 115: (a) Normalised permeability with tensile stress (b) Tensile stress against distance from cut edge (c) Normalised permeability with distance from cut edge due to a tensile component of stress.

Considering only the compressive component of the stress applied parallel to the direction of magnetisation, we also see permeability decreasing as the magnitude of the stress increases. However, as compressive stress increases with increasing distance from the edge, the permeability is seen to decrease with distance from the edge, illustrated in Fig. 116. Once again for simplicity, an exponential rate of change was assumed which can be described by (63).

$$\mu_{compressive}(x) = \gamma\mu_{bulk}(e^{-\alpha_2 x}) \tag{63}$$

Where x is the distance from the edge and α, γ are constants which describe the rate at which the permeability decreases and the initial decrease from the globally measured value at the edge respectively.

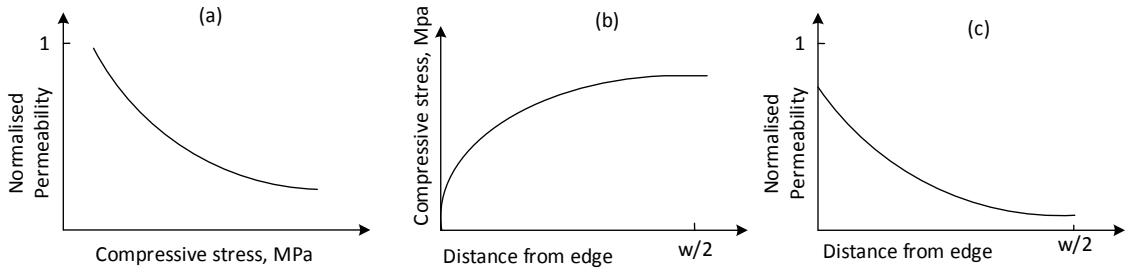

Figure 116:(a) Normalised permeability against compressive stress (b) compressive stress against distance from cut edge (c) Normalised permeability with distance from cut edge due to a compressive component.

The permeability profile is defined as the sum of the tensile and compressive permeability profiles and is described by (64) where *x* is the distance from the edge, μ_{bulk} is the bulk permeability of the sample and is valid over the range *0 < x < w/2* where *w* is the width of the sample.

$$\mu(x) = \beta\mu_{bulk}(1 - e^{-\alpha_1 x}) + \gamma\mu_{bulk}(e^{-\alpha_2 x}) \tag{64}$$

The input parameters were obtained by using a curve fitting approach and shown in Tables 26 and 27. The local permeability for all flux densities and at different IDs was compared against the modelled value, with the built-in data solver in Microsoft Excel

used to minimise the errors and the average values for each grade determined.

Due to the variation in materials and cutting type, the input parameters should be obtained from measurements on samples of the same grade and produced by the same cutting method as that which is to be modelled. The samples modelled here are grades M250-35A and M330-35A and produced by punching.

Parameter	Value
α_1	0.78
α_2	0.61
β	1.00
γ	0.86

Table 26: Input parameters for M250-35A

Parameter	Value
α_1	0.22
α_2	0.15
β	1.00
γ	0.86

Table 27: Input parameters for M330-35A

5.1.2.1. FEM Modelling

Comsol Multiphysics FEM software was chosen as the modelling software and a model constructed to calculate the magnetic fields produced for a multi-turn coil carrying a direct current around an electrical steel ring sample, shown in Fig. 117. This was done using the multi-turn coil domain feature with an automatic current calculation sub-feature.

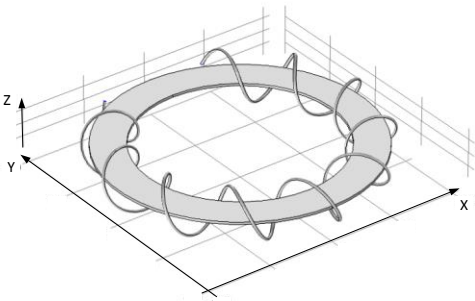

Figure 117 – Comsol geometry to simulate experimental setup in Fig. 118.

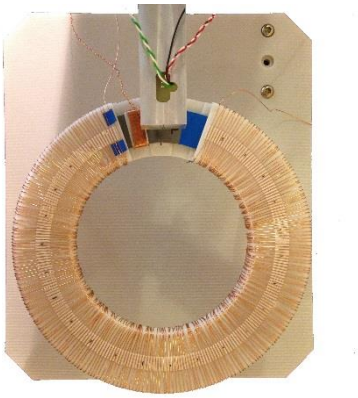

Figure 118 – Encased 150/200 mm ID/OD ring stack with a multi-turn coil wound around it.

The model could be further developed to calculate the eddy currents with the introduction of a sinusoidally varying current. The simulation results at specific positions were compared with measured experimental data at the same location.

5.1.2.2. Modelling Instructions

To create the model in Comsol 4.3b, a new 3D model was opened and the magnetic fields (mf) physics option was selected from the AC/DC module tree. The study steps were.

Geometry 1

The geometry was constructed in Solidworks and imported into Comsol using the LiveLink for Solidworks feature, shown in Fig, 119. A sphere was added as an outer boundary and the wire for the multi-turn coil was extended to form a union with the outer boundary.

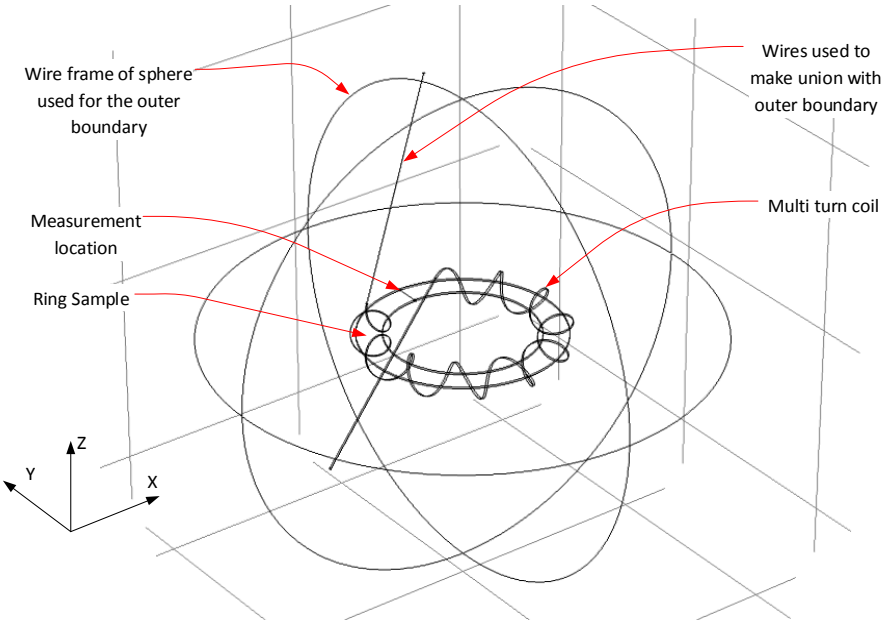

Figure 119 - Wireframe view showing the outer boundary and wire union. Designed in Solidworks and imported into Comsol

Interpolation Curve 1 was added to the geometry 1 between coordinates (0, Rin,0) and (0, Rout,0). This was at the position where the data for the line graphs was extracted and corresponds to the line of the probe. The interpolation curve is necessary to improve the meshing in this area. For example, for the model with inner diameter 150 mm and outer diameter 200 mm the coordinates were (0,0.075,0) and (0,0.100,0).

Global Definitions

The parameters to be used in the model were created. These allowed values that were used through the model to be referenced by their name, any changes only needed to be made once and they were automatically applied to where it was referenced in the model. Additional functions were added by right clicking global definitions and selecting the appropriate *function type*. An *analytic type* function, *R* and an *interpolation type* function, *Vmur*, were added, shown in Fig. 120.

The origin of the model is defined as the centre point of the ring and function *R* is the radial distance from the origin defined as (65).

$$R(x,y) = \sqrt{x^2 + y^2} \tag{65}$$

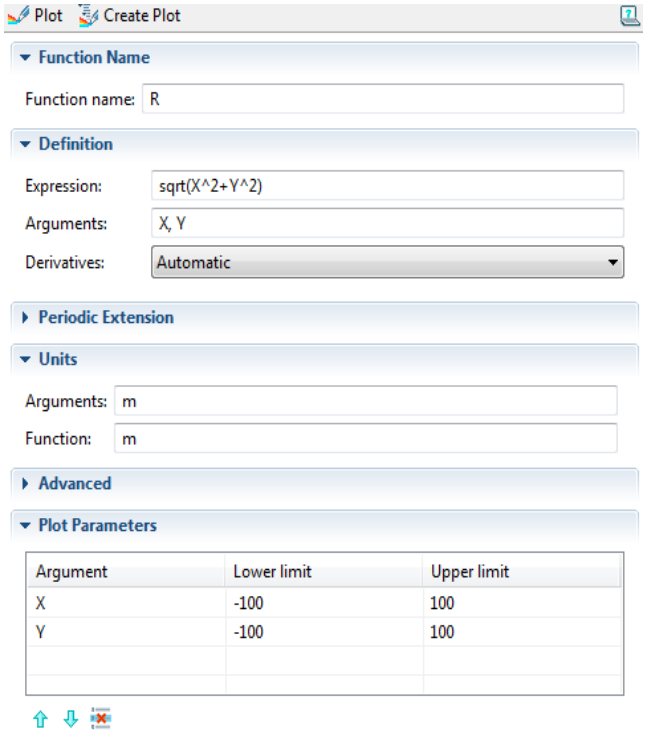

Figure 120 – Screenshot of Comsol input showing calculation of R using cartesian coordinate system which is to be used in specifying Vmur.

The values for Vmur, $\mu(x)$ were calculated using (66) where *x* is the distance from the edge, μ_{bulk} is the bulk permeability of the sample and α, β and γ are measured

parameters and are valid over the range *0 < x < w/2* where *w* is the width of the sample

$$\mu(x) = \beta\mu_{bulk}(1 - e^{-\alpha_1 x}) + \gamma\mu_{bulk}(-e^{-\alpha_2 x}) \quad (66)$$

The permeability as a function of distance from the edge was calculated for each sample using the appropriate input parameters. This was then converted to the form of an interpolation table where each radial position was allocated a permeability, shown in Table. 28. E.g, when *R* is 0.0750 m the distance from the cut edge is 0 mm and the corresponding permeability is 86 % of the globally measured permeability.

t	f(t)
0.0750	0.86*mur
0.0765	1.029*mur
…	…
0.0985	1.029*mur
0.1000	0.86*mur

Table 28: Vmur(R(x,y)) interpolation table for M250-35A with first and last two values shown.

The interpolation table saved as .txt files could be easily loaded into the models as required. Adding selections to the model improved usability by allowing certain parts to be easily called and by excluding certain domains/boundaries from the data sets. This was done by, right click *Definitions* and selecting *explicit* and picking the appropriate domains in the domain selection window.

Materials

The appropriate materials from the *Add Materials* tree were selected and added to the model. Air was used for the surrounding space, copper for the windings. The conductivity of air in the Material Library is zero. This was changed to 10 S/m to improve the stability of the solution determined from Comsol modelling examples obtained from the Comsol support website, the error introduced by this small conductivity is negligible.

Property	Name	Value
Electrical conductivity	sigma	10.[S/m]

Table 29: Altered material properties for air.

For the ferromagnetic ring, new materials were created: M250 and M330. Conductivity was taken from the material data sheet and relative permeability was the newly created V_{μ_r} which was a function of the radial distance, which itself was a function of the x and y coordinates.

Property	Name	Value
Electrical conductivity	sigma	sigma
Relative permittivity	Epsilon	1
Relative permeability	Mur	Vmur(R(x,y))

Table 30: Materials properties for newly created M250 and M330 material.

Magnetic fields (mf)

The Multi-turn coil feature was used to create the magnetic field. In order to use this feature the geometry of the coil needed to have a uniform cross-sectional area and no sharp turns. In order to specify the direction Input and Output surfaces needed to be selected. Coil type was *Numeric*, as it has 10 geometric turns the number of turns was *24* so to simulate 240 total turns. The coil excitation was *current* with an input current I_0.

Mesh 1

A mesh convergence check was performed to determine if the mesh was fine enough to be trusted, first by meshing the entire structure then refining locally at areas of high gradient and comparing the results. The mesh was constructed to be as fine as possible while still allowing the model to be solved in a reasonable time. The *extra fine* pre-defined element size was used. As there was a sudden change in permeability at a distanced d/2 from the edge it was desirable to have a node at that location. This was achieved by specifying the distribution along Interpolation Curve 1. A fixed number of

elements with the number of elements, *n* chosen so that *w/n* is a factor of *d*

Study 1

The study steps used were Coil *Current Calculation* and *Stationary* (Add a *frequency domain* study step for AC current input at different frequencies).

Results

Separate data sets were created to visualise the results in different domains independently. A solution was duplicated, then a selection applied choosing only the preferred geometric entities. A 3D cut line data set was created along *Interpolation Curve 1*. The values for various expressions including B and H were viewed along this line and compared to measured results shown in Section 4.2.1. Estimates for the power loss were performed using a statistical loss separation model (67). The total power loss was made up of the addition of the hysteresis, eddy current and excess losses described in Chapter 2, Section 4.3. Where *B* and *f* are the peak flux density and magnetisation frequency and k_{eddy} , $k_{hysteresis}$ *and* k_{excess} are parameters that were specific to the material and calculated from bulk power loss measurements and described in Section 5.3.1.1.

$$P = k_{hyst} f B_{max}^2 + k_{eddy} f^2 B_{max}^2 + k_{excess} f^{1.5} B_{max}^{1.5} \quad (67)$$

The values for the flux density were calculated through the sample, the values at the location of the probe, for the example 150 mm ID, 25 mm wide ring in Fig. 121 these would be at coordinates (0,100) to (0,75) and compare to the measured results. This is shown in Section 5.2.2.

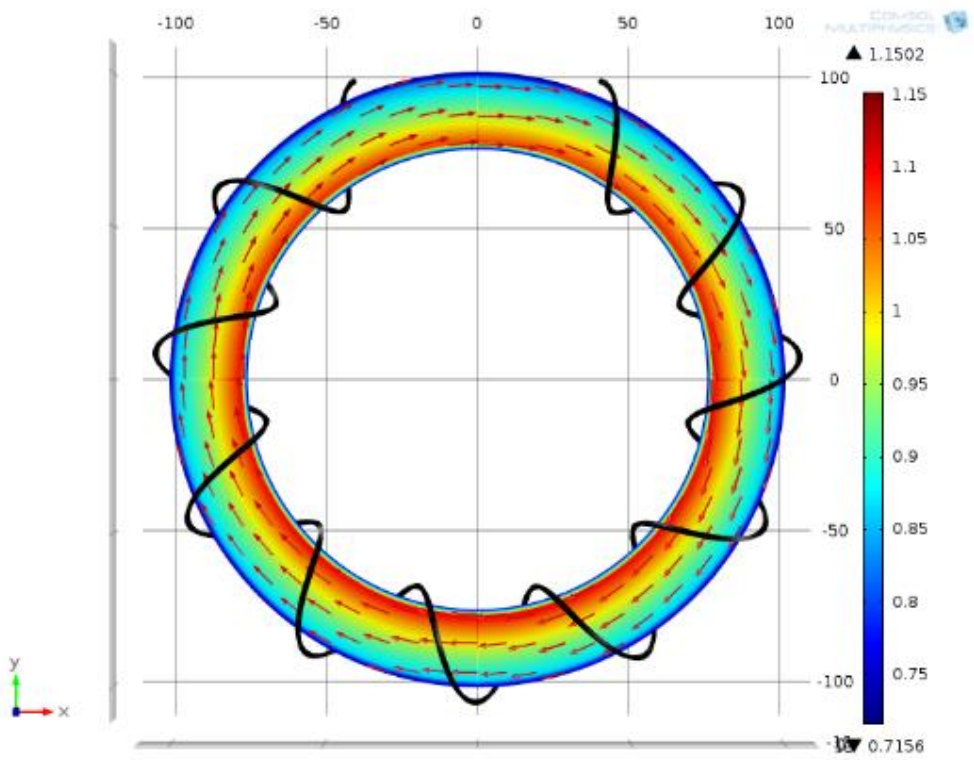

Figure 121 – Plan view (XY plane) of M250, 150 mm ring simulation showing the distribution of flux throughout the sample.

5.2. RESULTS

5.2.1. Model A – Discreet Permeability Model (DPM)

Fig. 122 to 125 show a comparison between the predicted and measured power loss for both grades at a range of flux densities and frequencies. The results show that power loss increases slightly with decreasing width until widths of approximately 10 mm. For narrower samples, of the order of 5 mm, the increase in power loss is more pronounced.

The measured values are indicated with blue markers; diamonds for 1.0 T, squares for 1.3 T, triangles for 1.5 T, circles for 1.7 T and connected with dashed lines. The predicted values are displayed as a solid red line, with 5 % error bars.

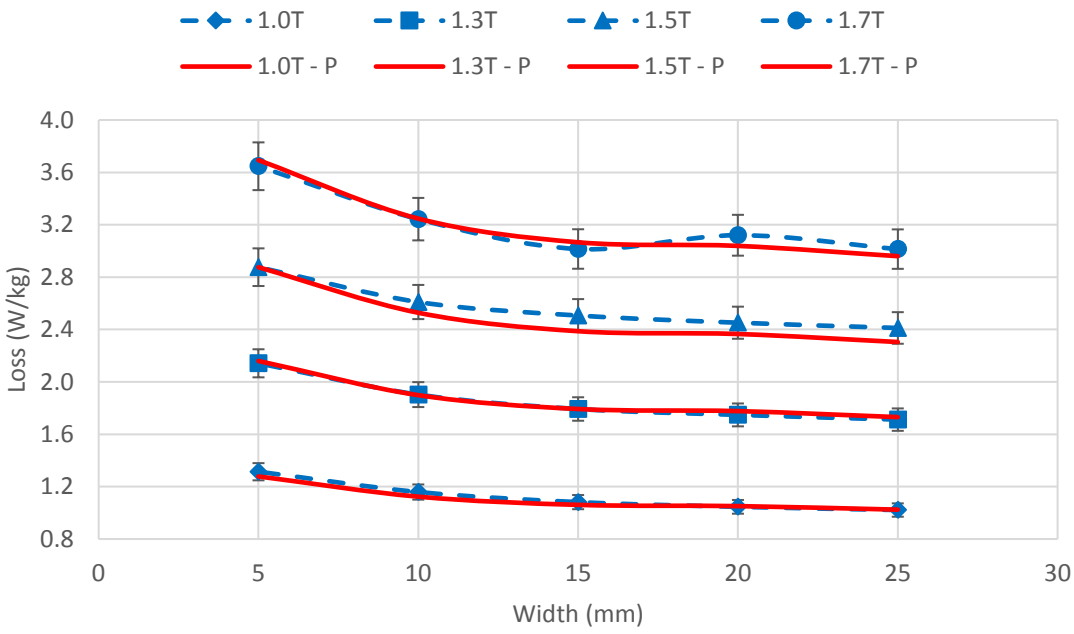

Figure 122 – Comparison between the predicted and measured results for M250-35A rings at 50 Hz and 1.0, 1.3, 1.5 and 1.7 T and for widths 5 to 25 mm

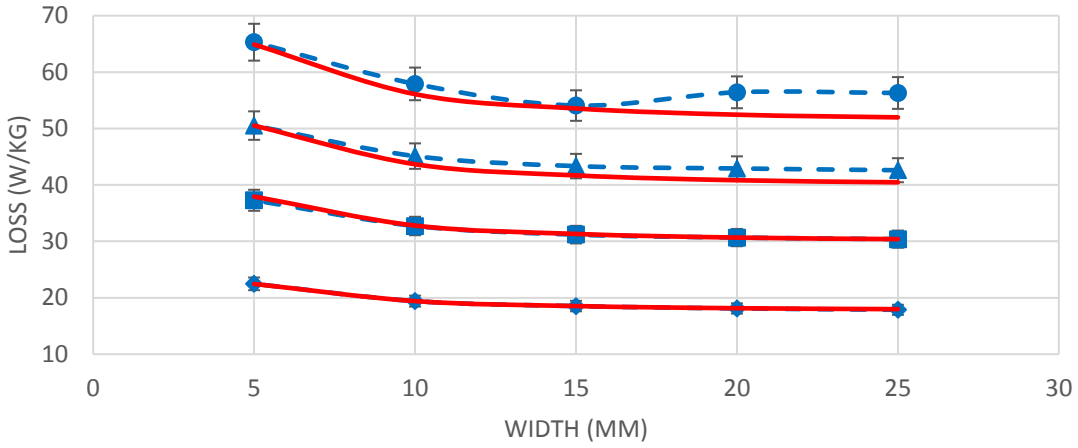

Figure 123 – Comparison between the predicted and measured results for M250-35A rings at 400 Hz and 1.0, 1.3, 1.5 and 1.7 T and for widths 5 to 25 mm

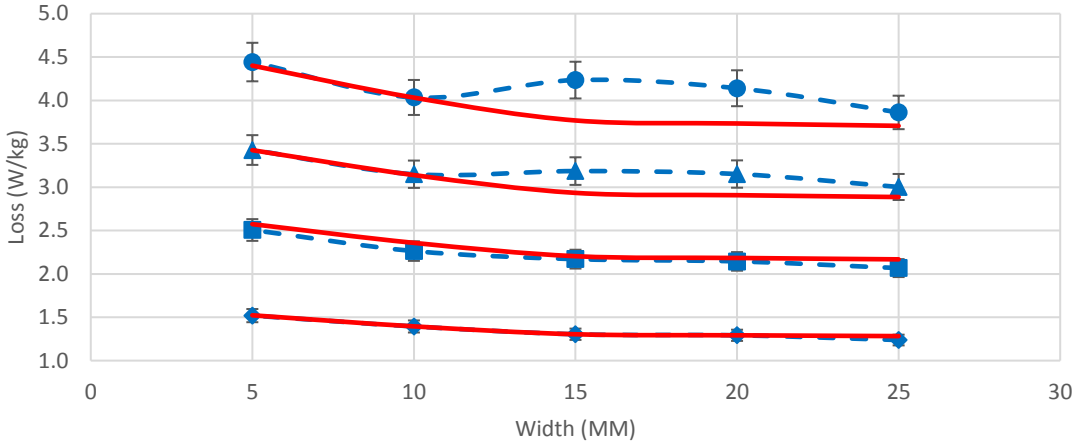

Figure 124 – Comparison between the predicted and measured results for M330-35A rings at 50 Hz and 1.0, 1.3, 1.5 and 1.7 T and for widths 5 to 25 mm

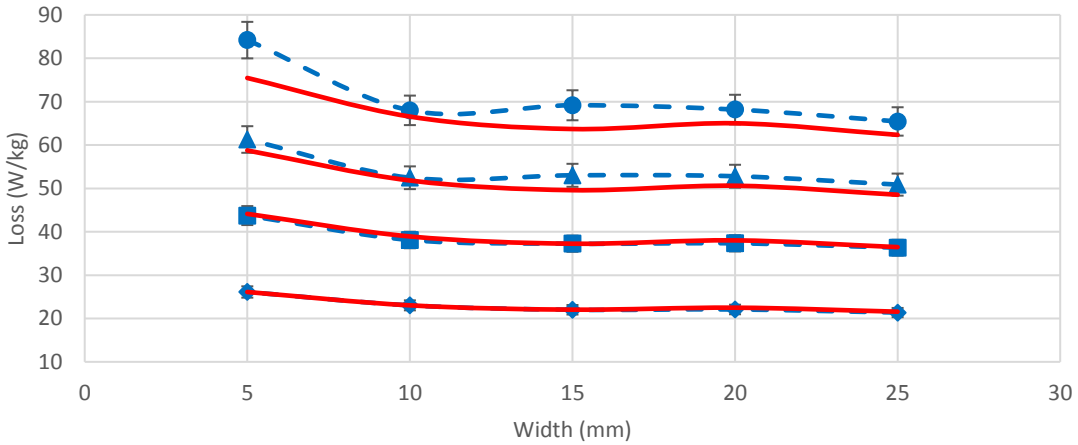

Figure 125 – Comparison between the predicted and measured results for M330-35A rings at 400 Hz and 1.0, 1.3, 1.5 and 1.7 T and for widths 5 to 25 mm

The calculated degradation depth, *d, was* obtained by optimising (61) to produce the lowest cumulative error averaged over the different frequencies.

The mean value and standard deviation of *d* at different frequencies are given in Table 31. Assuming the stress is distributed equally between the two edges this results in the damaged region extending 0.301 mm and 0.323 mm into the M250-35A and M330-35A samples respectively.

ID (mm)	d_{M250} (3.2% Si)	Std	d_{M330} (2.4% Si)	Std
150	0.603	0.019	0.639	0.011
160	0.606	0.023	0.644	0.009
170	0.602	0.023	0.642	0.011
180	0.599	0.032	0.648	0.019
190	0.602	0.057	0.657	0.030
Average	0.602	0.029 (4.8 %)	0.646	0.011 (1.7 %)

Table 31: Damaged area total length, d averaged over measured flux densities for different diameters and grades of NOES

If one assumes that the cutting force applied is constant and the stress is proportional to the length of the cut edge, there would exist a larger damaged region at the inner edge, summarised in Table 32.

ID (mm)	d (mm)	d_{ID} (mm)	d_{OD} (mm)
M250-35A	0.602	0.326	0.281
M330-35A	0.646	0.352	0.308

Table 32: Damaged area length for ID and OD edge as a ratio of cut edge lengths

The values for k_u at different frequencies are shown for the M250-35A rings and the M330-35A rings in Fig. 126 and 127 respectively.

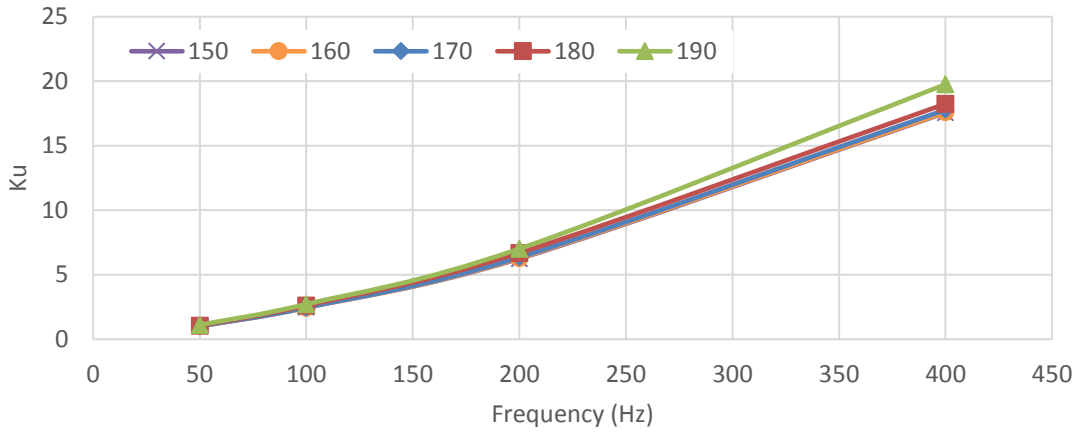

Figure 126 - k_u for the different ID rings with frequency for grade M250-35A. Legend refers to ID the OD is a constant 200 mm for all samples i.e. 150 is the 150 mm ID, 25mm wide sample

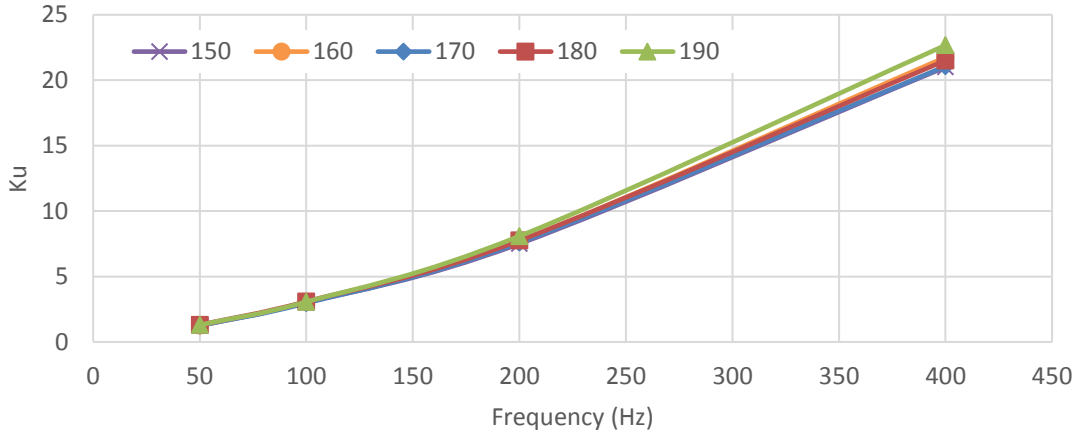

Figure 127 - k_u for the different ID rings with frequency for grade M330-35A. Legend refers to ID the OD is a constant 200 mm for all samples i.e. 150 is the 150 mm ID, 25mm wide sample

The average values for k_u are shown in Fig 128. This is approximately proportional to the frequency raised to the power 1.36 to within 5% up to 400Hz.

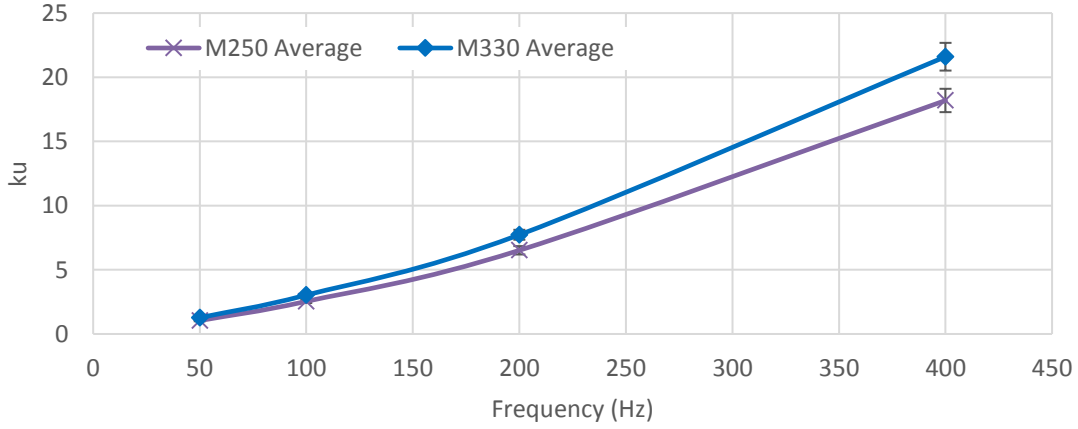

Figure 128 – k_u averaged over the different diameters with frequency for M330-35A($k_u \approx 0.0046f^{1.36}$) and M250-35A ($k_u \approx 0.0059f^{1.36}$) Error bars 5%

It is shown in Fig. 129 and 130 that there is a linear relationship between the k_u parameter and the area of the cut face per unit mass.

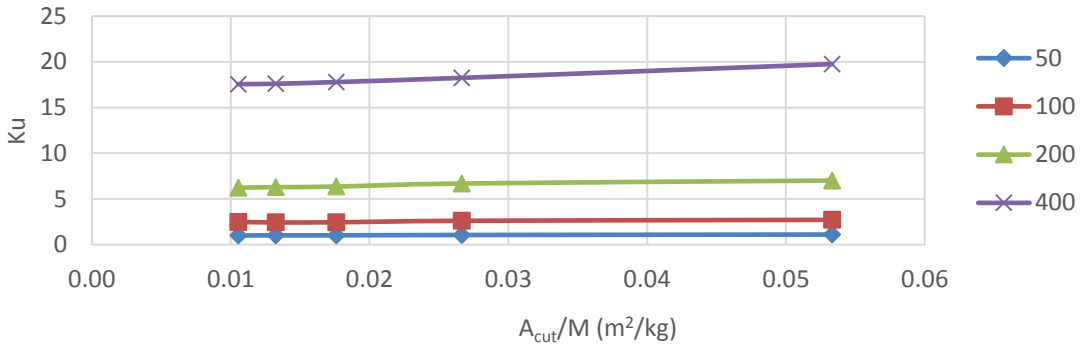

Figure 129 – k_u as a function of cut area per unit mass for the M250-35A sample at frequencies 50Hz (bottom), 100 Hz, 200 Hz and 400 Hz (top)

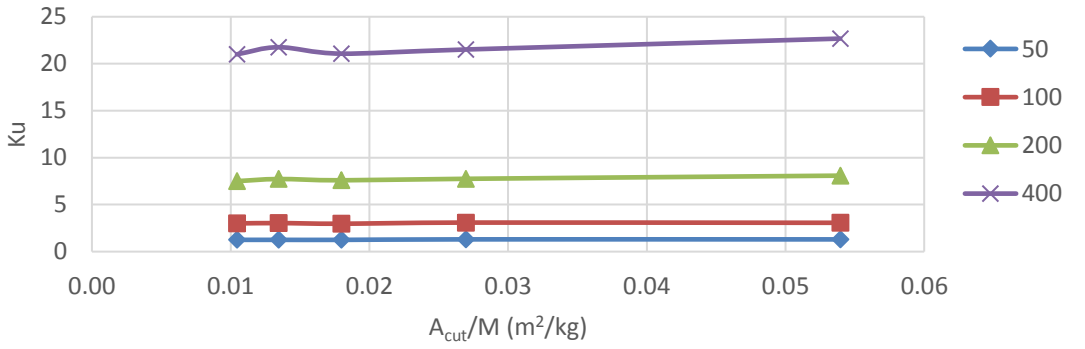

Figure 130 – k_u as a function of cut area per unit mass for the M330-35A sample at frequencies 50Hz (bottom), 100 Hz, 200 Hz and 400 Hz (top)

5.2.2. Model B - Comparison of FEM and Measured Data

Fig. 131 to 138 compare the results of the FEM models performed using the variable permeability method in Comsol with the mean average of the three locations measured. The input for the bulk permeability was obtained from bulk measurements of the different rings at the relevant flux density and frequency. Power loss predictions based on the statistical loss separation model outlined in the previous chapter, use coefficients derived from the same bulk measurements which are discussed in Section 5.3.1.1. The input current was selected to produce a secondary flux density equal to the measurement point.

M250-35A, 150 mm ID, 1.0 T, 400 Hz

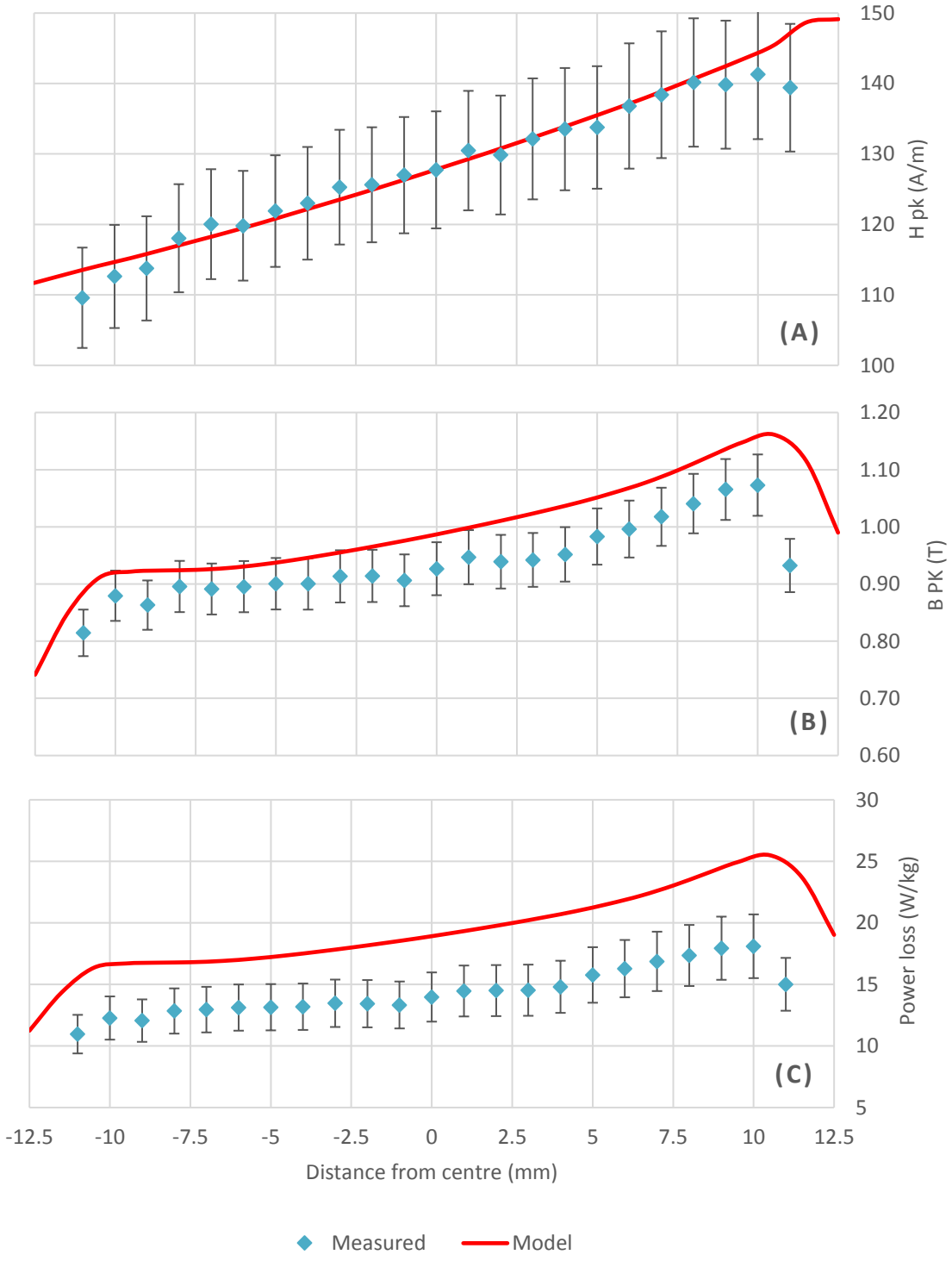

Figure 131 - Local measurements of (a) H peak, (b) B peak, (c) Power loss for M250-35A, 150 mm ID sample at 1.0 T and 400 Hz negative values are towards the OD and positive values towards the ID

M250-35A, 150 mm ID, 1.3 T, 400 Hz

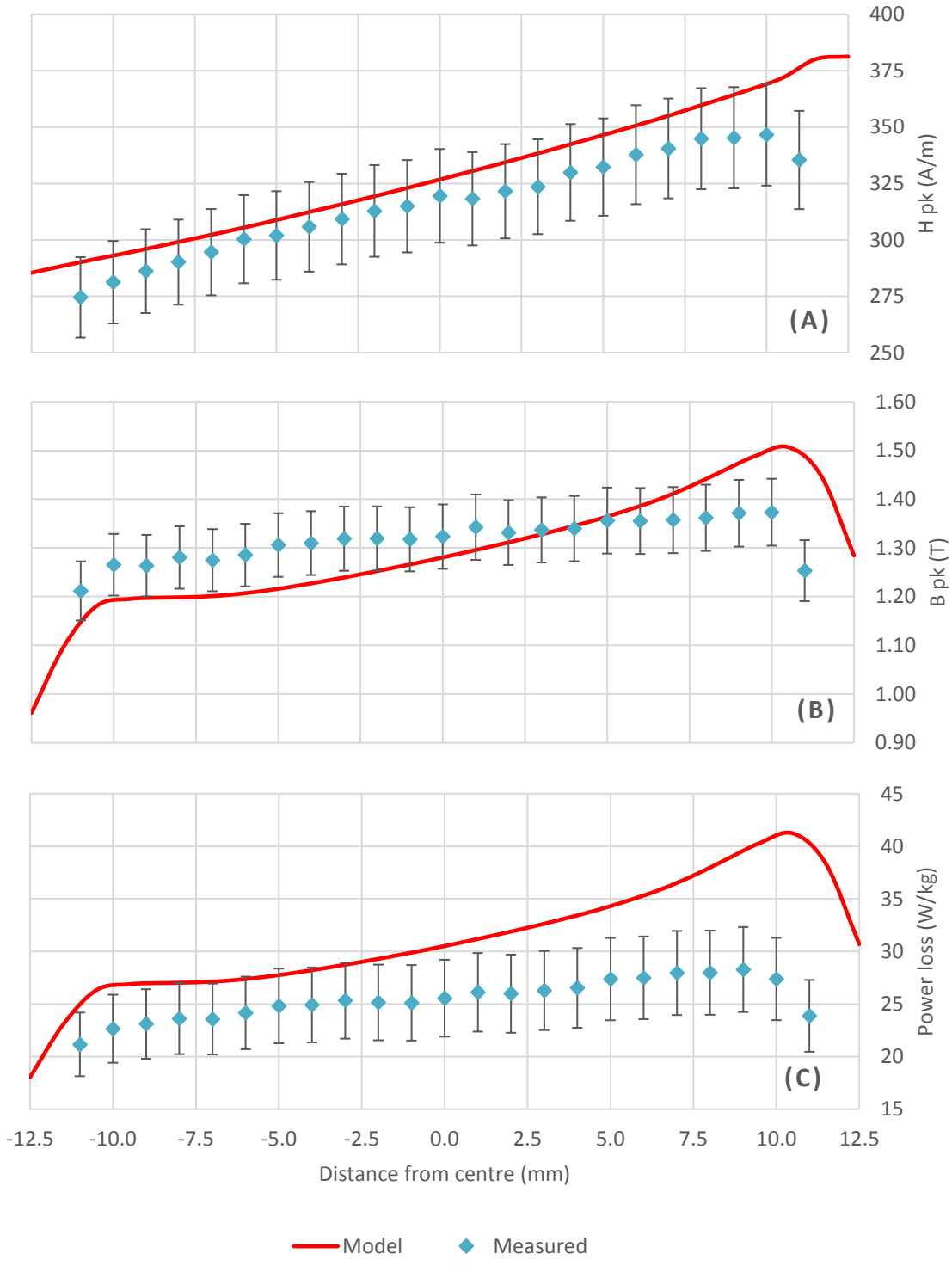

Figure 132 - Local measurements of (a) H peak, (b) B peak, (c) Power loss for M250-35A, 150 mm ID sample at 1.3 T and 400 Hz negative values are towards the OD and positive values towards the ID

M250-35A, 180 mm ID, 1.0 T, 400 Hz

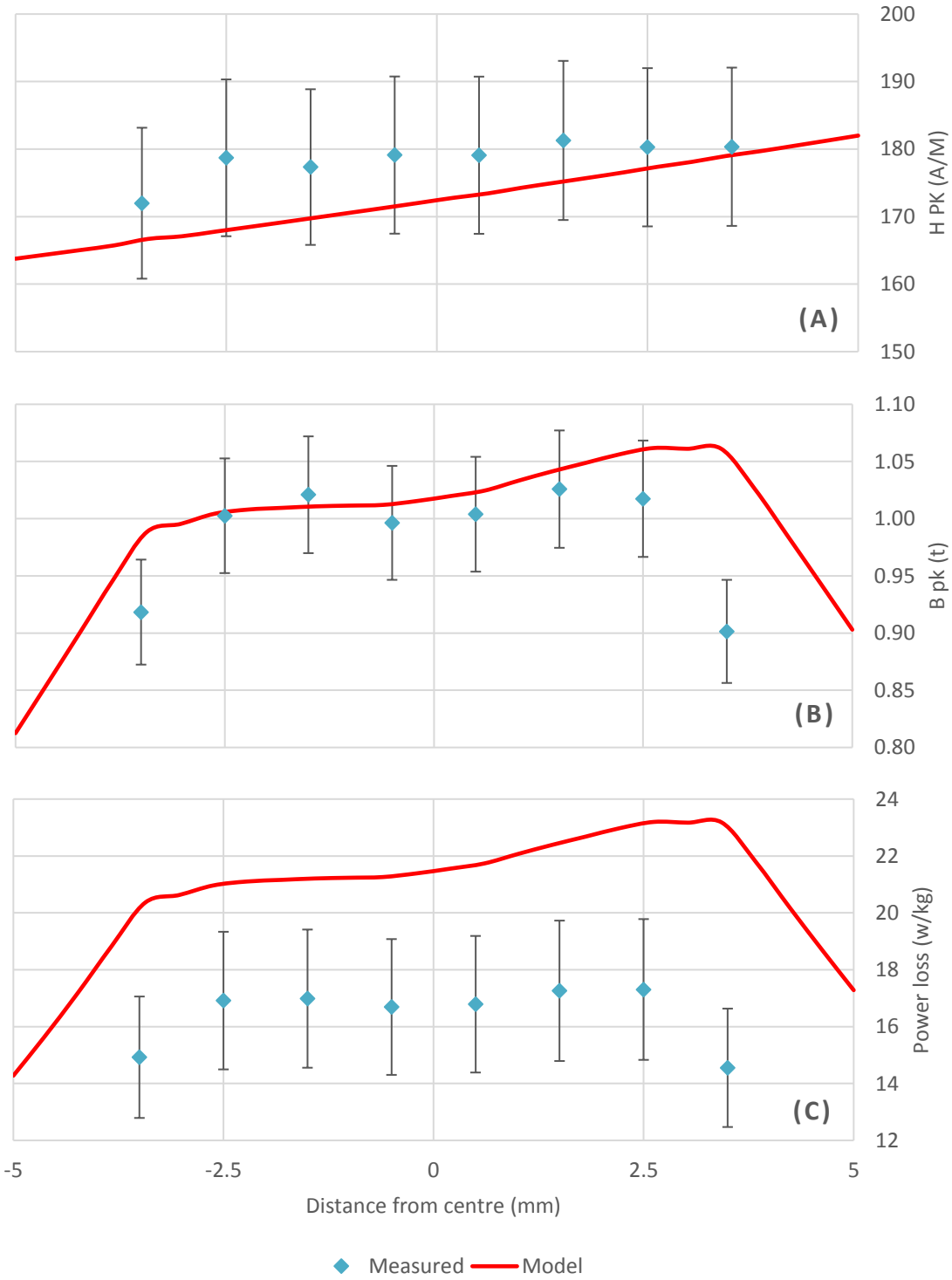

Figure 133 - Local measurements of (a) H peak, (b) B peak, (c) Power loss for M250-35A, 180 mm ID sample at 1.0 T and 400 Hz negative values are towards the OD and positive values towards the ID

M250-35A, 180 mm ID, 1.3 T, 400 Hz

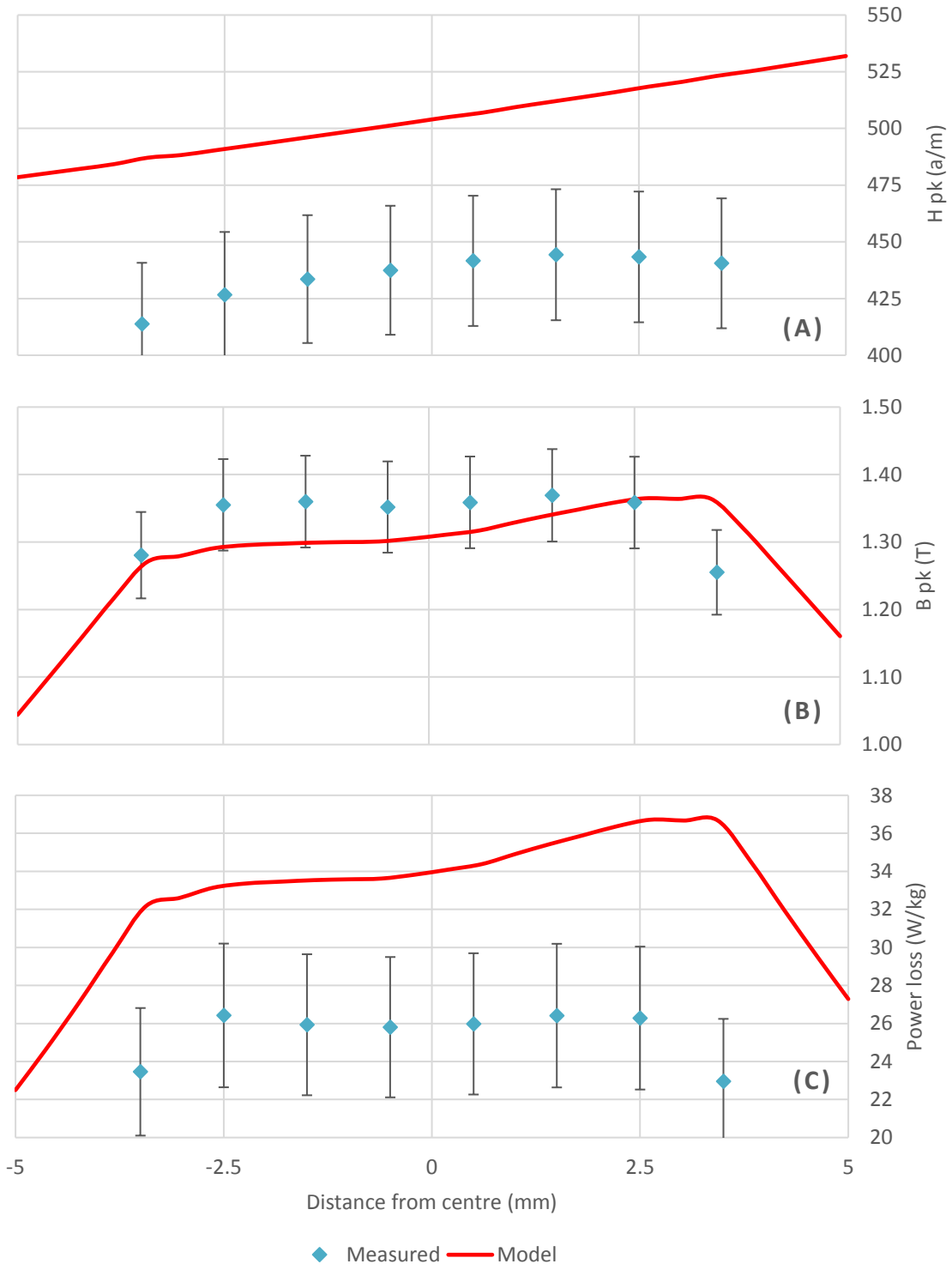

Figure 134 - Local measurements of (a) H peak, (b) B peak, (c) Power loss for M250-35A, 180 mm ID sample at 1.3 T and 400 Hz negative values are towards the OD and positive values towards the ID

M330-35A, 150 mm ID, 1.0 T, 400 Hz

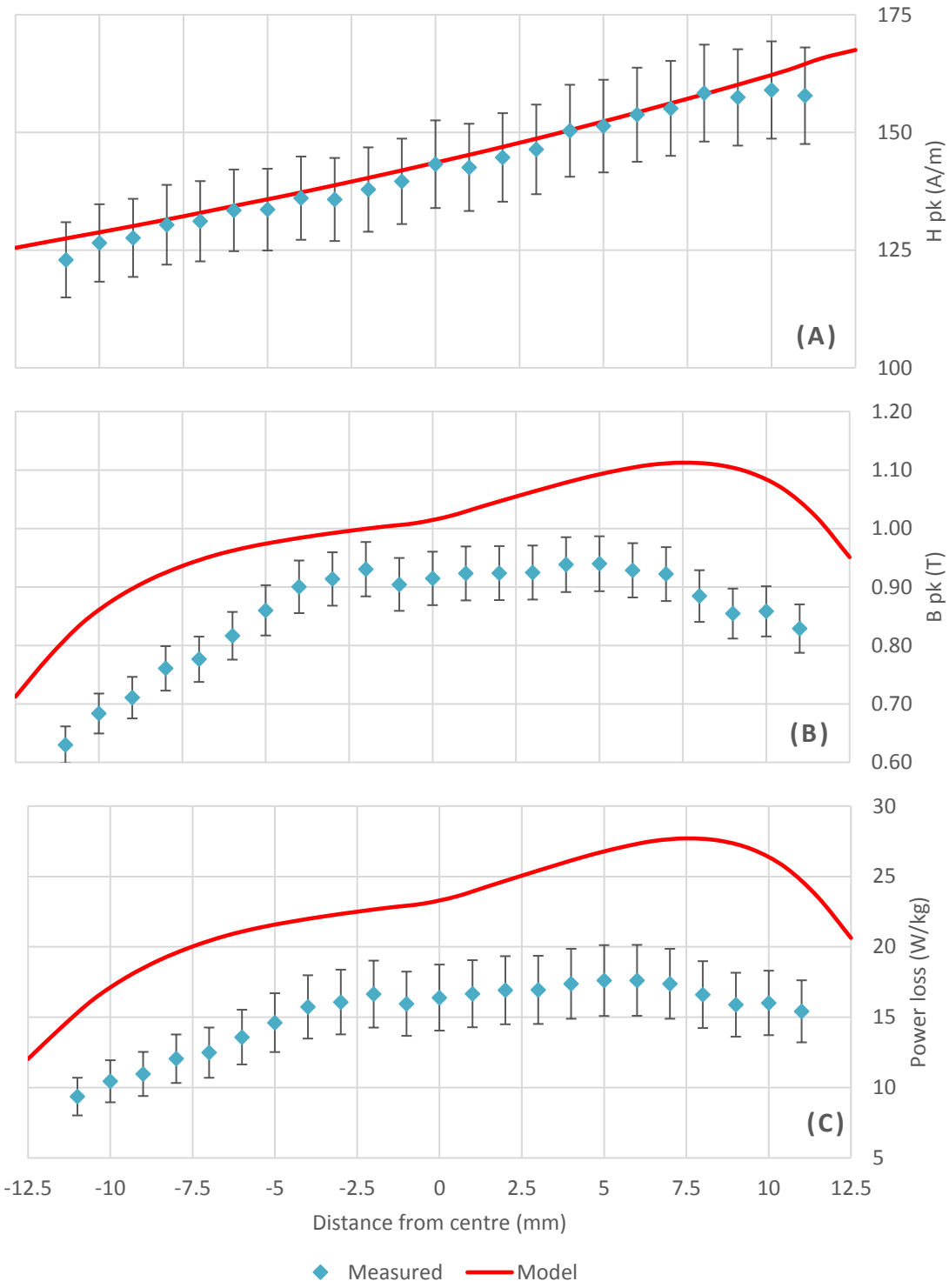

Figure 135 - Local measurements of (a) H peak, (b) B peak, (c) Power loss for M330-35A, 150 mm ID sample at 1.0 T and 400 Hz negative values are towards the OD and positive values towards the ID

M330-35A, 150 mm ID, 1.3 T, 400 Hz

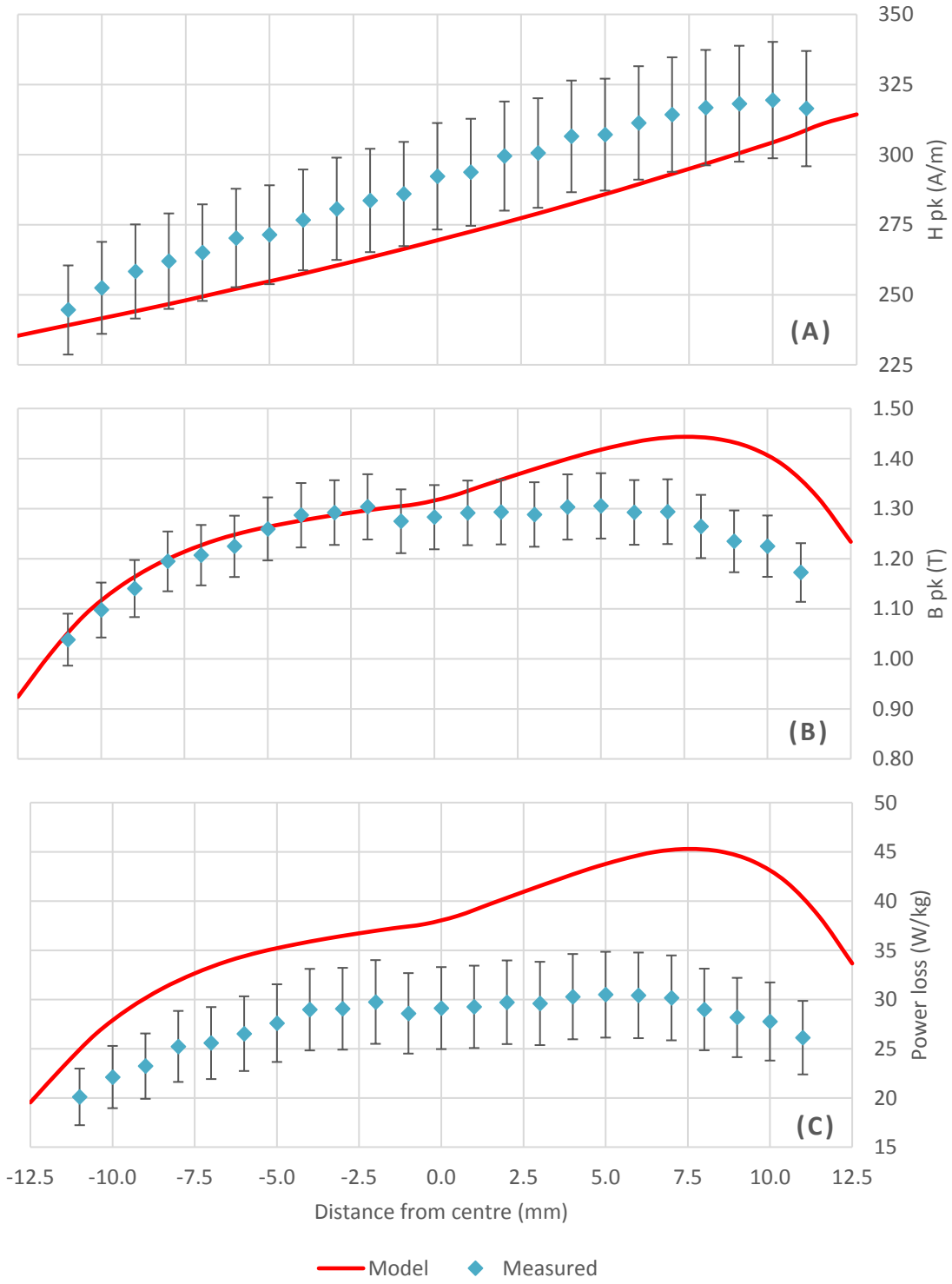

Figure 136 - Local measurements of (a) H peak, (b) B peak, (c) Power loss for M330-35A, 150 mm ID sample at 1.3 T and 400 Hz negative values are towards the OD and positive values towards the ID

M330-35A, 180 mm ID, 1.0 T, 400 Hz

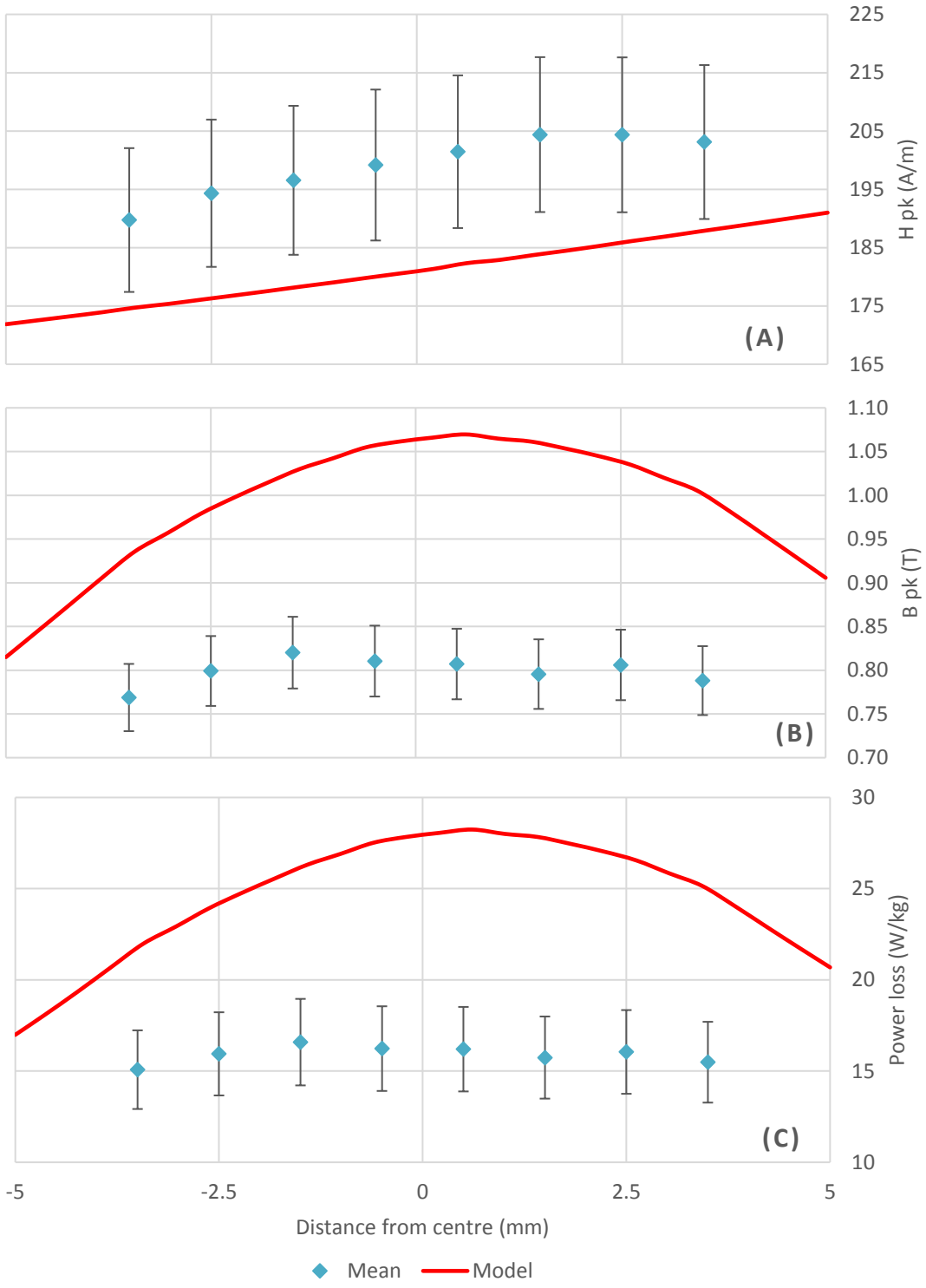

Figure 137 - Local measurements of (a) H peak, (b) B peak, (c) Power loss for M330-35A, 150 mm ID sample at 1.3 T and 400 Hz negative values are towards the OD and positive values towards the ID

M330-35A, 180 mm ID, 1.3 T, 400 Hz

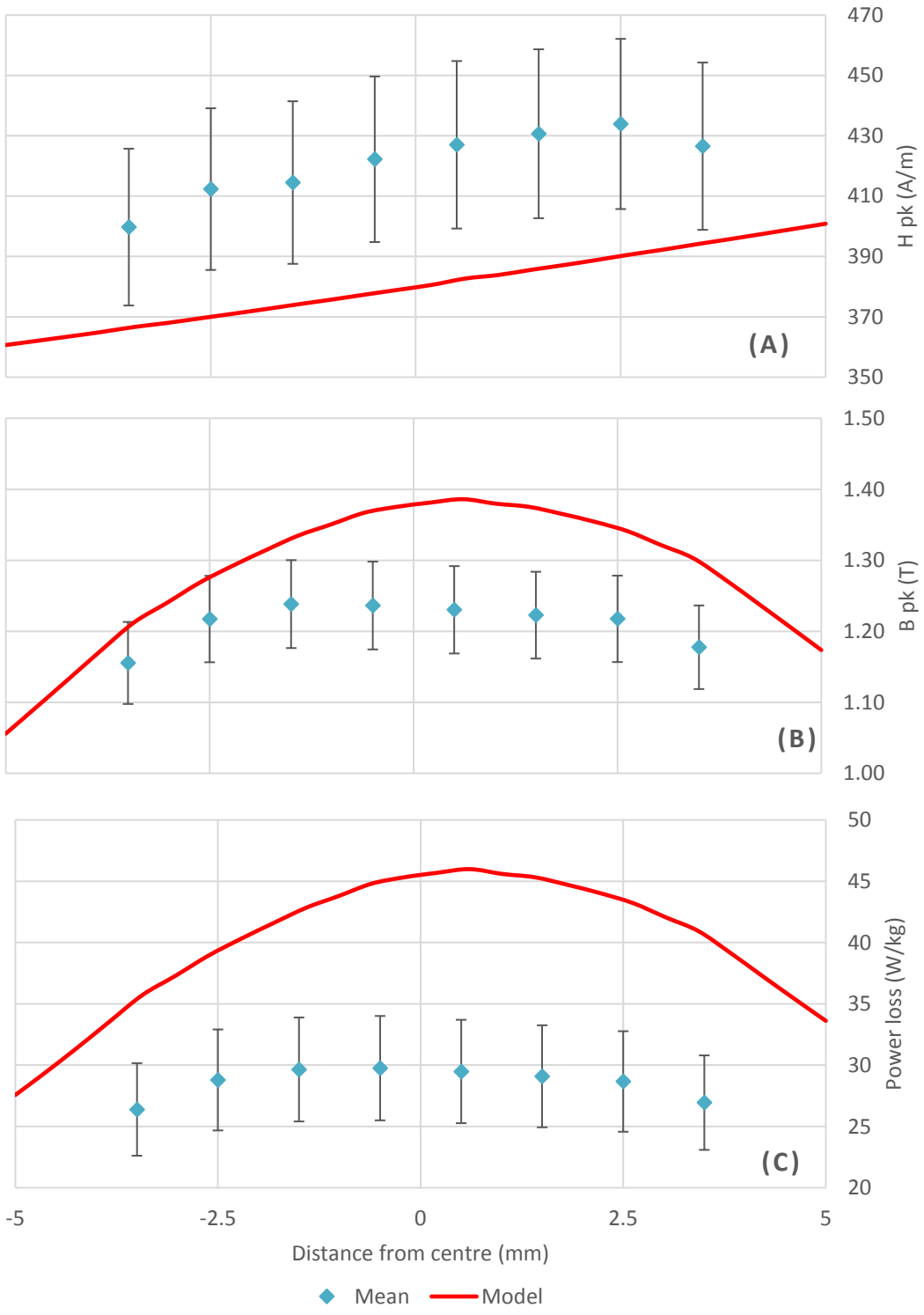

Figure 138 - Local measurements of (a) H peak, (b) B peak, (c) Power loss for M330-35A, 150 mm ID sample at 1.3 T and 400 Hz negative values are towards the OD and positive values towards the ID

5.3. DISCUSSION

5.3.1. Model A – Discreet Permeability Model (DPM)

The results show that the power loss increases slightly with decreases in the width until widths of approximately 10 mm. For samples narrower than this, the increase in power loss is more pronounced; this could be due to the stress fields and increased dislocation density generated by each cut edge starting to overlap in the centre of the sample.

The damaged width increases slightly as the sample width decreases with a larger increase evident for the 190 mm M330-35A samples. This is not unexpected. Although the damaged width being caused by shear stresses during the punching process is independent of frequency, it would play a larger role in the area available for the flux at high frequencies. This may be what is indicated here. This would imply that the assumption that the flux only travels through the undamaged region would only be valid where w>>d.

Revisiting (61) we can amend it based on a numerical analysis of the data. The square of the ratio of the total width to undamaged width is approximated as a function of the total width, *w*. The parameter k_u is best described as a function of frequency, the power to which the frequency is raised is consistent for both samples. The constants can be combined to produce a single material dependent property, K. An approximation for the power loss up to a frequency of 400 Hz with an average error of 6.23 % is given in (68)

$$P_w \approx K w^{-0.15} f^{1.36} B_w^2$$
$$K = \begin{cases} 7.09 \times 10^{-3}, & M250 \\ 9.23 \times 10^{-3}, & M330 \end{cases} \quad for\ f \leq 400\ Hz \tag{68}$$

For higher frequencies above 400 Hz, the power loss is best described using (69),

which has an average error of 6.69 %

$$P_w \approx Kw^{-0.15} f^{1.54} B_w^2$$
$$K = \begin{cases} 3.30 \times 10^{-3}, & M250 \\ 3.96 \times 10^{-3}, & M330 \end{cases} \quad for\ f > 400Hz \tag{69}$$

The M330 has less deviation from the mean compared to the M250 sample with both showing increased deviation as the sample width decreased with a noticeable jump in both cases for the 190 mm ID rings. There is a consistency across the frequency range.

The damaged widths for the M330 samples are on average 6.75% greater than their respective M250 samples. This can be explained by increased plastic deformation in the M330 sample The higher Si content of the M250 grade and resulting increase in point dislocations act as hardening agents which disrupt the movement of the line dislocations through the material, increasing its hardness, reducing the amount of plastic deformation caused and resulting in a smaller damaged width.

5.3.1.1. Loss Separation

The power loss was analysed and separated into the three components; hysteresis, eddy and excess described in Section 2.3.4 with the coefficients determined using the following method.

Firstly, the power loss divided by the frequency was plotted against the square root of the frequency for both grades and all IDs. Curve fitting, shown in Fig. 139 was used to find the coefficients *a*,*b* and *c* of the polynomial that had the best fit to the data points, where (70) is the general form. The coefficients were calculated for the different grades, widths and flux densities using (71) where α = 2.

$$\frac{P}{f} = af + bf^{0.5} + c \tag{70}$$

$$k_{hyst} = \frac{c}{B_{max}^{\propto}}, \qquad k_{eddy} = \frac{a}{B_{max}^{\propto}}, \qquad k_{excess} = \frac{b}{B_{max}^{1.5}} \tag{71}$$

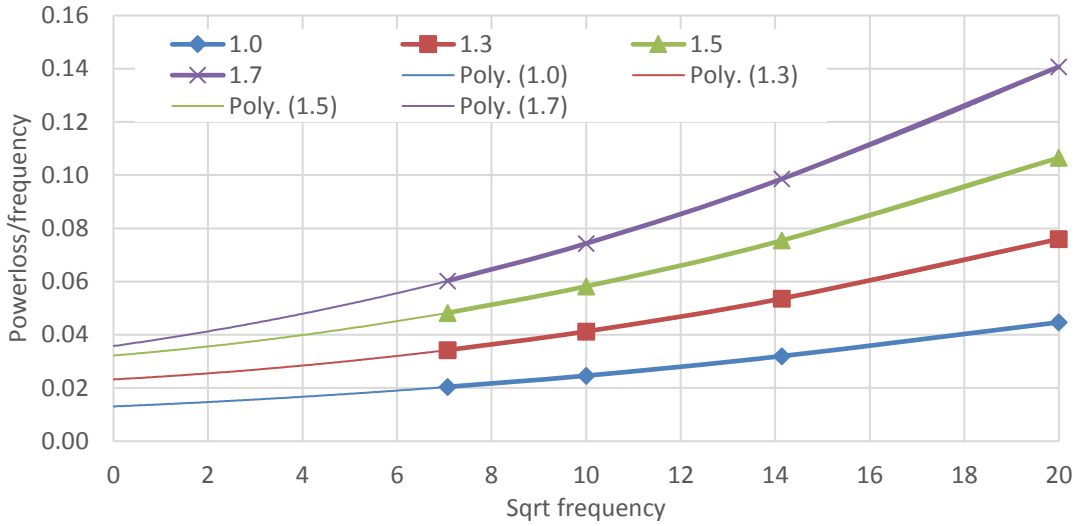

Figure 139 – Power loss/frequency against the square root of the frequency for the 150 mm ID, M250-35A rings for flux densities 1.0, 1.3, 1.5 and 1.7 T used for determination of loss separation coefficients.

Fig 140 to 145 show the calculated values for the hysteresis, eddy and excess loss coefficients for both the M250-35A and M330-35A samples.

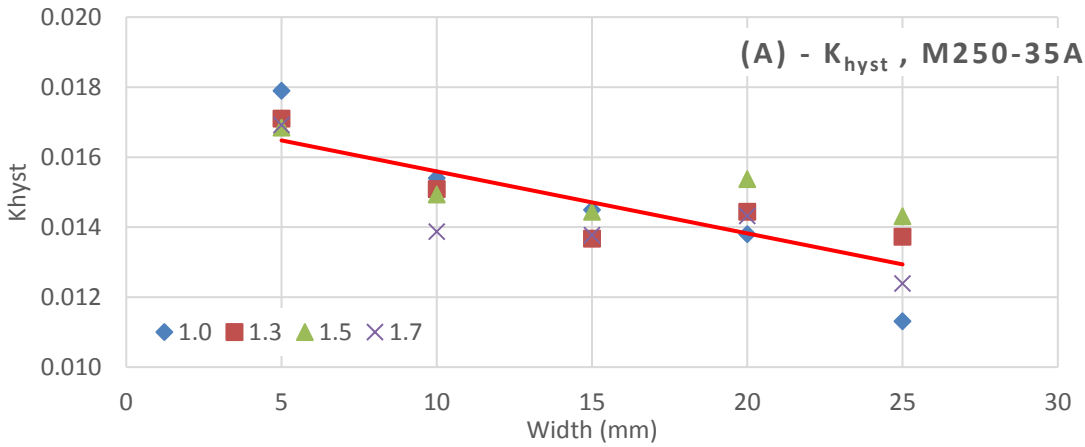

Figure 140 – Hysteresis loss coefficient, k_{hyst} for M250-35A sample for different widths and at flux densities 1.0, 1.3, 1.5, 1.7 T with a line of best fit.

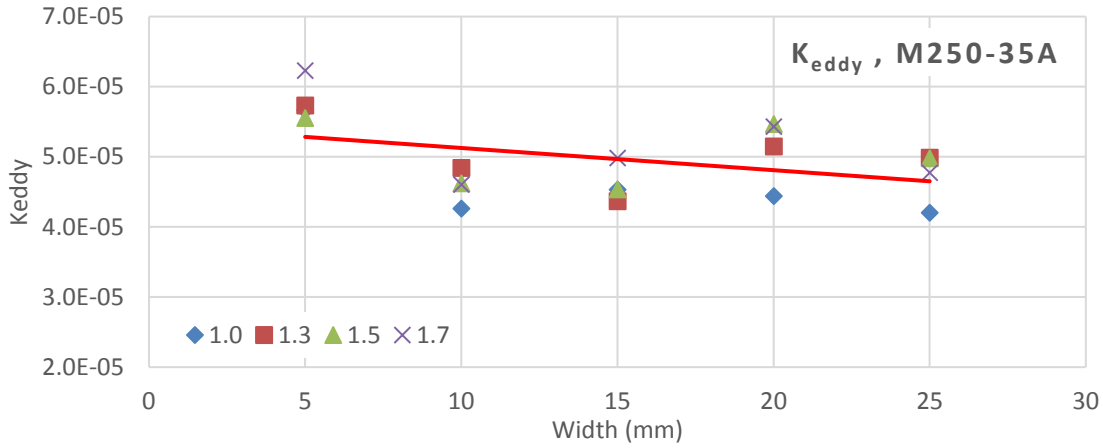

Figure 141 – Eddy current loss coefficient, k_{eddy} for M250-35A sample for different widths and at flux densities 1.0, 1.3, 1.5, 1.7 T with a line of best fit.

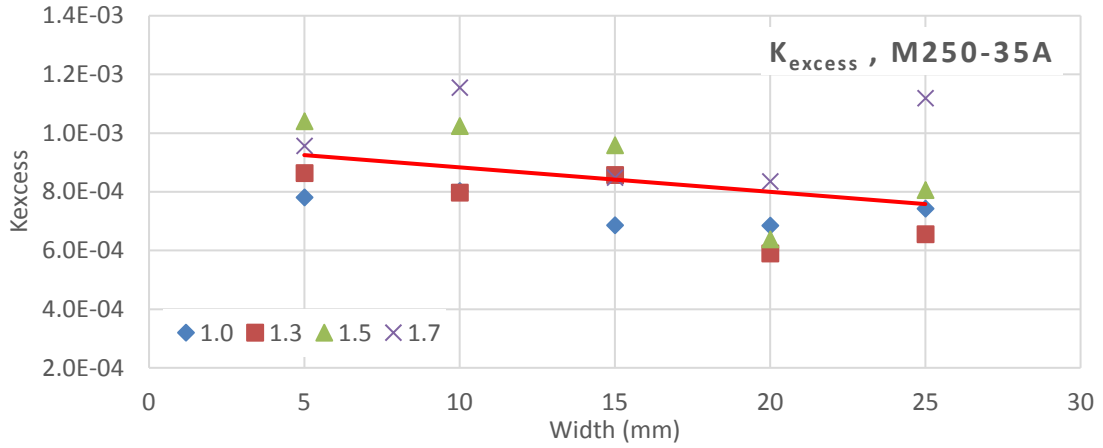

Figure 142 – Excess loss coefficient, k_{excess} for M250-35A sample for different widths and at flux densities 1.0, 1.3, 1.5, 1.7 T with a line of best fit.

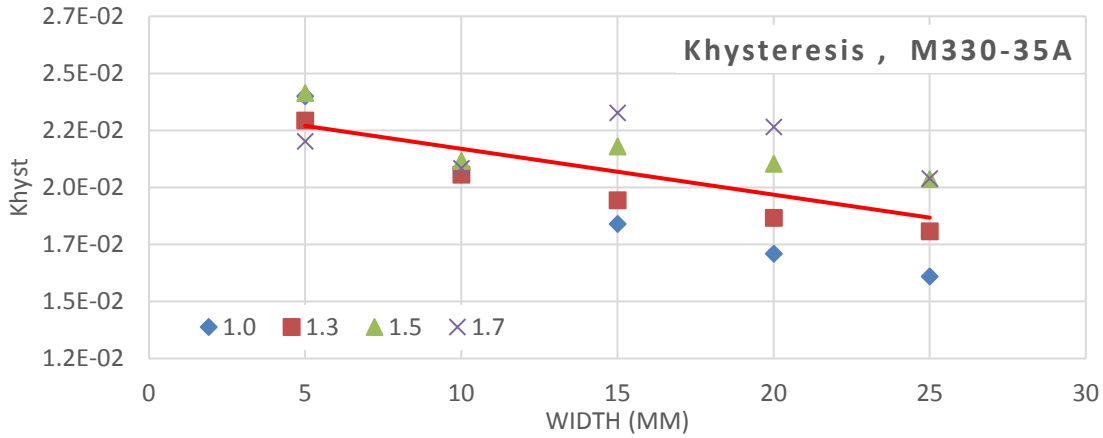

Figure 143 – Hysteresis loss coefficient, k_{hyst} for M330-35A sample for different widths and at flux densities 1.0, 1.3, 1.5, 1.7 T with a line of best fit.

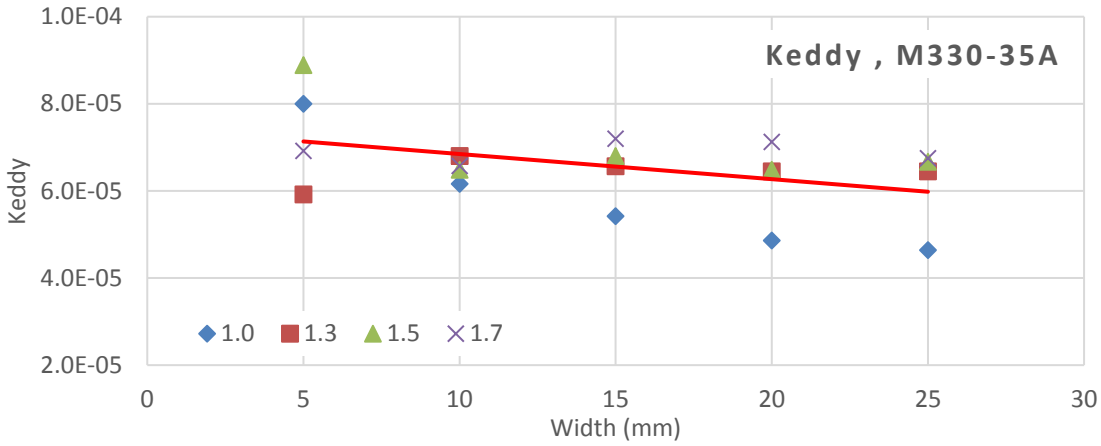

Figure 144 – Eddy current loss coefficient, k_{eddy} for M330-35A sample for different widths and at flux densities 1.0, 1.3, 1.5, 1.7 T with a line of best fit.

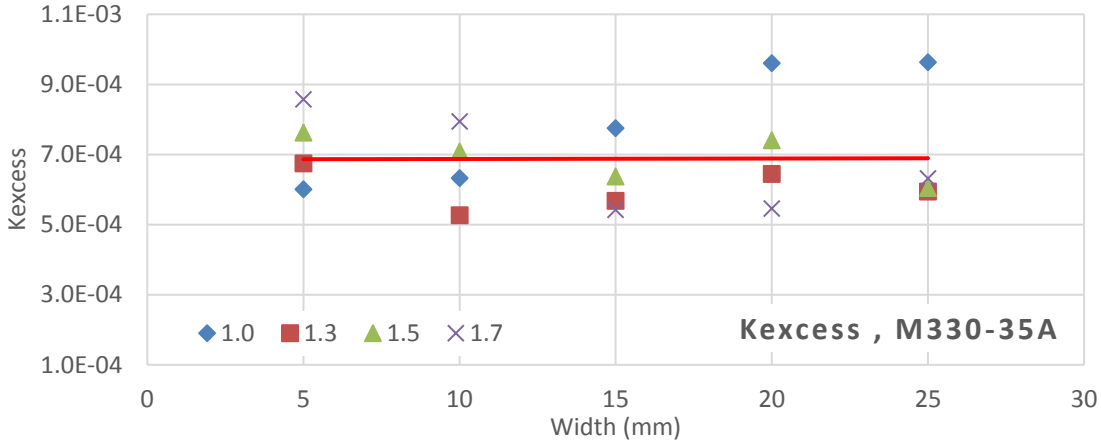

Figure 145 – Excess loss coefficient, k_{excess} for M330-35A sample for different widths and at flux densities 1.0, 1.3, 1.5, 1.7 T with a line of best fit.

These results indicate that there is no significant change in the eddy and excess loss as the width decreases. However, the hysteresis loss does increase as the samples get narrower. The rate of change of the hysteresis coefficient is approximately three orders of magnitude greater than other loss components. The rate of change per mm for the different loss coefficients is summarised in Table. 33.

	k_{hyst}	k_{eddy}	k_{excess}
M250-35A	2×10^{-4}	3×10^{-7}	8×10^{-6}
M330-35A	2×10^{-4}	6×10^{-7}	1×10^{-7}

Table 33: Magnitude of the gradient for the average power loss coefficients calculated from the different width rings samples for M250-35A and M330-35A samples

The assumption that the punching process mainly affects the hysteresis loss and as such the power loss can be described as being proportional to B^2 is validated at frequencies up to 400 Hz. While still bearing in mind that as the width reduces, any potential increase in the eddy current and excess loss coefficients, although minor at the frequencies considered, would become of interest at high frequencies as these components are proportional to higher powers of frequency.

The average loss coefficients for the different ID rings are shown in Table 34 and compared with coefficients calculated using an Epstein frame in Table 35. To simulate a ring the strips used in the Epstein frame were alternated between RD and TD. The percentage increases in the ring samples compared to the Epstein frame is shown in Table 36. As the hysteresis loss increases as the samples get narrower at the rate of 0.0002 per mm an increase of 0.003 or approximately 10 % would be expected between the 30 mm wide Epstein frame samples and the average ring width of 15 mm.

	k_{hyst}	k_{eddy}	k_{excess}
M250-35A	1.47×10^{-2}	4.97×10^{-5}	8.42×10^{-4}
M330-35A	2.02×10^{-2}	6.56×10^{-5}	6.88×10^{-4}

Table 34: Average power loss coefficients calculated from the different width rings samples

	k_{hyst}	k_{eddy}	k_{excess}
M250-35A	1.36×10^{-2}	4.89×10^{-5}	5.22×10^{-4}
M330-35A	1.78×10^{-2}	6.67×10^{-5}	4.84×10^{-4}

Table 35: Power loss coefficients calculated using Epstein frame and 12 RD and 12 TD strips

	k_{hyst}	k_{eddy}	k_{excess}
M250-35A	7 %	2 %	38 %
M330-35A	12 %	-2 %	30 %

Table 36: Percentage increase in power loss coefficients for ring samples compared to Epstein frame

5.3.1.2. Incorporation into FEM Software.

The accuracy of this model can be improved by using an increasing number of bands to more closely resemble the continuous nature of the permeability change. However, this would add increasing layers of complexity which would detract from the model's main advantage, its simplicity. Another advantage is that there is only one input, the material coefficient, which is calculated using the bulk measurement of rings stacks of different widths. This approach has the advantage of being more accessible, with the coefficients of new materials able to be obtained relatively easily.

However, there is no attempt made to describe or profile the power loss throughout the sample as it merely gives a prediction for the bulk power loss which is adjusted to consider the effect of punching. To do this a sample would be partitioned into segments which could be assigned a width between cut edges, power loss adjustments made for each segment and summed to produce a total for the bulk.

If bands of reduced permeability like those proposed in the DPM were to be incorporated into FEM software, the abrupt change of properties at the boundary between the different zones would require a fine mesh around the boundary area increasing the time needed to run the models. In addition, including reduced permeability regions in conjunction with adjusting the power loss to address the reduced width would effectively compensate for the effect of cutting twice, there either approach could be used but not both.

In conclusion, a simple model to predict power loss as a function of width is proposed. The power loss increases as sample width decreases. This is due to a higher dislocation density throughout the sample because of the damaged region occupying a larger proportion of the sample.

5.3.2. Model B – Variable Permeability Model (VPM)

The shape of the profiles predicted for the flux density accurately replicate the measured values with the two different shapes associated with the different grades accounted for with the change of only two of the four input parameters. This model is also able to reproduce the dip in the central part of the larger ID rings. There is an overestimation of the flux density especially for the M330-35A which is increased as the samples get narrower.

The bulk power loss was calculated as the volume integral over the whole sample and using the statistical loss separation formula (67) described in Section 5.1.2.1 using the coefficients in Section 5.3.1.1. Table 33. These are compared to the experimentally measured bulk values and shown in Fig 146 - 149. For ring samples, this is the average power loss taken at the three different locations. Average Epstein frame measurements are taken with 12 strips having the long axis parallel to the RD and 12 with the long axis parallel to in the TD.

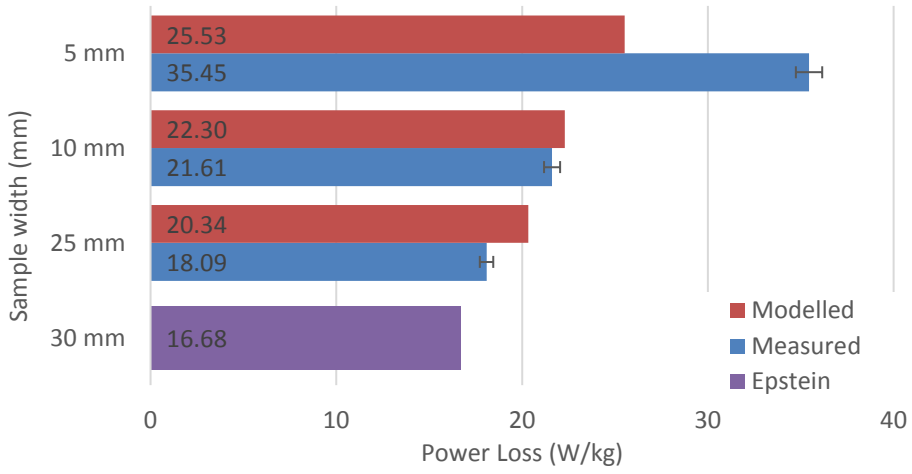

Figure 146 – Comparison of predicted bulk power loss with measured ring values and average Epstein frame measurements for M250-35A at various widths and at flux density 1.0 T and frequency 400 Hz.

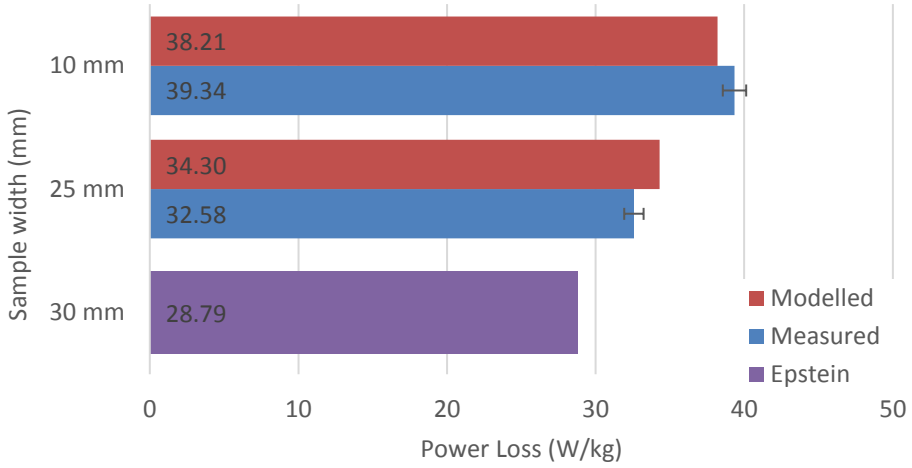

Figure 147 – Comparison of predicted bulk power loss with measured ring values and average Epstein frame measurements for M250-35A at various widths and at flux density 1.3 T and frequency 400 Hz.

In most cases, there is good agreement between the modelled and measured results with the model able to track the increase in power loss for the narrower samples which is something that Epstein frame measurements are unable to do.

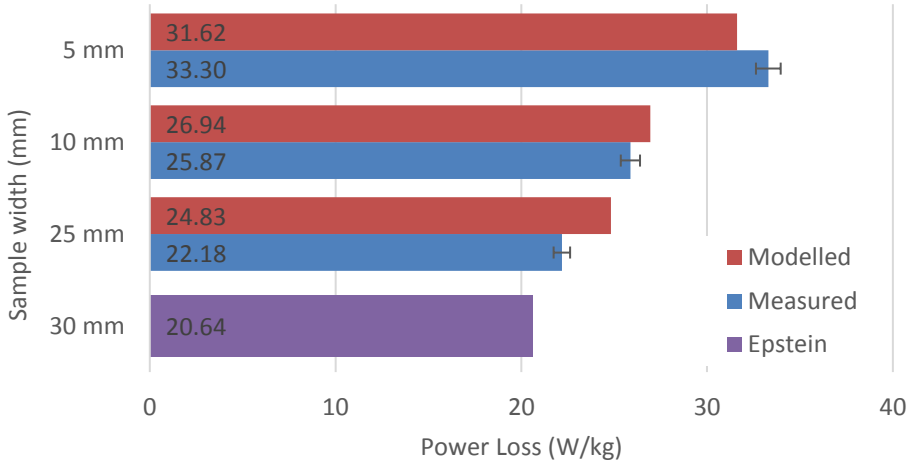

Figure 148 – Comparison of predicted bulk power loss with measured ring values and average Epstein frame measurements for M330-35A at various widths and at flux density 1.0 T and frequency 400 Hz.

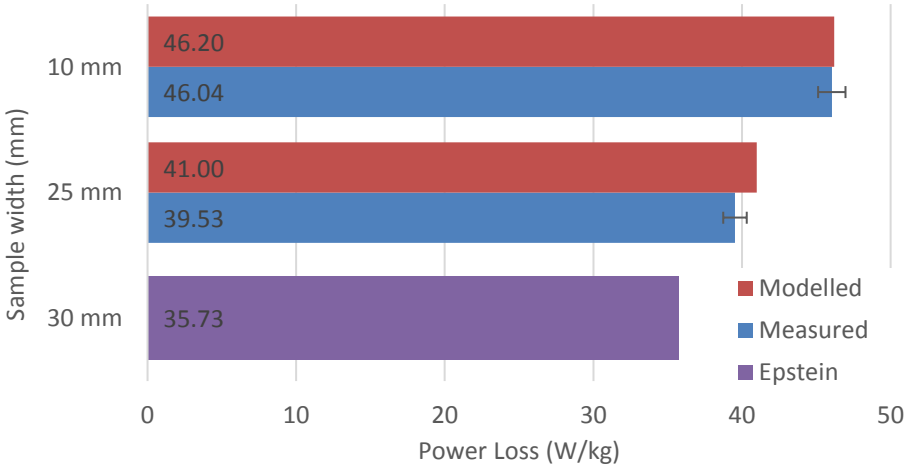

Figure 149 – Comparison of predicted bulk power loss with measured ring values and average Epstein frame measurements for M330-35A at various widths and at flux density 1.3 T and frequency 400 Hz.

The power loss coefficients used are the average for the ring samples. The result of this is that the hysteresis coefficient doesn't change with width. The consequence is that the hysteresis coefficient is too small for samples narrower than 10 – 15 mm resulting in an underestimation. Correspondingly the hysteresis coefficient is too large for samples wider than 10 – 15 mm leading to an overestimation. Modifying the hysteresis coefficient to be a function of the width improves the accuracy of the power loss estimate. Fig 150 and 151 show the comparison between the power loss predictions using the average ring and variable coefficients.

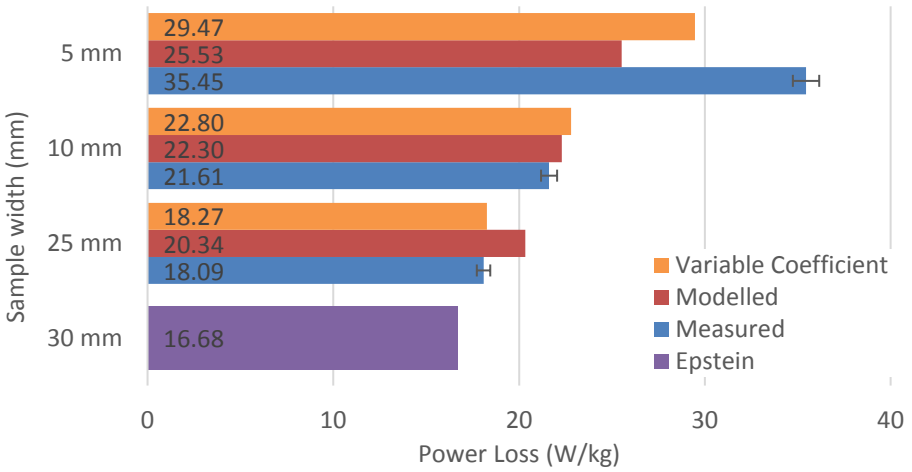

Figure 150 – Comparison of predicted bulk power loss using variable hysteresis coefficient with measured ring values and average Epstein frame measurements for M250-35A at various widths and at flux density 1.0 T and frequency 400 Hz.

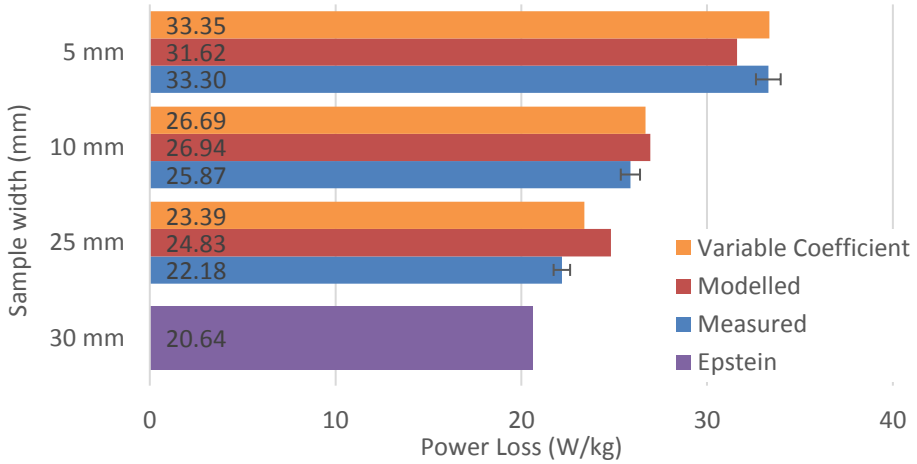

Figure 151 – Comparison of predicted bulk power loss using variable hysteresis coefficient with measured ring values and average Epstein frame measurements for M330-35A at various widths and at flux density 1.0 T and frequency 400 Hz.

There is improved accuracy for both the wider and narrower samples with the middle, 10 mm sample showing variable results but still within 5 % of the measured value. For the M250-35A sample the narrowest, 5 mm sample is still underestimated suggesting that a linear relationship between the width and power loss coefficient may not be the most appropriate. This is not the case for the M330-35A samples. However, the overestimates of the flux density for the narrower samples could account for this.

There is no anisotropy accounted for in the FEM model, the distribution of flux which can be seen in Fig 121. is cylindrically symmetric. The addition of an angular component would be necessary to vary the permeability with distance from an edge with angle to the RD.

We have, at present, a four-parameter model that can successfully describe the changes in the flux density throughout the sample. Any future investigations would involve correlating these parameters with material properties or manufacturing processes.

5.3.2.1. Incorporation into FEM Software.

The incorporation of a variable permeability model into existing FEM software could conceivably consist of several stages. Firstly it would be necessary to obtain the

parameters for additional grades of electrical steel, namely; α_1, α_2, β, γ, μ_{bulk} and the power loss coefficients. For this it would be necessary to obtain local measurements with the use of the system described in Chapter 4 from which these parameters can be calculated and a database or look up tables for the different grades produced. It would then be a case of selecting the appropriate material in the FEM package library and applying it to the model.

The use of rings to obtain these parameters was cumbersome as the winding of the rings had to be done for each sample and a bespoke die was necessary to punch the samples. The use of local measurements on strips was investigated as a possible alternative to using rings. A double yoke setup was used with a case designed for local measurements of strips, shown in Fig. 152.

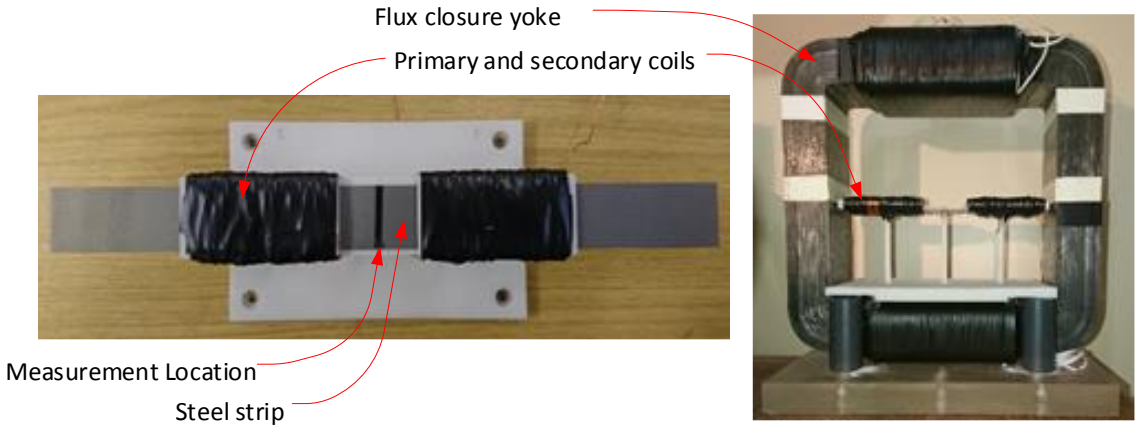

Figure 152 – Case (left) with probe access and double yoke system (right) constructed for testing of local properties of strip samples.

This reduced the measurement time considerably as strips of different widths could be cut on site and the primary winding did not have to be rewound for each sample. Further investigation is needed, however results appear promising that a strip set up could be used to obtain the necessary parameters.

To apply the VPM it would be necessary to designate the cut face of the material from which the permeability profile extended. This may present an issue for complex

geometries which will have coordinates which are different distances away from the cut edge and as such may not have a unique solution. Efforts should be made to ensure a continuous profile by appropriate selection of cut faces and simplification of the geometry by the user as necessary.

Modifying the power loss coefficients with width would require careful partitioning of the sample into segments. Each segment would have a predicted power loss which could then be summed to create an estimate for the sample. This would improve the bulk power loss estimates however it could create problems with discontinuities affecting local measurements for power loss especially at the boundary between segments.

In conclusion, a model to predict the flux density profile across a sample considering the effect of cutting is proposed. The parameters necessary for this model are obtained from local measurements. Future work could focus on correlating these parameters to material properties reducing the need for measurements. The power loss is calculated using a statistical loss separation method; the hysteresis loss is shown to increase with decreasing width with adjustments to the hysteresis power loss coefficient shown to improve predictions.

CHAPTER 6.

CONCLUSIONS

The local magnetic properties of rings of non-oriented electrical steel samples were investigated. The analysis of the magnetic properties observed in the region approaching the cut edge resulted in an improved understanding of lamination materials of electrical machines in a condition closer to their operational state. The three main conclusions which can be drawn from this research are as follows.

6.1. MAIN CONCLUSIONS

6.1.1. System Development and Validation

A measurement system was successfully developed and validated. Localised measurements of the magnetic field and magnetic flux density were successfully made using a probe consisting of a Hall effect sensor and a pair of needle tipped test probes. This system was able to accurately and repeatedly select locations on a sample and as a result, this new approach to precision measurement is capable of mapping the variation in the magnetic properties across an electrical steel sample.

6.1.2. Material Investigation

The profile of the magnetic properties was investigated and was found to be heavily influenced by the material properties, silicon content and grain size, magnetising conditions and orientation to the rolling direction. Two different grades of non-oriented electrical steel of five different widths and at three locations were tested; M250-25A with 3.2% Si and M330-25A which has 2.4% Si. Both samples displayed compressive strain of the order 0.1 at the edges, in response to punching. The propagation of residual stress into the interior of the samples varied between samples. Increasing the silicon content

hindered the progression of newly created dislocations into the interior of the sample resulting in a more pronounced degraded zone, with a sharp change in permeability extending over approximately 2.5 mm from the edge. Lowering the silicon content results in a more gradual decrease in permeability over a larger distance. Silicon content appears to be an important factor in determining the permeability profile at the cut edge.

Unlike other work that only examines the cut edges, looking at the entire sample width showed a permeability dip in the centre of the samples attributed to the changing nature of the residual stress

The mean average of localised needle probe and bulk measurements are in close agreement. The difficulty in producing stable measurement conditions limited the range of frequencies and flux densities over which measurements could be taken.

6.1.3. Development of Models Suitable for FEM Software

A model was proposed, which by defining the permeability as a function of the distance from the cut edge was able to accurately predict the shape of the flux density profile. This model produced good agreement with measurements conducted on ring laminations and therefore it is reasonable to suggest it would be applicable to more complex geometries. The power loss calculated using the localised flux density predictions were in reasonable agreement with measured values. This model is suitable for incorporation into FEM software and would aid electrical machine designers by improving on the existing ability to model the flux density in lamination, particularly in the region close to punched edges.

6.1.4. Summary

A measurement system was designed, constructed and validated which unlike other systems has the unique ability to rapidly measure complex geometries.

Two commonly used lamination materials produced using an industrial punching process were investigated. The profile was discovered to not always parabolic as previously thought and depends on material properties. A new physical theory was developed which can accurately reproduce these profiles.

A new predictive model for flux density and power loss that can accurately reproduce these different profiles was developed and validated using FEM software.

- This work can aid electric motor designers by improving the accuracy of their models. Material and manufacturing processes can be addressed at the design phase. By removing barriers and reducing prototyping this can streamline the process, increasing efficiency and reducing costs.
- Built designs can be rapidly tested with results used to feedback into and improve the model e.g. tying measured parameters to material properties.

6.2. FUTURE WORK

This investigation has identified the need for future research with the aim of improving the characterisation of the post-manufacturing magnetic properties of electrical steel. The desired outcome would be improvements in the overall efficiency of electrical machines through the selection and refinement of the core materials.

In the short to medium term, this entails analysis of different materials, with different cut edge characteristics and further refinement of the magnetising system to allow a wider range of flux densities and frequencies to be measured. Longer term this would enable the influences that manufacturing processes and operational conditions have on the magnetic properties to be incorporating into FEM models. The ability to not only select appropriate electrical steel grades but to refine the manufacturing processes to minimise magnetically deleterious effects will contribute to the increased efficiency of

the electrical machines which will be playing a fundamental role in an increasing electrified society.

This research demonstrates that the punching process and the negative effect on the magnetic properties which follows, are highly material dependent and propagate further from the cut edge than previously stated. The stress profile is influenced by silicon content and crystal orientation. This effect can be estimated and should be included in the modelling of cut non-oriented electrical steel which may be of benefit in the design of electrical machines.

The parameters necessary for the proposed model are obtained from local measurements. Work focusing on correlating these parameters to material properties and manufacturer provided data could reduce the need for measurements, increasing end user ease of use and expand the appeal and usability.

CHAPTER 7.

REFERENCES

7.1. REFERENCES

[1] J. M. D. Coey, *Magnetism and Magnetic Materials*: Cambridge University Press, 2010.

[2] D. Jiles, *Introduction to magnetism and magnetic materials*. London: Chapman and Hall, 1998.

[3] R. M. Bozorth, *Ferromagnetism*: Wiley, 1993.

[4] K. Günther, F. Bölling, and H. Huneus, "Detrimental effect of oxidation on magnetic properties of nonoriented electrical steel sheet," *Journal of Applied Physics,* vol. 64, pp. 5347-5349, 1988.

[5] D. S. Petrovič and M. Jenko, "A HRAES study of the morphology of non-metallic inclusions in non-oriented electrical steel containing Cu and Se," *Vacuum,* vol. 71, pp. 33-40, 2003/05/09/ 2003.

[6] B. D. Cullity, *Introduction to magnetic materials*: Addision-Wesley.

[7] R. Hilzinger and W. Rodewald, *Magnetic Materials*: Wiley, 2013.

[8] S. Somkun, A. J. Moses, P. I. Anderson, and P. Klimczyk, "Magnetostriction Anisotropy and Rotational Magnetostriction of a Nonoriented Electrical Steel," *IEEE Transactions on Magnetics,* vol. 46, pp. 302-305, 2010.

[9] K. Senda, M. Ishida, K. Sato, M. Komatsubara, and T. Yamaguchi, "Localized magnetic properties in grain-oriented electrical steel measured by needle probe method," *Electrical Engineering in Japan,* vol. 126, pp. 1-11, 1999.

[10] K. Senda, M. Kurosawa, M. Ishida, M. Komatsubara, and T. Yamaguchi, "Local magnetic properties in grain-oriented electrical steel measured by the modified needle probe method," *Journal of Magnetism and Magnetic Materials,* vol. 215–216, pp. 136-139, 6/2/ 2000.

[11] X. T. Xu, "Localised Variation of Magnetic Properties of Grain Oriented Electrical Steels," PhD, Cardiff University, 2014.

[12] C. P. Steinmetz, "On the Law of Hysteresis," *Transactions of the American Institute of Electrical Engineers,* vol. IX, pp. 1-64, 1892.

[13] G. Houze Jr, "Domain-Wall Motion in Grain-Oriented Silicon Steel in Cyclic

Magnetic Fields," *Journal of Applied Physics*, vol. 38, pp. 1089-1096, 1967.

[14] G. Bertotti, "General properties of power losses in soft ferromagnetic materials," *IEEE Transactions on Magnetics*, vol. 24, pp. 621-630, 1988.

[15] Cogent, "M250-35A Datasheet," ed, 2008.

[16] Cogent, "M330-35A Datasheet," ed, 2009.

[17] S. Somkun, "Magnetostriction and Magnetic Anisotropy in Non-oriented Electrical Steels and Stator Core Laminations," PhD Thesis, Cardiff University, 2010.

[18] K. Senda, A. Fujita, A. Honda, N. Kuroki, and M. Yagi, "Magnetic properties and domain structure of nonoriented electrical steel under stress," *Electrical Engineering in Japan*, vol. 182, pp. 10-18, 2013.

[19] L. Vandenbossche, S. Jacobs, D. Van Hoecke, and E. Attrazic, "Impact of mechanical stresses on the magnetic performance of non-oriented electrical steels and its relation to electric machine efficiency," in *Transportation Electrification Conference and Expo (ITEC), 2015 IEEE*, 2015, pp. 1-6.

[20] N. Leuning, S. Steentjes, M. Schulte, W. Bleck, and K. Hameyer, "Effect of elastic and plastic tensile mechanical loading on the magnetic properties of NGO electrical steel," *Journal of Magnetism and Magnetic Materials*, vol. 417, pp. 42-48, 2016/11/01/ 2016.

[21] Y. Oda, H. Toda, N. Shiga, S. Kasai, and T. Hiratani, "Effect of Si Content on Iron Loss of Electrical Steel Sheet Under Compressive Stress," *IEEE Transactions on Magnetics*, vol. 50, pp. 1-4, 2014.

[22] C. M. Burt, X. Piao, F. Gaudi, B. Busch, and N. Taufik, "Electric motor efficiency under variable frequencies and loads," *Journal of irrigation and drainage engineering*, vol. 134, pp. 129-136, 2008.

[23] Ş. Bayraktar and Y. Turgut, "Effects of different cutting methods for electrical steel sheets on performance of induction motors," *Proceedings of the Institution of Mechanical Engineers, Part B: Journal of Engineering Manufacture*, vol. 0, p. 0954405416666899.

[24] Cogent Power Ltd. (28/06/2017). Available: https://cogent-power.com/technology/stress-relief-annealing

[25] A. Schoppa, J. Schneider, and C. D. Wuppermann, "Influence of the manufacturing process on the magnetic properties of non-oriented electrical steels," *Journal of Magnetism and Magnetic Materials*, vol. 215–216, pp. 74-78, 6/2/ 2000.

[26] North West Wire EDM. (30/06/2017). *Wire EDM Advantages*. Available:

http://www.northwestwireedm.com/wire_edm_advantages.php

[27] EDM Precision Technologies Ltd. (30/06/2017). *Advantages and Disadvantages EDM*. Available: http://edmprecision.com/advantages-and-disadvantages-edm/

[28] Engineers Edge. (30/06/2017). *Electrical Discharge Machining (EDM) Design Considerations Process Capabilities*. Available: http://www.engineersedge.com/edm.shtml

[29] I. Uslan, "CO2 laser cutting: Kerf width variation during cutting," *Proceedings of the Institution of Mechanical Engineers, Part B: Journal of Engineering Manufacture*, vol. 219, pp. 571-577, 2005.

[30] A. K. Dubey and V. Yadava, "Laser beam machining—A review," *International Journal of Machine Tools and Manufacture*, vol. 48, pp. 609-628, 2008/05/01/ 2008.

[31] Charles Day. (30/06/2017). *Laser Cutting*. Available: http://www.daysteel.co.uk/laser-cutting/

[32] C. Kong, "Water-Jet Cutting," in *CIRP Encyclopedia of Production Engineering*, L. Laperrière and G. Reinhart, Eds., ed Berlin, Heidelberg: Springer Berlin Heidelberg, 2014, pp. 1297-1301.

[33] Charles Day. (30/06/2017). *WaterJet Cutting*. Available: http://www.daysteel.co.uk/waterjet-cutting/

[34] S. Kalpakjian and S. Schmid, *Manufacturing Processes for Engineering Materials*, 5th Edition in SI units ed.: Pearson Education, 2016.

[35] Dragon Laser Ltd. (30/06/2017). *Laser - Quality*. Available: http://www.dragonlaser.co.uk/quality.html

[36] Wingard Hydroblanking. (18/07/2017). *Wingard Hydroblanking*. Available: http://www.hydroblanking.com/hydroblanking.html

[37] T. Nakata, M. Nakano, and K. Kawahara, "Effects of Stress Due to Cutting on Magnetic Characteristics of Silicon Steel," *IEEE Translation Journal on Magnetics in Japan*, vol. 7, pp. 453-457, 1992.

[38] K. Senda, M. Ishida, Y. Nakasu, and M. Yagi, "Influence of shearing process on domain structure and magnetic properties of non-oriented electrical steel," *Journal of Magnetism and Magnetic Materials*, vol. 304, pp. e513-e515, 9// 2006.

[39] L. Vandenbossche, S. Jacobs, F. Henrotte, and K. Hameyer, "Impact of cut edges on magnetization curves and iron losses in e-machines for automotive traction," *The 25th World Battert, Hybrid and Fuel Cell Electric Vihicle Symposium & Exhibition,*

vol. EVS-25, 2010.

[40] M. Emura, F. Landgraf, W. Ross, and J. Barreta, "The influence of cutting technique on the magnetic properties of electrical steels," *Journal of Magnetism and Magnetic Materials*, vol. 254, pp. 358-360, 2003.

[41] E. G. Araujo, J. Schneider, K. Verbeken, G. Pasquarella, and Y. Houbaert, "Dimensional Effects on Magnetic Properties of Fe–Si Steels Due to Laser and Mechanical Cutting," *IEEE Transactions on Magnetics*, vol. 46, pp. 213-216, 2010.

[42] Y. Kurosaki, H. Mogi, H. Fujii, T. Kubota, and M. Shiozaki, "Importance of punching and workability in non-oriented electrical steel sheets," *Journal of Magnetism and Magnetic Materials*, vol. 320, pp. 2474-2480, 10// 2008.

[43] T. Omura, Y. Zaizen, M. Fukumura, K. Senda, and H. Toda, "Effect of Hardness and Thickness of Non-Oriented Electrical Steel Sheets on Iron Loss Deterioration by Shearing Process," *IEEE Transactions on Magnetics*, vol. PP, pp. 1-1, 2015.

[44] H. Cao, L. Hao, J. Yi, X. Zhang, Z. Luo, S. Chen, *et al.*, "The influence of punching process on residual stress and magnetic domain structure of non-oriented silicon steel," *Journal of Magnetism and Magnetic Materials*, vol. 406, pp. 42-47, 5/15/ 2016.

[45] A. Pulnikov, P. Baudouin, and J. Melkebeek, "Induced stresses due to the mechanical cutting of non-oriented electrical steels," *Journal of Magnetism and Magnetic Materials*, vol. 254–255, pp. 355-357, 1// 2003.

[46] G. Loisos and A. J. Moses, "Effect of mechanical and Nd:YAG laser cutting on magnetic flux distribution near the cut edge of non-oriented steels," *Journal of Materials Processing Technology*, vol. 161, pp. 151-155, 4/10/ 2005.

[47] R. Rygal, A. J. Moses, N. Derebasi, J. Schneider, and A. Schoppa, "Influence of cutting stress on magnetic field and flux density distribution in non-oriented electrical steels," *Journal of Magnetism and Magnetic Materials*, vol. 215–216, pp. 687-689, 6/2/ 2000.

[48] A. Peksoz, S. Erdem, and N. Derebasi, "Mathematical model for cutting effect on magnetic flux distribution near the cut edge of non-oriented electrical steels," *Computational Materials Science*, vol. 43, pp. 1066-1068, 10// 2008.

[49] R. Siebert, J. Schneider, and E. Beyer, "Laser Cutting and Mechanical Cutting of Electrical Steels and its Effect on the Magnetic Properties," *IEEE Transactions on Magnetics*, vol. 50, pp. 1-4, 2014.

[50] H. Naumoski, B. Riedmüller, A. Minkow, and U. Herr, "Investigation of the influence of different cutting procedures on the global and local magnetic properties of non-oriented electrical steel," *Journal of Magnetism and Magnetic Materials,* vol. 392, pp. 126-133, 10/15/ 2015.

[51] M. Hofmann, H. Naumoski, U. Herr, and H. Herzog, "Magnetic Properties of Electrical Steel Sheets in Respect of Cutting: Micromagnetic Analysis and Macromagnetic Modeling," *IEEE Transactions on Magnetics,* vol. PP, pp. 1-1, 2015.

[52] A. Schoppa, H. Louis, F. Pude, and C. von Rad, "Influence of abrasive waterjet cutting on the magnetic properties of non-oriented electrical steels," *Journal of Magnetism and Magnetic Materials,* vol. 254–255, pp. 370-372, 1// 2003.

[53] Y. Liu, S. K. Kashif, and A. M. Sohail, "Engineering considerations on additional iron losses due to rotational fields and sheet cutting," in *2008 18th International Conference on Electrical Machines*, 2008, pp. 1-4.

[54] G. von Pfingsten, S. Steentjes, A. Thul, T. Herold, and K. Hameyer, "Soft magnetic material degradation due to manufacturing process: A comparison of measurements and numerical simulations," in *Electrical Machines and Systems (ICEMS), 2014 17th International Conference on*, 2014, pp. 2018-2024.

[55] M. Bali and A. Muetze, "Modeling the Effect of Cutting on the Magnetic Properties of Electrical Steel Sheets," *IEEE Transactions on Industrial Electronics,* vol. 64, pp. 2547-2556, 2017.

[56] Z. Gmyrek, A. Cavagnino, and L. Ferraris, *Estimation of Magnetic Properties and Damaged Area Width Due to Punching Process: Modeling and Experimental Research*. New York: IEEE, 2012.

[57] Z. Gmyrek, A. Cavagnino, and L. Ferraris, "Estimation of the Magnetic Properties of the Damaged Area Resulting From the Punching Process: Experimental Research and FEM Modeling," *Industry Applications, IEEE Transactions on,* vol. 49, pp. 2069-2077, 2013.

[58] M. Bali, H. D. Gersem, and A. Muetze, "Determination of Original Nondegraded and Fully Degraded Magnetic Properties of Material Subjected to Mechanical Cutting," *IEEE Transactions on Industry Applications,* vol. 52, pp. 2297-2305, 2016.

[59] M. Bali, H. De Gersem, and A. Muetze, "Finite-Element Modeling of Magnetic Material Degradation Due to Punching," *IEEE Transactions on Magnetics,* vol. 50,

pp. 745-748, 2014.

[60] F. Ossart, E. Hug, O. Hubert, C. Buvat, and R. Billardon, "Effect of punching on electrical steels: Experimental and numerical coupled analysis," *Magnetics, IEEE Transactions on*, vol. 36, pp. 3137-3140, 2000.

[61] S. Elfgen, S. Boehmer, S. Steentjes, D. Franck, and K. Hameyer, "Continuous model of magnetic material degradation due to cutting effects in the numerical simulation of electro laminations," in *IKMT 2015; 10. ETG/GMM-Symposium Innovative small Drives and Micro-Motor Systems*, 2015, pp. 1-6.

[62] L. Vandenbossche, S. Jacobs, X. Jannot, M. McClelland, J. Saint-Michel, and E. Attrazic, "Iron loss modelling which includes the impact of punching, applied to high-efficiency induction machines," in *Electric Drives Production Conference (EDPC), 2013 3rd International*, 2013, pp. 1-10.

[63] V. Maurel, F. Ossart, and R. Billardon, "Residual stresses in punched laminations: Phenomenological analysis and influence on the magnetic behavior of electrical steels," *Journal of Applied Physics*, vol. 93, pp. 7106-7108, 2003.

[64] G. Crevecoeur, P. Sergeant, L. Dupre, L. Vandenbossche, and R. Van de Walle, "Analysis of the Local Material Degradation Near Cutting Edges of Electrical Steel Sheets," *IEEE Transactions on Magnetics*, vol. 44, pp. 3173-3176, 2008.

[65] D. Eggers, S. Steentjes, and K. Hameyer, "Advanced Iron-Loss Estimation for Nonlinear Material Behavior," *IEEE Transactions on Magnetics*, vol. 48, pp. 3021-3024, 2012.

[66] J. Gyselinck, L. Vandevelde, J. Melkebeek, P. Dular, F. Henrotte, and W. Legros, "Calculation of eddy currents and associated losses in electrical steel laminations," *IEEE Transactions on Magnetics*, vol. 35, pp. 1191-1194, 1999.

[67] S. Steentjes, M. Lessmann, and K. Hameyer, "Advanced iron-loss calculation as a basis for efficiency improvement of electrical machines in automotive application," in *Electrical Systems for Aircraft, Railway and Ship Propulsion (ESARS), 2012*, 2012, pp. 1-6.

[68] S. Zurek. (07/04/2015) Rotational Magnetisation. *Transformers Magazine*. Available: https://www.researchgate.net/publication/286778874_Rotational_magnetisation

[69] S. Steentjes, G. von Pfingsten, and K. Hameyer, "An Application-Oriented Approach for Consideration of Material Degradation Effects Due to Cutting on Iron Losses and Magnetizability," *IEEE Transactions on Magnetics*, vol. 50, pp. 1-4,

2014.

[70] A. Ahmed Abou-Elyazied and D. Luc, "A Rogowski–Chattock coil for local magnetic field measurements: sources of error," *Measurement Science and Technology*, vol. 21, p. 107003, 2010.

[71] E. Werner, "Austrian Patent no 191 015," Austria Patent 191015, 1949.

[72] O. Stupakov, "System for controllable magnetic measurement with direct field determination," *Journal of Magnetism and Magnetic Materials,* vol. 324, pp. 631-636, 2// 2012.

[73] Honeywell, "Sensing and Control Interactive Catalog," in *Solid State Hall Effect Sensors SS490 Series* ed.

[74] T. Yamaguchi, K. Senda, M. Ishida, K. Sato, A. Honda, and T. Yamamoto, "Theoretical analysis of localized magneticflux measurement by needle probe," *Journal de Physique iv,* 1998.

[75] S. Zurek, T. Meydan, and A. J. Moses, "Analysis of twisting of search coil leads as a method reducing the influence of stray fields on accuracy of magnetic measurements," *Sensors and Actuators A: Physical,* vol. 142, pp. 569-573, 4/10/ 2008.

[76] G. Loisos and A. J. Moses, "Critical evaluation and limitations of localized flux density measurements in electrical steels," *IEEE Transactions on Magnetics,,* vol. 37, pp. 2755-2757, 2001.

[77] H. Pfutzner and G. Krismanic, "The needle method for induction tests: sources of error," *Magnetics, IEEE Transactions on,* vol. 40, pp. 1610-1616, 2004.

[78] M. De Wulf, L. Dupré, D. Makaveev, and J. Melkebeek, "Needle-probe techniques for local magnetic flux measurements," *Journal of Applied Physics,* vol. 93, pp. 8271-8273, 2003.

[79] G. Loisos and A. J. Moses, "Demonstration of a new method for magnetic flux measurement in the interior of a magnetic material," *Sensors and Actuators A: Physical,* vol. 106, pp. 104-107, 9/15/ 2003.

[80] S. Zurek and T. Meydan, "A novel capacitive flux density sensor," *Sensors and Actuators A: Physical,* vol. 129, pp. 121-125, 2006/05/24/ 2006.

[81] National Instruments, "NI 6115/6120 Specifications," ed.

[82] S. Zurek, P. Marketos, T. Meydan, and A. J. Moses, "Use of novel adaptive digital feedback for magnetic measurements under controlled magnetizing conditions," *IEEE Transactions on Magnetics,* vol. 41, pp. 4242-4249, 2005.

[83] UKAS, "M3003: The expression of uncertainty and confidence in measurement.," ed.

[84] A. Ghasemi and S. Zahediasl, "Normality Tests for Statistical Analysis: A Guide for Non-Statisticians," *International Journal of Endocrinology and Metabolism,* vol. 10, pp. 486-489, 2012.

[85] M. Takashima, M. Komatsubara, and N. Morito, "{001}<210>; Texture Development by Two-stage Cold Rolling Method in Non-oriented Electrical Steel," *ISIJ International,* vol. 37, pp. 1263-1268, 1997.

[86] D. Hull and D. J. Bacon, "Chapter 8 - Origin and Multiplication of Dislocations," in *Introduction to Dislocations (Fifth Edition)*, ed Oxford: Butterworth-Heinemann, 2011, pp. 157-169.

[87] D. Roylance. (2001). *The Dislocation Basis of Yield and Creep*.

[88] O. Hamrit, O. d. l. Barrière, M. LoBue, and F. Mazaleyrat, "Anisotropy of Losses in Non-Oriented Iron Silicon Sheets: Influence on Electrical Machine Applications," *IEEE Transactions on Magnetics,* vol. 52, pp. 1-7, 2016.

[89] B. Cornut, A. Kedous-Lebouc, and T. Waeckerlé, "From metallurgy to modelling of electrical steels: A multiple approach to their behaviour and use based on physics and experimental investigations," *Journal of Magnetism and Magnetic Materials,* vol. 160, pp. 102-108, 1996/07/01/ 1996.

[90] K. Chwastek, "Anisotropic properties of non-oriented steel sheets," *IET Electric Power Applications,* vol. 7, pp. 575-579, 2013.

[91] J. Schindelin, C. T. Rueden, M. C. Hiner, and K. W. Eliceiri, "The ImageJ ecosystem: an open platform for biomedical image analysis," *Molecular reproduction and development,* vol. 82, pp. 518-529, 2015.

[92] J. Schindelin, I. Arganda-Carreras, E. Frise, V. Kaynig, M. Longair, T. Pietzsch, *et al.*, "Fiji: an open-source platform for biological-image analysis," *Nature Methods,* vol. 9, 2012.

[93] ASTM, "E112-12, Standard Test Methods for Determining Average Grain Size," ed. ASTM International, West Conshohocken, PA, 2012.

[94] T. Omura, Y. Zaizen, M. Fukumura, K. Senda, and H. Toda, "Effect of Hardness and Thickness of Nonoriented Electrical Steel Sheets on Iron Loss Deterioration by Shearing Process," *IEEE Transactions on Magnetics,* vol. 51, pp. 1-4, 2015.